ADVANCING THE FUNDAMENTAL UNDERSTANDING OF ACTIVE LAYER FORMATION FOR DEVELOPING HIGH-PERFORMANCE NANOFILTRATION MEMBRANE

By

Yuanzhe Liang

Dissertation

Submitted to the Faculty of the

Graduate School of Vanderbilt University

in partial fulfillment of the requirements

for the degree of

DOCTOR OF PHILOSOPHY

In

Interdisciplinary Material Science

December 12, 2020

Nashville, Tennessee

Approved:

Shihong Lin, Ph.D.

Jian Jin, Ph.D.

Kane Jennings, Ph.D.

Piran Kadimbi, Ph.D.

Kelsey Hatzell, Ph.D.

To my family and friends,

who accompanied, supported, and loved me along the journey

ACKNOWLEDGEMENTS

I express my sincere gratitude to Dr. Shihong Lin, my Ph.D. advisor, not only for his guidance and support in my research work, but also for his trust and kindness throughout my four-year study. Dr. Lin took me in his group when I had trouble continuing my Ph.D. and needed transferring research groups immediately at the end of my first-year Ph.D. study, and then provided me such an amazing platform where I enjoy the fun of research and develop experimental, thinking and writing skills in order to become an independent researcher. His enthusiasm for science and work, care and respect for students also greatly influence me in my future academic career.

I am thankful and fortunate to work with Dr. Jian Jin and Dr. Yuzhang Zhu, from suzhou institute of nano-tech and nano-bionics (SINANO), CAS, who provided indispensable support to my research project and enlightened me in pursuing my Ph.D. degree. I appreciate Dr. Kane Jennings, Dr. Piran Kadimbi and Dr. Kelsey Hatzell for being my dissertation committee members.

I am also indebted to the former and present members of Dr. Lin's group for their care, advice and friendship: Yuxi Huang, Kofi Christie, Zhangxin Wang, Li Wang, Yuanmiaoliang Chen, Drew Horseman, Ruoyu Wang, Fei Gao, Yujiao Li and Rui Chen.

Last but not the least, I express my greatest thankfulness to my parents, Mr. Xiaodong Liang and Mrs. Liying Huo, for their unconditional love and support. Thank my parents for doing everything possible to put me on the path to greatness. Without them, I would not be who I am today.

TABLE of CONTENTS

Page

LIST OF TABLES

Table Page

LIST OF FIGURES

Figure Page

CHAPTER 1

INTRODUCTION

1.1.Coping with global water scarcity: desalination technology

Growing water scarcity is one of the leading challenges of our time, impacting over one-third of the world's population[1]. The challenge of supplying fresh water for the world's inhabitants is further exaggerated due to the rapid population growth and pollution from industrial, agricultural and untreated human waste[2]. At this time, the demand for new sources of freshwater is motivating scientists and engineers worldwide to seek efficient technological solutions to alleviate the stress of water supply. While several measures have been taken to improve water-usage efficiency among the industrial and domestic water consumption, these methods can only improve the usage of existing water resources instead of increasing them. The only approach to increasing the available water supply is through desalination and water purification[3].

State-of-the-art desalination technologies consist of two major categories, i.e., thermal and membrane technologies[4]. Thermal desalination process, e.g., multistage flash distillation (MSF), multi-effect distillation (MED) and vapor compression (VC), involves heating the feedwater source to generate water vapor, which is then condensed and collected as clean water[5]. Membrane-based desalination generally falls into two types, a pressure-driven process, e.g., reverse osmosis (RO)[6] and nanofiltration (NF)[7], and a voltage-driven process, e.g., electrodialysis (ED)[8] and capacitive deionization (CDI)[9]. In comparison to most existing desalination technologies, pressure-driven membrane processes represent a more promising, energy-efficient, and cost-effective approach for fast, continuous molecular separations and water purification[10].

1.2.Overview of Pressure-driven membrane technology

In essence, a membrane is a discrete, thin barrier that permits the selective mass transport of solutes and solvents across the interface. Separation is achieved by selectively passing one or more components of a stream through the membrane while retarding the passage of one or more

other components. Pressure-driven membrane separation represents a highly-efficient approach to achieving molecular level separation because it requires only one-tenth energy to process an equivalent amount of liquid as compared to other industrial separation processes, e.g., evaporation and distillation, due to the latent heat of vaporization[4,11]. Therefore, synthetic membranes are widely used in many technically and commercially relevant separation processes, from industrial-scale ones—seawater desalination, wastewater reclamation, and gas separation to small scale processes—dialysis, sterile filtration, and chemical purification[12]. The common pressure-driven membrane processes are primarily distinguished from each other in terms of the molecular size of the solutes that they can remove, for example, Microfiltration (MF, 0.1-10 um), Ultrafiltration (UF 1-100 nm), Nanofiltration (NF, 0.1-10 nm) and Reverse Osmosis (RO, <0.1 nm)[13].

In general, pressure-driven membrane separation enables two kinds of separation processes, solute-solvent separation, and solute-solute separation. In a solute-solvent separation process, a feed solution containing a series of solutes passes through a semipermeable membrane driven by pressure, thus producing a permeate stream containing fewer solutes and a waste stream, referred to as retentate, containing a high concentration of solutes. In a solute-solute separation process, a feeds stream containing multiple solute species permeates through the membrane, and the separation results from different transport rates of various solutes through the semipermeable membrane.

In a specific separation process, the characteristics of the feed solution and the desired permeate quality determine the choice of the membrane type, module design, operation condition, etc. In addition, pretreatment is often required to remove certain oxidative or reactive chemicals to prevent the degradation of membranes, for example, ultrafiltration and nanofiltration are used to remove chlorine in an RO system to prevent the degradation of the polyamide selective layer[14]. Post-treatment consideration often includes remineralization of permeate and pH adjustment[6,15,16]. Last but not the least, the use of anti-scaling agents should also be considered to prevent membrane scaling or in discharge outlets due to the concentration of calcium sulfate, magnesium carbonate, etc., above their solubility[17,18].

1.3.Nanofiltration: a fast and precise molecular sieving process

Nanofiltration (NF) has received increasing interest in recent years due to its strong potential in addressing many of the environmental problems under growing stringent regulations and higher requirements for water quality in a variety of applications[7,19–22]. It is technically competent in many applications including, but not limited to, desalination of brackish groundwater, water softening, and wastewater reuse[23,24,25]. With properties in between reverse osmosis (RO) and ultrafiltration (UF)[26], NF membranes are potent in the separation of monovalent/divalent inorganic salts and small organic molecules (Molecular weight cutoff, MWCO > 200 Da) with several folds' water permeability higher than RO[19]. The separation mechanism of NF membrane involves multiple physicochemical phenomena, i.e., Donnan (charge), steric (size) and dielectric exclusion[27,28], ion dehydration, etc. Specifically, solutes with larger hydrated radii than the pore size of the NF membrane are retained due to size sieving[29], meanwhile, the surface charge electrostatically repels co-ions and attracts counterions[30]. These properties have allowed NF to be used not only in the solute/solvent separations but more importantly in the solute/solute separations. This type of "molecular sieving" separation has important applications in pharmaceutical[31], petrochemical[19], and energy industries[27,32].

Thin-film-composite (TFC) polyamide-based NF membranes have served as the industry's gold-standard membranes for more than thirty years[19,33]. The polyamide active layer of TFC-PA NF membranes is formed via the interfacial polymerization (IP). IP was first discovered in 1959 and remains the state-of-the-art method for large-scale fabricating commercial polyamide nanofiltration (NF) and reverse osmosis (RO) thin-film-composite (TFC) membranes[7,34–36]. In this process, an ultrafiltration (UF) membrane (as the support layer) is wetted with an aqueous amine solution and then brought into contact with an immiscible organic solution containing acid chloride. Upon contact, amine molecules diffuse from the pores of the support membrane, across the water/oil interface, and react with acid chlorides in the oil phase to form the polyamide network[37].

There is a whole other class of nanofiltration membranes fabricated by Layer-by-layer polyelectrolyte multilayer assembly[38,39]. In fabricating PEM-NF membranes using LbL deposition of polyelectrolyte, two types of oppositely charged polyelectrolytes alternately deposit onto an ultrafiltration membrane substrate. The irreversible LbL deposition of polyelectrolytes is mainly driven by electrostatic attractions between the oppositely charged polyelectrolytes[40–43]. Several critical membrane properties, such as the pore size distribution, surface charge, active layer

thickness, are affected by multiple factors in the LbL deposition process, such as the type of polyelectrolytes[44,45], polyelectrolyte concentration[44], ionic strength of the polyelectrolyte solution [46–48], pH[49–51], and temperature[52,53]. Adjusting these parameters provides avenues to control the membrane permeance and ion selectivity. Beyond these parameters, integrating various types of additives (e.g., nanomaterials) into the PEM is also a widely explored approach to enhance the perm-selectivity[54,55].

1.4.Designing the next generation separation membrane

Increasing demands for more energy-efficient and more precise separations in the applications including desalination, chemical synthesis, and gas separation have stimulated the vigorous research interests in designing the next generation separation membranes[12,56–59]. All synthetic membranes suffer from the intrinsic trade-off between membrane permeability and selectivity, which are the most important membrane performance metrics, with the former affecting the pressure required for separation and overall energy consumption, and the later determining the target application where the membrane is useful. A recent analysis suggests that increasing water permeability of reverse osmosis (RO) membranes beyond the state of the art has an only marginal contribution to reducing the energy consumption or membrane area, mostly due to concentration polarization (CP)[56]. However, for NF applications, CP has a much smaller impact on energy consumption or flux because (1) the feed osmotic pressure is fairly low, (2) NF membranes are permeable to solutes that contribute to a large fraction of the feed osmotic pressure, and thus do not cause significant accumulation of salts near the membrane surface. Therefore, enhancing the water permeability of an NF membrane without sacrificing its rejection of target solutes will have a significant positive impact on reducing either the capital or operating cost of NF[60]. Specifically, for the same operating pressure, an NF membrane with enhanced permeability will significantly improve the water flux and thus reduce the required membrane area for achieving target productivity, thereby reducing the capital cost. For the same membrane area, the use of an NF membrane with enhanced water permeability will significantly reduce the operating pressure required to achieve a certain flux, thereby reducing the energy cost. In the past few decades, membrane scientists have made numerous attempts to enhance the membrane permeability without undermining the membrane selectivity including (1) incorporation of nanoparticles (e.g., TiO_2[61–

[63], silica[64–66], silver[67,68], MOF[69–71], etc.) to enhance the surface hydrophilicity and construct water channels, (2) surface modification with hydrophilic functional groups (e.g., PEG[72–74], polydopamine[75–77], zwitterionic molecules[78], chlorine-resistant coatings[79,80]) to increase the surface hydrophilicity, reduce surface roughness and membrane fouling, and enhance the membrane resistance to chloride attack, (3) use of sacrificial templates (e.g., ZIF[81,82], MOF[83,84], and metal hydroxide[85,86]) as the support substrate in the fabrication of NF membranes during IP and LBL, to promote the formation of a thinner active layer and increase the excess surface area ratio.

Another important avenue to next-generation separation membrane leads to the design of the molecular sieving membrane for precise solute/solute separation[58]. Compared to solvent/solute separations, solute/solute separation is much more challenging because it demands that the membranes have pores that are not only sufficiently small enough to reject the smallest 'unwanted' solutes but also sufficiently uniform so that small and large solutes can be separated, i.e., large solutes can be completely rejected by the membrane whereas small solutes can mostly pass through the membrane[58]. When the size difference between the two solutes to be separated is small, a very high degree of uniformity of pore size is required to achieve the target separation[58].

For separation of micron-sized particles, track-etched membranes with highly uniform pore sizes have been successfully commercialized[87]. For the separation of nanoscale particles, such as biomolecules, recent advances in using self-assembled soft materials have enabled the potentially scalable fabrication of membranes with highly uniform nanoscale pores[59]. Therefore, the most challenging solute/solute separation is that of solutes on the sub-nanometer scale. Such separation has important applications in low-energy water softening, mineral extraction, organic solvent separation, and pharmaceutical separations[10,88,89].

Fabricating highly uniform sub-nanometer scale "pores" is technically challenging. Notable recent efforts include the stacking of two-dimensional nanomaterials (2-D NMs)[58,59,71]. Examples including graphene oxide (GO), molybdenum disulfide and zeolite nanosheets have been proposed as a scalable method of producing laminated membranes to enable molecular-level sieving[90–92]. GO and its chemical derivatives have been the most studied materials due to its high perm-selectivity, low fabrication costs, and excellent chemical resistance[93]. However, stacked GO membranes suffer from swelling in aqueous solutions, which increases interlayer spacing to the degree that is no longer suitable for ionic separation[94]. Other recent approaches

include the development of polymer membranes with intercalated and aligned carbon nanotubes, biological water channel proteins (e.g., aquaporin), and biomimetic artificial water-channels[1,59,95–97]. While these approaches are fundamentally intriguing and have shown promise in developing membranes for precise chemical separation, scaling them up for roll-to-roll fabrication is very challenging.

Given the advantages of the TFC-PA nanofiltration membranes, such as large-scale fabrication, low separation cost, long membrane lifetime, etc., TFC-PA-based membranes have served the desalination industry for more than three decades. Although many researchers have been exploring new materials, such as graphene, GO[90–92], MOF[71], aquaporin[98], etc., none of which outperform the conventional TFC-PA membranes. Therefore, the TFC-PA-based membrane is an ideal candidate as the next-generation separation membrane for precise separation. However, fabricating TFC-PA membranes with highly uniform pores that are suitable for solute/solute separations remains challenging using IP, especially considering that IP is a very fast interfacial process involving multiple phenomena and is thus prone to generate heterogeneity[35,36,99].

1.5.Objectives and Hypothesis

The overarching goal of this dissertation is to advance the fundamental understandings of the active layer formation mechanism of two most commonly used NF membranes, i.e., TFC-PA NF membranes and polyelectrolyte multilayer NF membranes, and to design and fabricate the next-generation nanofiltration membranes with multi-fold enhancement of perm-selectivity. There are three specific objectives as below:

The first objective is to develop a universally applicable approach (i.e. independent of monomer species) that enables the formation of highly uniform “pores” (or more precisely, free volume) in the PA active layer in NF membranes formed via interfacial polymerization. Our core hypothesis is that the IP process can be regulated by the presence of a dynamically self-assembled and highly organized “network” of surfactants at the hexane/water interface to form a PA active layer with significantly enhanced homogeneity (of pore size), which will enable ultra-sharp selectivity that is required for precise solute/solute separation. The specific objectives serving the over-arching goal include

- Demonstrate that selected surfactants can indeed sharpen the selectivity of the TFC-PA NF membrane and enable more precise solute/solute separations.
- Investigate the impact of the functional groups and structures of the surfactants on the material properties and separation performance of the TFC-PA NF membrane formed via SARIP.
- Investigate the impact of surfactant self-assemblies on the kinetics of amine diffusion across hexane/water interface in the absence and presence of polymerization (with acid chloride).

The second objective is to develop high-performance nanofiltration (NF) membranes using layer-by-layer (LbL) deposition of polyelectrolytes with the integration of surfactant micelles. The novelty of the proposed membrane fabrication approach is the innovative use of surfactant micelles as an additive to create a unique structure of the semipermeable layer. We hypothesize that the novel polyelectrolyte/micelle multilayer nanofiltration membranes (PMM NF) will have significantly better performance than the conventional polyelectrolyte multilayer nanofiltration membranes (PM NF). The specific objectives serving the over-arching goal include

- Assess whether surfactant micelle integration is a universally applicable approach for improving the performance of NF membranes fabricated using LbL deposition.
- Investigate the impact of the functional groups and structures of the surfactants on the material properties and separation performance of polyelectrolyte/micelle multilayer nanofiltration membranes.
- Investigate the state of surfactants on an oppositely charged surface and mechanism of performance enhancement due to the intercalation of surfactant micelles.

The third objective is to develop a technique based on four-electrode electrochemical impedance spectroscopy (EIS) system for studying the kinetics of polyelectrolyte adsorption onto porous support in the context of fabricating PEM nanofiltration (NF) membrane. We hypothesize that the four-electrode EIS system is capable of detecting subtle electro-chemical changes of the properties in the solution near the membrane surface and in the polyelectrolyte

multilayer in each deposition step, which is able to reflect the kinetics of polyelectrolyte adsorption. The specific objectives serving the over-arching goal include

- Demonstrate that the four-electrode EIS system enables the defection of change of solution property (interfacial solution resistance) and polyelectrolyte multilayer property (film resistance) in the layer-by-layer deposition of PEM.
- Correlate the interfacial solution resistance and film resistance extracted from the EIS measurements with the NF performance of the PEM membrane.
- Investigate the impact of types and structures of various polyelectrolytes on the adsorption kinetics in the context of fabricating the PEM nanofiltration (NF) membrane.

1.6.Structure of the Dissertation

This dissertation is organized into seven chapters. Chapter 1 gives a brief introduction to the membrane-based separation technology, in particular, nanofiltration membrane, and summarizes the challenges of designing the next-generation separation membrane. In chapter 2, we investigate the limitations of the conventional interfacial polymerization for TFC-PA NF membrane fabrication and propose a novel approach to regulate the conventional IP reaction via the addition of ionic surfactants, which leads to TFC-PA membranes with sub Angstrom-level precision separation. In chapter 3, we explore the role of nonionic hydrophilic and lipophilic surfactants in IP on the formation of TFC-PA NF membranes as compared to the ionic surfactants in the previous chapter. Chapter 4 presents a mechanistic study of the layer-by-layer self-assembly of polyelectrolyte multilayer NF membranes with the addition of surfactant assemblies and demonstrates a universally applicable method of enhancing the perm-selectivity of polyelectrolyte multilayer NF membranes for effective salt removal. In Chapter 5, we employ the methodology reported in chapter 4 to fabricate a ‘loose’ polyelectrolyte multilayer nanofiltration with a ~ 5-fold increase of permeability for natural organic matters and dye removal. Chapter 6 reports a novel approach based on electrochemical impedance spectroscopy for in-situ monitoring of the adsorption kinetics in preparing polyelectrolyte multilayer nanofiltration membranes using a layer-by-layer deposition. Chapter 7 summarizes the major discoveries of the work in this dissertation.

CHAPTER 2

POLYAMIDE NANOFILTRATION MEMBRANE WITH HIGHLY UNIFORM SUB-NANOMETRE PORES FOR SUB-1 Å PRECISION SEPARATION

This chapter has been published in *Nature communications* as the following peer-reviewed manuscript: Liang, Y., Zhu, Y., Liu, C., Lee, K. R., Hung, W. S., Wang, Z., ... & Lin, S. (2020). Polyamide nanofiltration membrane with highly uniform sub-nanometre pores for sub-1 Å precision separation. *Nature Communications*, 11(1), 1-9.

2.1.Introduction

Membranes capable of precise separation of ions and small molecules will have a transformative impact on the energy, water, chemical, and pharmaceutical industries[1,3,58,92,100]. Such separations require membranes with highly uniform pore sizes to obtain precise molecular sieving and solute differentiation[101,102], which has been technically challenging to achieve. While the fabrication of highly precise membranes has been attempted recently using approaches such as stacking 2D nanomaterials or integrating aligned synthetic or biological channels[94,103,104], no study thus far reported sub-Angstrom precision for separating sub-nanometer sized solutes in membrane filtration under applied pressure and crossflow. Moreover, these approaches face substantial technical challenges for the scalable fabrication of defect-free membranes[105].

Nanofiltration (NF) based on thin-film-composite polyamide (TFC-PA) membranes is a mature and energy-efficient technology for separating small solutes from liquid solvents[7,10,34]. The selective layer of polyamide-based NF membranes is formed by interfacial polymerization (IP) on a porous support. In a typical IP process, amine monomers in an aqueous solution diffuse into an organic solvent phase where they vigorously react with acyl chlorides at the water/organic interface via a Schotten-Baumann reaction[35,106]. Such uncontrolled diffusion and fast polymerization form a polyamide (PA) layer with multiscale heterogeneity and non-uniform pore sizes[99,107]. The mechanism of IP continues to attract heightened research interest due to the substantial use of TFC-PA membranes for desalination and water purification along with the lack of a thorough understanding of IP. While recent studies have explored different ways to improve the perm-selectivity of PA membranes[108–110], achieving precise separation of ions and small

molecules using PA membranes requires enhancing the pore size homogeneity, which entails a paradigm shift in engineering the PA active layer.

Here, we demonstrate the fabrication of an ultra-selective TFC-PA NF membrane capable of remarkable precise separation via alteration of the conventional IP process. In conventional IP, the NF membrane is formed via irreversible polymerization between piperazine (PIP) and trimesoyl chloride (TMC) at the water/hexane interface (Figure 2.1A). To fabricate an ultra-selective NF membrane, we create a self-assembled network of amphiphiles at the water/hexane interface via the addition of sodium dodecyl sulfate (SDS). The well-organized and flexible interfacial network regulates the transport of PIP across the interface (Figure 2.1A), forming a PA active layer with a highly uniform pore size distribution. Such an IP process in the presence of a self-assembled surfactant interfacial network is herein referred to as surfactant-assembly-regulated interfacial polymerization, or SARIP.

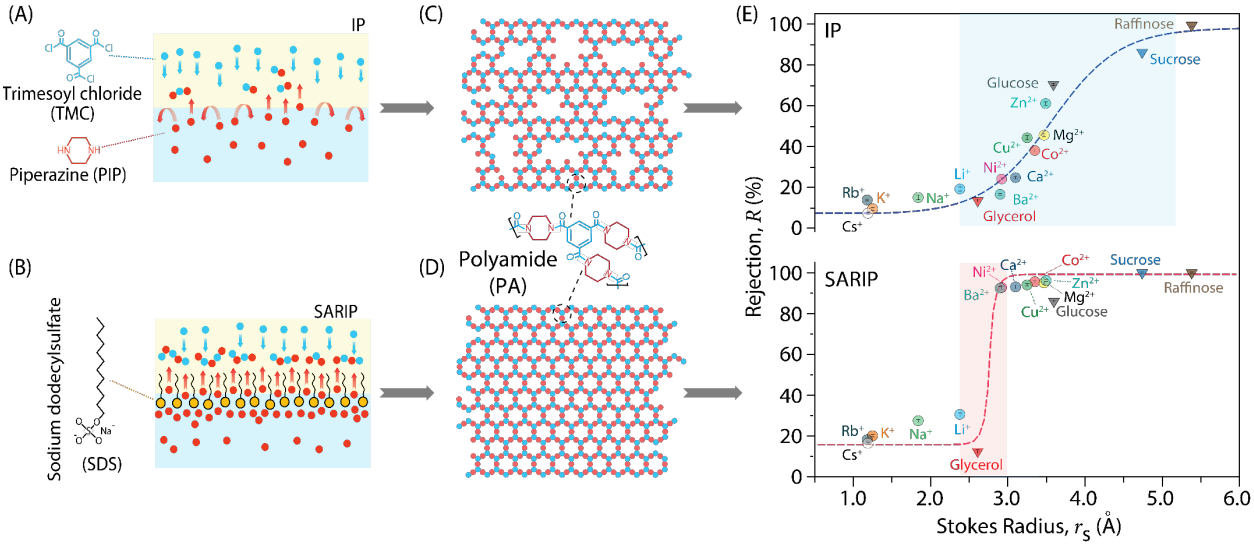

Figure 2.1 Conventional IP vs. SARIP. Schematic illustration of (A) the conventional IP and (A) SARIP. In both cases, PIP molecules in aqueous phase diffuse across the water/hexane interface to react with TMC in the hexane phase. In SARIP, SDS molecules added into the aqueous phase form a self-assembled dynamic network at the interface and regulate the interfacial transport of PIP. (C, D) Schematic illustrations of the PA active layer formed via conventional IP (top), which has heterogeneous pore size distribution, and SARIP (bottom), which has uniform pore size distribution. (E) Rejection of different solutes (circles for cations and inverted triangles for neutral organics) as a function of the Stokes radius for the PA membranes fabricated using conventional IP (top) and SARIP (bottom). Ion rejection vs. hydrated radius is also presented in

Figure A.1 and Table A.1, which demonstrates a qualitatively similar comparison between the two PA membranes as shown here. The aqueous SDS concentration in SARIP is 2.1 mM. The rejection of different species was measured from NF experiments with the respective membranes using a cross-flow filtration cell with an operating pressure of 4 bar and a crossflow velocity of 2.9 cm s^{-1}. Rejection data of each solute represents the average of three runs and error bar represents the standard deviation of three replicate measurements.

2.2.Materials and methods

2.2.1. Materials and chemicals

Piperazine (PIP, 99%), trimesoyl chloride (TMC, >98%), sodium dodecyl sulfate (SDS, ≥ 99.0%), hexadecyltrimethylammonium bromide (CTAB, BioXtra ≥ 99%), 3-(N,N-Dimethylmytristylammonio) propane sulfonate (SB3-14, ≥ 98%), sodium dodecylbenzene sulfonate (SDBS, technical grade), sodium p-toluene sulfonate (95%) poly(ethyleneimine) solution (average Mn ~ 10000, 50% in water), glycerol (≥ 99%), anhydrous D-(+)-Glucose, sucrose (≥99.5%), D-(+)-Raffinose pentahydrate (≥ 98%), $K_3Fe(CN)_6$ (≥ 99%), Na_2SO_4 (≥ 99%), $MgSO_4$ (≥ 99.5%), $ZnCl_2$ (99.99%), $CuCl_2$ (99.99%), $MgCl_2$ (≥ 99.99%), $CoCl_2$ (99.9%), $CaCl_2$ (≥ 97%), $NiCl_2$ (98%), $BaCl_2$ (99.99%), LiCl (≥ 99%), NaCl (≥ 99%), KCl (≥ 99%), RbCl (≥ 99%), CsCl (99.9%) were purchased from Sigma Aldrich (St. Louis, MO) and were all used as received. Anhydrous N-hexane and ethanol (HPLC) were purchased from Fisher Scientific. Polyester sulfone ultrafiltration (NADIR UH050, MWCO 50000 Da) membrane was purchased from Microdyn-Nadir (Germany).

2.2.2. Membrane fabrication

2.2.2.1.Preparation of Poly(piperazine-amide) nanofiltration membrane via conventional interfacial polymerization (IP)

Interfacial polymerization was first discovered in 1959 and remains a state-of-the-art method for large-scale fabricating commercial polyamide nanofiltration (NF) and reverse osmosis (RO) thin-film-composite (TFC) membranes[7,34–36]. In this process, an ultrafiltration (UF)

membrane (as the support layer) is wetted with an aqueous amine solution and then brought into contact with an immiscible organic solution containing acid chloride. Upon contact, amine molecules diffuse from the pores of the support membrane, across the water/oil interface, and react with acid chlorides in the oil phase to form the polyamide network.

In this study, conventional IP was performed using an aqueous solution of 0.25 % w/v piperazine and an n-hexane solution of 0.2 % w/v trimesoyl chloride on a commercial polyethersulfone (PES) UF membrane as the support layer. In the following discussion, all IP or SARIP recipes use this specified concentration of PIP and TMC unless otherwise noted. The PES UF membrane was first placed on a glass plate and then impregnated with a PIP solution for 30 s. The glass plate was drained vertically, and a rubber roller was used to remove excess PIP solution from the UF membrane surface. Then the TMC solution was poured onto the membrane surface for another 30 s which resulted in the formation of a polyamide active layer over the PES membrane. The resulting TFC-PA membrane was immersed in n-hexane for 30 s to remove unreacted TMC, then heat-cured at 60 ^{o}C for 30 min to increase the crosslinking degree of the polyamide network. The membrane after heat curing was stored in water at 4 ^{o}C to promote the hydrolysis of unreacted chloride groups in the polyamide network.

2.2.2.1.1. Poly(piperazine-amide) nanofiltration membrane from conventional IP with varying PIP concentrations

Conventional interfacial polymerization was conducted with varying PIP concentrations to study the effect of PIP concentration on the polyamide structure and performance. The PIP concentrations tested are 0.05 % w/v, 0.15 % w/v, 0.25 % w/v and 0.5 % w/v. The TMC concentration remained as 0.2 % w/v in all cases.

2.2.2.1.2. Poly(piperazine-amide) nanofiltration membrane from conventional IP (with sodium p-toluene sulfonate)

Sodium p-toluenesulfonate was added to PIP aqueous solution, as a comparison to sodium dodecyl sulfate, to study the effect of sulfate groups on the polyamide structure and performance. The concentrations of sodium p-toluenesulfonate correspond to the same molar concentration of sulfate groups as sodium dodecyl sulfate in water (4.1 mM Ts-Na vs. 0.5 CMC SDS, 8.2 mM Ts-Na vs. 1 CMC SDS, and 12.3 mM vs. 1.5 CMC SDS).

2.2.2.2. Preparation of polyamide nanofiltration membrane via surfactant assembly regulated interfacial polymerization (SARIP)

The fabrication procedure in SARIP is similar to that in conventional IP as described in 2.1, except that surfactants are added to the PIP solution for forming an interfacial network. More details regarding the addition of the surfactants are described below.

2.2.2.2.1. SARIP with the anionic surfactant, sodium dodecyl sulfate (SDS)

2.2.2.2.1.1. SARIP with SDS, PIP as amine

In this series of experiment, the SDS concentrations used were 2.05 mM (0.25 CMC), 4.1 mM (0.5 CMC), 8.2 mM (1 CMC) and 12.3 mM (1.5 CMC).

2.2.2.2.1.2. SARIP with SDS, polyethyleneimine (PEI) as amine

An aqueous solution of poly(ethyleneimine), or PEI, at a concentration of 0.25 % w/v was used in SARIP with an SDS concentration of 8.2 mM (1 CMC). The TMC concentration was 0.2 % w/v.

2.2.2.2.2. SARIP with the cationic surfactant, centrimonium bromide (CTAB)

Centrimonium bromide (CTAB), a cationic surfactant, as opposed to SDS as an anionic surfactant, was tested in SARIP to investigate the impact of charge of surfactant network on the properties of the PA layer. The concentrations of CTAB used in PIP solution were 0.23 mM (0.25 CMC), 0.46 mM (0.5 CMC), 0.92 mM (CMC), 1.84 mM (2 CMC), 2.76 mM (3 CMC), 4.6 mM (5 CMC), 7.36 mM (8 CMC), 9.2 mM (10 CMC) and 13.8 mM (15 CMC).

2.2.2.2.3. SARIP with the zwitterionic surfactant, 3-(N, N-Dimethylmyristylammonio) propane sulfonate (SB3-14)

A zwitterionic surfactant, 3-(N, N-Dimethylmyristylammonio) propane sulfonate (SB3-14) was also tested in SARIP for comparison with CTAB (cationic) and SDS (anionic) for their impacts on the properties of the resulting PA layer. The concentrations of SB3-14 used in PIP solution were 0.1 mM (0.25 CMC), 0.4 mM (1 CMC). 0.8 mM (2 CMC), 1.6 mM (4 CMC), 3.2 mM (8 CMC), 4.8 mM (12 CMC), 6.4 mM (16 CMC), 9.6 mM (24 CMC), 12.8 mM (32 CMC).

2.2.2.2.4. SARIP with sodium dodecylbenzene sulfonate (SDBS)

Another anionic surfactant, sodium dodecylbenzene sulfonate (SDBS), was investigated because the SDBS chemical structure resembles that of SDS and should theoretically lead to qualitatively similar improvement of the properties of the PA layer according to the SARIP theory. The mechanism was explained in the following contents. The concentrations of SDBS in PIP solution were 0.6 mM (0.5 CMC), 1.2 mM (1 CMC) and 8.2 mM (1 CMC of SDS).

2.2.3. Membrane characterization

2.2.3.1.Positron annihilation spectroscopy (PAS)

A slow positron beam (VMSPB) was used to determine the free volume size and distributions of the TFC-PA membrane from conventional IP and SARIP with SDS. This radioisotope beam used 50 mCi of ^{22}Na as the positron source. Two positron annihilation spectroscopies were collected to explore the microstructure of the TFC-PA membrane: Doppler energy spectroscopy (DBES) and positron annihilation lifetime (PAL) spectroscopy. The DBES spectra were determined using PAS with a variable mono energy slow positron beam (0-30 keV) and recorded using an HP Ge detector (EG&G Ortec). Two parameters, R and S, were reported from the DBES measurement. The S parameter, which was from the o-Ps 2g pick-off annihilation in free volume, yielded information about the depth profile of the free volume (Å to nm) in the polyamide layer. Whereas the R parameter, defined as the 3g to 2g annihilation ratio, indicated the existence of large pores (nm to um) in which ortho-Positrinium (o-Ps) underwent 3g annihilation. The PAL spectra were analyzed using the PATFIT to obtain the o-Ps lifetime $\boldsymbol{\tau_3}$ (1-5 ns), which was used to calculate the mean radius of the free volume (Å to nm) based on a semiempirical equation from a spherical-cavity model. The continuous o-Ps lifetime distribution was obtained from the MELT program to show the corresponding distribution of free volume in the PA network. Detailed descriptions of slow positron beam and PAS data analysis could be found elsewhere[111].

2.2.3.2.X-ray photoelectron spectroscopy (XPS)

The surface elemental composition of polyamide active layers from conventional IP and SARIP was analyzed using a Thermal Fisher Scientific ESCALAB 250 Xi X-Ray photoelectron spectrometer. XPS specimens were prepared by carefully mounting polyamide films onto a silicon wafer. High-resolution scans in the carbon, nitrogen, oxygen, sulfur, and bromine regions were performed at 0.5 eV increments with a sweep time of 5000 s/eV and 25 energy sweeps for each region. XPS peak fitting was performed with XPSPEAK41 software.

2.2.3.3. Transmission electron microscopy (TEM)

Cross-sectional TEM images of TFC-PA membranes prepared from conventional IP and SARIP were obtained using an FEI Tecnai G2 F20 S-twin 200kV field-emission transmission electron microscope. TEM specimens were prepared by embedding TFC-PA membranes into epoxy resins, then ultrathin sections were prepared with a Leika EM UC7/FC7 microtome and carefully mounted onto lacey carbon support grids.

2.2.3.4. Contact angle measurement

The contact angle of the PIP aqueous solution with a variety of surfactants on the PES UF substrate was measured on an OCA20 instrument (Data-Physics, Germany) system at ambient temperature. PES membranes were dried before measurement and mounted on glass slides. A drop of PIP aqueous solution (~10 ul) with different concentrations of surfactant was placed on the PES surface with a syringe. An optical image of the drop outline on the PES membrane surface was captured, and the corresponding water contact angle was calculated with a circle fitting method by drop shape analysis software.

2.2.3.5. Interfacial surface tension measurement

The interfacial surface tension between n-hexane and PIP aqueous solution with and without surfactants was measured using the pendant drop method with OCA20 instrument (Data-Physics, Germany). A transparent cubic container was filled with n-hexane, and one drop of PIP solution was generated from a syringe tip into hexane. An optical image of the drop hanging on the dosing needle was captured and the corresponding IFT value was calculated based on the Young-Laplace equation.

2.2.3.6.Streaming potential measurement

The surface streaming potential of TFC-PA membranes prepared via conventional IP and SARIP with various surfactants was performed on an electro-kinetic Analyzer (SurPASS, Anton Paar, Ashland, VA) with an adjustable gap cell. The streaming potential values were measured from pH 3 to 10 using 1 mM KCl solution as the background electrolyte at ambient temperature.

2.2.3.7.NF performance test of polyamide nanofiltration membranes from conventional IP and SARIP

The performance of the fabricated NF membranes was tested using a system with three parallel stainless cross-flow filtration cells. The active area of membranes in each cell was 7.1 cm^2. The pure water permeability of the PA NF membrane was measured using DI water before performing any NF experiments with feed solution containing solutes. The cross-flow velocity was 60 L h^{-1} and the applied pressure was 4 bar. The feed concentration of salts was 1000 ppm. The permeate flux was determined by measuring the weight change with respect to time, and ion selectivity was calculated based on the electrical conductivity of the feed and the permeate which was measured when stable permeating flux was achieved. Rejection of organic species (200 ppm) was also evaluated by measuring the Total Organic Carbon (TOC) of the feed and permeate solutions using a TOC instrument (OI Analytical Aurora Model 1030). The rejections of organic species of different molecular weights are fitted to determine the molecular weight cutoff (MWCO) and the pore size distribution of TFC-PA NF membranes.

The pure water permeability of TFC-PA membrane was calculated by the following equation:

$$PWP = \frac{\Delta V}{S \Delta t \Delta P}$$

where PWP is the pure water permeability of TFC-PA membrane (L m^{-2} h^{-1} bar^{-1}), ΔV is the permeate water volume (L) collected over the period Δt (h), S is the effective membrane area (m^2), and ΔP was the applied pressure (bar), respectively.

The volumetric flux of water, J (L m^{-2} h^{-1} bar^{-1}), was calculated using the following equation:

$$J = \frac{\Delta V}{S\Delta t}$$

The salt rejection, R (%), was calculated using the following equation:

$$R = \left(1 - \frac{c_p}{c_f}\right) \times 100\%$$

where R is the salt rejection (%), $\boldsymbol{c_p}$ and $\boldsymbol{c_f}$ are the salt concentrations of the permeate and feed solution (ppm), respectively.

2.2.3.8.Determination of MWCO, pore size, and pore size distribution of polyamide nanofiltration membranes from conventional IP and SARIP

The pore size of the polyamide network was determined by the rejection of a series of neutral organic compounds with increasing molecular weight. The neutral organic compounds tested in this study include glycerol (92 Da), glucose (180 Da), sucrose (342 Da), and raffinose (504 Da). The concentration of each organic species solution was 200 ppm and the applied pressure in the filtration experiments was 4 bar. The MWCO of TFC-PA membranes was defined as the molecular weight at which the rejection equals 90%. The pore size distribution curve is expressed as a probability density function (PDF) that was established based on the following assumption: (1) There is no steric or hydrodynamic interaction between these organic solutes and the membrane pores; (2) The mean pore size of the polyamide membrane equals the Stokes radius of the organic solute with a measured rejection of 50%; (3) The distribution of the membrane pore size is characterized by the geometric standard deviation of the PDF curve, which is the ratio between the Stokes radius with a rejection of 84.13% to that with a rejection of 50%[112].

$$\frac{dR(r_p)}{dr_p} = \frac{1}{r_p ln\sigma_p \sqrt{2\pi}} \exp\left[-\frac{(lnr_p - ln\mu_p)^2}{2(ln\sigma_p)^2}\right]$$

where μ_p is the mean pore size, σ_p is the geometric standard deviation of the PDF curve and $\boldsymbol{r_p}$ is the Stokes radius of the organic solute. The Stokes radii of these molecules correlate with their molecular weight[112]:

$$\ln(r_p) = -1.4962 + 0.4654 \ln(MW)$$

where MW is the molecular weight of each organic solute. Based on the above equation, the Stokes radii for glycerol, glucose, sucrose, and raffinose are 0.261, 0.359, 0.462, and 0.538 nm, respectively.

2.2.4. Computational modeling

2.2.4.1.Molecular Dynamic simulation

An Amorphous Cell module in Materials Studio was used to simulate the trans-interface diffusion of PIP from water to hexane with and with SDS. Two Molecular Dynamics (MD) systems were constructed, one with a self-assembled SDS network at the water/hexane interface and the other without SDS. Both systems were comprised of the same numbers of H_2O (5000), pip (100), and C_6H_{14} (500) molecules in a lattice cell (50×50×140 $Å^3$). In the MD model with SDS network, a total number of 36 SDS molecules were placed between water and hexane phases. After that, both MD systems were simulated for 20 picoseconds with NVE thermodynamic ensemble at 298.0 K temperature. All the four reference energies (potential, non-bond, kinetic, and total energy) have reached the steady values after 10ps. Meanwhile, the system temperature remained at the present value. The configurations at 15 ps in both MD systems were captured to analyze the population of pip molecules with and without the self-assembled SDS network. The relative concentrations of PIP, water and SDS molecules were shown in Fig 3b,c.

To further explore the effect of the SDS dynamic network on the kinetics of PIP interfacial diffusion, we calculated the binding energy (E_{binding}) of a PIP molecule to its surroundings at three sites: PIP bulk solution, water/hexane interface with and without SDS, and hexane.

$$E_{\mathrm{binding}} = E_{\mathrm{X+pip}} - E_{\mathrm{X}} - E_{\mathrm{pip}}$$

where E_{pip} is the energy of one PIP molecule, $E_{\mathrm{X+pip}}$ is the total energy of the system including the PIP molecule and its surrounding, and E_{X} is the energy of the system without the PIP molecule, respectively.

2.2.4.2.Density functional theory (DFT) simulation

To get the insight of how the interaction between a PIP molecule and an SDS molecule changed during the transport of PIP from water to hexane, we also performed a DFT simulation with Dmol modules in Material Studio. The molecular Frontier Orbital of the PIP molecule and SDS molecule was calculated first in order to identify the population of the Highest Occupied Molecular Orbital (HOMO) and the Lowest Unoccupied Molecular Orbital (LUMO).

To simplify the DFT calculation, the transport of one PIP molecule along one SDS molecule was divided into three parts according to the location of PIP relative to SDS (Fig, 3d). Part 1 described the attraction between the SDS sulfate group and the PIP molecule in bulk solution (The distance between pip and SDS is around 5Å); Part 2 was the engagement of the PIP molecule with the sulfate group; and in part 3, five different sites along the SDS alkane backbone were selected to discuss the change of interaction between PIP and SDS during transport. The adsorption energy (E_{ads}) of PIP at each site was calculated using the follow equation:

$$E_{\mathrm{ads}} = E_{*+\mathrm{pip}} - E_{*} - E_{\mathrm{pip}}$$

where E_{pip} was the energy of a single PIP molecule, $E_{*+\mathrm{pip}}$ was the energy of the SDS molecule with the adsorption of PIP, and E_{*} was the corresponding energy of the SDS molecule without adsorption of PIP.

2.2.4.3.Monte Carlo simulation

We perform simplified Monte Carlo (MC) simulations to illustrate the relationship between the energy barrier for diffusion and the homogeneity of the resulting diffusive flux. In such an MC simulation, a group of generic particles (mimicking PIP molecules) attempts to pass a grid of cells (10 × 10 in this study) with a certain energy barrier, ΔE_{B}. We assume that the intrinsic kinetic energy of these particles follows a Maxwell-Boltzmann distribution as expressed in using following equation:

$$\frac{dN}{N} = \left(\frac{m}{2\pi k_{\mathrm{B}} T}\right)^{1/2} exp\left(-\frac{mv^2}{2k_{\mathrm{B}} T}\right) dv$$

where *dN/N* is the fraction of PIP molecules moving at velocity *v* to *v* + *dv*, m is the mass of the PIP molecule, k_B is the Boltzmann constant and *T* is the absolute temperature. Therefore, the probability of one PIP molecule moving with a speed of v in three dimensions can be expressed as

$$p(v) = 4\pi \left(\frac{m}{2\pi k_B T}\right)^{3/2} v^2 exp\left(-\frac{mv^2}{2k_B T}\right)$$

For each diffusion attempt across a cell in the grid, we randomly assign kinetic energy to a particle according to the Maxwell-Boltzmann distribution. If the energy of that particle is higher than the energy barrier (i.e., $\boldsymbol{\varepsilon_i} > \Delta E_B$), the attempt is considered as successful and one additional particle is recorded as passing that specific cell. Otherwise, the attempt is considered as a failure and we move onto the next cell for the next diffusion attempt. Each cell has one diffusion attempt in each round (which comprises 100 attempts). The simulation continues until 1,000 particles have successfully diffused across the 10 × 10 grids, resulting in an average of 10 particles per grid.

2.3.Results and discussion

2.3.1. Performance and properties of PA membrane formed via SARIP.

The PA active layer formed via conventional IP has heterogeneous pore (free volume) size distribution (Figure 2.1C). The presence of the SDS interfacial network in SARIP promotes the formation of a more uniform PA network (Figure 2.1D), which in turn results in more precise differentiation between solutes of similar size. Although the addition of surfactants, including SDS, has been explored in numerous previous studies, they were added to promote the wetting of the support layer or the spreading of the water/oil interface; and the achievement of sub-1Å level precision of solute-solute separation via surfactant addition has not been reported before[110,113–116]. SARIP provides a fundamentally different perspective regarding the impact of surfactants on interfacial diffusion of amine monomers and the overall IP process. While more quantitative evidence and mechanistic explanation will be provided later, the important impact of the interfacial regulation by the SDS network on the precision of solute sieving or selectivity of the PA layer is shown by comparing the rejection of different small solutes by TFC-PA membranes synthesized using IP and SARIP (Figure 2.1E).

The TFC-PA membrane formed via conventional IP has a very wide range of rejection for solutes with Stokes radius, $\boldsymbol{r_s}$, between 2.5 and 5.0 Å (Figure 2.1E, top). This wide distribution of rejection for species of similar size suggests that electrostatic and ion dehydration mechanisms contribute to ion rejection besides size-based sieving. While multivalent anions (e.g. SO_4^{2-} and $Fe(CN)_6^{3-}$) are well rejected via Donnan exclusion by the negatively charged PA membrane formed via conventional IP, the rejection of multivalent cations is generally low and varies considerably with ion size (Table A.1). In contrast, the presence of an interfacial SDS network in SARIP dramatically changes the solute separation behavior of the resulting PA membrane.

Notably, solute rejection becomes strongly dependent on the ion size and the measured rejection curve demonstrates a sharp, step-wise transition at $\boldsymbol{r_s}$~ 2.7 Å, separating monovalent and divalent cations with remarkable precision (Figure 2.1D, bottom). Comparing the rejection curves for PA membranes prepared using IP and SARIP (Figure 2.1D) shows that SARIP not only decreases the molecular weight cutoff, MWCO (i.e., the $\boldsymbol{r_s}$ corresponding to 90% rejection), but also reduces the range of the transition regime in the rejection curve, thus enabling differentiation of solutes with sub-1Å selectivity (i.e., the rejections of two ions with a size difference smaller than 1Å have a difference of at least 60%). For example, the rejections of Li^+ ($\boldsymbol{r_s}$ =2.4 Å) and Ba^{2+} ($\boldsymbol{r_s}$=2.9 Å) are 30% and 93%, respectively, with the PA membrane obtained using SARIP, whereas their rejections are very similar (19% and 17%) with the PA membrane-derived using conventional IP. While Figure 1E is based on Stokes radii to include both ions and neutral molecules, presenting the results for ions using a hydrated radius reveals a similarly dramatic enhancement in the precision of ion-ion separation (Figure A.1).

The precise separation achieved by the TFC-PA membrane fabricated using SARIP is attributable to the more uniform pore size distribution of the SARIP-derived PA active layer as confirmed by both positron annihilation lifetime spectroscopy (Figure 2.2A) and characterization of pore size distribution using neutral solutes (Figure 2.2B). Positron annihilation lifetime spectroscopy (PALS) was used to probe the free volume distribution of the active layers[117], which have a thickness between 30 to 40 nm as confirmed by cross-sectional transmission electron microscopy (TEM) images of the TFC-PA membranes (Figure 2.2C, D). Specifically, the distribution of the *S* parameter of the TFC-PA membranes fabricated using the two different approaches suggests that SARIP yields pores that are both smaller and more uniform (Figure 2.2A

and Table A.2). These results from PALS are consistent with those obtained by fitting the rejection of neural organic molecules of different molecular weights (Figure 2.2B). From both measurements, the sharpened pore size distribution of the PA layer resulting from SARIP still falls within the pore size distribution of the PA layer obtained using conventional IP (Figure 2.2A, B insets). Hence, the primary effect of SARIP was in sharpening the pore size distribution instead of merely shifting the pore size distribution to a smaller range.

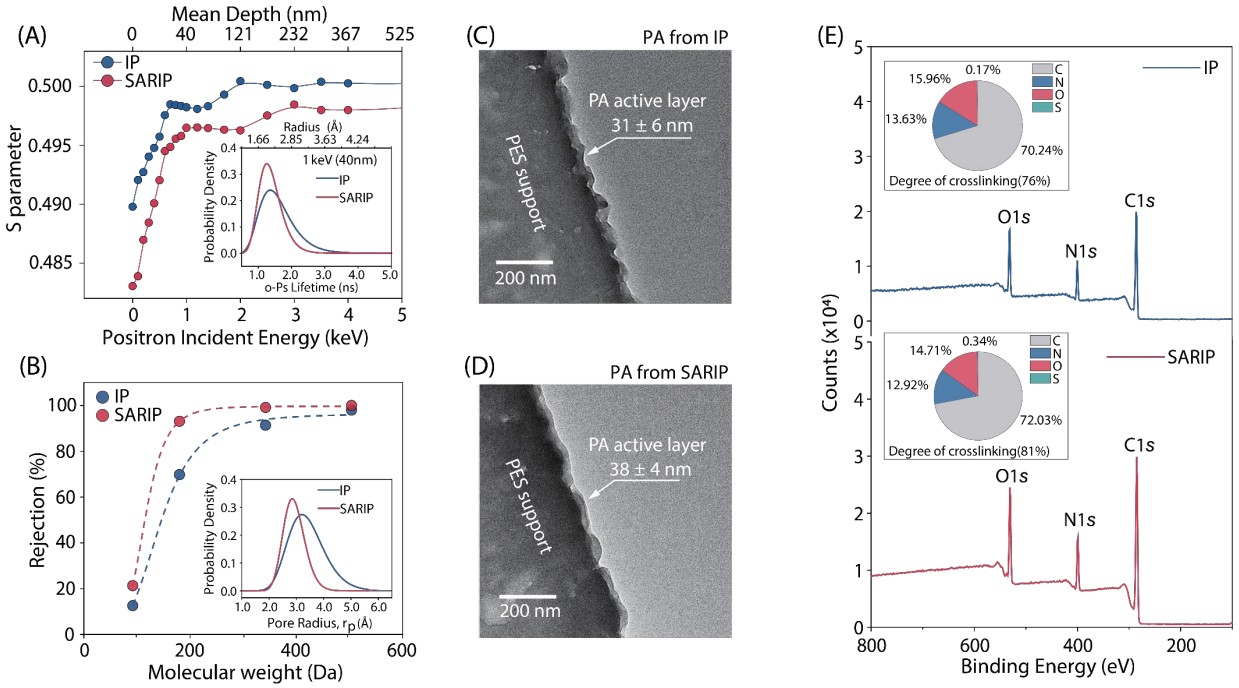

Figure 2.2 Properties of the PA active layers from IP and SARIP. (A) Evolution of S parameters for the PA active layers obtained using IP (blue circles and curve) and SARIP (red circles and curve). Inset: free-volume size distribution of PA active layers derived from the annihilation lifetime distribution of ortho-positronium (o-Ps) with an incident energy of 1 keV. (B) Rejections of uncharged model solutes including raffinose, sucrose, glucose, and glycerol by TFC-PA membrane obtained from IP (blue circles and dashed curve) and SARIP (red circles and dashed curve). Inset: pore size distribution of PA active layers derived from rejection curves of uncharged solutes[118]. (C) and (D) TEM images of the cross-sections of the PA membranes fabricated using IP and SARIP, respectively. The translucent film in each image is the PA active layer and its thickness is analyzed using ImageJ at eight different locations. The reported PA layer thickness represented the average of eight measurements and the error bar represents the standard deviation of eight measurements. (E) XPS spectra and the corresponding elemental compositions (insets) of PA active layer for TFC-PA membranes fabricated using IP (top) and SARIP (bottom), respectively. The degree of crosslinking (shown in insets) is determined based on the ratio between elements O and N[119].

While surface charge of the polymer plays a crucial role in Donnan exclusion—an important mechanism for ion rejection in NF[120,121] —streaming potential measurements reveal no discernable difference between the zeta potentials of the TFC-PA membranes formed via IP and SARIP (Figure A.3). Further, X-ray photoelectron spectroscopy (XPS) analysis of the sulfur content in the PA active layers formed via the two fabrication methods suggests no integration of SDS molecule into the PA active layer, as long as the SDS concentration does not exceed the critical micelle concentration, CMC (Figure A.4,5 and Table A.3,4). The smaller pore size of the TFC-PA membrane fabricated using SARIP is likely attributable to the higher degree of crosslinking between the TMC and PIP in the PA structure (Table A.3). The elemental composition of the PA active layer as probed by XPS reveals that the degrees of crosslinking are 76% and 81% for the PA active layers formed via conventional IP and SARIP (Figure 2.2E, Table A.3), respectively.

2.3.2. Mechanism of SARIP

The formation of PA via IP is a complex, non-equilibrium, diffusion-reaction process. It is widely believed that PIP monomers in the aqueous phase diffuse across the water/hexane interface before they react with the TMC monomers in the hexane phase[35,106]. The trans-interface diffusion of PIP is the rate-limiting step because PIP only weakly partitions from water into hexane, whereas the reaction between PIP and TMC in hexane is fast. SARIP accelerates this rate-limiting PIP diffusion and also enhances the uniformity of the diffusional flux, which results in spatially more homogeneous polymerization that leads to a more uniform pore size distribution of the PA active layer.

To support our proposed mechanism, we performed molecular dynamics (MD) simulation of the diffusive transport of PIP monomers across the water/hexane interface in the presence of SDS (Figure 2.3A and Figure A.6-8). After the MD relaxation, we obtain an equilibrated structure, which forms a dynamic SDS network with an areal density of ~1.1 nm^{-2}. This areal density is

consistent with the experimentally measured surface excess concentration (Table A.5). The presence of SDS promotes the accumulation of PIP monomers near the water/hexane interface via electrostatic attraction between the negatively charged sulfonic group of SDS and the slightly positively charged PIP molecule (Figure 2.3B, C and Figure A.7).

Density function theory (DFT) simulation of the interaction between a PIP molecule and an SDS molecule in water shows that the mediated transport of a PIP molecule along the SDS chain is in general energetically favorable from the sulfonic head toward the dodecyl tail (Figure 2.3A and Figure A.9,10). In addition, based on the binding free energy of a PIP molecule at multiple locations estimated from MD simulation results (without considering concentration gradient), the presence of SDS substantially reduces the binding energy penalty for a single PIP molecule to transport from the water phase to the hexane phase (Fig, 2.3E and Figure A.10). At the level of an ensemble, the elevated PIP concentration at the water/hexane interface and the very fast reaction in the hexane phase induce a large concentration gradient and enhance the trans-interface transport of PIP. Overall, the interfacial network of SDS in SARIP facilitates the trans-interface transport of PIP from water to hexane by reducing the associated Gibbs free energy barrier.

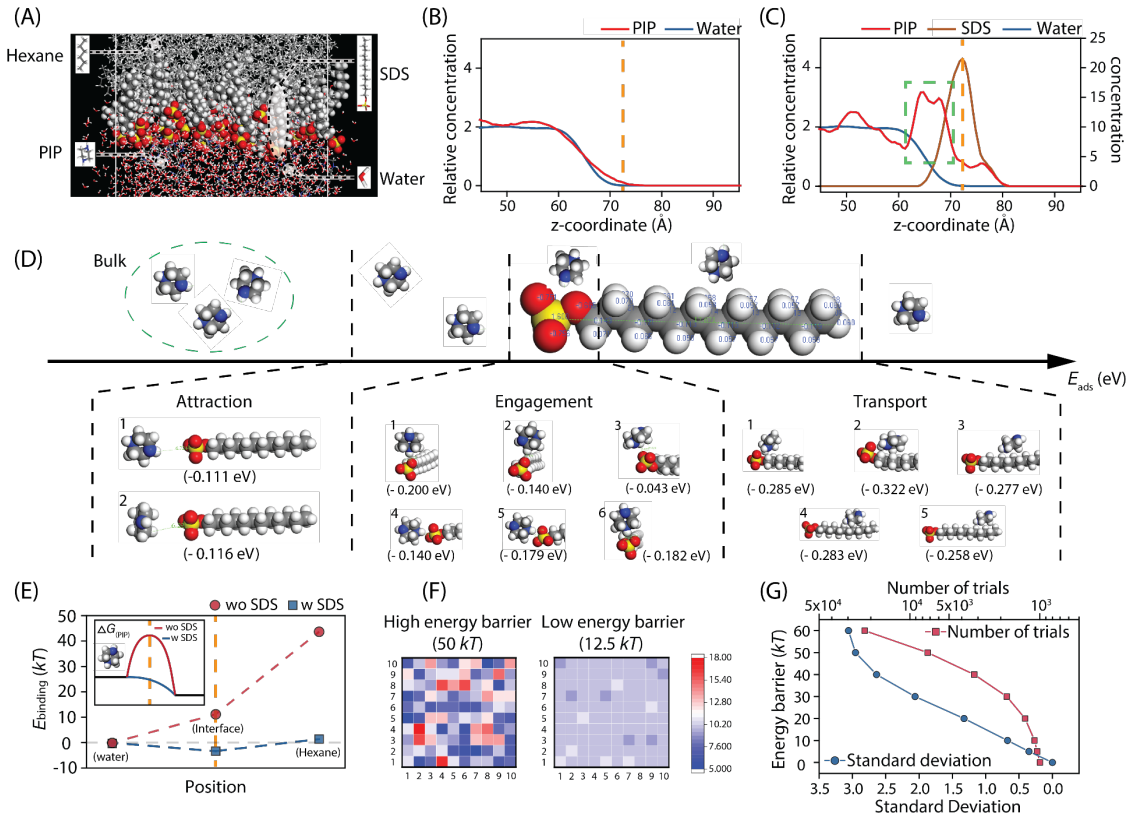

Figure 2.3 Facilitated trans-interface transport of PIP in SARIP. (A) A snapshot of the water/hexane interface in the MD simulation (Figure A.6). (B) Relative abundance of PIP (red curve) and water (blue curve) across the interface (at ~70Å, orange dashed line) in the absence of SDS. (C) Relative abundance of PIP (red curve), water (blue curve), and SDS (brown curve) across the interface (orange dashed line). SDS molecules accumulate at the interface and attract the PIP molecules. (D) DFT simulation of the potential energy for interaction between PIP and SDS molecules (with multiple configurations) at different interaction stages including attraction, engagement, and transport. (E) MD simulation of the binding free energy ($E_{binding}$) with the PIP molecule at different locations (Figure A.8). The MD simulations were performed with (blue squares) and without SDS (red circles). Inset: schematic illustration of how the Gibbs free energy barrier is reduced by the presence of SDS. (F) Monte Carlo simulation of particles with distributed energy passing through a 10 ×10 grid. The energy of the particles follows a Maxwell-Boltzmann distribution at 298 K. The color map represents the numbers of particles passing through different pixels (according to the scale bar) with an energy barrier of 50 kT (left) and 12.5 kT (right). (G) The total diffusion attempts (red squares and curve) and the standard deviation (blue circles and curve) of the spatial distribution of successful passages for 1,000 particles passing through a 10 ×10 grid as functions of the free energy barrier.

Both the SDS-induced accumulation of PIP at the water/hexane interface, which creates a larger initial gradient for interfacial transport, and the SDS-modified energy landscape of trans-interface PIP transport, promote faster transport of PIP across the water/hexane interface and

enhance the kinetics of the IP process. However, increasing the kinetics of IP is insufficient for forming a PA layer with more uniform pore sizes. For instance, increasing the kinetics of IP by using a higher PIP concentration can increase the degree of crosslinking and reduce MWCO (Figure A.11,12 and Table A.6,7), but it cannot result in the formation of more uniform pore size or precise differentiation of the rejections of monovalent and divalent ions (Figure A.13 and Table A.7). More importantly, the SDS-facilitated trans-interface transport of PIP also results in spatially more uniform diffusion of PIP across the interface, which is essential for the formation of a PA membrane with a uniform pore size distribution. The relationship between energy barrier and flux uniformity can be semi-quantitatively illustrated by Monte Carlo simulations of the trans-interface transport of a group of particles with their kinetic energy following a Maxwell-Boltzmann distribution at a specific temperature. The underlying assumption is that, if the energy state of a particle exceeds a given energy barrier for trans-interface diffusion, that specific particle can successfully cross the interface. With this assumption, Monte Carlo simulations of trans-interface diffusion events for 1,000 particles across a 10×10 grid suggest that a lower energy barrier results in faster and more uniform flux across the interface (Figure2.3F, G). The total number of diffusion-attempts (trials) and the standard deviation of the numbers of particles passing through each grid opening decrease systematically as the energy barrier decreases (Figure 2.3G), which suggests that reduced energy barrier does not only accelerate interfacial transport of PIP but also renders it more uniform. Additionally, the self-assembled SDS network at the water-hexane interface may also impose steric hindrance against the diffusion of newly formed PA fragments to water, which reduces the competing hydrolysis reaction and thereby also increases the degree of crosslinking. Therefore, both the enhancement of PIP diffusion and the suppression of undesirable hydrolysis synergistically lead to a higher degree of crosslinking (Figure 2.2E) and a more homogeneous pore size distribution (Figure 2.2A).

2.3.3. SARIP with other types of ionic surfactants

According to the mechanisms discussed above, not all surfactants can promote the formation of a more uniform PA active layer, even though they all reduce the interfacial tension between water and hexane (Figure A.14) and promote better wetting of the support layer (Figure

A.15, Table A.8). For SARIP to achieve a more uniform PA layer, it requires the surfactants to be negatively charged so that they attract the positively charged PIP molecules. For example, SARIP with sodium dodecyl benzene sulfonate (SDBS), another anionic surfactant, shows a qualitatively similar effect of enhancing pore size uniformity as imparted by SARIP with SDS (Table 2.1, Figure A.16-18, and Table A.9,10). However, due to the steric hindrance of the benzene rings, SDBS has a lower interfacial packing density as compared to SDS (Table A.5) and is thus less effective in improving pore size uniformity. In contrast, adding other types of surfactants such as cetyltrimethylammonium bromide (CTAB, cationic) and sulfobetaine 3-14 (SB 3-14, zwitterionic) is ineffective in forming an active layer with more uniformly distributed pore size (Table 2.1, Figure A.19-28, and Table A.11-14). In particular, SARIP with CTAB undermines the selectivity of the PA active layer, resulting in larger and more heterogeneous pore size distribution (Table 2.1, Figure A.19-22, Table A.11,12). The repulsion between the positively charged CTAB and PIP increases the energy barrier for trans-interface PIP diffusion, consequently leading to slower and more heterogeneous transport of PIP and hence less uniform pore size distribution. Lastly, sodium p-toluene sulfonate, which has a sulfonic group as SDS and SDBS but is nonetheless not a surfactant, shows no effect in improving the pore size distribution and the selectivity of the PA active layer (Table 2.1, Figure A.29-31, and Table A.15-18). This observation provides another indirect evidence that the enhanced selectivity of the PA layer formed via SARIP is attributable to the regulation of trans-interface PIP transport by the self-assembled surfactant network.

The effectiveness of SARIP in promoting more precise selectivity is not limited to the system of PIP and TMC as the reactive monomers. For example, it is well known that PA active layer formed from the reaction between polyethyleneimine (PEI) and TMC has a larger pore size distribution than that from PIP/TMC reaction[122]. Applying SARIP to the PEI/TMC system also resulted in smaller pore size and improved uniformity of pore size distribution as compared to the reference TFC-PA membrane formed via conventional IP with PEI and TMC (Table 2.1, Figure A.32-34, and Table A.19).

Because SDS self-assembly serves as a network of facilitators to enhance PIP transport across the water/hexane interface, increasing the interfacial density of such transport facilitators via increasing its bulk concentration is expected to enhance the positive effect of SARIP. Indeed, increasing the SDS concentration in the PIP solution up to 1 CMC enhances the salt rejection systematically (Figure 2.4A) due to the smaller and more uniform size distribution of the resulting

PA active layer (Figure 2.4B and inset). However, using an SDS concentration of 1.5 CMC reverses the trend of the rejection improvement (Figure 2.4A), likely due to the integration of SDS into the PA layer when micelles form. While the exact mechanism of micelle-assisted transport of SDS into the hexane phase remains to be elucidated, and S-2*p* peak was observed only in the XPS spectrum of the PA layer formed using SARIP with 1.5 CMC, but not in any XPS spectra of the PA layer formed using SARIP with 1.0 CMC and below (Figure A.8). Further increasing the SDS concentration to 2 CMC leads to a more drastic reduction of salt rejection of the TFC-PA NF membrane (Figure A.34).

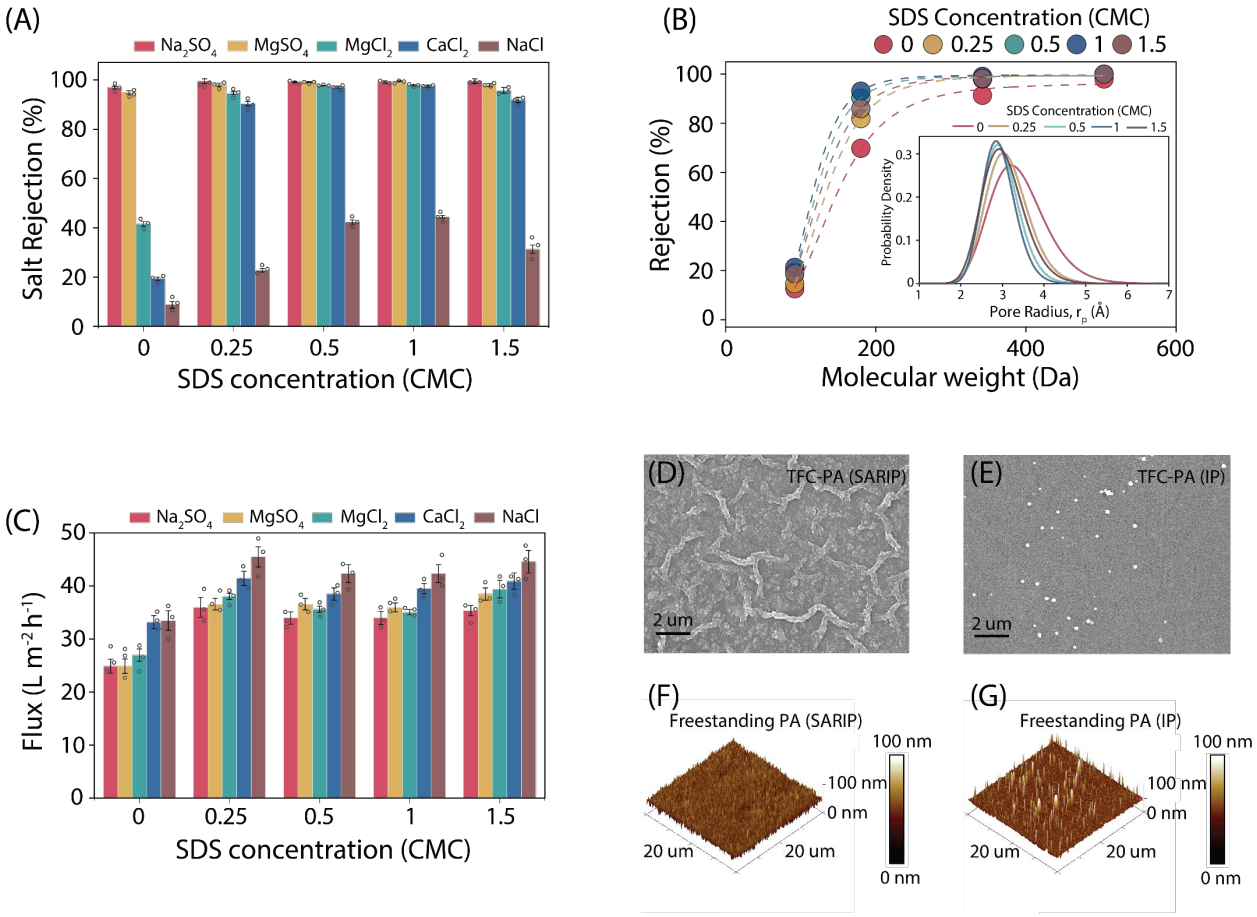

Figure 2.4 Concentration-dependent performance and active layer morphology. (A-C) Impacts of SDS concentration on the performance and properties of the TFC-PA membranes, including (A) rejection of various salts; (B) rejection of uncharged model solutes including raffinose, sucrose, glucose, and glycerol. Inset: pore size distribution of PA active layers derived from rejection curves of uncharged solutes (Table A.20); and (C) water flux. The hydraulic pressure was 4 bar and the salt concentration in the feed solution was 1000 ppm. (D) and (E) SEM images of the surface of TCF-PA membranes obtained using SARIP and conventional IP performed on a PES support, respectively; (F) and (G) AFM topography of free-standing PA films from SARIP and

conventional IP, respectively. The free-standing films were fabricated without support and then transferred to silicon wafers. The error bars represent the standard deviation of data from three replicate measurements.

The presence of SDS in the aqueous solution substantially enhances the membrane permanence, although the exact concentration of the SDS only has a comparatively minor impact (Figure 2.4C). The permeance enhancement, even with a tightened pore sized distribution, is largely attributable to the larger specific surface area of the TFC-PA membranes formed via SARIP, as SARIP leads to the formation of a textured surface (Figure 2.4D) compared to the presence of only sporadic protrusions on the surface of a TFC-PA membrane formed via conventional IP (Figure 2.4E). The considerable enhancement of permeance by the formation of local texture has been extensively reported[81,109,123]. The formation of surface texture is not associated with the pore size distribution of the PA layer, as the texture characteristic length scale is two to three orders of magnitude larger than that of the pores. Rather, the emergence of the ridged structure is attributable to the enhanced wetting of the porous susbtrate[123]. Notably, performing SARIP at the water-hexane interface without the porous support yields a relatively smooth free-standing PA layer (Figure 2.4F), In contrast, performing conventional IP (i.e., on porous support) in the same setting still yields a PA layer with sporadic and large (h>100 nm) protrusions (Figure 2.4G).

Table 2.1 Water permeance, rejection of selected salts, MWCO, and pore size distribution for different NF membranes

Type*	Water Permeance	Rejection (%)					MWCO	$< r_p >$	σ_P
	(L m^{-2} h^{-1} bar^{-1})	Na_2SO_4	$MgSO_4$	$MgCl_2$	$CaCl_2$	NaCl	(Da)	*(nm)*	
PIP (2.5% w v^{-1}) with TMC									
None[⊥]	12.6 ± 0.7[§]	97.1 ± 0.5	95.3 ± 0.6	45.5 ± 0.8	24.7 ± 0.6	15 ± 1.1	274	0.334	1.219
SDS	17.1 ± 0.7	99.6 ± 0.9	98.2 ± 0.6	95.0 ± 0.6	93.0 ± 0.8	27.0 ± 0.7	208	0.31	1.177
SDBS	14.9 ± 0.8	98.8 ± 0.8	97.4 ± 0.7	82.0 ± 1.4	77.0 ± 1.1	21.3 ± 1.6	224	0.309	1.208
SB3-14	20.3 ± 0.9	99.1 ± 0.2	98.3 ± 0.8	89.6 ± 0.6	77.9 ± 0.3	20.9 ± 2.5	220	0.313	1.189
CTAB	26.2 ± 0.7	98.1 ± 0.3	90.9 ± 0.2	66.0 ± 1.3	32.0 ± 0.6	9.9 ± 0.7	302	0.362	1.194
TsNA[#]	14.9 ± 0.8	98.0 ± 0.2	95.4 ± 0.9	50.0 ± 1.2	29.2 ± 0.9	14.8 ± 1.0	255	0.326	1.212
PEI (2.5% w v^{-1}) with TMC									
None	28.3 ± 0.9	39.7 ± 2.2	73.2 ± 2.6	88.6 ± 0.6	82.8 ± 1.3	30.7 ± 1.3	449	0.341	1.345
SDS	38.2 ± 0.9	62.5 ± 2.7	93.1 ± 3.1	95.8 ± 0.8	94.1 ± 0.9	46.1 ± 1.6	203	0.291	1.217

Definitions: MWCO: molecular weight cutoff, determined using rejection curve of neutral solutes as in Figure 2.2B; $< r_p >$: mean pore size; σ_p: geometric standard deviation.

***** Multiple concentrations have been tested for each additive (Appendix 9.1) and the best performing results are reported here.

[⊥] No additive is added. This membrane serves as the baseline.

[§] Each data is obtained based on three replicate experiments and the error represents standard deviation.

[#] All other additives are surfactants except for this case (sodium p-toluene sulfonate, or TsNA).

2.4.Conclusion

Overall, SARIP represents a universally applicable process where the diffusive transport of amine monomers across the water/hexane interface is regulated by an organized and flexible network of anionic surfactants. Such a dynamic network promotes faster and more uniform flux of amine monomers across the water/hexane interface, which is necessary for the formation of a more homogeneous PA active layer. SARIP provides a fundamentally different perspective of the impact of surfactants on interfacial diffusion of amine monomers and the overall IP process. Notably, SARIP requires minimal alteration of the established techniques for fabricating conventional TFC-PA NF membranes, and can thus be readily implemented for the scalable fabrication of ultra-selective NF membranes for precise solute-solute separation.

CHAPTER 3

POLYAMIDE NANOFILTRAITON MEMBRANES FROM INTERFACIAL POLYMERIZATION IN THE PRESENCE OF NONIONIC EMULSIFIERS

3.1.Introduction

Growing water scarcity is one of the leading challenges of our time, impacting over one-third of the world's population[1]. The challenge of supplying fresh water for the world's inhabitants is further exaggerated due to the rapid population growth and pollution from industrial, agricultural, and untreated human waste[2]. Membrane-based desalination and water purification technologies have received tremendous interests as it represents so far the most energy-efficient approach to achieving molecular separation[3]. Compared to the conventional thermal desalination tehcnologies, e.g., multistage flash distillation (MSF), multi-effect distillation (MED) and vapor compression (VC), membrane-based processes, e,g., reverse osmosis (RO), nanofiltration (NF) and electrodialysis (ED), require only one-tenth as much energy to desalinate the equivalent amount of liquid. Therefore, membrane separations have been widely used in seawater desalination, desalination of brickish water, wastewater treatment and other industrial, medical and environmental applications.

Nanofiltration is a low-pressure membrane-based process that is widely used in brackish water desalination and wastewater reclamation[19,20]. Compared to RO membranes, NF membrane typically has a relatively 'looser' active layer that enables its operation at low pressure, high flux and selective removal of mixed solutes by Donnan (charge) and steric (size) exclusion[27,28]. Specifically, solutes with larger hydrated radii than the pore size of NF membrane are retained due to size sieving[29], meanwhile, the membrane charge electrostatically repels co-ions and attracts counterions[30]. Thin-film-composite (TFC) polyamide-based NF membranes have served as the industry's gold-standard membranes for more than thirty years[7,19,33,124]. The polyamide active layer of TFC-PA NF membranes is formed via interfacial polymerization of piperazine (PIP) and trimesoyl chloride (TMC) at an oil-water interface[81]. Resulting polyamide film physically adheres

to a porous support substrate, which typically consists of a polysulfone or polyestersulfone layer formed by phase inversion on a non-woven fabric backing as mechanical support[59].

The formation mechanism of polyamide active layer in IP has attracted increasing interests due to the substantial usage of TFC-PA NF membranes in the desalination industry. Conventional IP fails to provide effective control of the membrane pore structure (e.g., pore size and thickness) due to uncontrolled trans-interface diffusion of PIP monomers and the fast polymerization between PIP and TMC, which lead to the formation of a polyamide active layer with multiscale heterogeneity and a large distribution of pore size[35,36,99,107]. Recently, we showed that the addition of anionic surfactant, particularly sodium dodecyl sulfate (SDS), creates a self-assembled amphiphiles 2D network at the water-hexane interface that regulates the PIP diffusion across the interface and leads to the formation of a PA active layer with a highly uniform pore size distribution. Such an IP process is referred to as surfactant-assembly-regulated interfacial polymerization (SARIP). The effect of the other types of ionic surfactants, such as anionic sodium dodecylbenzenesulfonate (SDBS), cationic Cetrimonium bromide (CTAB) and zwitterionic 3-(N, N-Dimethylmyristylammonio) propanesulfonate (SB3-14), are also evaluated and found to be less effective as SDS.

In addition to the various ionic surfactants, there is a whole other class of surfactants, nonionic surfactants. Although some studies had been carried out on the effect of nonionic surfactants on the formation of polyamide active layer in IP, they shared the same focuses of using surfactants to promote the wetting of PIP aqueous solution on the support membrane or using surfactants as additives to the polyamide active layer[110125]. However, the effect of the nonionic surfactants, for example, their charge neutrality as compared to the ionic surfactants, and more importantly, the variation of individual hydrophilicity and lipophilicity and their distinct roles in creating w/o emulsions or o/w emulsions in IP on the formation of polyamide active layer has never been explored before. We hypothesize that the nonionic surfacntants-assisted w/o or o/w emulsions would generate new microreactors in hexane or water for interfacial polymerization in addition to the extensive polyamide formation at the hexane/water interface, which as a result would entail a transformative impact on the resulting polyamide active layer.

In this study, we investigate the effect of adding hydrophilic/lipophilic nonionic surfactants in IP during the formation of TFC-PA NF membranes. The distinct roles of two nonionic surfactants in the IP process lie in their behaviors in favor of creating water/hexane or hexane/water

emulsions, which lead to the formation of a unique reaction zone in each system. We fabricate the reference TFC-PA NF membranes with PIP and TMC using conventional IP, and the TFC-PA NF membranes with the hydrophilic nonionic surfactant (Tween 80) added in the PIP aqueous solution and the lipophilic nonionic surfactant (Span 80) added in the TMC-hexane solution. The resulting TFC-PA NF membranes are extensively characterized including their surface morphology, surface charge density, surface hydrophilicity and elemental compositions of the polyamide active layer, to relate the physicochemical properties of the selective layer to their membrane performance. We further demonstrate the mechanism of how the water/hexane and hexane/water emulsions formed due to the addition of hydrophilic and lipophilic nonionic surfactants affect the IP process, highlighting the potential use of surfactants to tailor the structure and performance of TFC-PA NF membranes.

3.2.Materials and methods

3.2.1. Materials and chemicals

Piperazine (PIP, 99%), trimesoyl chloride (TMC, >98%), polysorbate 80 (Tween® 80, BioXtra, Mw ~1310), sorbitan oleate (Span® 80, Mw ~428), beta-carotene (≥ 93%) glycerol (≥ 99%), anhydrous D-(+)-Glucose, sucrose (≥99.5%), D-(+)-Raffinose pentahydrate (≥ 98%), Na_2SO_4 (≥ 99%), $MgSO_4$ (≥ 99.5%), $MgCl_2$ (≥ 99.99%), $CaCl_2$ (≥ 97%), NaCl (≥ 99%) were purchased from Sigma Aldrich (St. Louis, MO) and were all used as received. Anhydrous N-hexane and ethanol (HPLC) were purchased from Fisher Scientific. Polyester sulfone ultrafiltration (NADIR UH050, MWCO 50000 Da) membrane was purchased from Microdyn-Nadir (Germany).

3.2.2. Preparation of polyamide nanofiltration membrane via interfacial polymerization

The reference TFC-polyamide nanofiltration membrane was prepared using piperazine (PIP, 0.25% w/v aqueous solution) and trimesoyl chloride (TMC, 0.2% w/v in n-hexane) on a commercial

polyestersulfone (PES) ultrafiltration (UF) membrane as the support layer via conventional Interfacial polymerization (IP). The concentration of PIP and TMC remained the same in the following discussion. In a standard IP process, the PES UF support membrane was first placed on a glass plate and the surface of the UF membrane was impregnated with the aqueous PIP solution for 30 s. The excess PIP solution was then gently removed from the UF support membrane surface using a rubber roller. Next, a hexane solution of TMC was poured onto the UF membrane surface and kept still for another 30 s, which resulted in the formation of a thin PA active layer over the PES support membrane surface. The resulting TFC-PA membrane was rinsed with excessive n-hexane to remove unreacted TMC from the surface and then cured in an oven at 60 ºC for 30 min to increase the degree of crosslinking. After curing, the TFC-PA membrane was stored in DI water at 4ºC to facilitate the hydrolysis of unreacted chloride groups in the polyamide network.

To investigate the effect of nonionic surfactants on interfacial polymerization and the resulting TFC-PA membranes, the hydrophilic nonionic surfactant was added into the PIP solution for impregnating the PES support layer, whereas the lipophilic nonionic surfactant was added in the TMC hexane solution. The first nonionic surfactant, Tween 80, has a hydrophilic-lipophilic balance (HLB) value of 15 and is thus considered as a good oil-in-water emulsifier (which typically has an HLB value in the range from 8 to18)[126]. The second nonionic surfactant is Span 80, has an HLB value of 4 and is thus considerd as good water-in-oil emulsifier (which typically has an HLB value in the range from 4-6)[127]. The concentration of Tween 80 (in water) and Span 80 (in hexane) vary from 0% w/v to 0.5% w/v to evaluate the effect of surfactant concentration on the resulting polyamide nanofiltration membrane.

3.2.3. Membrane characterization

We characterized the surface potentials of the TFC-PA NF membranes fabricated from conventional IP and IP with the addition of hydrophilic or lipophilic nonionic surfactants using streaming potential analyzer (SurPASS electrokinetic analyzer, Anton Paar, Ashland, VA). The background polyelectrolyte was a 1mM KCl solution. Scanning electron microscope (SEM) imaging was performed to characterize the surface morphology of the TFC-PA NF membranes using a high-resolution Zeiss Merlin SEM equipped with GEMINI II column with an accelerating

voltage of 3 kV. All SEM membrane samples were sputter-coated with 5 nm gold coating to avoid the charging effect. X-Ray photoelectron spectrometer (XPS) was performed using a Thermal Fisher Scientific ESCALAB 250 Xi to obtain the surface elemental compositions of polyamide active layers prepared from conventional IP and IP with nonionc surfactants.

To evaluate the pore size distribution of the TFC-PA NF membranes, we performed filtration experiments with a series of neutral organic molecules (e.g., glycerol (92 Da), glucose (180 Da), sucrose (342 Da), raffinose (504 Da)) using a custom cross-flow NF system. The feed concentration was 200 ppm for all species and the applied pressure was 4 bar. We collected feed and permeate samples and measured the total organic carbon (TOC) using a TOC analyzer (OI Analytical Aurora Model 1030, OI Analytical, Inc., College Station, TX, USA) to determine the organic concentration of the feed and permeate samples. The MWCO and pore size information of the TFC-PA NF membranes were calculated using the rejection of the organic solutes. Specifically, the MWCO of the membrane is defined as the molecular weight of solute with a rejection of 90%, whereas the mean pore size corresponds to the Stokes radius of the neutral solute with a measured rejection rate of 50%. The pore size distribution of the TFC-PA NF membrane is expressed as the geometric standard deviation of the probility density function (PDF) curve (Equation 3), which is the ratio of the stokes radius with a rejection of 84.13% to that with a rejection of 50%[112].

$$\frac{dR(r_p)}{dr_p} = \frac{1}{r_p ln\sigma_p \sqrt{2\pi}} \exp\left[-\frac{(lnr_p - ln\mu_p)^2}{2(ln\sigma_p)^2}\right]$$

where μ_p is the mean pore size, σ_p is the geometric standard deviation of the PDF curve and r_p is the Stokes radius of the organic solute. The Stokes radii of these molecules correlate with their molecular weight[112] (Equation 4):

$$\ln(r_p) = -1.4962 + 0.4654 \ln(MW)$$

where MW is the molecular weight of each organic solute. Based this correlation, the Stokes radii for glycerol, glucose, sucrose, and raffinose are 0.261, 0.359, 0.462, and 0.538 nm, respectively.

3.2.4. Dye-partitioning at water/hexane interface

We measured the in-air water contact angle of the TFC-PA NF membranes fabricated in the aforementioned conditions using an optical tensiometer (Theta Lite, Biolin Scientific, Stockholm, Sweden) to evaluate the surface wetting properties. The interfacial surface tension of water and hexane as a function of Tween 80 or Span 80 concentrations was determined using pendant drop tensiometry (Theta Lite, Biolin Scientific, Stockholm, Sweden). We also characterized the effect of Tween 80 concentration on the wettability of the PIP solution on the PES substrate using an optical tensiometer.

3.2.5. Dye-partitioning at water/hexane interface

We performed dye partitioning experiments to investigate how solutes in one phase partition to another phase in the IP process with surfactants. Specifically, we used a water-soluble dye (blue) added in the water to mimic the partitioning behavior of PIP in hexane during the IP process with Span 80, and a lipid-soluble dye (yellow) added in the hexane to mimic the partitioning behavior of TMC in water during the IP with Tween 80. The aqueous solution containing dye only or dye with Tween 80 was first added to a beaker, and then we used a transfer pipet to add hexane solution containing Span 80 only or Span 80 with dye onto the water phase (Six scenarios summarized in Table 3.1). Photos were taken and videos were recorded using a optical camera.

Table 3.1. Dye-partitioning experiment at water/hexane interface with Tween 80 and Span 80.

Type of surfactant	**Experiment No.**	**Components in each phase**	
		Water phase	Hexane phase
Tween 80	1-1	None	Dye (yellow)
	1-2	Tween 80	Dye (yellow)
	1-3	Tween 80, dye (blue)	None
Span 80	2-1	Dye (blue)	None
	2-2	Dye (blue)	Span 80
	2-3	None	Span 80, dye (yellow)

3.2.6. Nanofiltration performance evaluation.

The performance matirx of the TFC-PA NF membranes was evaluated using an NF testing system with three stainless steel cross-flow cells in parallel. Each cell has an active membrane area of 7.1 cm2. All membranes were compacted with deionized water overnight prior to any test with salt solution. Membrane permeance and salt selectivity were evaluated with five types of common salt solutions (1000 ppm), including Na2SO4, MgSO4, MgCl2, CaCl2 and NaCl. The cross-flow velocity was 2.5 cm s-1 and the applied pressure was 4 bar. The permeance of the TFC-PA NF membrane, P (L m-2 h-1 bar-1), was determined using the following equation:

$$P = \frac{J}{\Delta P}$$

where J is the volumetric flux of water (L m-2 h-1), and ΔP was the applied pressure (bar), respectively. The rejection of solute by the TFC-PA NF membrane was determined by measuring the steady-state electrical conductivity of the feed and permeate solution using the following equation.

$$R = \left(1 - \frac{c_p}{c_f}\right) \times 100\%$$

where c_p and c_f are the solute concentration of permeate and feed solution, respectively,

3.3.Results and discussion

3.3.1. Impacts of non-ionic surfactants on TFC-PA membrane surface morphology

The addition hydrophilic and lipophilic surfactants in IP has a substantial impact on the surface morphology of the resulting TFC-PA NF membranes (Figure 3.1). As a baseline, the reference TFC-PA NF membrane prepared from conventional IP (without any surfactant) has a relatively smooth surface (Figure B1). The addition of hydrophilic nonionic surfactants (Tween 80) in the PIP solution leads to the formation of nodular structures on the PA surface (Figure 3.1A). As the Tween 80 concentration increases from 0.005% w/v to 0.05% w/v in the PIP solution, the nodular structure transforms into a crumpled structure (Figure 3.1B) and the density of the crumpled structure increases with increasing the Tween 80 concentration (Figure 3.1C). The

formation of nodular and crumpled structures is attributed to the enhanced wetting of PIP solution on the PES UF substrate (Figure B2) [123]. In comparison, the addition of lipophilic nonionic surfactants (Span 80) in the n-hexane solution of TMC yields structures of deflated spheres on the PA surface (Figure 3.1D). The areal number density of the deflated structures increases with increasing Span 80 concentration (Figure 3.1E). At high enough Span 80 concentration, these deflated sphere structures become interconnected (Figure 3.1F).

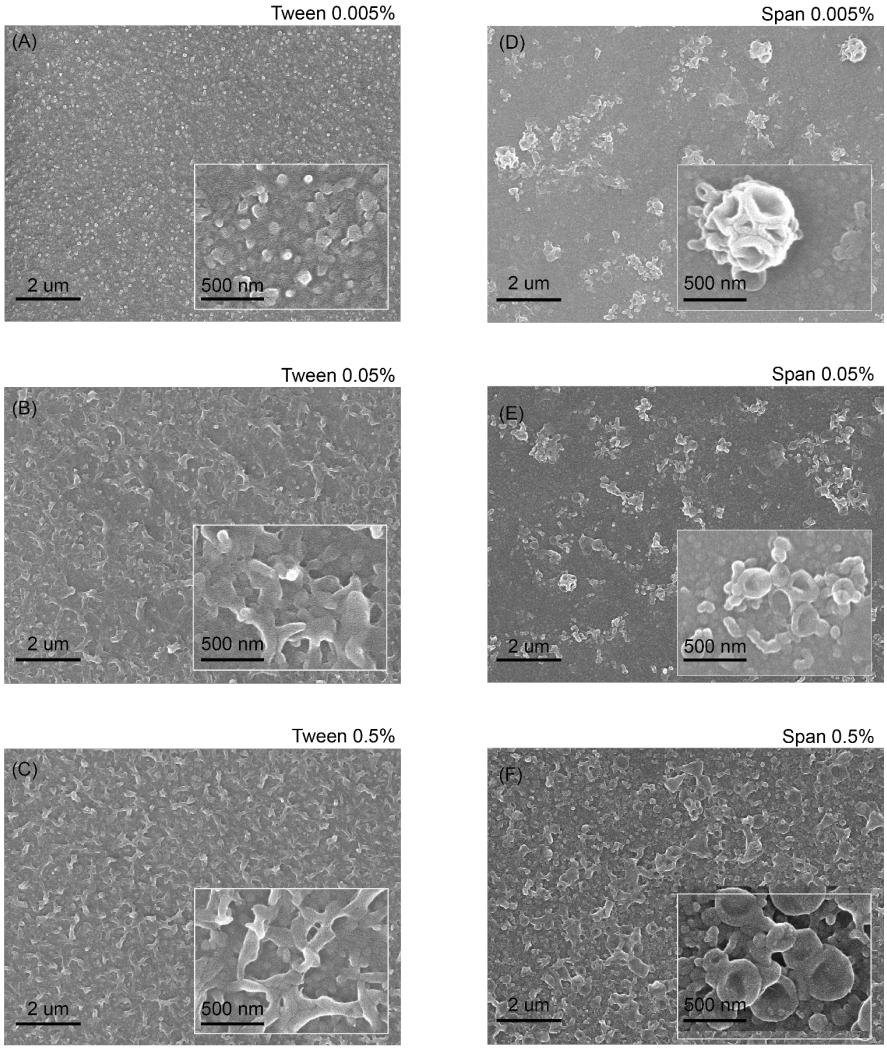

Figure 3.1 SEM images of the surface morphology of TFC-PA NF membranes formed via IP with the addition of (A, B, C) the hydrophilic nonionic surfactant (Tween 80) and (D, E, F) the lipophilic nonionic surfactant (Span 80) as a function of surfactant concentrations.

3.3.2. Impacts of non-ionic surfactants on TFC-PA membrane surface properties

The streaming potential measurements reveal no discernable difference between the zeta potentials of the reference TFC-PA NF membrane prepared via conventional IP and the TFC-PA NF membrane prepared via IP with Tween 80 added in the PIP solution (Figure 3.2A), suggesting that the addition of Tween 80 in IP reaction did not alter the surface functional groups of the polyamide active layer. However, the addition of Span 80 in the TMC solution results in a noticeable reduction of the absolute values of the surface potential (i.e., the addition of Span 80 in IP reaction makes the TFC-PA membrane less charged) but without shifting the isoelectric point (IPE). The addition of nonionic surfactants in the IP process also has a substantial impact on the wetting property of the resulting TFC-PA membrane (Figure 3.2B). Specifically, the presence of Span 80 increased the water contact angle (WCA) systematically with a higher Span 80 concentration (in hexane) leading to a higher WCA. In comparison, the addition of Tween 80 has a less profound effect on the surface wetting property. Specifically, increasing the dosing concentration of Tween 80 (in water) first slightly reduced the WCA but then increased the WCA when the Tween 80 concentration exceeded 0.125% (w/v).

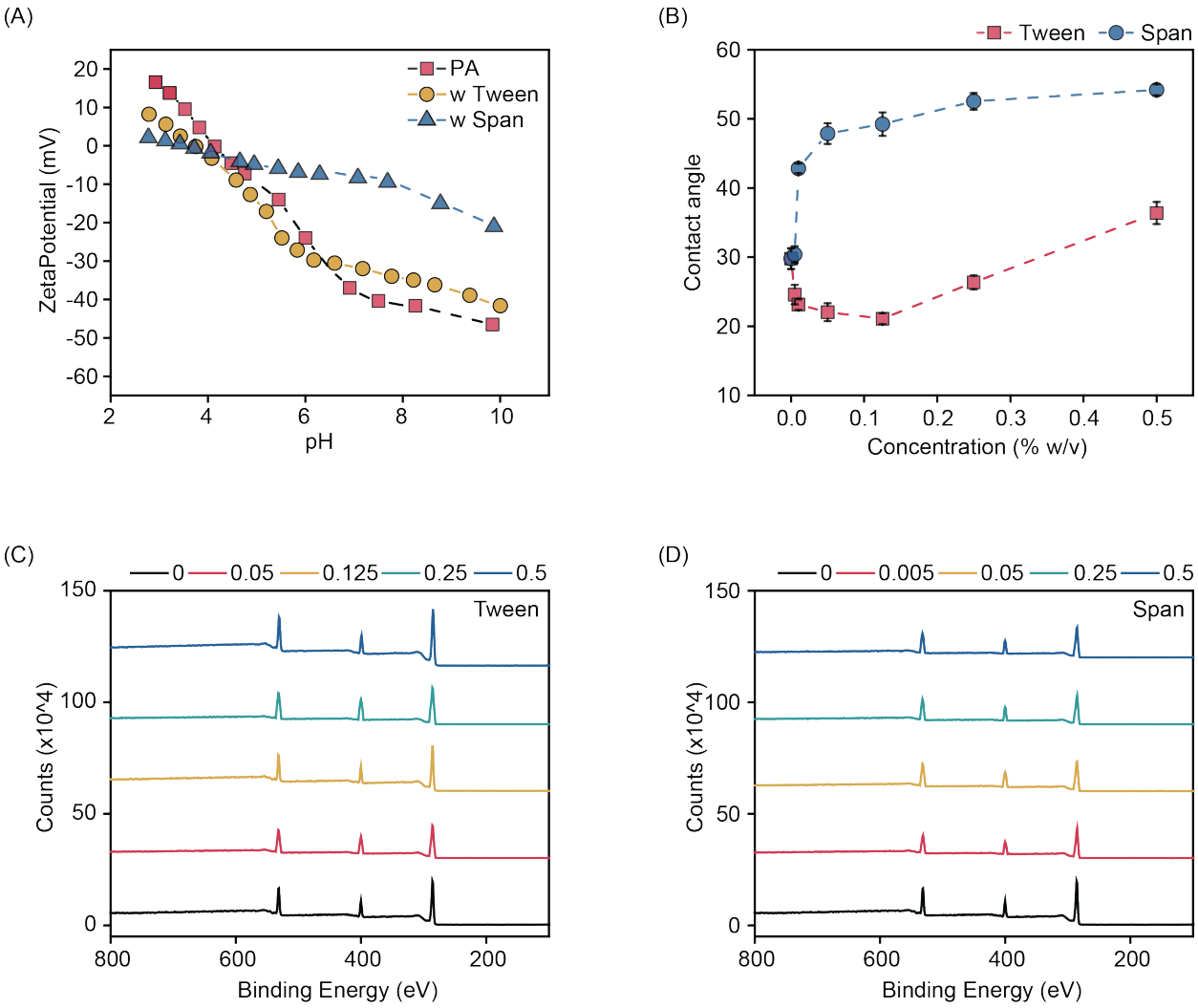

Figure 3.2 (A) Surface streaming potential of TFC-PA membranes prepared from IP, and IP with the addition of the hydrophilic nonionic surfactant (Tween 80) and the lipophilic nonionic surfactant (Span 80). (B) Water contact angle of TFC-PA NF membrane formed via IP with the addition of the hydrophilic nonionic surfactant (Tween 80) and the lipophilic nonionic surfactant (Span 80) as a function of surfactant concentrations. XPS survey of polyamide active layer formed via IP with the addition of (C) the hydrophilic nonionic surfactant (Tween 80) and (D) the lipophilic nonionic surfactant (Span 80) as a function of surfactant concentrations.

The elemental compsotion of the TFC-PA surface is also dependent on both the type and concentration of the dosing surfactants. Analyzing the XPS spectra of the surface of the TFC-PA membranes fabricated using different conditions (Figure 3.2 C,D) suggests the possible integration of surfactants into the PA matrix. Specifically, the N/O ratio decreased systematically with an increasing Span 80 concentration (Table 3.2). When Tween 80 was dosing agent, the N/O ratio

first increased and then decreased when the concentration exceeded 0.125% (w/v) (Table 2). While the N/O ratio is often used to quantify the degree of crosslinking, the degree of changes for these TFC-PA membranes far exceed what is typically expected from the difference in crosslinking degree[37,85]. The only plausible explanation is therefore the integration of the surfactants which induces changes in the elemental composition of the PA layer.

Table 3.2 Elemental composition and degree of crosslinking of polyamide active layer formed from IP with (A) the hydrophilic nonionic surfactant (Tween 80) and (B) the lipophilic nonionic surfactant (Span 80).

Membrane type		C(%)	N(%)	O(%)	N/O
Reference (no surfactant added)		70.24	13.63	15.96	76
Tween 80	0.05%	70.37	13.71	15.87	78
	0.125%	71.04	13.37	15.24	80
	0.25%	70.90	13.36	15.55	77
	0.5%	71.38	12.68	15.81	67
Span 80	0.005%	73.40	11.32	15.08	57
	0.05%	69.52	12.40	18.08	44
	0.25%	71.41	11.03	17.55	32
	0.5%	73.62	10.00	16.38	27

Interestingly, the WCA (Figure 3.2B) negatively correlates with the N/O ratio (Table 3.2) in a semi-quantitative way for both Tween 80 and Span 80 (Figure S2). The TFC-PA membranes prepared from IP with Span 80 exhibited an increase in surface hydrophobicity (WCA) and a decrease in N/O ratio even at an extremely low Span 80 concetration (0.005% w/v). Increasing Span 80 concentration made membrane more hydrophobic and reduced the N/O ratio because more Span 80 integrated in the polyamide matrix. Whereas, Tween 80 shows much less serve integration in the polyamide matrix at low concentrations (below 0.25% w/v), as the N/O ratio remains nearly the same. The slight decrease in WCA may come from the increase in surface roughness (Figure 1A-C, Figure S1). The WCA began to increase when the Tween 80 concentration (i.e., 0.25% w/v or 0.5% w/v) is equal or larger than the PIP concetration (0.25% w/v). Under this circumstance, Tween 80 is no longer considered as additives because its concentration is equal to or 2 times as

the PIP concentration, therefore the reaction between PIP and TMC is servely interfered because the aboundant Tween 80 strongly interact with PIP due to attraction force between hydroxyl groups (from Tween 80) and amino groups (from PIP). Therefore, it increases the possibility of uncomplete crosslinking between PIP and TMC because part of PIP molecules is surrounded by Tween 80, which leads to the integration of Tween 80 in the polyamide matrix and reduces the N/O ratio.

3.3.3. Mechanism of nonionic surfactant-mediated interfacial polymerization

Many of the surfactants that have been explored in IP are ionic surfactants have very high HLB values and are thus ineffective in forming emulsions. These surfactants include, but are not limited, to anionic surfactants, sodium dodecyl sulfate (SDS, HLB=40) and sodium dodecylbenzene sulfonate (SDBS, HLB=20), cationic surfactant, Cetyltrimethylammonium bromide (CTAB, HLB=10), and zwitterionic surfactant, 3-(N,N-Dimethyltetradecylammonio)propanesulfonate (SB3-14, HLB=48). The primary roles of these surfactants are to serve as acid accepter[7,115], promote better wetting of the support layer and better wetting between the water/hexane interface[123], and in some cases, faster and more homogenous transport of the amine monomers via the regulation by an interfacial surfactant self-assembly[37].

Like any other surfactant, non-ionic surfactant, Tween 80, also promotes better wetting of the support layer (Supporting Information Figure S2) and between the oil/water interface (Figure 3.3A). Unlike other ionic surfactants, however, the two non-ionic surfactants used in this study have much lower HLB values, which enables them to be very effective emulsifiers[128]. For example, Tween 80 (HLB~15) is a good oil-in-water (o/w) emulsifier (HLB range: 8-18), whereas Span 80 (HLB~4.3) is a good water-in-oil (w/o) emulsifier (HLB range: 4-6). To illustrate the effectiveness of these surfactants in emulsification, we performed experiments to show the stability of the oil/water interface when the surfactants are added into the one of the two phases. Specifically, the oil phase was dosed with an orange, water-insoluble dye (beta carotene) and the water phase was dosed with a blue, oil-insoluble dye to clearly show the oil/water interface.

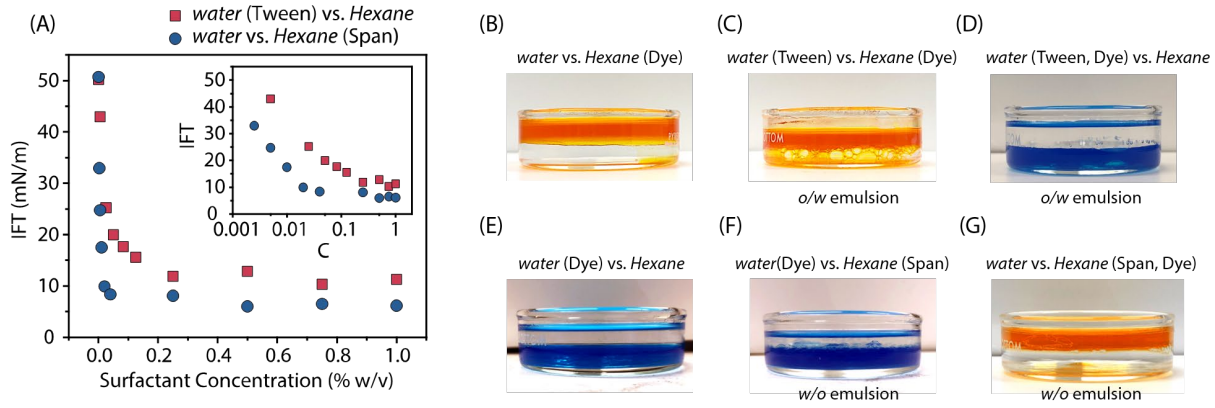

Figure 3.3 (A) Interfacial surface tension of water and hexane as a function of Tween 80 concentration in water (red square) or Span 80 concentration in hexane (blue circle). Demonstration of the presence of Tween 80 in water leading to the formation of oil-in-water emulsion upon mixing of water and hexane: (B) control experiment: when tween 80 is absent, no emulsion (yellow color) is observed in water. (C) the presence of Tween 80 results in the formation of oil-in-water emulsion (yellow bubbles) in water. (D) control experiment: Tween 80 does not lead to the formation of water-in-oil emulsion (no blue color) in hexane. Demonstration of the presence of Span 80 in hexane leading to the formation of water-in-oil emulsion upon mixing of water and hexane: (E) control experiment: when Span 80 is absent, no color (emulsion) is observed in hexane. (F) The presence of Span 80 results in the formation of water-in-oil emulsion (blue bubbles) in hexane. (G) control experiment: Span 80 does not lead to the formation of oil-in-water emulsion (no yellow color) in water.

With no surfactants added, the water/hexane interface was distinct and stable (Figure 3.3B, C). No oil dye partitions into the clear water phase (Figure 3.3B) and no water dye partitions into the clear oil phase (Figure 3.3C). When Tween 80 was added into the (undyed) transparent water phase which was put into contact with the hexane phase containing orange dye, the water phase became murdy and orange, which indicates the formation of o/w emulsion containing the organe dye (Figure 3.3D). Similarly, when Span 80 was added into the transparent hexane phase which was put into contact with the blue-dyed water phase, the hexane phase also showed clear evidence of the formation of w/o emulsions containing the blue dye (Figure 3.3E).

In the experiments shown in Figure 3.3D, E, the dyes and the surfactants were added into different phases, which does not clearly show if emulsions were formed in the dyed phase. Therefore, we performed additional experiments where dyes and surfactants were added into the same phase. Specifically, when both Tween 80 and water-soluble dye were added into water, no formation of blue emulsion was observed in the clear oil phase (Figure 3.3F). The absence of

emulsification in the oil phase is attributable to the fact that Tween 80, being a good o/w emulsifier, is a poor w/o emulsifier. Similarly, when both Span 80 and the oil-soluble dye were added into the oil phase, no o/w emulsion was observed in the water phase (Figure 3.3G), because Span 80, though being an effective w/o emulsifier, is a poor o/w emulsifier.

The emulsification beahviors in the presence of non-ionic surfactants as illustrated using dyed solutions provide important insights into how interfacial polymerization (IP) may be affected by these surfactants. Specifically, we can consider the effect of monomer transport via emulsions containing contain those monomers, i.e., the emulsions serve as a "vehicle" to bring the monomers into another phase. For example, when Tween 80 was added into the PIP solution, o/w emulsions form in the aqueous phase bringing emulsified oil droplets containing TMC into the water phase. These o/w emulsions may serve as microreactors for local interfacial polymerization that leads to the formation of short PA fragments. These disconnected segments forming in the water phase will unlikely be integrated into the continuous PA layer forming in the hexane side of the water/hexane interface[35,36,124]. These segment will undergo fast hydrolysis and then embedded underneath the PA active layer, and will thus have limited impact on the properties of the PA layer.

In fact, the streaming potenital measurements reveal very almost no difference in surface potential between the PA layers formed with and without Tween 80 (Figure 3.2A). The presence of Tween 80 have a relatively small impact (as compared to Span 80 to be discussed) on the WCA and elemental composition of the PA layer (Figure 3.2B,C and Table 3.2), which is attributable to the integration of Tween 80 in the PA layer. We note that (1) the integration of a small amount of Tween 80 does not affect the surface potenital of the PA layer because Tween 80 is an non-ionic surfactants; and (2) the changes in WCA and elemental composition were hardly observed if oil-insouble and non-emulsifying surfactants (e.g., SDS or SDBS). These observations are all consistent with hypothesized picture described above regarding how Tween 80 may affect the PA formation. Lastly, the emergence of the nodular and crumpled structures (Figure 3.1A-C) results from the improved wetting the PES substrate by the surfactant-doesed PIP solution, which has been well elaborated by Niu et al.[123]

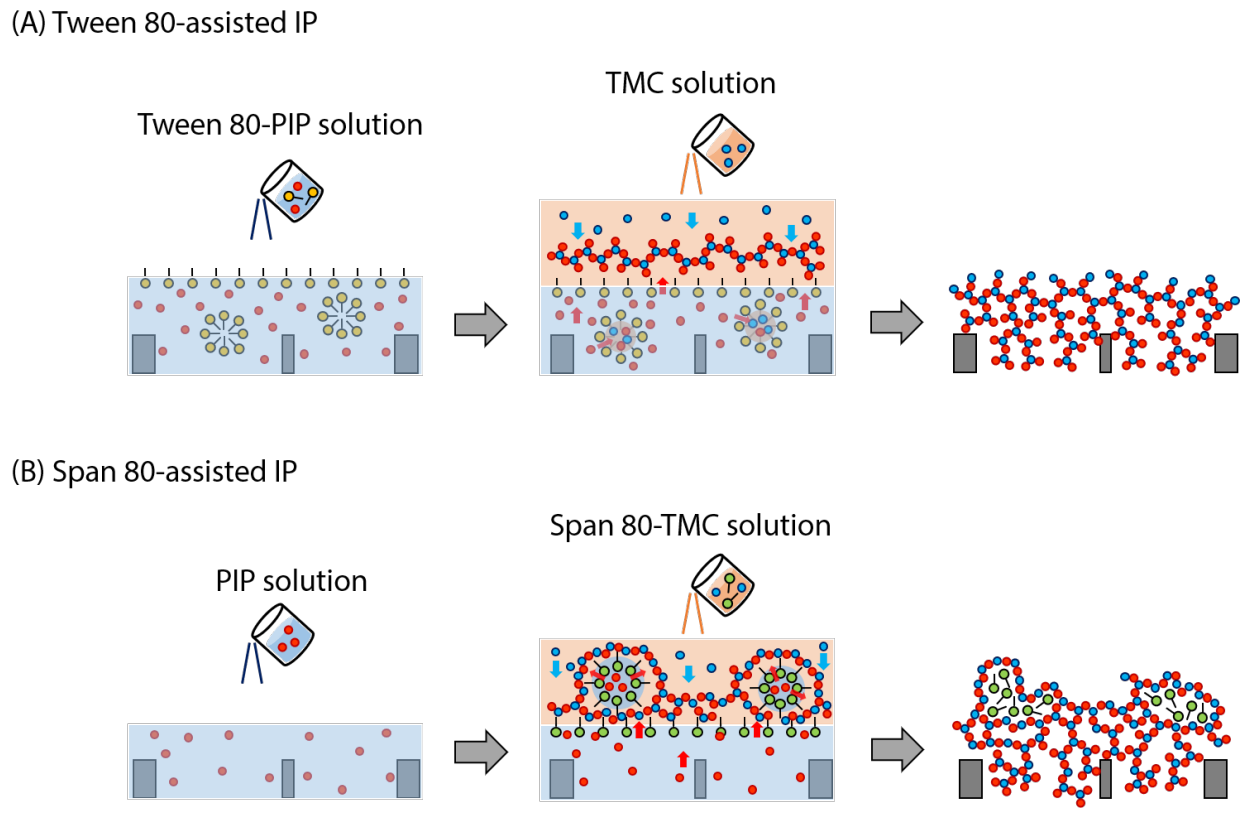

Figure 3.4 Schematic illustration of the polyamide active layer formation via IP with the addition of (A) the hydrophilic nonionic surfactant (Tween 80) and (B) the lipophilic nonionic surfactant (Span 80).

Compared to adding Tween 80 into the aqueous PIP solution, the impact of adding Span 80 into the hexane TMC solution on interfacial polymerization is very different. As Span 80 is an highly effective w/o emulsifier, PIP encapsulated in water-in-hexane emulsions transport to the hexane phase again via the "vehicle effect". The emulsion-facilitated transport of PIP adds to the trans-interface diffusion of PIP from the water to hexane. These w/o emulsions also serve as microreactors for interfacial polymerization, except that in this case the PA forms around the spherical emulsified droplets because PA tends to form in the hexane side of the water/hexane interface. These PA fragments are less susceptible to hydrolysis as the emulsion are in (bulk) hexane and are thus afforded the opportunity to continue to react with other PA fragments from the reaction between TMC and the PIP diffusing across the interface between the bulk water and bulk hexane. Eventually, these "PA vesicles" forming around the w/o emulsions merged with the PA film forming at the interface between the bulk water and bulk hexane phases. When the PA

membrane was tried, the evaporation of water inside these vesicles led to the formation of collapsed vesicles as observed in Figure 3.1D-F. In this case, the Span 80 surfactants are trapped in the collapsed PA and contribute substantially to the XPS-measured chemical composition of the PA layer (Table 3.1) and the physical properties of the PA layers such as surface potential (Figure 3.2A) and WCA (Figure 3.2B).

3.3.4. Membrane performance and pore structure

The addition of different nonionic surfactants in different phases results in distinct membrane performance. In the case when Tween 80 was added into the aqueous phase, the measured salt rejection of the TFC-PA NF membranes increased when Tween 80 concentration increased from 0% w/v to 0.125% w/v (Figure 3.5A). When the Tween 80 concentration exceeded 0.5% w/v, the salt rejections for several salts (except Na_2SO_4) declined. The initial increase of the salt rejection rates was attributable to a reduction of the molecular weight cut-off (MWCO) of the TFC-PA membranes prepared in the presence of Tween 80 (Figure 3.5B and inset). In particular, the TFC-PA membranes prepared with a Tween 80 concentration of 0.125% w/v exhibited a remarkable performance for precisely separating divalent and multi-valent ions (e.g., Zn^{2+}, Mg^{2+}, SO_4^{2-}, $Fe(CN)_6^{3-}$, etc.) from monovalent salt (K^+, Na^+, NO_3^-, etc.) (Figure S3).

This enhancement in the precision of separation by Tween 80 is similar to what has been observed in surfactant assembly-regulated interfacial polymerization (SARIP) using SDS[37]. We believe that the self-assembled Tween 80 network at the water-hexane interface regulates the trans-interface diffusion of PIP from the water phase to the hexane phase and thereby improves the homogeneity of the pore size distribution of the resulting PA membrane (Table 3.3). However, when the Tween 80 concentration reached 0.5% w/v, the separation performance became compromised as the rejections of divalent cations became substantially lower (Figure 3.5A) and the MWCO of the membrane became larger (Figure 3.5B). The deterioration in performance at high Tween 80 concentration is likely attributable to the integration of Tween 80 molecules in the PA active layer as indicated by both the measured WCA (Figure 3.5B) and active layer composition (Table 3.2)

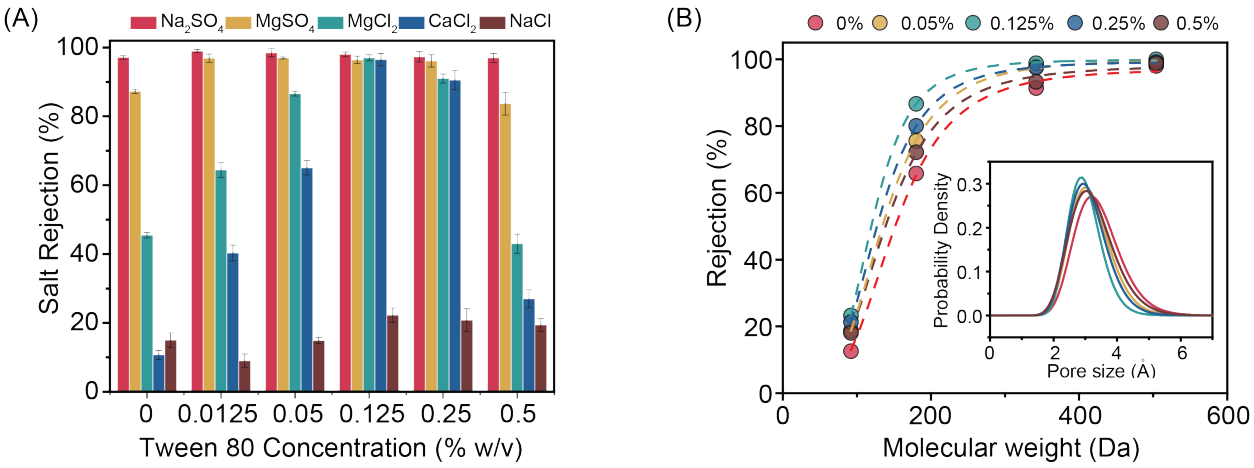

Figure 3.5 (A) Concentration-dependent salt rejection of the PA-TFC NF membranes prepared via IP with hydrophilic nonionic surfactant (Tween 80). (B) Rejection of uncharged organic molecules including glycerol, glucose, sucrose and raffinose. Inset: pore size distribution of the PA-TFC NF membranes as a function of Tween 80 concentration derived from the rejection curves of uncharged organic molecules. All measurements are carried out at an applied pressure of 4 bar. Rejection and flux data are reported as the average of three runs, and the error bar represents the standard deviation of three runs.

Table 3.3 Mean pore size and distribution of pore size of polyamide active layer formed from IP with (A) the hydrophilic nonionic surfactant (Tween 80) and (B) the lipophilic nonionic surfactant (Span 80).

Membrane type		**Mean pore size (A)**	**Pore size distribution**
Reference (no surfactant added)		3.312	1.238
Tween 80	0.05%	3.126	1.222
	0.125%	2.956	1.189
	0.25%	3.046	1.217
	0.5%	3.175	1.245
Span 80	0.005%	3.064	1.233
	0.05%	3.124	1.258
	0.25%	3.209	1.241
	0.5%	3.28	1.243

The impact of Span 80 on the performance of the resulting the TFC-PA NF membranes is different from the impact of Tween 80 as discussed above. The rejection of divalent ions increased dramatically even at very low Span 80 concentration (Figure 3.6A). The increase of membrane

rejection is likely attributable to the enhanced steric hindrance because of the surfactant insertion in the polyamide network. Unlike Tween 80, the presence of Span 80 at the water-hexane interface will cause the severe implementation of Span 80 molecules inside the PA network during the IP process even at a low concentration (Figure 3.3B). More importantly, the addition of lipophilic nonionic surfactants (e.g., Span 80) had little influence on the pore size distribution of the polyamide network (Figure 3.6C, D, Table 3.3). This is caused by the instability of water/hexane interface when the TMC-Span 80 hexane solution is added on the water surface, where Span 80 is unable to form a well-organized surfactant network at the water/hexane interface. Instead, it creates a number of w/o emulsions in the hexane, leading to the formation of irregular polyamide segments. As the Span 80 concentration increased, the rejection for divalent cations systematically declined, which is also consistent with the trend of change in MWCO (Figure 3.6B). The systematic changes in system performance and MWCO are consistent with the systematic variation of the active layer properties (Figure 3.2A and 3.2B) and composition (Table 3.2) as the Span 80 concnetraiton increases. Therefore, the integration of more Span 80 in the PA layer may likely be the cause of the larger MWCO and the reduced Mg^{2+} and Ca^{2+} rejections. The initial reduction in MWCO and enhancement of divalent cation rejections, however, are likely attributable partially to the effect of SARIP.

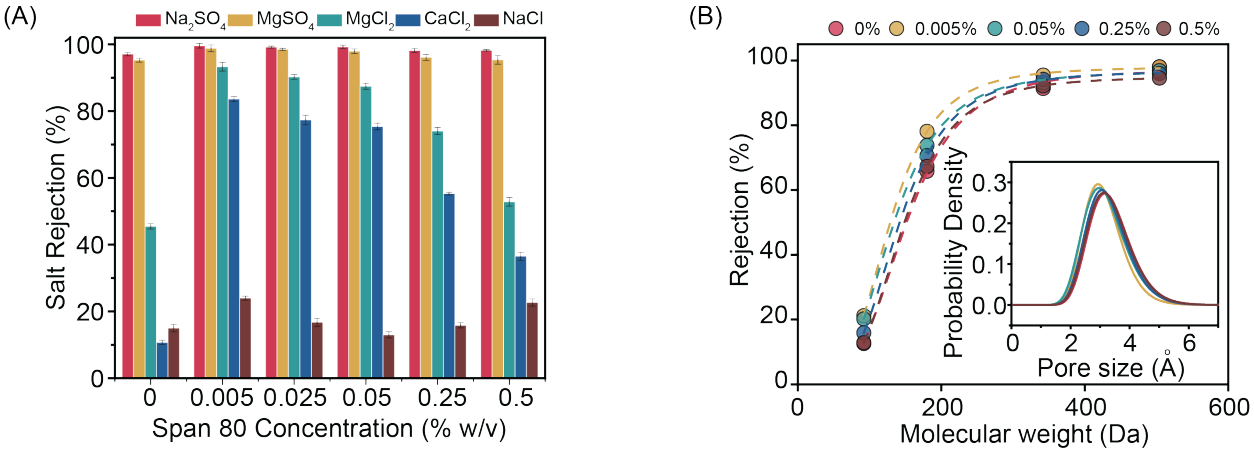

Figure 3.6 Concentration-dependent (A) salt rejection of the PA-TFC NF membranes prepared via IP with lipophilic nonionic surfactant (Span 80). (B) Rejection of uncharged organic molecules including glycerol, glucose, sucrose and raffinose for the PA-TFC NF membranes prepared via IP with Span 80. Inset: Pore size distribution of the PA-TFC NF membranes as a function of Span 80 concentration derived from the rejection curves of uncharged organic molecules. All

measurements are carried out at an applied pressure of 4 bar. Rejection and flux data are reported as the average of three runs, and the error bar represents the standard deviation of three runs.

3.4.Conclusion

In summary, our study has demonstrated the role of hydrophilic and lipophilic nonionic surfactant, Tween 80 in water and Span 80 in hexane, on the formation of polyamide active layer during the interfacial polymerization process. Unlike ionic surfactants, the nonionic surfactants create and stabilize the PIP/water-TMC/hexane emulsions in the water or hexane phases, which serve as new micro IP reaction cores. The individually formed polyamide fragment in hexane becomes attached to the surface of the polyamide active layer and thus creates a distinct surface morphology, whereas the additional polyamide fragments formed in water phases are eliminated quickly due to fast hydrolysis and washed away. This finding not only demonstrates the mechanism of nonionic surfactant-mediated IP, but also provides additional guidance for the surfactant selection to tailor the structure and performance of TFC-PA NF membranes.

CHAPTER 4

INTERCALATION OF ANIONIC SURFACTANTS DRAMATICALLY ENHANCES THE PERFORMANCE OF DENSE NANOFILTRATION MEMBRANE FOR SALT REMOVAL

4.1.Introduction

Nanofiltration (NF) has received growing attention in recent years in water and wastewater treatment applications[19,129]. It is an effective and chemical-free unit process for water softening and has also been widely explored in treating contaminated groundwater and in wastewater reuse[130–133]. The key advantage of NF is the ability to selectively reject the target species (from the permeate) while allowing other species to pass through[37,134]. This ability of selective species removal has important practical implications. For example, using NF instead of reverse osmosis (RO) for water softening significantly consumes significantly less energy due to the much lower osmotic pressure difference across an NF membrane leaky to most of the monovalent ions as compared to that across an RO membrane that rejects nearly all ions[1,4,135]. In another example, NF can be applied in wastewater reuse to remove heavy metals and micropollutants but allow nutrient ions (e.g. phosphate and ammonia) to stay in the permeate for direct fertigation[136–140]. In yet another example, NF can be used to concentrate organic contaminants for more cost-effective chemical treatment (of those contaminants)[141].

Enhancing the cost-effectiveness of NF requires membranes of high perm-selectivity, i.e., these membranes should have high water permeance and satisfactory rejection of the target species. However, in many cases, there is an intrinsic tradeoff between these two performance metrics, i.e., a membrane with higher water permeance typically has poorer performance in solute rejection[12,57]. Rational and innovative designs of the active layer of NF membranes are required to achieve a high perm-selectivity[56,59,142]. Among the different approaches to fabricate NF/RO membranes, using layer-by-layer (LbL) deposition of polyelectrolytes to construct a polyelectrolyte multilayer (PEM) as the active layer for separation is a highly flexible approach with the capability of fine-tuning the active layer properties[143–145].

In fabricating PEM-NF membranes using LbL deposition of polyelectrolyte, two types of oppositely charged polyelectrolytes alternately deposit onto an ultrafiltration membrane substrate.

The irreversible LbL deposition of polyelectrolytes is mainly driven by electrostatic attractions between the oppositely charged polyelectrolytes[40–43]. Several critical membrane properties, such as the pore size distribution, surface charge, active layer thickness, are affected by multiple factors in the LbL deposition process, such as the type of polyelectrolytes[44,45], polyelectrolyte concentration[44], ionic strength of the polyelectrolyte solution [46–48], pH[49–51], and temperature[52,53]. Adjusting these parameters provides avenues to control the membrane permeance and ion selectivity. Beyond these parameters, integrating various types of additives (e.g., nanomaterials) into the PEM is also a widely explored approach to enhance the perm-selectivity[54,55].

In our recent studies, we reported a novel and cost-effectively approach to dramatically enhance the permeance of "loose" NF membranes for removing of macromolecules (e.g., humic acid and dyes)[140,146]. This approach is based on the intercalation of surfactant bilayers between the polycations and polyanions and has been demonstrated to be capable of enhancing the performance by multiple folds without compromising the rejection of macromolecules. The use of surfactant bilayers as nanometer-thin "structural modifiers" to enhance NF performance is not only conceptually novel and interesting, but also generally more practical as compared to using nanomaterials. However, it remains unclear (1) how surfactant assemblies enhanced the water permeance without compromising solute rejection; and (2) if this novel approach is effective for enhancing the performance of salt-rejecting "dense" NF membranes which have an active layer with much smaller pore size than "loose" NF membranes. This work is performed with the aim to address these two questions.

In this study, we investigate how the intercalation of anionic surfactants (sodium dodecylsuflate) between the polycations and polyanions affects the perm-selectivity of the resulting NF membrane. The dense NF membrane for rejecting Na_2SO_4 is fabricated using poly(diallyldimethylammonium chloride) as the polycations and poly (sodium 4-styrenesulfonate) as the polyanions. We employ quartz crystal microbalance with dissipation (QCM-D) to investigate the impact of surfactant integration on polyelectrolyte adsorption. We also perform ellipsometry and polarization modulation-infrared reflection adsorption spectroscopy to probe the impact of surfactant integration on the thickness and molecular structure of the resulting PEM films. With PEM-NF membranes developed using LbL, we compare the pore size distribution, morphology, and interfacial properties between membranes with and without surfactant intercalation. We also evaluate the impact of surfactant intercalation on the NF performance of the

PEM-NF membranes and relate the NF performance to the membrane properties. Finally, we evaluate the long-term stability of surfactant-intercalated PEM NF membranes and its stability under various solution and operation conditions.

4.2.Materials and methods

4.2.1. Materials and chemicals

Polyacrylonitrile ultrafiltration (PAN, UF) membrane with a molecular weight cut-off of 50 kDa (GE Healthcare Life Science) was used as the substrate for preparing polyelectrolyte multilayer NF membrane. Poly (diallyldimethylammoniumchloride) (PDADMAC; MW 400,000–500,000 g mol^{-1}; 20% wt. in water), poly (sodium 4-styrenesulfonate) (PSS; MW 1,000,000 g mol^{-1}), sodium dodecyl sulfate (SDS, >99%), sodium hydroxide (NaOH, >98%), Na_2SO_4 (≥99%), $MgSO_4$ (≥99.5%), $MgCl_2$ (≥99.99%), NaCl (≥99%), anhydrous D-(+)-glucose (MW 180 g mol^{-1}, ≥99.5%), sucrose (MW 342 g mol^{-1}, ≥99.5%), D-(+)-raffinose pentahydrate (MW 594 g mol^{-1}, ≥ 98%) were purchased from Sigma Aldrich (St. Louis, MO, USA). All chemicals were used as received without purification. Silicon wafers were purchased from Pure Wafer, Inc. (San Jose, CA, USA). Deionized water (Millipore, USA) was used for solution preparation, membrane cleaning during the LbL process, and NF performance test.

4.2.2. Membrane fabrication

The PAN substrate membrane was pretreated using 2 M NaOH for 30 minutes to acquire a negative surface charge and then rinsed with DI water. The reference membranes, namely $(PD\text{-}PS)_n$ membranes, were prepared via alternate deposition of PDADMAC and PSS with and without the addition of NaCl (concentration varies from 0 to 0.1 M). The hydrolyzed PAN substrate was first exposed to the solution of cationic PDADMAC (1 g L^{-1}) for 30 min, rinsed with DI water for 5 min, then exposed to the solution of anionic PSS (2 g/L^{-1}) for another 30 min, and rinsed with DI water for 5 min (Figure 4.1A). The resulting membrane is referred to as the $(PD\text{-}PS)_1$ with the subscript "1" denoting one PD-PS bilayer. The same deposition cycle was repeated to form

additional bilayers (n=1 to 5). In this study, we focus on making PEM-NF for removing salts with divalent anions. Therefore, all membranes fabricated in this study were terminated with a polyanion (PSS) layer. The role of ionic strength on the properties and performance of the $(PD\text{-}PS)_n$ PEM-NF membrane was studied by adding NaCl into the aqueous polyelectrolyte solution during LbL deposition.

The fabrication of the SDS-intercalated PEM-NF (s-PEM-NF) membranes followed a similar procedure as that for preparing the reference PEM-NF membranes except for an additional step of surfactant deposition between the polycation and polyanion depositions (Figure 4.1B). Specifically, after each step of PDADMAC deposition, the membrane with PDADMAC-terminated surface was immersed into an aqueous SDS solution for 30 min (SDS concentration varies from 0 to 1.0 critical micelle concentration, CMC). The SDS-coated PDADMAC surface was rinsed with DI water for 5 min, and then further subject to PSS deposition. The resulting membrane was referred to as the $(PD\text{-}s\text{-}PS)_1$ membrane, with the subscript "1" representing one tri-layer of polyelectrolytes and surfactants. The same deposition procedure was repeated to form additional tri-layers (n=1 to 5). When studying the role of ionic strength on the structure of $(PD\text{-}s\text{-}PS)_n$ PEM-NF membranes, NaCl was only added into the polyelectrolyte solutions during membrane fabrication (i.e., it was not added to the surfactant solutions).

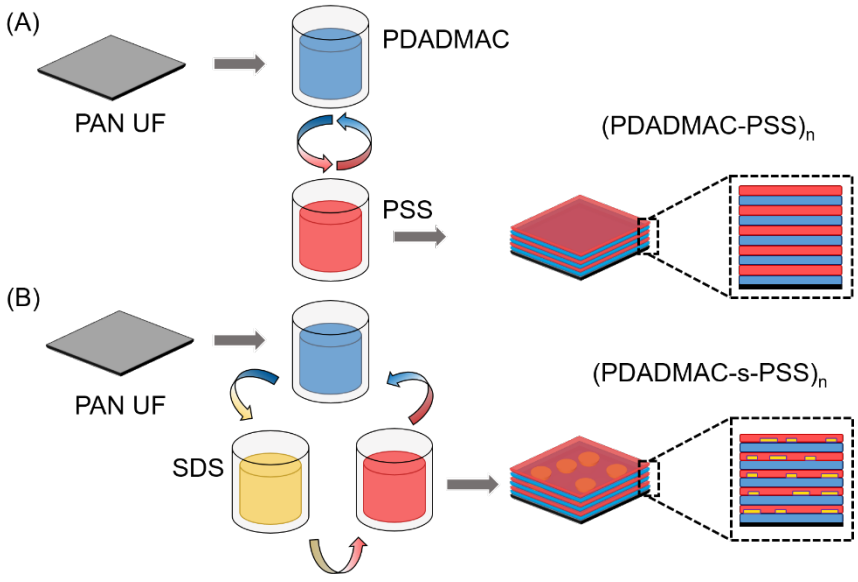

Figure 4.1 (A) Fabrication of reference $(PD\text{-}PS)_n$ multilayer NF membranes via alternating electrostatic deposition of polycation (PDADMAC) and polyanion (PSS) on a PAN ultrafiltration membrane. (B) Fabrication of the surfactant-integrated $(PD\text{-}s\text{-}PS)_n$ multilayer NF membrane via sequentially electrostatic deposition of polycation (PDADMAC), surfactant (SDS) and polyanion (PSS) on a PAN ultrafiltration membrane.

4.2.3. Probing polyelectrolyte deposition with QCM-D

The adsorption of polyelectrolytes and surfactants was quantified using a quartz crystal microbalance with dissipation (QCM-D) equipped with a SiO_2-modified quartz crystal sensor (Biolin Scientific Q-Sense E4). The QCM-D system has four parallel flow cells, and a peristaltic pump was used to circulate polyelectrolyte and surfactant solutions through these cells. In a QCM-D measurement, an AC voltage was applied to excite the oscillation of the crystal at its fundamental resonant frequency. The frequency (*F*) and dissipation (*D*) was determined by fitting the decay of the crystal oscillation. With QCM-D, we measured the frequency shifts and energy dissipation of the quartz crystal sensor during the polyelectrolyte deposition process, from which we can estimate the temporal evolution of the deposited mass and the viscoelastic properties of each polyelectrolyte layer.

Prior to use, the SiO_2-modified quartz crystal sensor was cleaned with ammonia (25%) and hydrogen peroxide (30%) and rinsed thoroughly with deionized water. The oscillation frequency of the SiO_2-modified quartz crystal sensor was first measured with Milli-Q water at a flow rate of 100 uL min^{-1}. The stable normalized frequency at the 3rd overtone was recorded as the baseline. For the deposition experiments, the aqueous polyelectrolyte solutions (1 g L^{-1} PDADMAC and 2 g L^{-1} PSS) and surfactant solution (SDS at its CMC) were introduced alternately, at a flow rate of 100 uL min^{-1}, following the same deposition sequence as described in the membrane fabrication section. Upon adsorption, the resonance frequency of the SiO_2-modified quartz crystal decreases with the continuous increased in the mass of the crystal, which is commonly described by the Sauerbrey relationship[147,148]:

$$\Delta m = -\frac{C\Delta f_n}{n}$$

where $\boldsymbol{\Delta m}$ is the mass of polyelectrolyte deposited on the crystal, $\boldsymbol{C}$ is the crystal constant, $\boldsymbol{\Delta f_n}$ is the shift in resonance frequency and $\boldsymbol{n}$ is the overtone number (the 3rd overtone is used in this

study). Both the frequency and dissipation data were collected at a frequency of 200 Hz. All measurements were carried out at 25 ºC.

4.2.4. Measuring PEM thickness with ellipsometry

Direct characterization of the film thickness of PEM on the PAN UF substrate is challenging due to the intrinsic roughness of the porous PAN substrate membrane. Therefore, we constructed PEM on atomically smooth silicon wafers to characterize the effect of surfactant intercalation on the PEM thickness using ellipsometry. For the thickness measurement, we repeated the LbL assembly of both the $(PD\text{-}PS)_n$ and surfactant-integrated $(PD\text{-}s\text{-}PS)_n$ multilayers (n=1 to 5) on silicon wafers and measured the thickness of resulting films at different deposition stages using a dual rotating-compensator spectroscopic ellipsometer (J.A. Woollam M-2000VI). The ellipsometer's light source and detector were attached to the chamber at viewport flanges, which were set at ~ 70º with respect to sample surface normal. The thickness of each PEM was measured three times at different locations.

4.2.5. Characterizing chemical structure of PEM using PM-IRRAS

To explore the effect of surfactant intercalation on the chemical characteristics of the PEM, we investigated the $(PD\text{-}PS)_5$ and $(PD\text{-}s\text{-}PS)_5$ multilayers deposited on Au/Si substrates by polarization modulation-infrared reflection adsorption spectroscopy (PM-IRRAS) (Bruker Tensor 27 spectrometer, USA). PM-IRRAS was performed using a Bruker Tensor 27 Fourier transform infrared spectrometer equipped with a PEM-90 photoelastic modulator and a liquid-nitrogen cooled mercury cadmium-telluride dector with a nondichroic BaF_2 window. The source beam employed a half-wavelength retardation modulated at a frenquency of 50 kHz and the incidence angle is set at 85º to the PEM sample surface. Spectra were collected over 360 scans at a resolution of 4 cm^{-1}.

To prepare a sample for PM-IRRAS characterization, a clean Au/Si substrate was immersed in an ethanol solution of 1 mM thioglycolic acid for 14 hours, then washed with an excess amount of ethanol and water and dried under nitrogen to prepare a negatively charged self-

assembled monolayer (SAM) surface. The successful deposition of SAMs was confirmed by the change of surface wetting property. Specifically, the advancing water contact angle (WCA) changed from 75±3 º for a pristine Au/Si surface to 5±3º for a SAM/Au/Si surface. The preparation of reference $(PD\text{-}PS)_5$ and SDS-intercalated $(PD\text{-}s\text{-}PS)_5$ PEM films on the SAM surface then followed a similar deposition sequence as in the membrane fabrication section.

4.2.6. Characterizing membrane pore size distribution and interfacial properties

To acquire properties of the PEM that are relevant to separation performance, we measured the surface zeta potentials of the $(PD\text{-}PS)_n$ and $(PD\text{-}s\text{-}PS)_n$ PEM-NF membranes at different deposition stages using a streaming potential analyzer (SurPASS electrokinetic analyzer, Anton Paar, Ashland, VA) using an adjustable gap cell with a channel width around 100 um. The zeta potentials of PEM NF membranes at different pH is determined via a pH titration from 10 to 3 using 1 mM KCl as the electrolyte solution at room temperature.

An optical tensiometer (Theta Lite, Biolin Scientific) was used to measure the contact angle of the (PD-PS)n and (PD-s-PS)n PEM NF membranes using the sessile drop method. A droplet volume of 5 ± 1 μL of DI water was used for each test at three random locations on three independent PEM NF membranes at different deposition stages. An optical image of the droplet on the surface was taken after being deposited and is used to estimate the contact angle. We also characterized the surface morphology of PEM NF membranes using scanning electron microscopy (SEM, Zeiss Merlin) and Atomic force microscopy (AFM, Bruker). The surface roughness of $(PD\text{-}PS)_n$ and $(PD\text{-}s\text{-}PS)_n$ membranes was compared based on the surface topography measured using AFM.

To estimate the pore size distribution of the $(PD\text{-}PS)_n$ and $(PD\text{-}s\text{-}PS)_n$ PEM-NF membranes, we tested the PEM-NF membranes with a series of neutral organic molecules, including glycerol (92 Da), glucose (180 Da), sucrose (342 Da), raffinose (504 Da) and β-cyclodextrin (1135 Da). The feed concentration of each organic species was 0.2 g L^{-1} and all measurements were carried out with an applied pressure of 4 bar. After the flux became stable, we collected feed and permeate samples and measured their solute concentrations using a Total Organic Carbon (TOC) analyzer. The molecular weight cut-off (MWCO) of the PEM-NF membrane is defined as the molecular

weight at which the rejection is 90%. The mean pore radius of the PEM-NF membrane equals the Stokes radius of the organic solute with a measured rejection of 50%. The distribution of the membrane pore size is determined as the geometric standard deviation of the PDF curve (equation below), which is the ratio between the Stokes radius corresponding to a rejection of 84.13% and that corresponding to a rejection of 50%[112].

$$\frac{dR(r_p)}{dr_p} = \frac{1}{r_p ln\sigma_p \sqrt{2\pi}} \exp\left[-\frac{(lnr_p - ln\mu_p)^2}{2(ln\sigma_p)^2}\right]$$

where μ_p is the mean pore size, σ_p is the geometric standard deviation of the PDF curve and r_p is the Stokes radius of the organic solute.

4.2.7. Evaluating membrane performance in nanofiltration

We evaluated the water permeance and solute rejection of the $(PD\text{-}PS)_n$ and $(PD\text{-}s\text{-}PS)_n$ PEM-NF membranes using a custom-made stainless steel NF cell with crossflow and an effective membrane area of 7.1 cm^2. All measurements were carried out at a constant temperature of 25 ± 0.5 °C and a crossflow velocity of 8.7 cm s^{-1}. Prior to filtration, we compacted the PEM-NF membranes overnight at the testing pressure of 4 bar. After compaction, we calculated the pure water permeance (*PWP*, unit: L m^{-2} h^{-1} bar^{-1}) of the PEM-NF membrane using the following equation:

$$PWP = \frac{J_w}{\Delta P}$$

where J_w is the volumetric flux of water (L m^{-2} h^{-1}), and ΔP is the applied pressure (bar), respectively. The salt rejection performance of the $(PD\text{-}PS)_n$ and $(PD\text{-}s\text{-}PS)_n$ PEM-NF membranes was evaluated with Na_2SO_4, $MgSO_4$, $MgCl_2$ and NaCl (1 g L^{-1} in all cases). The salt rejection rate was calculated using the following equation:

$$R = \left(1 - \frac{c_p}{c_f}\right) \times 100\%$$

where $\boldsymbol{c_p}$ and $\boldsymbol{c_f}$ are the solute concentration of permeate and feed solution, which are determined by measuring the electrical conductivity of the feed and permeate solution, respectively.

4.3.Result and discussion

4.3.1. Effect of surfactant intercalation on the kinetics of polyelectrolyte deposition

The LbL formation of the reference $(PD\text{-}PS)_5$ PEM film and surfactant-integrated $(PD\text{-}s\text{-}PS)_5$ PEM film is quantitatively captured by QCM-D measurements (Figure 4.2A, B). Based on the equation in section 4.2.3., the relationship between adsorbed mass and the shift of resonance frequency from the 3rd overtone, Δf, follows $\Delta m \approx -0.3\Delta f$.

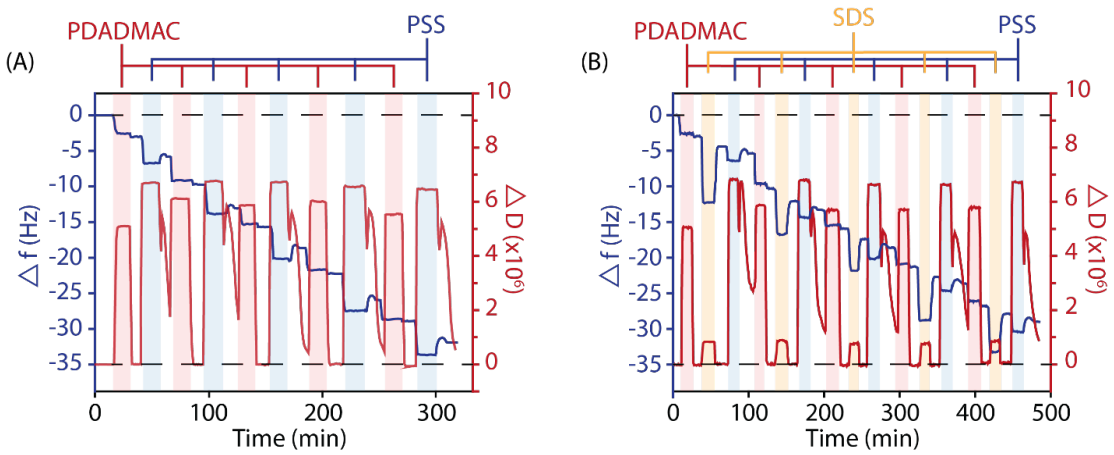

Figure 4.2 The change of frequency (from the third overtone) and energy dissipation as a function of the adsorption of the first five bilayers of (A) reference $(PD\text{-}PS)_n$ PEM film and (B) surfactant-integrated $(PD\text{-}s\text{-}PS)_n$ PEM film. Red column represents the deposition step of cationic PDADMAC, blue column represents the deposition step of anionic PSS and yellow column represents the deposition step of SDS. Empty column in between every two-colored columns represents the cleaning step using DI water.

In general, the introduction of polyelectrolyte to a quartz crystal sensor coated with oppositely charged polyelectrolyte led to a sharp decrease in resonance frequency due to the fast adsorption of polyelectrolyte via electrostatic interaction (Figure 4.2). Comparing the Δf for the adsorption of PDADMAC and PSS reveals that more PSS adsorbed onto the sensor surface than PDADMAC (Figure 4.2A, blue curve). Flushing the surface with DI water resulted in a negligible change of Δf after PDADMAC adsorption but a significant and consistent increase of Δf after PSS adsorption, likely due to the partial desorption of weakly bound PSS and the swelling of the adsorbed PSS layer[149]. Without intercalation of SDS, the total change of resonant frequency over

the deposition of five layers of PD-PS on the SiO_2-coated quartz crystal was ~32 Hz, which corresponds to an areal mass density of 96.1 ± 0.2 ng cm^{-2}.

The adsorption of both PDADMAC and PSS also led to sharp increases of dissipation (Figure 4.2A, red curve) due to the non-rigid nature of the adsorbed polyelectrolyte layer. However, when rinsing the system with DI water after each adsorption step, the dissipation experienced a significant drop because of the reconfiguration of adsorbed polyelectrolyte that resulted in a more compact and rigid layer[150]. In particular, the dissipation always reverted to zero almost immediately when a PDADMAC-coated surface was rinsed with DI water. For PSS-coated surface, however, the decline of dissipation was more gradual and did not reach zero in the limited rinsing time window.

The introduction of SDS dramatically changed the dynamics of the LbL process (Figure 4.2B). First, we observe from Δf that SDS deposited onto the surface in a substantial amount, resulting in an Δf that is multiple times of that for PDADMAC and PSS adsorption. However, the dissipation induced by SDS adsorption is very small, likely due to the higher degree of rigidness for a layer of short-chain molecules (as compared to polyelectrolytes). Rinsing the SDS-coated surface appeared to remove most of the SDS, suggesting that only part of the adsorbed SDS could remain on the surface after DI water rinsing. Interestingly, the presence of SDS on the PDADMAC surface reduced the consequent adsorption of the PSS. Specifically, the $\Delta \boldsymbol{f}$ of the 1st to 5th deposited PSS layers in the absence of SDS was approximately 2.8, 3.1, 3.0, 3.2, and 3.3 Hz, respectively (Figure 4.2A), much higher than that in the presence of SDS (approximately, 0.9, 1.1, 1.1, 1.1 and 1.1 Hz for the 1st to 5th layer, Figure 4.2B)

Because the partial desorption of PSS was as significant in the presence of SDS (Figure 4.2A) as in the absence of SDS (Figure 4.2B), the overall effect of less PSS adsorption and similar PSS desorption is the substantially reduced amount of net PSS adsorption in each step. The reduced net PSS adsorption is likely attributable to the presence of adsorbed SDS that occupies part of the positive adsorption sites provided by PDADMAC. The areal mass density of the $(PD\text{-}s\text{-}PS)_5$ membrane was 87.0 ± 0.1ng cm^{-2}, which is slightly lower than that of the $(PD\text{-}PS)_5$ membrane (96.1 ± 0.2 ng cm^{-2}) even with the additional adsorbed SDS.

4.3.2. Effect of surfactant intercalation on the thickness of PEM

The impact of SDS intercalation on the thickness of $(PD\text{-}PS)_n$ PEM film on an atomically smooth silicon wafer was characterized using a spectroscopic ellipsometer and the results are shown in Figure 4.3. The thickness increment for the deposition of each bilayer is slightly, but consistently, larger for reference $(PD\text{-}PS)_n$ multilayer film than for the $(PD\text{-}s\text{-}PS)_n$ multilayer film. In both cases, the thickness increment per additional bi- or tri-layer is constant except for the first bi- or tri-layer (Figure 4.3). Specifically, each additional bi- or tri-layer adds 6.1 ± 0.1 nm of thickness increment to the $(PD\text{-}PS)_n$ film and 5.3 ± 0.1 nm to the $(PD\text{-}s\text{-}PS)_n$ film, respectively. The initial non-linear increment of film thickness was caused by the fact that the first PDADMAC/PSS bilayer may not form a homogenous film and assemble into heterogeneous islands on the silicon wafer[151–153].

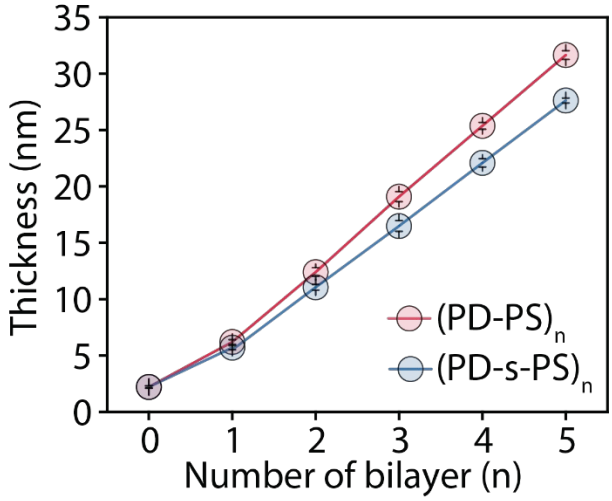

Figure 4.3 Thickness increment of the reference $(PD\text{-}PS)_n$ and surfactant-integrated $(PDADMAC\text{-}s\text{-}PSS)_n$ multilayer films on Si wafer as a function of bilayer number. The reported value represents the average of three measurements and the error bar indicates the standard deviation of three runs.

4.3.3. How does SDS intercalation change the PEM properties?

Chemical characteristics and pore size

The Fourier Transform Infra-Red (FTIR) spectrum of the $(PD\text{-}PS)_5$ PEM film shows two characteristic absorption peaks at 1184 cm^{-1} and 1042 cm^{-1} due to the asymmetric and symmetric

stretching vibrations of the $–SO^{3-}$ groups from PSS (Figure 4.4A), respectively. The absorption peak at 1468 cm^{-1} is characteristic of $–CH_3$ bending vibrations in PDADMAC. Notably, no new peak emerges beyond those characteristics of PSS and PDADMAC, which suggests the absence of covalent interaction between the two polyelectrolytes[154].

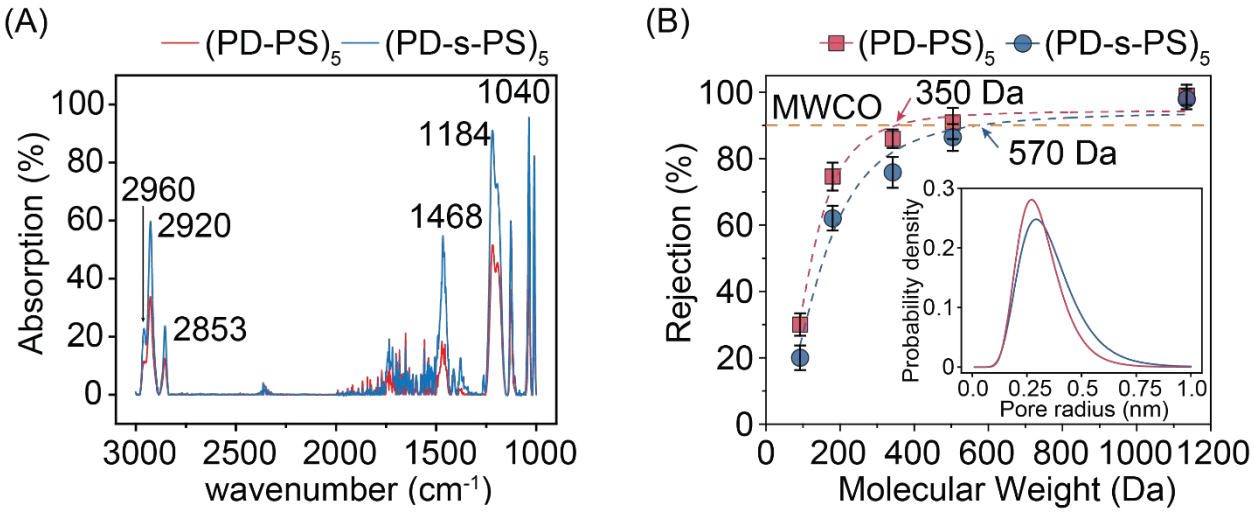

Figure 4.4 (A) FTIR spectra of the reference (PD-PS)n and the surfactant-intercalated (PD-s-PS)n multilayer films on SAMs surface. (B) Impacts of SDS integration on the molecular weight cut-off (MWCO) and pore size distribution of the (PD-PS)5 and (PD-s-PS)5 PEM NF membrane.

The intercalation of SDS into the $(PD\text{-}s\text{-}PS)_5$ PEM was confirmed by the emergence of an absorption peak at 2960 cm^{-1} that corresponds to symmetric -CH_3 stretching[155,156]. The presence of the SDS increases the intensity of all three characteristic peaks mentioned above due to the reduced crystallinity (increased number of gauche CH_2)[157]. The reduction of crystallinity increases the free volume of the PEM and thus potentially affects pore size distribution and enhances the membrane permeability. The increase in pore size distribution was confirmed by filtration experiments with a series of neutral organic compounds. Specifically, $(PD\text{-}PS)_5$ and $(PD\text{-}s\text{-}PS)_5$ PEM-NF membranes have an MWCO of 350 and 570 Da, respectively (Figure 4.4B), which correspond to a mean pore size of 0.3 and 0.34 nm, respectively (Figure 4.4B. Inset).

4.3.4. Wetting properties and surface potential

The NaOH-treated PAN UF membrane surface became hydrophilic with a water contact angle (WCA) of 12°, and carried a strongly negative surface charge (Figure 4.6, white squares). The adsorption of the first layer of PDADMAC increased the WCA to 45° (Figure 4.6A, B), similar to values reported in literature[158,159]. It also reversed the surface charge from -78 mV to 57 mV (Figure 4.5C). In the absence of SDS, the adsorption of the first layer of PSS substantially reduced the WCA of the surface (Figure 4.5A) as PSS is a more hydrophilic polymer than PDADMAC[158,159]. The adsorption of PSS also reverted the surface potential to be strongly negative (Figure 4.5C). Repeating the alternate deposition of PDADMAC and PSS always incurred the change of WCA and surface potential in a similar pattern as the first bilayer. However, the WCA of both the PDADMAC-coated surface and PSS-coated surface systematically increased (Figure 4.5A), while the surface potential of both the PDADMAC-coated surface and PSS-coated surface slightly but systematically decreased (Figure 4.5C), as the number of bilayers increased.

The adsorption of SDS onto a PDADMAC surface dramatically reduced the WCA (Figure 4.5B) and surface potential (Figure 4.5D), which suggests that SDS likely formed a bilayer with one side attaching onto the positively charged PDADMAC surface and the other side exposed. The adsorption of PSS onto an SDS-coated surface only resulted in slight changes of WCA and surface potential because of the suppressed PSS adsorption as shown in the QCM-D results (Figure 4.2A, B). The most notable effect of the SDS intercalation is enhancing the overall hydrophilicity of the PEM-NF membranes. Specifically, the WCA of the $(PD\text{-}s\text{-}PS)_n$ membrane in each deposition step is systematically lower than that of the reference $(PD\text{-}PS)_n$ membrane in the same deposition step. The enhanced hydrophilicity has been reported to be beneficial to membrane permeance[160,161]. Compared with the impact on WCA, the impact of SDS intercalation on surface potential is considerably smaller (Figure 4.5C, D).

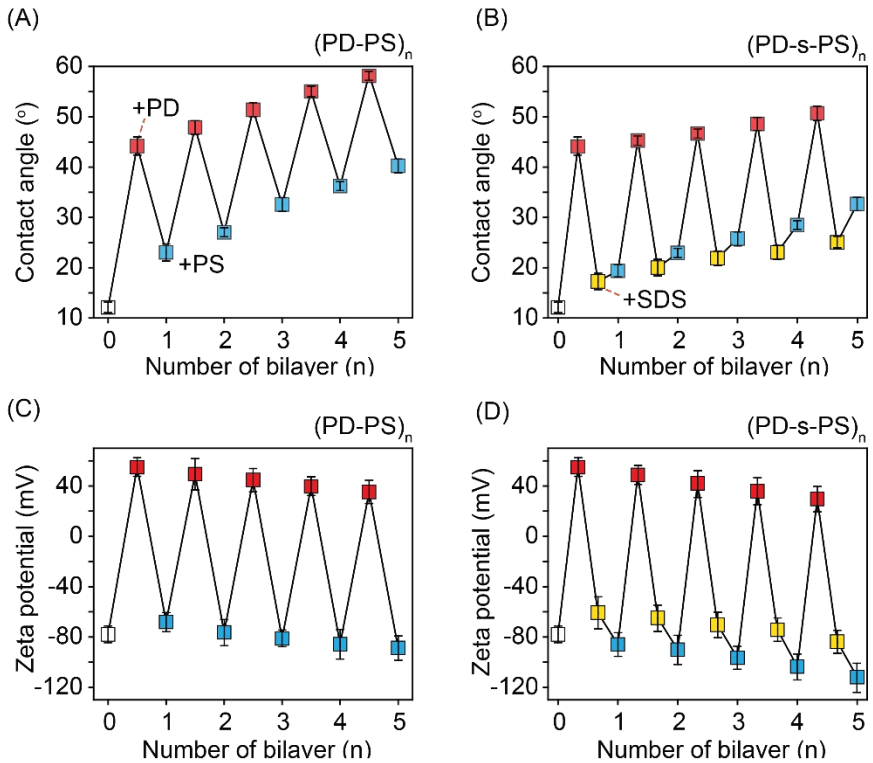

Figure 4.5 Contact angle of (A) reference $(PD\text{-}PS)_n$ and (B) surfactant-integrated $(PD\text{-}s\text{-}PS)_n$ PE-NF membranes at different deposition steps. Surface zeta potential of (A) reference $(PD\text{-}PS)_n$ and (B) surfactant-integrated $(PD\text{-}s\text{-}PS)_n$ PE-NF membranes at different deposition steps.

4.3.5. Surface morphology

The integration of SDS to the PEM-NF membrane leads to a smoother membrane surface (Figure 4.6A vs. 4.6B). Visually, the reference $(PD\text{-}PS)_5$ PEM-NF membrane has a heterogeneous surface with randomly distributed patches (Figure 4.6A), whereas the surface of the surfactant-integrated $(PD\text{-}s\text{-}PS)_5$ PEM-NF membrane is more homogenous with few patches (Figure 4.6B). The influence of SDS integration in the surface roughness of the PEM-NF membrane is further quantified using AFM (Figure 4.6C-F). The estimated surface roughness of the reference $(PD\text{-}PS)_5$ membrane and the $(PD\text{-}s\text{-}PS)_5$ membrane is R_q=37 nm (or R_a=29 nm) and R_q=30 nm (or R_a=21 nm), respectively.

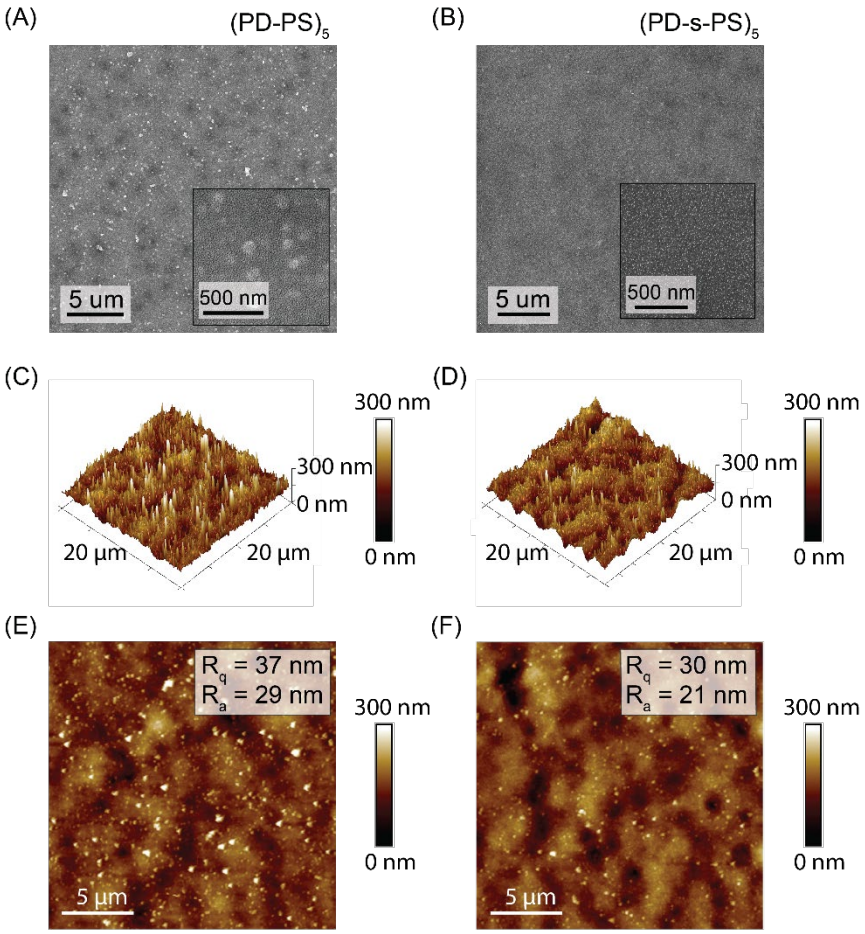

Figure 4.6 SEM image of (A) reference $(PD\text{-}PS)_5$ and (B) surfactant-integrated $(PD\text{-}s\text{-}PS)_5$ PEM-NF membranes. AFM images of (C, E) reference $(PD\text{-}PS)_5$ and (D, F) surfactant-integrated $(PD\text{-}s\text{-}PS)_5$ PEM-NF membranes.

The smoothening of the PEM-NF membrane by the intercalation of SDS is likely caused by the dampened adsorption of the similarly charged polyelectrolyte (PSS in this case) onto the SDS-coated surface[140]. For the reference $(PD\text{-}PS)_n$ PEM-NF membrane, the PDADMAC-coated surface is of strong positive charge and possesses abundant adsorption sites. Therefore, the PSS adsorption is fast and the density of the adsorbed PSS is high. The chain rearrangement and redistribution of newly adsorbed PSS molecules, which only partially anchor to the substrate and have a high density, are suppressed due to both conformational entropic penalty and steric hindrance from the neighboring PSS polymer chains[49,51,162].

For a negatively charged SDS-decorated PDADMAC surface (Figure 4.5D), the electrostatic repulsion between the surface and the PSS polyelectrolytes and the lower density of

available adsorption sites both led to substantially slower adsorption of PSS. Due to the much lower density of available adsorption sites, successful adsorption of PSS may occur only when the orientation of the PSS chains happens to favor the extension of the PSS along the surface to maximize the contact between PSS and the available adsorption sites on the SDS-decorated PDADMAC surface. Such a kinetically unfavorable adsorption process shares the similarity with the formation of more 'compact' aggregates in reaction-limited aggregation, a well-studied concept in colloidal physics[163,164]. Specifically, the reaction-limited aggregation is a kinetically unfavorable process that allows the primary particles to diffuse deeper into the center of a porous aggregate to form an aggregate of higher fractal dimension.

4.3.6. Nanofiltration Performance

The intercalation of SDS between the PDADMAC and PSS layers dramatically enhances the permeance of the resulting PEM-NF membrane (Figure 4.7A). The degree of the permeance enhancement is dependent on the number of bi- or tri-layers and the ionic strength of the polyelectrolyte solution used for the LbL deposition. The permeance enhancement is the most significant when no NaCl was added in the polyelectrolyte solution, especially for PEM-NF membranes with fewer layers. However, we observed that the rejection of Na_2SO_4 was unacceptably low (<90%) when NaCl was not added in the polyelectrolyte solution in the LbL deposition (Figure 4.7B). This is because the deposition of polyelectrolytes in the presence of salt typically results in the formation of a "looser" polyelectrolyte layer[165–167]. Therefore, the following discussion will focus primarily on results obtained with a polyelectrolyte solution containing NaCl.

With both ionic strengths (10 and 100 mM of NaCl), the intercalation of SDS nearly doubled the water permeance of the PEM-NF membranes (Figure 4.7A) without compromising the rejection of Na_2SO_4 (Figure 4.7B). For PEM-NF membranes obtained using an ionic strength of 100 mM, the rejections of Na_2SO_4 are 96.5% and 97.6% for the $(PD\text{-}PS)_5$ and $(PD\text{-}s\text{-}PS)_5$ membranes, respectively, whereas the permeance for the two membranes is 5.9 and 10.4 L m^{-2} h^{-1} bar^{-1}, respectively. The higher permeance of the $(PD\text{-}s\text{-}PS)_5$ membrane is attributable to its larger pore size distribution as compared to the reference $(PD\text{-}PS)_5$ membrane (Figure 4.5), which in turn is caused by less adsorption of PSS with SDS intercalation (Figure 4.2) that also results in a thinner

membrane (Figure 4.3). In addition, the electrostatic repulsion between SDS and PSS possibly induces microchannels around the SDS bilayers that are highly permeable to water, similar to the mechanism of nanoparticle-induced permeance enhancement in thin-film-nanocomposite polyamide membranes[168].

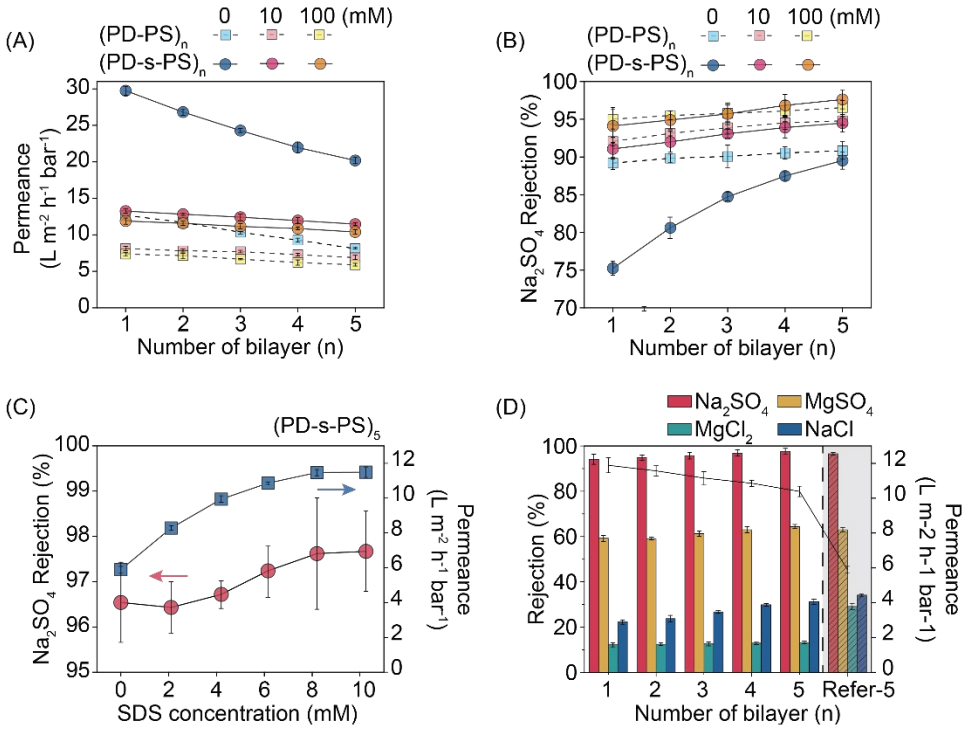

Figure 4.7 (A) Salt (Na_2SO_4) rejection and (B) Membrane permeance of surfactant-integrated $(PD\text{-}s\text{-}PS)_5$ PEM-NF membrane as a function of bilayer number with varying background ionic strength. (NaCl concentration, mM) (C) Impacts of SDS concentration on the perm-selectivity of surfactant-integrated $(PD\text{-}s\text{-}PS)_5$ PEM-NF membrane. (D) Perm-selectivity comparison of the reference $(PD\text{-}PS)_5$ and $(PD\text{-}s\text{-}PS)_n$ PEM-NF membranes with a different number of bilayers. The reported value represents the average of three measurements and the error bar indicates the standard deviation of three runs.

Despite the doubling of water permeance, the rejection of Na_2SO_4 was not compromised (Figure 4.7B). This is partly because the integration of SDS also renders the $(PD\text{-}s\text{-}PS)_5$ membrane slightly more negatively charged than the $(PD\text{-}PS)_5$ membrane (Figure 4.5). In other words, the weakened steric exclusion due to a larger pore distribution in a $(PD\text{-}s\text{-}PS)_5$ membrane is partially compensated by the stronger Donnan exclusion due to a stronger negative membrane charge.

However, it does not require "stronger repulsion" of the solute to maintain or even enhance rejection when water permeance increases substantially, which can be illustrated using the definition of solute rejection:

$$R = \left(1 - \frac{J_s}{J_w c_f}\right) \times 100\%$$

where J_s is the solute flux. While J_s tends to increase with increasing J_w that enhances advective solute transport, as long as $\boldsymbol{J_s}$ does not increase as rapidly as J_w, a higher R can be achieved mostly due to the substantial improvement of J_w.

The impacts of SDS concentration on the membrane permeance and Na_2SO_4 rejection of the $(PD\text{-}s\text{-}PS)_n$ membrane (fabricated using polyelectrolyte solutions with an ionic strength of 100 mM) is summarized in Figure 4.7C. Both the permeance and Na_2SO_4 rejection increases with increasing SDS concentration. Based on the explanation that SDS intercalation enhances perm-selectivity by enlarging pores and the increasing surface charge, a higher SDS concentration is expected to result in more SDS adsorption and thus larger improvement of perm-selectivity. Interestingly, the impacts of SDS concentration on permeance and Na_2SO_4 rejection appear to taper off and reach a limit around the critical micelle concentration (~8.2 mM), which suggests that the adsorption of SDS on the PDADMAC surface reaches a maximum when the SDS concentration reaches the critical micelle concentration. This is likely because only free surfactants (i.e., those not being part of a micelle) can effectively adsorb onto the PDADMAC surface to form SDS bilayers, which is consistent with the observation in a previous study for surfactant adsorption onto particulate surfaces[169].

The performance of the surfactant-intercalated $(PD\text{-}s\text{-}PS)_n$ PM-NF membrane was further evaluated using other types of salts, including $MgSO_4$, $MgCl_2$ and NaCl, with the results compared with the reference $(PD\text{-}PS)_5$ membrane (Figure 4.8). For the $(PD\text{-}s\text{-}PS)_n$ membrane, the rejection of all four salts increases slightly with an increasing number of bilayers, but at the cost of a moderate reduction in membrane permeance. Compared to the reference $(PD\text{-}PS)_5$ membrane, the $(PD\text{-}s\text{-}PS)_5$ membrane has similar or even better rejection of the sulfate salts, i.e., Na_2SO_4 and $MgSO_4$, but a lower rejection of NaCl and $MgCl_2$, in particular $MgCl_2$. The similarity and difference between the two membranes in rejecting different types of ions can be readily explained by the Donnan exclusion mechanism. As both membranes are negatively charged, they are effective in rejecting salts with divalent anions. For the same reason, neither membrane is effective

in rejecting salts with divalent cation and monovalent anion, such as $MgCl_2$. However, because the $(PD\text{-}s\text{-}PS)_5$ membrane is more negatively charged than $(PD\text{-}PS)_n$ membrane, the rejection of $MgCl_2$ by the $(PD\text{-}s\text{-}PS)_5$ membrane is lower than that by the $(PD\text{-}PS)_5$ membrane. For the rejection of NaCl, Donnan exclusion plays a less important role. Therefore, both membranes have a low rejection of NaCl but the $(PD\text{-}PS)_5$ membrane has a slightly higher rejection due to its smaller pore size distribution. If the treatment objective for the membrane is to remove sulfate, the ideal membrane in the investigated series appears to be the $(PD\text{-}s\text{-}PS)_1$ membrane with one bilayer intercalated with SDS, considering both water permeance and salt rejection performance.

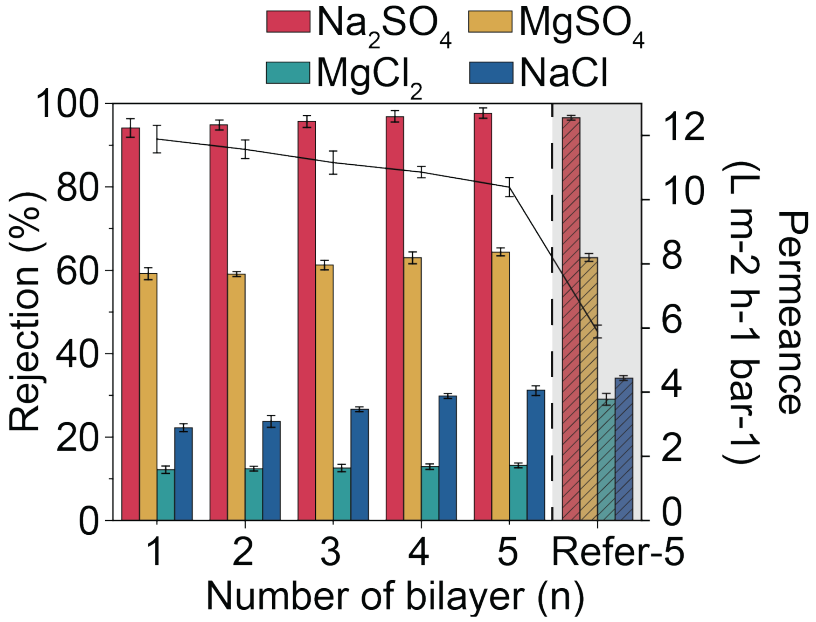

Figure 4.8 Perm-selectivity comparison of the reference (PD-PS)5 and (PD-s-PS)n PEM NF membranes with a different number of bilayers. The reported value represents the average of three measurements and the error bar indicates the standard deviation of three runs.

Based on the mechanism discussed above, the intercalation of anionic surfactant (SDS) in the performance enhancement of $(PD\text{-}s\text{-}PS)_n$ PEM NF membrane primarily has two major roles: (1) it reduces the amount of PSS adsorption, making a more compact and thinner PEM NF membrane; (2) it slightly enlarges the pore size but at the same time enhances the membrane surface charge. Simply reducing the amount of PSS adsorption by decreasing the PDADMAC concentration in fabricating the reference $(PD\text{-}PS)_5$ membrane (without adding surfactants) can reduce the thickness of the PEM NF membrane and achieve a dramatic increase of water permeance (Table 4.1). But the Na_2SO_4 rejection of the resulting membrane becomes heavily compromised due to

the substantially lower (negative) surface charge (Table 4.1). Lastly, we also show that intecalation of another surfactant, SDBS, which has similar characteristics as SDS, can also result in similar but slightly inferior performance enhancement as that achieved by SDS intercalation(Table 4.1). We believe SDBS is not as effective as SDS because SDBS has a lower packing density (or surface excess) due to the presence of a bulkier benzene ring [170].

Table 4.1 Permeance, Na_2SO_4 rejection, zeta potential, mean pore size and thickness of $(PD\text{-}PS)_5$ PEM NF membrane, SDS-intercalated and SDBS-intercalated $(PD\text{-}s\text{-}PS)_5$ PEM NF membranes.

	$(PD\text{-}PS)_5$ PEM NF (PD 0.5 g/L)[#]	$(PD\text{-}PS)_5$ PEM NF	$(PD\text{-}s\text{-}PS)_5$ PEM NF (SDS 1 CMC)[⊥]	$(PD\text{-}s\text{-}PS)_5$ PEM NF (SDBS 1 CMC)[△]
Thickness* (nm)	20.4±0.2	31.7±0.2	27.1±0.3	29.6±0.3
Na_2SO_4 Rejection (%)	54.6±2.9	96.5±3.2	97.7±3.8	97.5±4.5
Permeance ($L\ m^{-2}\ h^{-1}\ bar^{-1}$)	16.3±1.1	5.9±0.4	11.5±0.6	9.4±0.4
Zeta potential (mV)	68.4±5.3	88.9±6.7	103.2±5.9	94.2±7.5
Mean Pore size (nm)	0.305±0.017	0.298±0.021	0.335±0.017	0.322±0.019

[#]All PEM NF membranes are fabricated using PD (1 g/L) and PS (2g/L) except this case (PD concentration is 0.5 g/L)
*Thickness is measured using elliposometry by depositing PEM on a silicon wafer
[§] Each data is obtained based on three replicate experiments and the error represents standard deviation.
[⊥] SDS concentration is 8.2 mM
[△] SDBS concentration is 0.4 mM

4.3.7. Stability of the surfactant-intercalated PEM NF membrane

The performance PEM NF membrane was mostly stable under different operation and solution conditions and over long-term operation (Figure 4.9). Specifically, while the fluxes of both the $(PD\text{-}s\text{-}PS)_5$ and the reference $(PD\text{-}PS)_5$ membranes increased roughly linearly at higher pressure, the Na_2SO_4 rejections by both membranes were barely compromised (Figure 4.9A). When both membranes were subject to feed solutions of a wide range of pH, we observed that Na_2SO_4 rejections decreased with decreasing pH but only became considerably compromised when the pH was very low (Figure 4.9B). The dependence of Na_2SO_4 rejection on pH is consistent with the

dependence of the surface charge of the PSS-coated PEM surface on pH (Figure 4.9C). Interestly, the SDS-intercalated $(PD\text{-}s\text{-}PS)_5$ PEM NF membrane still maintained a Na_2SO_4 rejection of ~90% at a pH of 3 when the Na_2SO_4 rejection of the $(PD\text{-}PS)_5$ PEM NF membrane had delcined to 70%. We can therefore conclude that the intercalation of SDS improves the stability of the PEM NF membranes in acidic conditions. While these experiments with different pH were only performed for 12 hours, a recent study has reported that $(PD\text{-}PS)_n$ PEM NF membranes can maintain stable performance in extreme pH over a two-month filtration run[171]. Lastly, we also performed NF experiments for one week with both $(PD\text{-}PS)_5$ and $(PD\text{-}s\text{-}PS)_5$ membranes and found that their performance in terms of both water permeance and Na_2SO_4 rejection were stable throughout the experiments(Figure 4.9D), which also suggests that relative performance advantage of $(PD\text{-}s\text{-}PS)_5$ membrane vs. the reference $(PD\text{-}PS)_5$ was also maintained in long-term NF operation.

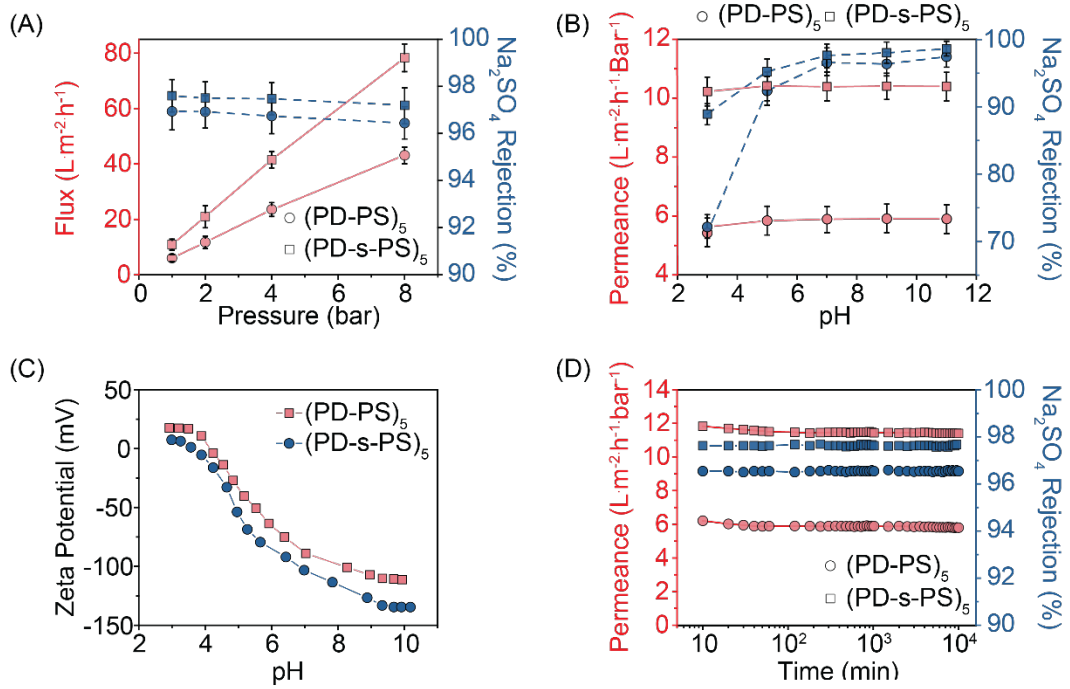

Figure 4.9 Stability evaluation of $(PD\text{-}PS)_5$ PEM NF and surfactant-intercalated $(PD\text{-}s\text{-}PS)_5$ PEM NF membranes (A) under various applied pressure and (B) at various testing pH. (Na_2SO_4 concentration: 1000 ppm, and pressure for pH stability evaluation: 4bar) The reported value represents the average of three measurements and the error bar indicates the standard deviation of three runs. (C) pH-dependent surface zeta-potentials of $(PD\text{-}PS)_5$ and $(PD\text{-}s\text{-}PS)_5$ PEM NF membranes. (D) Long-term stability test of $(PD\text{-}PS)_5$ PEM NF and surfactant-intercalated $(PD\text{-}s\text{-}PS)_5$ PEM NF membranes. (Na_2SO_4 concentration: 1000 ppm, pressure: 4 bar, time span: 7 days).

4.4.Implications

We have demonstrated in this study that the intercalation of SDS bilayers in PEM-based dense NF membranes can double the permeance without compromising salt rejection. Using multiple characterization techniques and by performing experiments on both model PEM films and PEM-NF membranes, we find that the reduced adsorption of polyelectrolyte and the formation of microchannels around the surfactant-bilayers are the likely major causes of the substantially enhanced water permeance. The intercalation of surfactant (bilayers) represents an emerging strategy, an alternative to the widely used method of embedding nanoparticle, to tailor and improve the performance of NF membranes. While such a method of surfactant intercalation has been proven successful for loose NF membranes that reject organic macromolecules, this study demonstrates its applicability for salt-rejecting dense NF membranes that have far more stringent requirements on the integrity and properties of the separation layer. These results suggest the possible universal effectiveness of this method of intercalation of surfactant-bilayers on all PEM-NF membranes fabricated using LbL deposition of polyelectrolytes, which leads to vast opportunities of substantially enhancing the performance of the many PEM-NF membranes that have been and will be developed.

CHAPTER 5

INTERCALATION OF ZWITTERIONIC SURFACTANTS DRAMATICALLY ENHANCES THE PERFORMANCE OF LOSSE NANOFILTRATION MEMBRANE FOR NATURAL ORGANIC MATTERS REMOVAL

This chapter has been published in *Journal of Membrane Science* as the following peer-reviewed manuscript: Liang, Y., & Lin, S. (2020). Intercalation of zwitterionic surfactants dramatically enhances the performance of low-pressure nanofiltration membrane. Journal of Membrane Science, 596, 117726.

5.1.Introduction

Nanofiltration (NF) has received increasing interests in research and development in recent years due to its strong potential as a cost-effect approach for addressing emerging water treatment needs in the face of growing water scarcity and more stringent regulation[7,19–22]. NF membranes are generally classified into two categories based on its pore sizes: dense NF (DNF) membranes and low-pressure (or loose) NF (LNF) membranes. Dense NF membranes are capable of rejecting multivalent ions to a great extent. The applications of dense NF include, but not are limited to, desalination of brackish groundwater[172], water softening[81,173] and wastewater reuse[25]. LNF membranes, on the other hand, refer to membranes with pore sizes between DNF membranes and ultrafiltration (UF) membranes. LNF has unique niches of applications. They can remove small organic molecules (e.g. dyes, or natural organic matter) that cannot be removed effectively by UF membranes, and at the same time have much higher water permeability and much lower pressure requirement than DNF or reverse osmosis that removes ionic species[25,174]. These characteristics enable LNF for highly efficient separation of organic molecules from feed water, which has a wide range of applications in treating non-saline feed water for water supply and wastewater reuse. Previous studies have shown LNF to be effective in removing hormones[175], pesticides[176], persistent organic pollutants (POPs)[177], pharmaceutically active compounds[136], and natural organic matters (NOMs) from surface water or ground water[178]. In particular, removal of NOMs by LNF can be a cost-effective approach as reverse osmosis pretreatment to control fouling[179], or as disinfection pretreatment to mitigate the formation of disinfection byproducts[180].

The cost-effective application of LNF requires LNF membranes with high perm-selectivity and fouling resistance. Significant enhancement of water permeability of NF membranes without sacrificing its selectivity can potentially result in a dramatic reduction of the required membrane area and energy consumption, which will translate to considerable cost reduction[60]. Toward this goal, various approaches have been explored for enhancing the water permeability of LNF membranes[60,64,181]. The specific approach for performance enhancement is strongly dependent on the fabrication method. One important and widely investigated fabrication method is layer-by-layer (LbL) deposition of polyelectrolytes[75,182,183]. In this method, polyanions and polycations are deposited onto a substrate membrane (typically a UF membrane) to form a polyelectrolyte multi-layer that serves as the active layer for molecular separation[184]. This method has several unique advantages, such as high controllability of the active layer composition and properties, good fouling resistance, and possibility of using aqueous solution only in the fabrication process[79,182,185,186].

The key performance parameters of an LNF membrane include the water permeability and the rejection of target solutes. With the method of LbL deposition of polyelectrolytes, these performance parameters can be adjusted by altering the concentration of the polyelectrolytes[46], the deposition duration[46], and the solution chemistry[51,187]. Previous approaches for enhancing the perm-selectivity of membranes fabricated using LbL deposition of polyelectrolyte include tailoring the active layer thickness via adding salts or tuning the pH during polyelectrolyte deposition to either improve ion separation or reduce the hydraulic resistance for water transport[165,188,189], enhancing the surface hydrophilicity via surface modification and crosslinking[183,185], and incorporating novel 2D materials such as graphene and carbon nanotubes to construct water channels[190,191]. However, LNF membranes with higher water permeability typically have compromised rejection of the target solutes, which is widely recognized as the intrinsic tradeoff of perm-selectivity for semi-permeable membranes[12,57].

Here, we report a novel approach for dramatically enhancing the perm-selectivity and fouling resistance of LNF membranes fabricated using LbL deposition of polyelectrolyte for filtering humic acid (HA)—a representative species of NOMs found in natural water. The reference LbL membrane is fabricated by depositing polyethyleneimine (PEI) and polystyrenesulfonate (PSS) alternately onto a polyacrylonitrile ultrafiltration membrane as the substrate. The main innovation of the reported approach is the intercalation of zwitterionic

surfactants (SB3-14) self-assemblies between the PSS and the PEI layers which drastically improves the water permeability of LNF membranes by several folds without compromising its selectivity. We fabricate and characterize the polyelectrolyte membranes with and without SB3-14, and systematically compare their performance in LNF in terms of water permeability, solute rejection, and fouling resistance.

5.2.Materials and methods

5.2.1. Materials and chemicals

Polyacrylonitrile ultrafiltration (PAN, UF) membrane (MWCO = 50 kDa, GE Healthcare Life Science) was used as the substrate for fabricating the NF membrane. Polyethylenimine (PEI, Mw = 750 kDa), Polystyrene sulfonate (PSS, 10 000 kDa), 3-(*N, N*-Dimethylmyristylammonio) propanesulfonate (SB3-14, ≥ 99%), (3-Aminopropyl) triethoxysilane (APTES) (99%), hydrochloric acid (HCl, ACS reagent, 37%), sodium hydroxide (NaOH, Bioxtra, ≥ 98%), Humic acid (HA), methyl blue (MB, Mw = 799.8), Na_2SO_4 (≥ 99%), $MgSO_4$ (≥ 99.5%), $MgCl_2$ (≥ 99.99%), NaCl (≥ 99%) were purchased from Sigma-Aldrich (St. Louis, MO US). All chemicals were used as received without purification. Deionized water (Millipore, US) was used to prepare polyelectrolyte solution and surfactant solution.

5.2.2. Fabrication of $(PEI\text{-}PSS)_n$ and $(PEI\text{-}s\text{-}PSS)_n$ LNF membrane

The reference membrane $(PEI\text{-}PSS)_n$ low-pressure nanofiltration (LNF) membrane was prepared by depositing PEI and PSS alternately on a PAN ultrafiltration (UF) membrane (the chemical structures of PEI and PSS are shown in Figure 5.1A). The PAN UF membrane was first treated with 2 mol L^{-1} NaOH solution for 30 minutes to acquire a negative surface charge, then immersed into DI water to remove excess NaOH, and dried in the oven at 30°C over night before use. The freshly hydrolyzed PAN membrane was exposed to the polycation solution (1 g L^{-1} PEI) for 30 minutes, rinsed with DI water, and then exposed to a polyanion solution (2 g L^{-1} PSS) for another 30 minutes, and finally rinsed with DI water. The resulting membrane is referred to as the $(PEI\text{-}PSS)_1$ with the subscript "1" representing one PEI-PSS bilayer (Figure 5.1B). The same

procedure was repeated to form additional bilayers, forming $(PEI\text{-}PSS)_2$ and $(PEI\text{-}PSS)_3$ (Figure 5.1C illustrates $(PEI\text{-}PSS)_2$). Regardless of the number of bilayers, these $(PEI\text{-}PSS)_n$ membranes are all referred to as the reference membranes.

The preparation of polyelectrolyte multilayer LNF membrane with surfactant intercalation followed a similar procedure as that for preparing the reference membranes except for an additional step of surfactant intercalation between the polycation and polyanion layers. (Figure 5.1D) Specifically, after each deposition of polycations (PEI) or polyanions (PSS) layer, the membrane was immersed into an aqueous solution of zwitterionic surfactant, SB3-14, for 30 min. The resulting polyelectrolyte multilayer membranes with intercalated surfactants are referred to as $(PEI\text{-}s\text{-}PSS)_n$, with the subscript "n" representing the number of "PEI-s-PSS" triple layers. We note that SB3-14 was also inserted between two adjacent "PEI-s-PSS" triple layers and that PSS was also used as the final layer of the membranes for performance testing. Polyanion PSS was chosen as the material for the capping layer because most natural contaminants are negatively charged and are thus more effectively rejected by a membrane with a negatively charged surface.

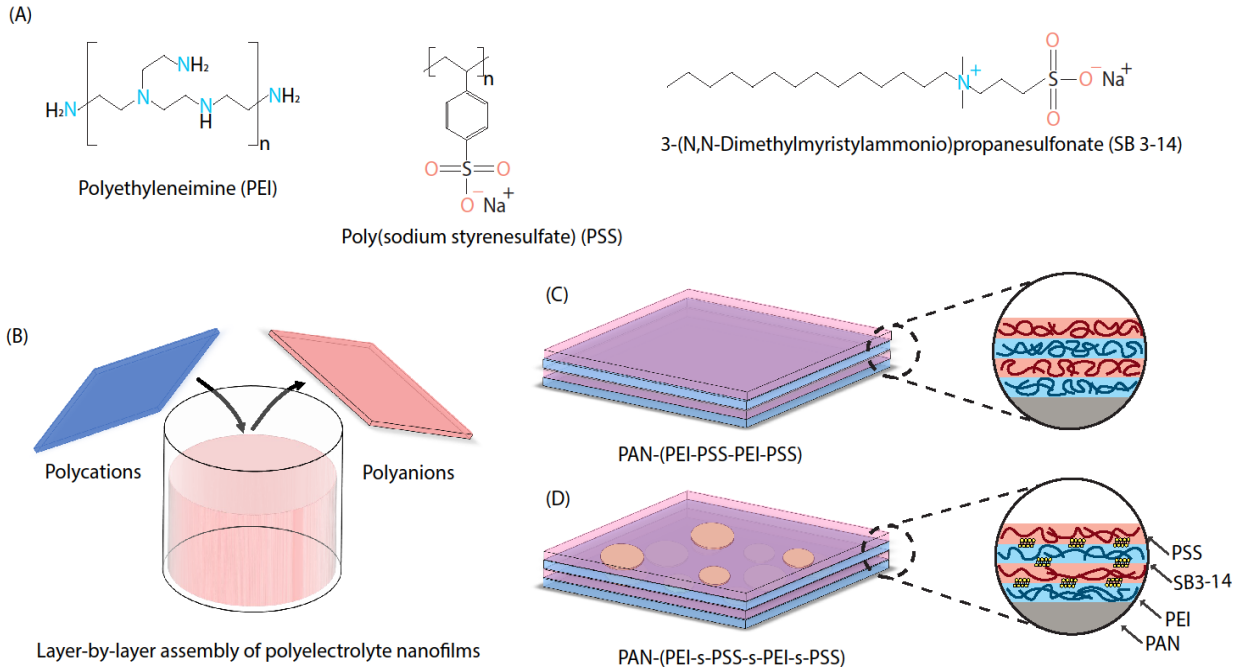

Figure 5.1 (A) Chemical structures of the two polyelectrolytes (PEI and PSS) and the zwitterionic surfactant (SB 3-14) used to prepare the LNF membranes based on LbL of polyelectrolyte. (B) Preparation of LbL polyelectrolyte membranes via the dip-coating method.

(C) Schematic of a four-layer $(PEI\text{-}PSS)_2$ LNF membrane. (D) Schematic of a seven-layer $(PEI\text{-}s\text{-}PSS)_2$ LNF membrane.

5.2.3. Membrane characterization

The ζ-potentials of the $(PEI\text{-}PSS)_n$ and $(PEI\text{-}s\text{-}PSS)_n$ membranes with different numbers of bilayers or triple layers were measured using a streaming potential analyzer (SurPASS electrokinetic analyzer, Anton Paar, Ashland, VA) with an adjusting gap cell and 1mM KCl solution as the background electrolyte. The surface hydrophilicity of the $(PEI\text{-}PSS)_n$ and $(PEI\text{-}s\text{-}PSS)_n$ membranes at different deposition steps was quantified using in-air water contact angle measured with an optical tensiometer (Theta Lite, Biolin Scientific). The surface morphology of the $(PEI\text{-}PSS)_n$ and $(PEI\text{-}s\text{-}PSS)_n$ membranes was characterized with a high-resolution Zeiss Merlin scanning electron microscope (SEM) equipped with GEMINI II column with an accelerating voltage of 3 kV. Atomic force microscopy (AFM) was also employed to characterize the surface roughness of $(PEI\text{-}PSS)_n$ and $(PEI\text{-}s\text{-}PSS)_n$ membranes.

5.2.4. Characterization of surfactant self-assembly on a solid-water interface.

Direct observation of SB3-14 self-assemblies on the polyelectrolyte active layer is challenging due to the intrinsic roughness of the polyelectrolyte coated UF membrane. Therefore, instead of using a UF membrane, we used a highly smooth substrate on which the morphology of SB3-14 self-assembly can be identified. Specifically, a molecularly smooth silicon (Si) wafer was first treated with a 0.1 M NaOH solution for 10 min and subsequently with 0.1 M HNO_3 solution for 10 min to acquire abundant surface hydroxyl groups. After being rinsed with water and dried with nitrogen, the treated Si substrate was then immersed in a toluene solution of 2.5 wt% aminopropyl trimethoxysilane (APTES) for 4 hours with the headspace filled with nitrogen. This step of APTES coating was intended to impart a positive charge to the Si substrate. The coated Si substrate was cleaned with toluene to remove excess APTES, dried under nitrogen, and then immersed in the aqueous solution of 0.4 mM SB3-14 (1 critical micelle concentration, CMC) for 30 min to obtain the self-assemblies of SB3-14 on the APTES-coated Si surface. The surface morphology of resulting Si substrate with SB3-14 adsorption was characterized by AFM.

5.2.5. NF performance evaluation

Nanofiltration performance of the $(PEI\text{-}PSS)_n$ and $(PEI\text{-}s\text{-}PSS)_n$ LNF membranes was evaluated using a cross-flow stainless steel filtration cell with an active membrane area of 7.1 cm^2. The pure water permeability of $(PEI\text{-}PSS)_n$ and $(PEI\text{-}s\text{-}PSS)_n$ membranes was evaluated using DI water before preforming any solute filtration. The cross-flow velocity was 10 L h^{-1}, the applied pressure was 2 bar and the temperature was kept at 25°C. We evaluated the rejection of HA (10 mg L^{-1}) and methyl blue (500 mg L^{-1}), which are the solutes intended to be removed by the fabricated LNF membranes. However, the rejections of common salts with monovalent and divalent ions, including Na_2SO_4, $MgSO_4$, $MgCl_2$ and NaCl, were also assessed to evaluate the "looseness/tightness" of the LNF. A concentration of 0.1 g L^{-1} was used in all tests for measuring salt rejection. The concentrations of HA and methyl blue of the permeate and feed solution were determined using the UV-vis photometry (with calibration curves) at corresponding absorption wavelengths of 254 nm and 660 nm, respectively. A standard correlation curve relating the UV-vis adsorption value and total organic carbon concentration was plotted to quantify the concentration of HA. The salt concentrations of the feed and permeate solutions were determined by measuring the electrical conductivity of each solution. All measurements were carried out after the system became stable.

The pure water permeability of LNF membrane was calculated by weight measurement using the following equation:

$$PWP = \frac{J}{\Delta P}$$

where PWP is the pure water permeability of LNF membrane (L m^{-2} h^{-1} bar^{-1}), where $\boldsymbol{J}$ is the volumetric flux of water (L m^{-2} h^{-1}), and ΔP was the applied pressure (bar), respectively. The rejection of solutes, R, is calculated using the following equation:

$$R = \left(1 - \frac{c_p}{c_f}\right) \times 100\%$$

where c_p and c_f are the solute concentration of permeate and feed solution, respectively.

5.2.6. Determination of MWCO and pore size distribution of $(PEI\text{-}PSS)_n$ and $(PEI\text{-}s\text{-}PSS)_n$ LNF membrane

The pore size of (PEI-PSS)n and (PEI-s-PSS)n LNF membrane was determined by the rejection of a series of neutral organic compounds with increasing molecular weight. The neutral organic compounds tested in this study include glucose (180 Da), sucrose (342 Da), raffinose (504 Da) and β-cyclodextrin (1135 Da). The concentration of each organic species solution was 200 ppm and the applied pressure in the filtration experiments was 2 bar. The MWCO of LNF membranes was defined as the molecular weight at which the rejection equals 90%. The pore size distribution curve is expressed as a probability density function (PDF) that was established based on the following assumption: (1) There is no steric or hydrodynamic interaction between these organic solutes and the membrane pores; (2) The mean pore size of the polyamide membrane equals the Stokes radius of the organic solute with a measured rejection of 50%; (3) The distribution of the membrane pore size is characterized by the geometric standard deviation of the PDF curve, which is the ratio between the Stokes radius with a rejection of 84.13% to that with a rejection of 50%[112].

$$\frac{dR(r_p)}{dr_p} = \frac{1}{r_p ln\sigma_p \sqrt{2\pi}} \exp\left[-\frac{(lnr_p - ln\mu_p)^2}{2(ln\sigma_p)^2}\right]$$

where μ_p is the mean pore size, σ_p is the geometric standard deviation of the PDF curve and r_p is the Stokes radius of the organic solute.

5.3.Results and discussion

5.3.1. Self-assembly of zwitterionic surfactants on the water-solid interface

The SB3-14 surfactants self-assembled on a smooth Si wafer surface, forming patches with an average height of 5 nm (Figure 5.2A). This average patch thickness is close to the thickness of SB3-14 micelles/bilayer measured using other characterization techniques[192–194]. The area of these patches varies from tens to thousands of nm^2 (Figure 5.2B, C). The relatively small aspect ratio between the width and the height for most SB3-14 self-assemblies suggests that the self-assemblies are mostly micelles or micelle-sized bilayers, which is consistent with previous studies of

adsorption of zwitterionic surfactants on hydrophilic silicon nitride or mica surfaces that reported micelle structure for the adsorbed aggregates[194,195]. In this case, however, large bilayers (i.e., "pancake" like structures) were also present according to the patch size statistics (Figure 5.2C).

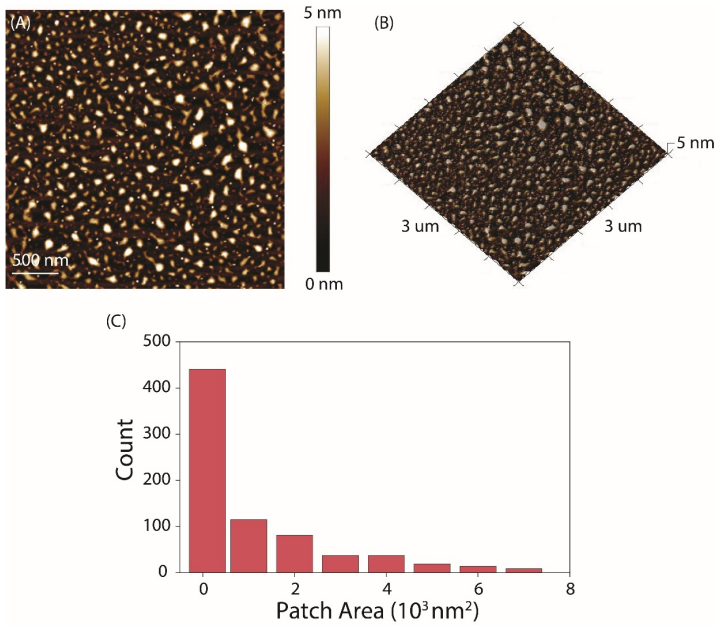

Figure 5.2 (A and B) AFM topography and 3D height image of self-assembled SB3-14 patches on a smooth silicon wafer coated with APTES. (C) Size distribution of self-assembled SB3-14 patches on the silicon wafer obtained by analyzing Figure 5.2A using Image-J.

Due to the significantly larger intrinsic roughness of the substrate membrane as compared to the that of the SB3-14 self-assemblies, we cannot directly perform a similar characterization of the morphology of SB3-14 self-assemblies on a substrate membrane. However, the results from the AFM characterization of the SB3-14 self-assemblies on a smooth Si wafer surface provide insights into how SB3-14 possibly behaves when they adsorb onto a membrane substrate.

5.3.2. Surface property of surfactant-integrated polyelectrolyte multilayer LNF membrane

The deposition of PSS onto a PEI-coated surface and the deposition of PEI onto a PSS-coated surface are confirmed with the alternating signs of the zeta potentials of the $(PEI\text{-}PSS)_3$ membrane at different deposition steps (Fig 5.3A). With a growing number of PEI-PSS layers, the

PEI-coated surface became slightly less positive and the PSS-coated surface became slightly more negative. When constructing the $(PEI\text{-}s\text{-}PSS)_3$ membrane, the adsorption of the SB3-14 onto the PEI-coated surface appears to be much more effective than onto the PSS-coated membrane according to the corresponding changes of zeta potential (Figure 5.3B). Specifically, the adsorption of SB3-14 consistently reversed the charge of the PEI-coated substrate to around -60 mV. Further adsorption of the PSS onto an SB3-14-coated PEI surface was confirmed by the additional reduction of zeta potential. However, such an additional reduction is relatively small compared to the reduction resulting from SB3-14 adsorption.

The unique chemical structure of a zwitterionic surfactant allows its adsorption onto both positively and negatively charged surfaces. In this case, SB3-14 can adsorb onto the negatively charged PSS surface because of the presence of the cationic quaternary ammonium. However, because the quaternary ammonium cations are located in the middle of the SB3-14 chains, the interaction between the cationic ammonium groups and the negatively charged PSS is hindered both sterically and electrostatically by the sulfonic groups at the end of the SB3-14 chains. Consequently, the change of zeta potential caused by the adsorption of SB3-14 onto PSS is dramatically smaller than that caused by the adsorption of SB3-14 onto PEI (Figure 5.3B).

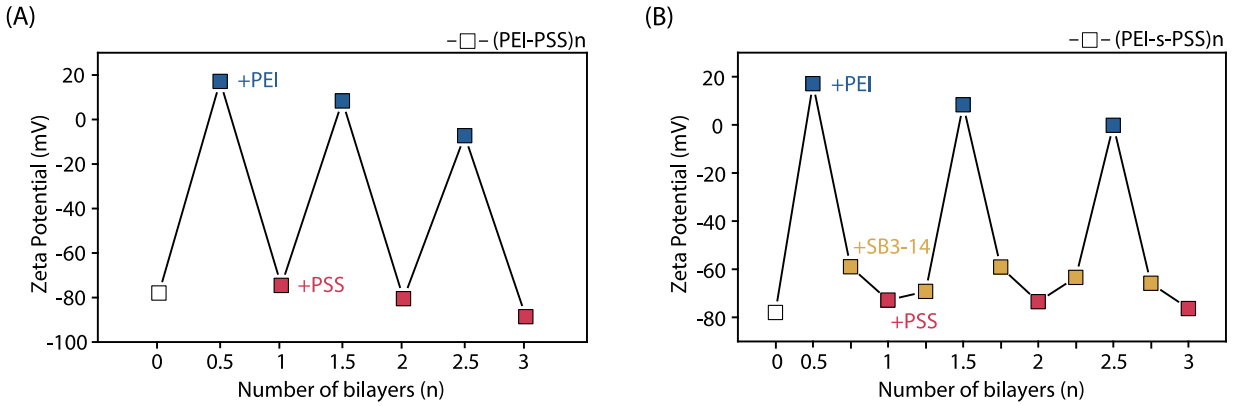

Figure 5.3 Surface zeta potential of the LNF membrane in different steps of the LbL deposition process: (A) $(PEI\text{-}PSS)_n$ LNF membrane; (B) $(PEI\text{-}s\text{-}PSS)_n$ LNF membrane.

As the growth mechanism of polyelectrolyte multilayers is primarily driven by charge overcompensation and spatial redistribution[46,187], the reduction of surface charge density by the

adsorption of zwitterionic surfactants decreases the degree of the subsequent adsorption of the oppositely charged polyelectrolyte. Therefore, the presence of SB3-14 self-assemblies leads to a thinner polyelectrolyte coating, which is beneficial for increasing membrane permeability as will be discussed later.

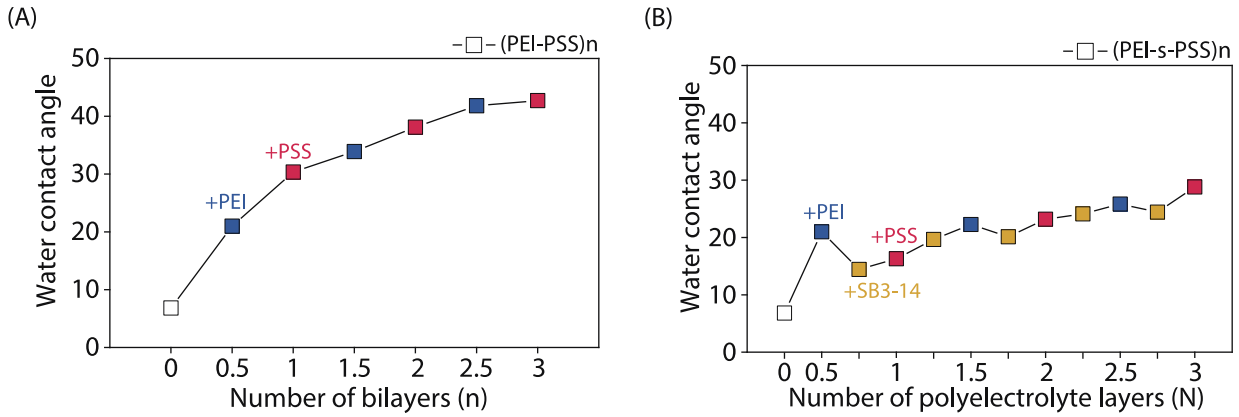

Figure 5.4 Water contact angle of the LNF membrane in different steps of the LbL deposition process: (A) $(PEI\text{-}s\text{-}PSS)_n$ LNF membrane; (B) $(PEI\text{-}PSS)_n$ LNF membrane.

The NaOH-treated PAN substrate membrane became strongly hydrophilic with a water contact angle (WCA) lower than 10º. When fabricating the $(PEI\text{-}PSS)_n$ membrane, the adsorption of polyanion and polycation consistently increased the WCA, especially for the first few layers. (Figure 5.4A) The impact of SB3-14 addition is more complicated when fabricating the $(PEI\text{-}s\text{-}PSS)_n$ membrane. The adsorption of SB3-14 onto a PEI-coated surface decreased the WCA consistently, even though the WCA reduction becomes increasingly smaller with a growing number of layers. (Figure 5.4B) The reduction of WCA by the adsorption of the SB3-14 is additional indirect evidence that SB3-14 exists on the membrane substrate as bilayers instead of monolayers, as otherwise, the exposed hydrophobic tails in a monolayer would undoubtedly have increased the WCA. However, the adsorption of the SB3-14 onto a PSS-coated surface increased the WCA, possibly because the zwitterionic charged head of SB3-14 does not interact with water as strongly as the sulfonic group in the PSS. Comparing the WCA between the $(PEI\text{-}PSS)_n$ and $(PEI\text{-}s\text{-}PSS)_n$ membranes, the addition of SB3-14 makes the LNF membrane considerably more hydrophilic.

5.3.3. Morphology and surface roughness of $(PEI\text{-}s\text{-}PSS)_n$ LNF membrane

The surface morphology of the $(PEI\text{-}PSS)_n$ and $(PEI\text{-}s\text{-}PSS)_n$ LNF membranes with different numbers of polyelectrolyte active layers was characterized using SEM and AFM. For $(PEI\text{-}PSS)_n$ membrane, increasing the polyelectrolyte layers results in more heterogeneous surface morphology, i.e., the formation of self-assembled polyelectrolyte patches on the membrane surface (Figure 5.5A-C). The increase of polyelectrolyte roughness was attributed to the so-called "nonmonotonic adsorption behavior" that occurs when strong polyelectrolytes adsorb onto a weakly charged polyelectrolyte surface[166,196,197]. If the degree of the ionization of the weak polyelectrolyte in the multilayers is below a critical charge density, the following adsorption of a fully charged polyelectrolyte will encounter a thermodynamic frustration. Specifically, the adsorption of PSS onto the PEI surface was carried out at pH of 7, where PEI (pka ~7) was approximately 50% ionized[198]. When the fully ionized polyelectrolyte (PSS) adsorbed onto the weakly ionized PEI surface, the enthalpic gain for the PSS chain to extend horizontally and maximize its contact with the substrate surface is insufficient to overcome the entropic penalty associated with this conformation[49]. Therefore, the absorbed PSS chains onto the PEI surface formed a large number of tails and loops, which increased the surface roughness. Such an effect of non-extended adsorption became growingly significant with an increasing number of layers, as the positive charge of PEI continued to decrease as the number of layers increased[49].

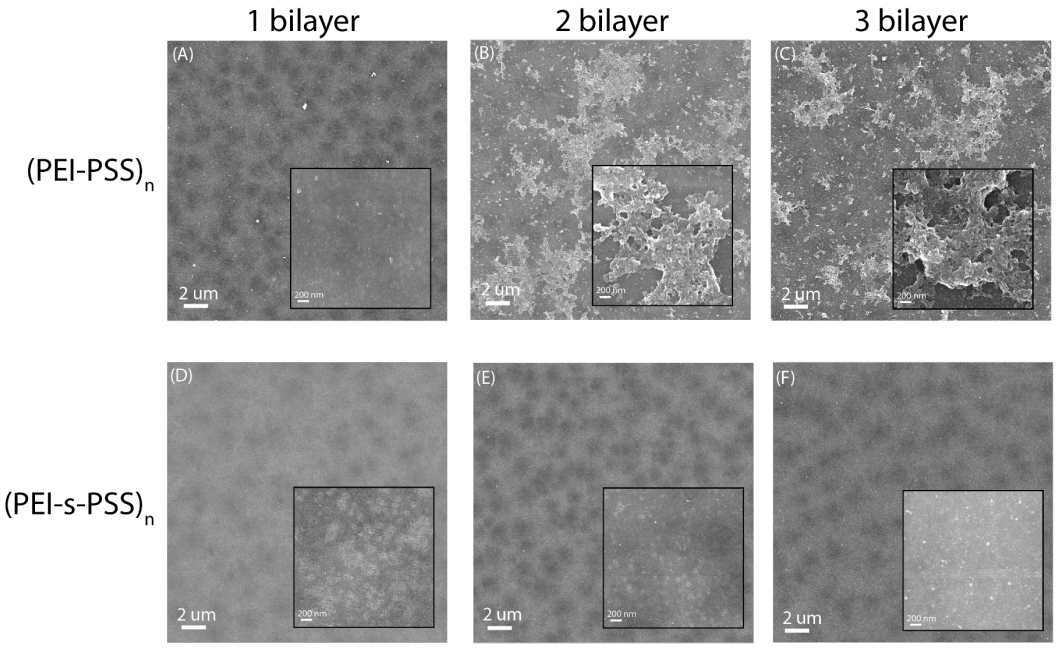

Figure 5.5 Surface morphology of the LNF membrane in different steps of the LbL deposition process: (A, B and C) $(PEI\text{-}PSS)_n$ LNF membrane (D, E and F) $(PEI\text{-}s\text{-}PSS)_n$ LNF membrane.

The morphology of the $(PEI\text{-}s\text{-}PSS)_n$ membrane is dramatically different from that of the $(PEI\text{-}PSS)_n$ membrane. The integration of surfactants between the polycation and polyanion eliminates the surface heterogeneity. Specifically, the $(PEI\text{-}s\text{-}PSS)_n$ membrane surface is free of large heterogeneous patches observed on the surface of the $(PEI\text{-}PSS)_n$ membrane (Figure5. 5D-F). The morphological difference between the $(PEI\text{-}PSS)_n$ and $(PEI\text{-}s\text{-}PSS)_n$ membranes is further confirmed by comparing their respective AFM micrographs (Figure 6A-6F) from which the surface roughness was quantified (Figure 5.6G). The roughness of the $(PEI\text{-}PSS)_n$ membrane increased rapidly as the number of polyelectrolyte layers increased, whereas the roughness of the $(PEI\text{-}s\text{-}PSS)_n$ membrane constantly remained low (Figure 5.6G).

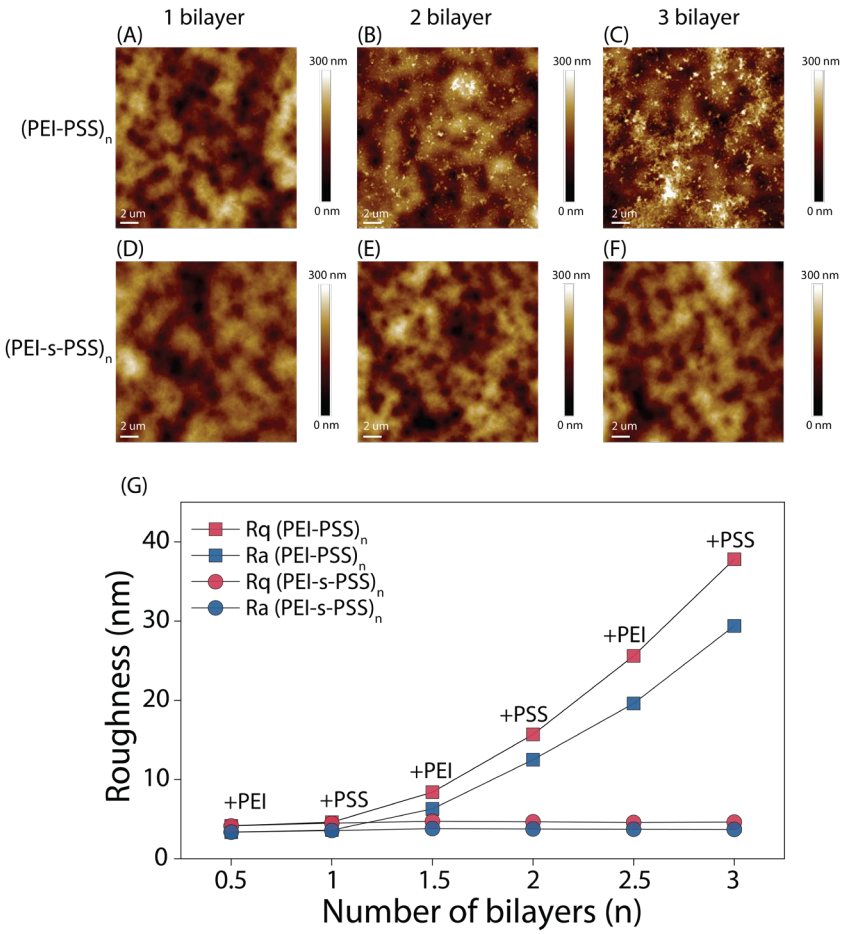

Figure 5.6 Surface morphology of (A, B, C) $(PEI\text{-}PSS)_n$ LNF membranes and (D, E, F) $(PEI\text{-}s\text{-}PSS)_n$ LNF membranes. (G) Surface roughness of $(PEI\text{-}PSS)_n$ and $(PEI\text{-}s\text{-}PSS)_n$ LNF membranes in different steps of the LbL deposition process.

This dramatic effect of surfactant intercalation on smoothening the membrane formed via LBL of polyelectrolytes has not been documented in the literature. The zeta potentials at different steps of constructing the $(PEI\text{-}PSS)_n$ and $(PEI\text{-}s\text{-}PSS)_n$ membranes (Figure 5.3) suggest that substantially less PSS adsorbed onto the $(PEI\text{-}s\text{-}PSS)_n$ membrane than onto the $(PEI\text{-}PSS)_n$ membrane. The likely explanation for this difference is the elimination of available adsorption sites on PEI by the patchy SB3-14 bilayers in constructing the $(PEI\text{-}s\text{-}PSS)_n$ membrane. Even though ammonium groups are also present in the SB3-14, the screening of the adjacent sulfonic groups renders the ammonium groups hardly available for PSS adsorption.

Let us compare the adsorption of PSS onto a PEI-coated surface, as in constructing a $(PEI\text{-}PSS)_n$ membrane, and onto a PEI-coated surface with adsorbed SB3-14, as in constructing a (PEI-

s-PSS)$_n$ membrane. Because the PEI-coated surface is positively charged and has relatively abundant adsorption sites, the adsorption of PSS is fast, but the full extension of PSS along the PEI surface is prohibited by both conformational entropic penalty and steric hindrance (between neighboring PSS molecules). When the PEI-coated substrate is decorated with SB3-14, the surface is highly negative (Figure 5.3B) and the uncoated adsorption sites on PEI become limited. Therefore, PSS adsorption is substantially slower due to the overall electrostatic repulsion, and successful adsorption can only occur if the orientation of the PSS chains happens to favor the extension of the PSS along the surface to maximize the contact between PSS and the distributed uncoated adsorption sites on PEI. The fact that a more compact PSS layer can form when the PSS adsorption is kinetically unfavorable is to a certain extent similar to the formation of more "compact" aggregates in reaction-limited aggregation, which has been well studied in colloidal physics[49,198]. Specifically, reaction-limited aggregation is kinetically unfavorable, which in turn allows the primary particles to diffuse deeper into the center of porous aggregate, leading to the growth of aggregates with a higher fractal dimension.

5.3.4. Pure water permeability of (PEI-s-PSS)$_n$ LNF membrane

The intercalation of SB3-14 dramatically enhances the pure water permeability of the resulting (PEI-s-PSS)$_n$ LNF membranes (Figure 5.7). The degree of permeability enhancement depends on the number of layers and the surfactant concentrations used in the intercalation step. In general, a higher SB3-14 concentration results in a more significant enhancement of water permeability, regardless of the number of polyelectrolyte layers. With a given SB3-14 concentration, the permeability decreased with a higher number of layers deposited. However, the relative (i.e., in terms of percentage) performance differences between membranes with the different number of polyelectrolyte layers are the most salient for (PEI-PSS)$_n$ membrane without any surfactant integration. In other words, the integration of surfactants does not only enhance the water permeability but also reduce the relative difference in water permeability between (PEI-s-PSS)$_n$ with different numbers of layers. Notably, using 1.0 mM of SB3-14 for intercalation improves the water permeability of (PEI-PSS)$_1$ and (PEI-PSS)$_3$ membranes by ~300% and ~500%, respectively.

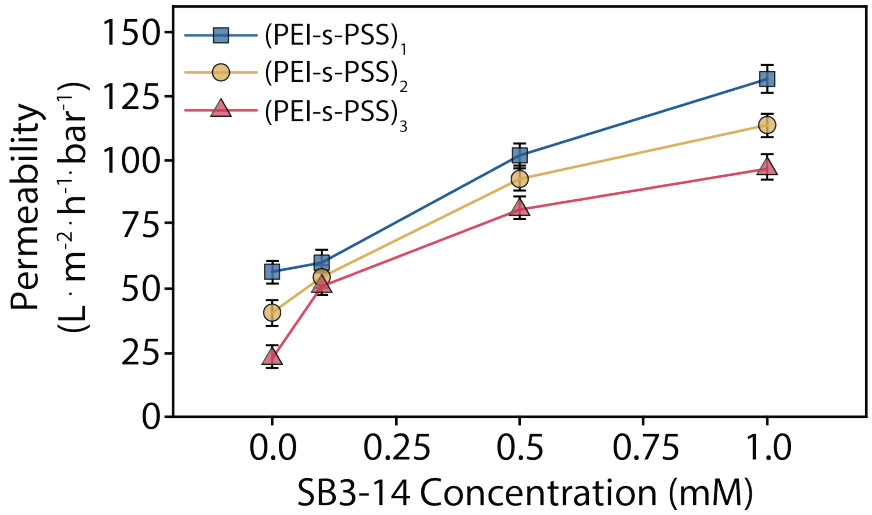

Figure 5.7 Water permeability of the $(PEI\text{-}s\text{-}PSS)_n$ with different surfactant concentrations and different numbers of assembly layers. (Permeability data represents the average of three runs)

5.3.5. Solute rejection of $(PEI\text{-}s\text{-}PSS)_n$ LNF membrane

The integration of zwitterionic surfactants did not only enhance the water permeability substantially but also increased the rejection of humic acid (Figure 5.8A). In fact, as the concentration of SB3-14 in the intercalation step increased, the HA rejection of the $(PEI\text{-}s\text{-}PSS)_1$ membrane increased from 97% to 99%. We note that a higher rejection of HA does not necessarily mean the membrane is "less permeable" to HA because the rejection of a solute represents the relative permeability of a membrane to solute as compared to water. In this case, because the addition of SB3-14 enhances the water permeability by ~3 folds, as long as the permeability of HA does not increase by the same degree or more, the rejection of HA increases. A previous study on fabricating $(PEI\text{-}PSS)_n$ LNF membrane using similar compositions of PEI and PSS but without the surfactant intercalation reported an HA rejection of 97% even with five layers of PEI and PSS[178]. The corresponding water permeability for that $(PEI\text{-}PSS)_5$ membrane was only ~ 12 L m^{-2} h^{-1} bar^{-1}, which is less than 1/10 of the water permeability of a $(PEI\text{-}s\text{-}PSS)_1$ LNF membrane fabricated in this work (~131 L m^{-2} h^{-1} bar^{-1}) even though the membrane reported in this work has an even higher HA rejection.

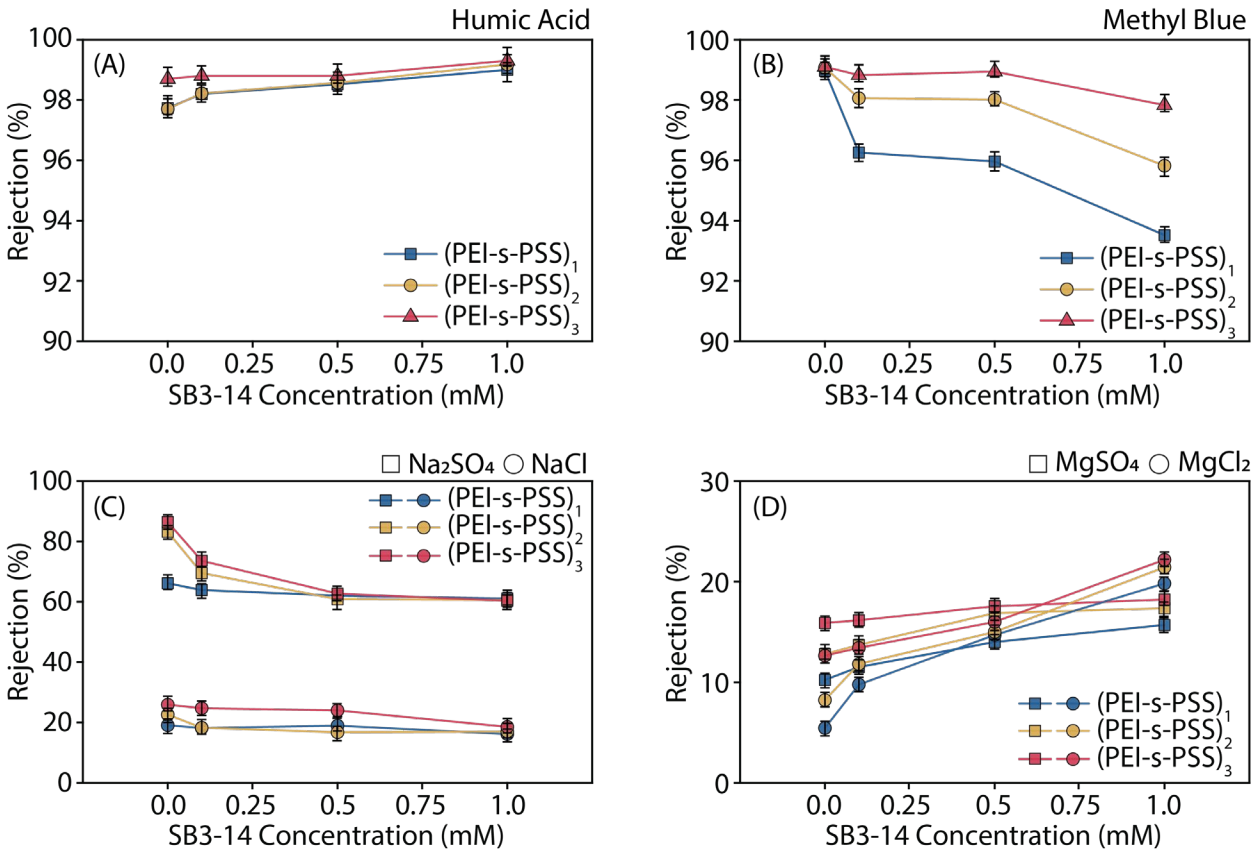

Figure 5.8 Separation performance of the $(PEI\text{-}s\text{-}PSS)_n$ LNF membranes with different surfactant concentrations and number of assembly layers. (A) Humic acid (B) Methyl Blue (C) Na_2SO_4 and NaCl (D) $MgSO_4$ and $MgCl_2$ (rejection data represents the average of three runs)

While the intercalation of SB3-14 is effective in maintaining, or even increasing, the HA rejection, it compromises the rejection of methyl blue which is a negatively charged dye molecule (Figure 8B). For relatively small charged molecules (as compared to HA), the Donnan exclusion effect has an important contribution to the overall solute rejection[163,164]. Compared with the $(PEI\text{-}PSS)_n$ membranes, the $(PEI\text{-}s\text{-}PSS)_n$ membranes have less negative zeta potential (Figure 3B), possibly due to reduced adsorption of the PSS. Consequently, the Donnan exclusion of negatively charged methyl blue molecules is also weaker. However, because the differences in zeta potential between $(PEI\text{-}PSS)_n$ and $(PEI\text{-}s\text{-}PSS)_n$ are relatively small, we also speculate that the zwitterionic group on SB3-14 is ineffective in repelling methyl blue molecules due to the co-existence of cationic and anionic moieties near each other, even though the overall contribution of SB3-14 to surface potential is negative according to Figure 3B. Additionaly, the intercalation of SB3-14 also

increased the MWCO and the pore size of $(PEI\text{-}PSS)_n$ LNF membrane (see Figure C.1). Despite the negative impact of SB3-14 intercalation on the rejection of methyl blue, the absolute rejection of methyl blue still exceeds 93% in all cases. For membranes with three layers, integrating SB3-14 at a concentration of 1 mM only reduced the methyl blue rejection of ~99% for $(PEI\text{-}PSS)_3$ to ~98% for $(PEI\text{-}s\text{-}PSS)_3$—a very small compromise as compared to the tremendous gain in water permeability.

The salt rejection of the $(PEI\text{-}s\text{-}PSS)_n$ LNF membranes was also evaluated, even though salt rejection is expectedly low for any LNF membranes. Specifically, the intercalation of SB3-14 reduced the rejection of Na_2SO_4, especially for membranes with two and three layers (Figure 5.8C). When the SB3-14 concentration exceeds 0.5 mM, the Na_2SO_4 rejection is consistently ~60% regardless of the number of layers. In comparison, the integration of SB3-14 does not seem to have a major impact on NaCl rejection. The rejection of NaCl is consistently low (~20%) regardless of the number of layers and the presence (and concentration) of SB3-14. Lastly, the integration of SB3-14 seems to enhance the rejection of Mg^{2+} salt, even though the rejection can barely exceed 20% in all cases. It is well known that a negatively charged membrane is better in rejecting solutes with multivalent anions (e.g., Na_2SO_4) than in rejecting solutes with multivalent cations (e.g., $MgCl_2$), which is attributable to the fact that Donnan exclusion is a major rejection mechanism. The fact that the integration of SB3-14 undermines the rejection of Na_2SO_4 but improves the rejection of $MgCl_2$ is additional evidence that the presence of the SB3-14 bilayers reduces electrostatic interaction with solutes as compared to a PSS surface without surfactant intercalation.

5.3.6. Overall performance of $(PEI\text{-}s\text{-}PSS)_n$ membrane versus the state-of-the-art

As discussed in sections 3.4 and 3.5, the intercalation of SB3-14 dramatically enhances the water permeability of the LNF membrane without sacrificing its HA rejection. The $(PEI\text{-}s\text{-}PSS)_n$ membranes have exceptional performance not only just compared to the reference $(PEI\text{-}PSS)_n$ membranes but also compared to the state-of-the-art according to literature (Figure 5.9A). Only two membranes reported in previous work could achieve a water permeability above 40 L m^{-2} h^{-1} bar^{-1} while maintaining an HA rejection beyond 90% (“o” and “p” in Figure 5.9). However, the $(PEI\text{-}s\text{-}PSS)_1$ membrane attains an exceptional water permeability of ~131 L m^{-2} h^{-1} bar^{-1} and an outstanding HA rejection of 99%, far exceeding the state-of-the-art performance of LNF

membranes for filtering HA solutions. The same conclusion can be drawn when comparing the rejection of methyl blue of $(PEI\text{-}s\text{-}PSS)_n$ membranes with the NF membranes reported in the literature. (Figure 5.9B) Although the intercalation of SB3-14 slight induces a trade-off of the membrane permeability and its rejection of methyl blue, the 3-bilayer $(PEI\text{-}s\text{-}PSS)_n$ membrane still yields a high rejection of 99% while maintaining the water permeability of 82 L m^{-2} h^{-1} bar^{-1}, which is superior than state-of-the-art NF membranes reported in the literature.

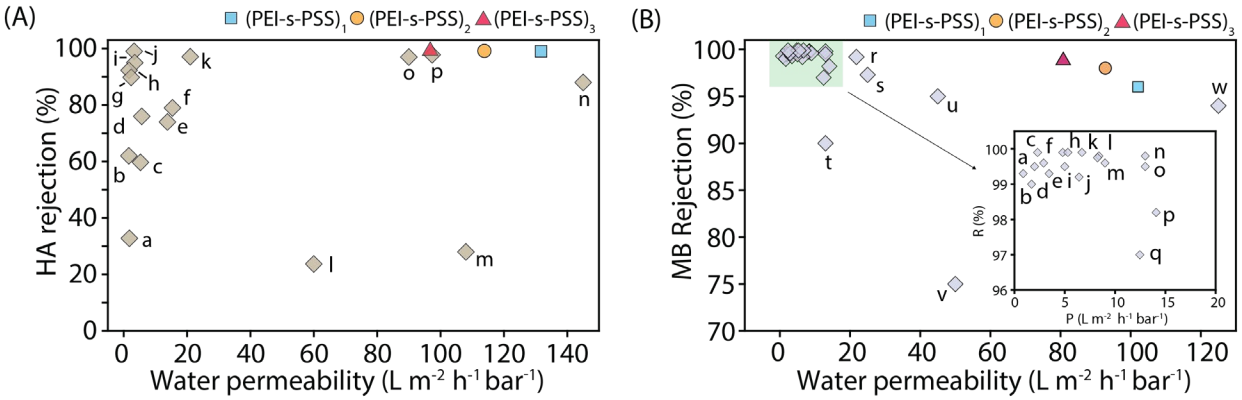

Figure 5.9 (A) Comparison of water permeability and HA rejection of (PEI-s-PSS)n LNF membrane (SB3-14 concentration is 1 mM) with other NF membranes reported in the literature. (a,b, [199]; c,f, [200]; d, [201]; e, [202]; g,h, [203], i,[204]; j, [202]; k, [178]; l,m, [205]; n, [62]; o, [206]; p, [146]) (B) Comparison of water permeability and methyl blue rejection of (PEI-s-PSS)n LNF membrane (SB3-14 concentration is 0.5 mM) with other NF membranes reported in the literature. (a [207]; b [208]; c,d,g,h [209]; e,o,p [186]; f [210]; i [66]; j [72];k [211]; l, [212]; m,n [213]; q,s [214]; r [215]; t [64];u [70]; v [216]; w [146])

5.3.7. Reduced fouling of the $(PEI\text{-}s\text{-}PSS)_n$ LNF membranes

It is widely recognized in the literature that membranes that are smoother and more hydrophilic are less prone to fouling[146,206–209]. Compared with the $(PEI\text{-}PSS)_3$ membrane, the $(PEI\text{-}s\text{-}PSS)_3$ LNF membrane was dramatically smoother (Figure 5.5) and slightly more hydrophilic (Figure 5.4). Consequently, the $(PEI\text{-}s\text{-}PSS)_3$ LNF membrane was substantially more fouling resistant than the $(PEI\text{-}PSS)_3$ LNF membrane in long-term filtration experiments with HA as the feed solution (Figure 5.10). Not only the initial flux decline was much slower with the $(PEI\text{-}s\text{-}PSS)_3$ LNF membrane (Figure 5.10A and 5.10B), but its normalized flux at steady-state (i.e., no more flux decline) was also considerably higher than that with the $(PEI\text{-}PSS)_3$ LNF membrane.

Specifically, ~67% and ~45% of the initial fluxes were maintained at steady state with the (PEI-s-PSS)$_3$ and (PEI-PSS)$_3$ LNF membranes, respectively (Figure 5.10B). The advantage of (PEI-s-PSS)$_3$ over (PEI-PSS)$_3$ is all the more salient if we consider the fact that the initial flux of the former is two to three folds of the later (Figure 5.10A). The steady-state water flux for the (PEI-s-PSS)$_3$ membrane was 230 L m^{-2} h^{-1}, whereas that for the (PEI-PSS)$_3$ membrane was only 57.2 L m^{-2} h^{-1}.

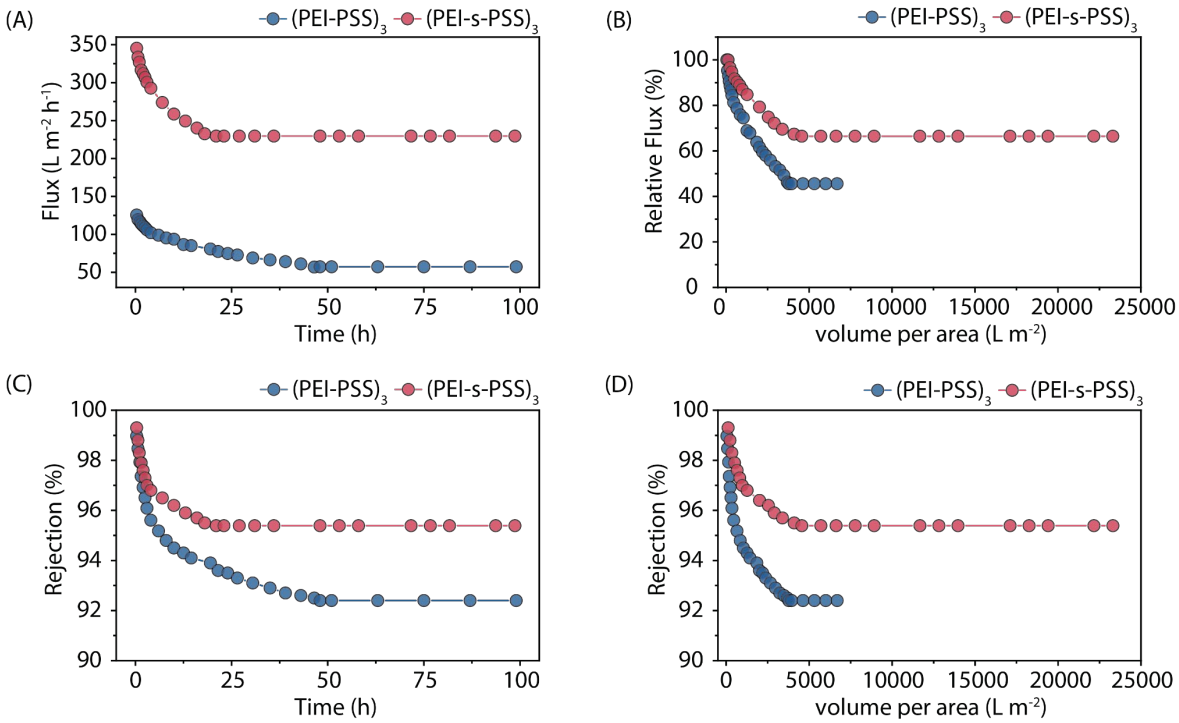

Figure 5.10 (A) absolute flux as a function of time; (B) normalized flux as a function of permeate volume per membrane area; (C) HA rejection as a function of time; (D) HA rejection as a function of permeate volume per membrane area. In all panels, blue and red symbols represent data obtained using (PEI-PSS)$_3$ and (PEI-s-PSS)$_3$ membranes, respectively.

We have shown in Section 3.5 that the integration of SB3-14 did not compromise, but even slightly improved, the HA rejection of the (PEI-PSS)$_n$ LNF membrane. When both membranes were subject to long-term filtration of an HA solution, an appreciable drop of HA rejection was observed for both membranes (Figure 5.10C, D). Interestingly, the drop of rejection synchronized with the flux decline and reached a steady-state (i.e., no more drop of rejection) when ~ 4,500 L

and 3,700 L of feed water was filtered through 1m^2 of $(PEI\text{-}s\text{-}PSS)_3$ and $(PEI\text{-}PSS)_3$ LNF membranes, respectively (Figure 5.10D). As discussed in section 3.5, rejection is not only dependent on how permeable a membrane is to a specific solute but dependent on the water permeability. The synchrony between the changes of flux and HA rejection suggests that the reduction of HA rejection is primarily attributable to the reduction of flux. Because the $(PEI\text{-}PSS)_3$ LNF membrane was subject to a larger percent of flux decline as compared to the $(PEI\text{-}s\text{-}PSS)_3$ membrane, it also suffered a more substantial reduction in HA rejection. Specifically, the HA rejection for $(PEI\text{-}PSS)_3$ and $(PEI\text{-}s\text{-}PSS)_3$ membranes dropped from ~99% to 92.2% and 95.5%, respectively, when filtration reached steady-state. Overall, the results in Figure 5.10 suggest that the $(PEI\text{-}s\text{-}PSS)_3$ is systematically better than $(PEI\text{-}PSS)_3$ in long-term filtration of an HA feed solution, demonstrating slower flux decline, higher steady-state flux, and higher steady-state HA rejection.

5.4.Conclusion

We show in this study the effectiveness of using SB3-14 intercalation to dramatically improve the performance of LNF membranes formed via LbL deposition of PSS and PEI. The presence of SB3-14 self-assemblies resulted in smoother and more permeable LNF membranes. The resulting $(PEI\text{-}s\text{-}PSS)_n$ membrane achieved an outstanding water permeability of 131 L m^{-2} h^{-1} bar^{-1} while maintaining an exceptional rejection of HA (99%). Compared to the reference $(PEI\text{-}PSS)_3$ membrane, the performance of the $(PEI\text{-}s\text{-}PSS)_3$ was also much more stable in long-term LNF operation as indicated by not only substantially less decline of normalized flux but also less decline in HA rejection. We attribute these remarkable improvements in performance and long-term stability to the unique active layer structure imparted by the integration of the SB3-14 self-assemblies. We believe that this strategy of surfactant intercalation is universally applicable for enhancing LNF membrane formed via LbL deposition of polyelectrolytes.

CHAPTER 6

IN-SITU MONITORING OF POLYELECTROLYTES ADSORPTION KINETICS BY ELECTROCHEMICAL IMPEDANCE SPECTROSCOPY: APPLICATION IN FABRICATING NANOFILTRATION MEMBRANES VIA LAYER-BY-LAYER DEPOSITION

6.1.Introduction

Nanofiltration (NF) is a membrane-based solute and molecular separation process that has been playing an increasingly important role in water treatment and wastewater reclamation[81,130,172,217–220]. It is a low-pressure membrane process with separation performance between reverse osmosis (RO) and ultrafiltration (UF)[19,37,221]. Unlike RO membrane that rejects almost all solutes from the feed solution, NF membranes typically have a comparatively loose active layer that partially rejects large ions and small organic molecules. The selectivity of NF membrane is mainly dependent on the pore size and the surface charge[30,222]. In general, NF membranes retain solute larger than the pore size and/or with charge similar to the surface and pore of the membrane[134,223].

Most existing commercial NF membranes are thin-film-composite polyamide (TFC-PA) membrane fabricated via interfacial polymerization (IP) [19,37,221]. Although polyamide-based NF membranes exhibit excellent perm-selectivity in many NF applications, they suffer from the propensity to organic and biological fouling and the poor chlorine resistance that prohibits aggressive membrane cleaning, which results in increased energy consumption in long-term operation and a relatively short membrane lifetime[4,20,224,225]. As an alternative to IP, Layer-by-Layer (LbL) deposition has been actively explored to fabricate membranes with a polyelectrolyte multilayer (PEM) active layer. Over the last few decades, fabrication of PEM-nanofiltration (PEM-NF) membranes using LbL deposition has received growing interests due to its vast potential for tuning NF membrane performance with fine control of active layer film properties[55,143,144,165,226,227]. These features allow for engineering functional PEM-NF membranes with outstanding perm-selectivity, excellent fouling resistance and chemical stability in harsh conditions[79,186,228,229].

Typically, a PEM-NF membrane is formed by electrostatic self-assembly of two oppositely charged polyelectrolytes[146,187]. The kinetics of adsorption of polyelectrolytes onto an oppositely charged surface is primarily regulated by diffusion and charge overcompensation [46,144,152,230].

Many competing factors affect the kinetics of polyelectrolyte adsorption, including polyelectrolyte type (e.g., strong or weak polycations vs. polyanions), molecular weight, concentration, substrate charge density, and the presence of inert, non-adsorbing electrolytes [46]. Studying the impacts of these factors on polyelectrolyte deposition and optimizing NF membrane synthesis based on LbL deposition requires an effective approach for monitoring the kinetics of polyelectrolyte adsorption. An ideal method for probing the kinetics of polyelectrolyte adsorption in NF membrane fabrication should be in-situ, non-interfering with the membrane fabrication process, and does not require the use of special substrates as sensors.

Unfortunately, existing approaches of monitoring adsorption kinetics fail to satisfy all these requirements. These methods include UV/Vis spectroscopy[166,231], small-angle X-ray scattering[232], quartz crystal microbalance with dissipation (QCM-D)[233,234], conductometric and potentiometric titration[235], ion-sensitive field-effect sensors and transistors[236]. While these techniques can provide useful information about polyelectrolyte deposition, each of them has their respective limitations. For instance, UV/Vis spectroscopy can only be applied to polyelectrolytes with optically sensitive functional groups [166]. Conductometric and potentiometric titrations require the presence of titratable functional groups in the polyelectrolyte species. X-ray scattering is a powerful tool to characterize the change of the film thickness, but provides limited information on adsorption kinetics [225]. QCM measurements can only be performed using piezoelectric crystal, which limits the choices of adsorption substrates and cannot be applied in real membrane fabrication processes [233]. A similar limitation also applies to methods based on ion-sensitive field-effect sensors and transistors [236].

Electrochemical impedance spectroscopy (EIS) is a powerful technique with diverse applications in studying reactions and interfacial processes, including corrosion[237], coatings[238], electrocatalytic reactions[239], and redox reactions[240]. Efforts have been made to analyze the adsorption of polyelectrolyte onto a modified electrode, which provides insights into the growth kinetics of PEM films[241,242]. In those studies, the application of EIS was limited to studying PEM grown on special substrates, such as silicon and quartz electrodes. However, it remains challenging to directly study the kinetics of adsorption on porous membranes to monitor the growth of PEM in real membrane fabrication processes.

Here, we report a novel technique based on a four-electrode EIS system for studying the kinetics of polyelectrolyte adsorption onto a porous support in the context of fabricating PEM

nanofiltration (NF) membrane. This technique provides an in-situ and non-destructive method for monitoring the growth of the PEM forming on a membrane substrate via LbL deposition. Specifically, we use a model system comprising poly (diallyldimethylammonium chloride) (PD) as the polycations, and poly (sodium 4-styrene sulfonate) (PS) as the polyanions. This model system has been widely investigated for preparing PEM-NF membranes via LbL deposition[165,243]. We perform EIS measurements during the sequential depositions of the six layers of polycation and polyanion on a polyacrylonitrile (PAN) ultrafiltration membrane substrate and extract the solution resistance and charge transfer resistance from the EIS spectra. Finally, we characterize the PEM-NF membrane with different adsorption time and correlate the membrane properties and NF performance with the characteristics of the adsorption process.

6.2.Materials and methods

6.2.1. Materials and chemicals

Polyacrylonitrile (PAN) ultrafiltration membrane (MWCO = 50 kDa, GE Healthcare Life Science) was used as the substrate for fabricating the PEM-NF membrane. Poly(diallyldimethylammonium chloride) solution (PD, 25%, 400-500 kDa), Poly(sodium 4-styrenesulfonate) (PS, 1000 kDa), hydrochloric acid (HCl, ACS reagent, 37%), sodium hydroxide (NaOH, Bioxtra, ≥ 98%) and Na_2SO_4 (≥ 99%), were purchased from Sigma-Aldrich (St. Louis, MO US). All chemicals were used as received without further purification. Deionized water (Millipore, US) was used to prepare polyelectrolyte solutions and surfactant solution.

6.2.2. Fabrication of PEM-NF membrane

The PEM-NF membrane was prepared by depositing PD and PS alternately onto a PAN ultrafiltration (UF) membrane (the chemical structures of PD and PS are shown in Figure 6.1). The PAN-UF membrane was first treated with a 2 mol L^{-1} NaOH solution for 30 minutes to acquire a negative surface charge, then immersed into DI water to remove excess NaOH, and finally dried in the oven before use. The hydrolyzed PAN membrane was exposed to the polycation solution (2

g L^{-1} PD), rinsed with DI water, then exposed to a polyanion solution (2 g L^{-1} PS), and finally rinsed with DI water. The resulting membrane is referred to as the $(PD\text{-}PS)_1$ with the subscript "1" representing one PD-PS bilayer. The same procedure was repeated to form additional bilayers, forming $(PD\text{-}PS)_2$ and $(PD\text{-}PS)_3$.

6.2.3. EIS measurement, equivalent circuit, and parameters extraction

In each polyelectrolyte deposition step, EIS measurement was performed using a potentiostat (SP-150 BioLogic, France) equipped with a custom-made EIS cell (Figure 6.1A, also Figure D.1). The cell dimension is 80 mm ×80 mm × 80 mm with an effective membrane area of 4.52 cm^2. The cell consists of two chambers, each containing an electrode for injecting current (the working and counter electrodes) and an electrode for measuring the potential across the membrane (the working sense electrode and the reference electrode)[244]. The polycation and polyanion solutions were alternately introduced to the PAN substrate in a non-flow electrochemical cell, and the process of polyelectrolyte deposition was in-situ monitored. The four-electrode system separates the measurements of current and voltage, and thereby eliminates the complicating effects of the frequency-dependent impedance at the interface between the solution and the working electrode.

This setup, shown in Figure 6.1A and 6.1B, enables the simultaneous measurements of solution resistance near the interface and the film resistance without mutual interference. The working and counter electrodes are responsible for current injection, whereas the working sense and reference electrodes are for measuring potential differences across the PEM. The working electrode is a platinum ring placed in the polyelectrolyte solution, whereas the counter electrode is a platinum foil placed in the polyelectrolyte-free solution contacting the opposite side of the membrane. The working sense electrode and the reference electrode are two platinum wires placed in direct contact of the two sides of the substrate membrane, respectively. The direct contact of the working sense electrode and the reference electrode with the membrane is critical to the measurement consistency, whereas the use of wires (instead of foil) minimizes the interference of the electrodes with the polyelectrolyte deposition.

The input was a sinusoidal perturbation signal with an amplitude of 10 mV (vs. the open-circuit potential). Unless specified, an impedance spectrum was recorded every 120s with a sweep frequency from 50 kHz to 0.1 Hz. However, we also performed some EIS measurements only within the high frequency range to shorten the scan time to extract the early stage evolution of certain parameters. Each polyelectrolyte deposition experiment was repeated for three times and the average and standard deviation of the parameters extracted from the EIS measurements are reported. Fitting of the impedance data was performed using commercial software, ZView®.

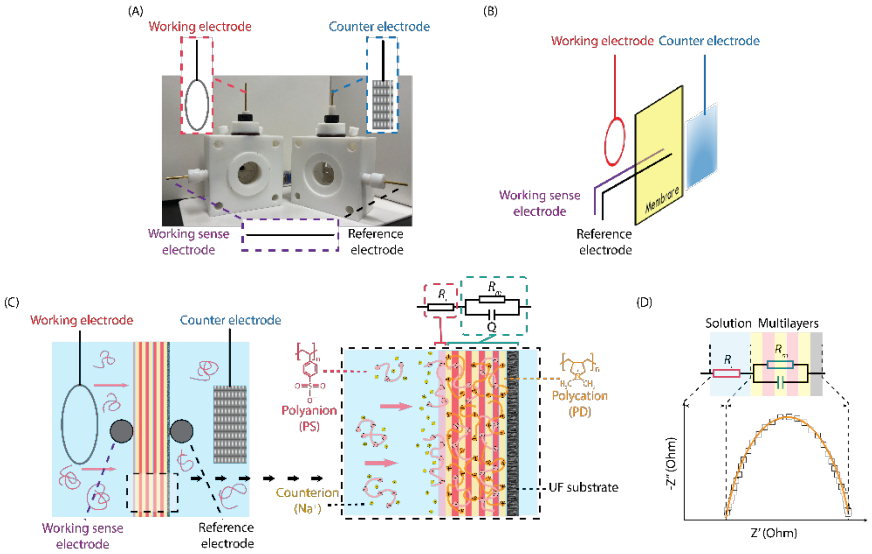

Figure 6.1 (A) A custom-made EIS cell for EIS measurements. (B) Schematic illustration of the electrodes' positions in the EIS measurements. (C) The R_i-(R_m/Q) equivalent circuit used to fit the EIS spectra. The equivalent circuit comprises a parallel circuit R_m/CPE connected in series to a resistance R_i. (C) Illustration of Nyquist plot of the measured impedance and its interpretation using the equivalent circuit. The intercept of the x-axis represents the interfacial solution layer resistance, R_i. The film resistance R_m, and the non-ideal capacitive behavior, Q, are related to the size of the semi-circle.

The EIS spectra were modeled using a R_i-(R_m/Q) equivalent circuit connecting a resistance R_i with an RC circuit of R_m/Q (Figure 6.1C)[245]. Specifically, R_i stands for the interfacial solution resistance which is the resistance of a thin film of solution near the membrane surface. The value of this resistance primarily depends on the abundance of the counter ions of the immobilized polyelectrolyte, and is thus closely related to the surface charge of the membrane[246,247]. R_m

represents the film resistance corresponding to the diffusion resistance of mobiles ions across the PEM-NF membrane[245,248–251]. Lastly, Q represents the constant phase element (CPE) accounting for the non-ideal capacitive behavior. In the EIS spectrum, R_i is the first x-intercept in the Nyquist plot, while R_m and Q relate to the size of the semi-circle. Confidence limits of the best-fit model parameters were quantified by evaluating the variance-covariance matrices of the Levenberg-Marquardt algorithm employed in a non-linear R^2 minimization between the model and data [252].

While the interfacial electrochemical adsorption has been extensively studied for electrodes and functionalized conductive substrates using three-electrode systems[247,252], a three-electrode system does not enable direct characterization of the adsorption of charged species to a dielectric such as a membrane. This challenge is overcome in our four-electrode system where a pair of electrodes for measuring potential difference are attached to the two sides of the membrane to detect the subtle potential difference when electrostatic adsorption occurs at the solution-membrane interface. Despite the large resistance from the membrane substrate, the four-electrode system was sufficiently sensitive to detect the slight change of interfacial solution resistance (R_i) and film resistance (R_m) related to polyelectrolyte deposition. These two parameters extracted from the EIS spectra following the equivalent circuit model provide useful insights into understanding the process of LbL deposition.

6.2.4. NF membrane characterization and performance testing

As charge overcompensation is the primary driving force of polyelectrolyte adsorption, the change of surface charge density or potential is an important indicator of the adsorption progress. We prepared the $(PD\text{-}PS)_n$ (n=1,2,3) membranes with different adsorption time, ranging from 0 to 60 min, for the adsorption of the PS top-layer onto underlying polyelectrolyte multilayers (capped with PD before PS adsorption). Except for this top layer of PS for which we intentionally varied the adsorption time, each layer of the underlying polyelectrolyte was prepared with a 30 min deposition time. The ζ-potentials of the $(PD\text{-}PS)_n$ membranes with different top-layer PS adsorption time were determined by streaming current measurements using a streaming potential analyzer (SurPASS electro-kinetic analyzer, Anton Paar, Ashland, VA) with an adjusting gap cell

with a channel width around 100 um and 1mM KCl solution as the background electrolyte. The zeta potential is calculated according to the method by Helmholtz-Smoluchowski[253]:

$$\zeta = \frac{dl}{dp}\frac{\eta}{(\varepsilon - \varepsilon_0)}\frac{L}{A}$$

where ζ is the zeta potential, dl/dp is the slope of streaming current vs. differential pressure, η is the dynamic viscosity of the liquid, ε is the dielectric coefficient of solvent, ε_0 is vacuum permittivity, L is the length of the streaming channel and A is the cross-section of the streaming channel. We note that while the charged porous substrate may have impacts on the measured zeta potential[254–256], this effect is difficult to quantify due to the technical challenge of accurately distinguish the properties of the active layer and the PEM. However, relative change of surface zeta potential of the PEM would not be affected without considering the impact of the substrate porosity.

NF performance of the $(PD\text{-}PS)_n$ (n=1,2,3) membranes with different adsorption time was evaluated using a cross-flow filtration cell with an active membrane area of 7.1 cm^2. The pure water permeability of the $(PD\text{-}PS)_n$ membranes was evaluated using DI water. The crossflow velocity was 0.62 m s^{-1} and the applied pressure was 2 bar. We evaluated the rejection of Na_2SO_4 (1 g L^{-1}), which is commonly used in NF performance testing. The salt concentrations of the feed and permeate solutions were determined by measuring the electrical conductivity of the solutions with a calibration curve. The pure water permeability of the NF membrane was defined using the following equation:

$$PWP = \frac{J}{\Delta P}$$

where PWP is the pure water permeability of the NF membrane (unit: L m^{-2} h^{-1} bar^{-1}), $\boldsymbol{J}$ is the volumetric flux of water (unit: L m^{-2} h^{-1}), and ΔP was the applied pressure (unit: bar), respectively. The solute rejection, R, is calculated using the following equation:

$$R = \left(1 - \frac{c_p}{c_f}\right) \times 100\%$$

where c_p and c_f are the solute concentrations of permeate and feed solution, respectively.

6.3.Results and discussion

6.3.1. Evolution of interfacial solution and film resistances reflects polyelectrolytes growth

Both the interfacial solution resistance and film resistance changed throughout the adsorption process (Figure 6.2). Each semi-circle represents a full EIS spectrum at a certain period in the adsorption process (Figure 6.2A). The frequency of the spectrum scan ranged from 50 kHz to 0.1 Hz. The spectrum initially shifted to the right before shifting back toward the left as the polyelectrolyte deposition continued, which suggests that R_i increased slightly at the beginning of the adsorption process due to the loss of mobile counterions in the interfacial layer and then gradually decreased as the mobile ions concentration restored (Figure 6.2B). In comparison, the film resistance, R_m, which quantifies the diffusion resistance of mobile ions (counterions) across the PEM-NF membrane, monotonically increased as the adsorption process occurred and eventually approached a maximum (Figure 6.2C). The increase in R_m results from more difficult ion transport across the membrane as the PEM layer grows thicker. While more discussion will be provided later, the EIS data in Figure 6.2 show that the temporal evolution of both interfacial solution resistance (R_i) and film resistance (R_m) reasonably reflects the dynamics of polyelectrolyte adsorption.

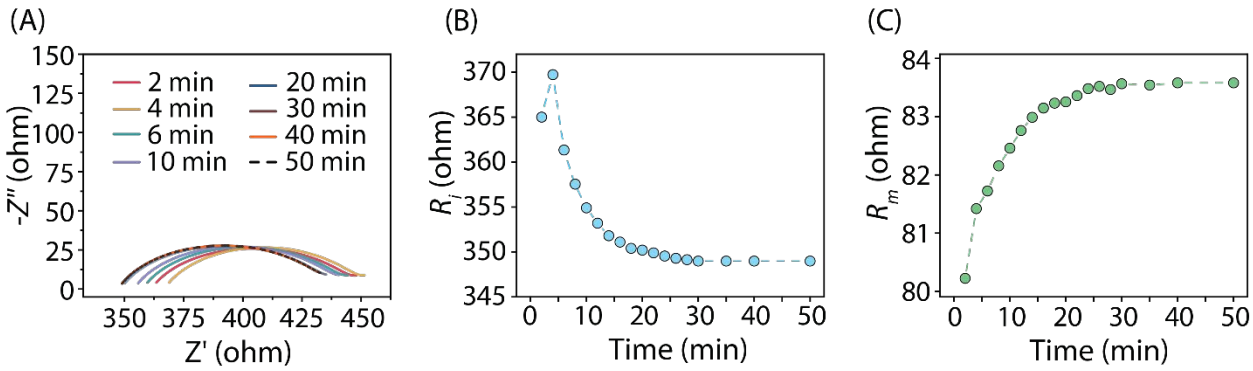

Figure 6.2 (A) Example Nyquist plots of impedance of the solution near the solution-membrane interface and the polyelectrolyte active layer as a function of time during the deposition of the second PS layer onto the PAN-(PD-PS-PD) surface. (B) Change of solution resistance (R_i) as a function of time deduced from Nyquist plot. (C) Change of film resistance (R_m) as a function of time deduced from Nyquist plot.

6.3.2. Time-dependent interfacial and film resistances during polyelectrolytes growth

Polyelectrolyte adsorption is a process driven by electrostatic interaction and limited by diffusion. In such a process, polyelectrolyte molecules first diffuse from the bulk solution to the interfacial layer near the membrane surface under a concentration gradient due to the consumptive adsorption, and then bind onto the charged substrate via electrostatic attraction. Upon contact with the PEM surface, a small segment of the polyelectrolyte chain is anchored onto the surface forming a large number of loops (segments with two anchor point on the PEM surface) and tails (segments with one anchor point on the PEM surface), while a large portion of segments still protrudes into the solution[166,257]. In a salt-free environment, the electrostatic attraction between two strong polyelectrolytes, e.g. PD and PS, leads to the spatial rearrangement of polyelectrolyte chain because the enthalpy reduction associated with the increased contact between the substrate and the polymer with a more extended configuration outweighs the corresponding loss of entropy[258].

Probing the R_i extracted from EIS data provides useful information regarding the kinetics and extent of adsorption. The adsorption dynamics in each step is illustrated using the inverse of normalized interfacial resistance, defined as the ratio between the final interfacial resistance, $R_{i,f}$, and the real-time interfacial resistance, R_i, i.e., $R_{i,f}/R_i$ (Figure 6.3A and Figure D.2). The value of $R_{i,f}/R_i$ roughly quantifies the real-time abundance of counter ions on the membrane surface as compared to that at adsorption equilibrium, as $1/R_i$ positively correlates to the abundance of counter ions.

Instead of scanning the full frequency range, we performed partial spectrum scans only in the high-frequency range (10kHz to 0.3kHz) to shorten the time of each scan (Figure D.3). For both PS adsorption onto PD-coated surfaces and PD adsorption onto PS-coated surfaces, $R_{i,f}/R_i$ dropped slightly in the initial stage of adsorption (Figure 6.3A), as the substrate surface became neutralized[259]. After this initial stage, $R_{i,f}/R_i$ continued to increase as the surface became increasingly overcharged. The increase of $R_{i,f}/R_i$ eventually leveled off as the adsorption approached completion. Comparing the adsorption of the two polyelectrolytes, we find that the initial-stage adsorption is faster for PD adsorption onto the PS-coated surfaces than for PS adsorption onto PD-coated surfaces, which is reflected by the earlier emergence of the minimum $R_{i,f}/R_i$ when PD adsorb onto the PS-coated surfaces.

The faster initial adsorption of PD can be explained by the much higher surface charge (in absolute value) of the PS-coated surface (Figure 6.3B, circles) than that of PD-coated surface (Figure 6.3B, squares). Therefore, the initial driving force for PD adsorption onto the PS-coated surface is much stronger than that for PS adsorption onto the PD-coated surface. In addition, the diffusion rate of PD (Mw~400-500 kDa) is estimated to be ~1.5 times larger than that of PS (Mw~1000 kDa)[260,261]. Consequently, the low adsorption rate of PS onto the PD-coated PEM surface and the low diffusion rate of PS from bulk solution to the membrane surface synergistically delayed the emergence of the $R_{i,f}/R_i$ minimum.

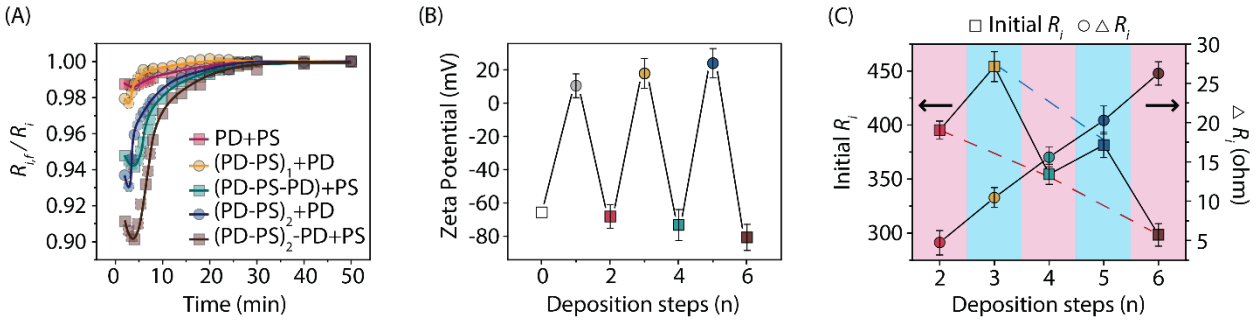

Figure 6.3 (A) Temporal evolution of the inverse of the normalized interfacial resistance, $\boldsymbol{R_{i,f}/R_i}$ at different deposition stages as extracted from EIS data (squares for PS adsorption onto a PD-coated surface and circle for PD adsorption onto a PS-coated surface). (B) Surface zeta potential of PEM-NF membranes with different layers of polyelectrolytes. The deposition time of each polyelectrolyte layer was 30 min. Error bars represent standard deviations of three replicate measurements. (C) Initial R_i (before the new step of adsorption) and the change of R_i for each deposition step.

The trend of initial R_i value in each adsorption step throughout a sequential six-layer LbL deposition is shown in (Figure 6.3C squares). On one hand, the initial R_i of the same type of surface decreased as more layers of polyelectrolytes were deposited. On the other hand, growing a PS layer on a PD surface increased the R_i of the previously PD-coated surface. The change of interfacial solution resistance in each deposition step (of either PS or PD), ΔR_i, continued to grow with a larger number of deposited layers (Figure 6.3C, circles). This implies that more polyelectrolytes deposit in the later steps of the LbL process, which is consistent with the

growingly larger difference in zeta potential between two adjacent layers as the number of layers increased (Figure 6.3B).

The EIS spectra also yield another important parameter, namely the film resistance (R_m), which quantifies the transmembrane diffusion resistance of mobile ions across the PEM-NF membrane. The resistance R_m of a film is directly related to ionic permeability[245,248], and is dependent on surface charge, film thickness, and the ion diffusivity. The temporal variation of R_m as extracted from fitting the equivalent circuit suggests that R_m rapidly increased in the early stage of adsorption and gradually leveled off as adsorption approached completion (Figure 6.4A). The increase in R_m resulted from more difficult trans-membrane diffusion as the more polyelectrolyte accumulated on the membrane surface, and R_m reached a maximum value when the polyelectrolyte adsorption ended due to saturation of surface adsorption site. In addition, the R_m increased following an exponential function in the form of $1 - \exp(-kt)$ and leveled off at the end of adsorption which also reflects the accumulation of polyelectrolyte on the PEM surface. Regardless of the adsorption step in the LbL deposition process, R_m always reached a maximum at roughly 30 mins. The adsorption time reflected by the temporal evolution of R_m is highly consistent with that measured using the interfacial solution layer resistance, R_i(Figure 6.3A).

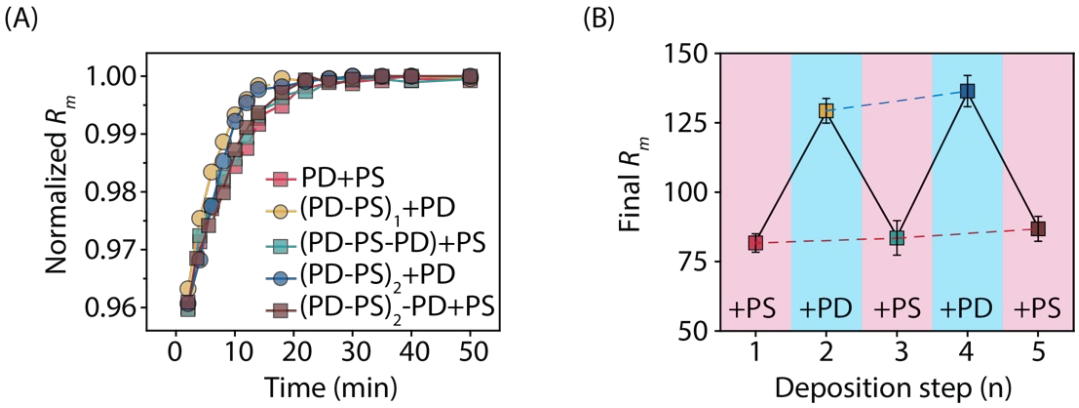

Figure 6.4 (A) Temporal evolution of R_m in different deposition steps, with squares representing PS adsorption onto a PD-coated surface and circle representing PD adsorption onto a PS-coated surface). (B) Final R_m (i.e., R_m at the end of each adsorption step) for each deposition step.

Comparing the temporal evolution of R_m at different deposition steps also reveals that R_m increased slightly faster for polycation (PD) adsorption than for polyanion (PS) adsorption (Figure 6.4A). The difference in the rates of R_m increase is attributable to the fact that PS-coated membrane surfaces were more strongly charged whereas PD-coated surfaces had surface potentials that were closer to zero (Figure 6.3C). Specifically, the fastest adsorption was observed with the positively charged PD adsorbing onto the membrane covered with $(PD\text{-}PS)_2$ which had the most negative charge among surfaces subject to further adsorption (no additional adsorption was performed beyond $(PD\text{-}PS)_3$ which was even more negative). The same conclusion could also be drawn from the PS adsorption: the adsorption rate increased with the number of polyelectrolyte layers.

The final values of R_m also reveal important insights regarding the properties of the PEM layers. First, the final values of R_m for the PD-capped film are systematically higher than that of the PS-capped film (Figure 6.4B). This is likely because (1) the PD-capped surface is substantially less charged than the PS-capped surface (Figure 6.3B) and (2) the counter anion for PD, Cl^-, has a substantially smaller Stoke radius (1.21 Å) as compared with that of the counter cations for PS, Na^+ (1.84 Å)[262]. Second, comparing the PEM-NF of the same capping polyelectrolyte across different steps of deposition, R_m, increased systematically as the number of layers increased (Figure 6.4B). Even though the absolute values of the surface potential increased (Figure 6.3B), which tends to enhance ion permeability and thus reduces R_m, R_m still increased systematically due to the increase of the PEM film thickness.

6.3.3. Correlating membrane property and performance with film resistance

Because of observations from Figure 6.3A and Figure 6.4A suggest the effective time of the adsorption was consistent ~30 mins regardless of the step in the LbL deposition, we hypothesize that the membrane property and performance depend on the polyelectrolyte adsorption time until it reaches 30 mins. To test such a hypothesis, we fabricated a series of PEM-NF membranes with different PD-PS bilayers (1, 2, and 3 bilayers) with each surface layer obtained using different adsorption time (from 0 to 60 min). We note that the different adsorption time applies only to the top layer, whereas the underlying PEMs all have the same composition.

Therefore, the membrane sample with 0-minute adsorption time is a membrane with the complete underlying layers but not the top layer. Thirty membrane samples were fabricated following such an experimental design. The surface potential, water permeability, and rejection of Na_2SO_4 were measured for each membrane sample and are presented in Figure 6.5, along with the temporal evolution of R_m that has been shown in Figure 6.4A also presented in Figure 6.5A, 6.5B and 6.5C to facilitate comparison.

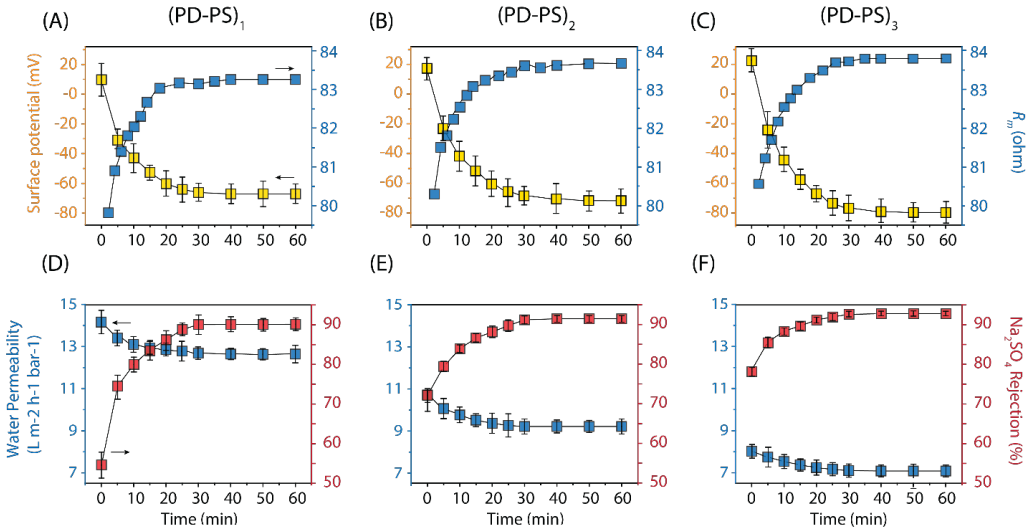

Figure 6.5 (A, B, C) Surface streaming potential (orange squares, left axis), R_m at a different time of the adsorption is also presented (green squares, right axis). (D, E, F) Membrane water permeability (blue squares, bottom row, left axis), and Na_2SO_4 rejection (red squares, bottom row, right axis) for PEM-NF membranes fabricated using different deposition time. All four sets of data are presented for PEM-NF membranes with one layer (PD-PS, first column), two layers ($(PD-PS)_2$, second column), and three layers of ($(PD-PS)_3$, third column).

Regardless of the number of PD-PS layers, the surface potential of the PEM-NF membranes as a function of adsorption time followed the opposite trend for the temporal evolution of R_m. As the EIS data in Figure 6.3 suggests, the polyelectrolyte deposition was completed at ~30 minutes. This is again confirmed by the temporal evolution of surface potential that reached its minimum at ~30 minutes. Similar behaviors were also observed with the membrane performance. Specifically, the water permeability decreased, and the salt rejection increased, with increasing deposition time, before they leveled off at ~30 minutes, which is in a good agreement with the

change of R_m (Figure 6.5). This evidence is congruent in supporting the conclusion that ~ 30 minutes is required for this specific PEM system to reach completion of each deposition step (i.e., reaching an adsorption equilibrium beyond which membrane properties no longer change).

The validation of the hypothesis derived from EIS measurement suggests that we can indeed use data from a single EIS measurement to determine the extent of the deposition as a function of the deposition time. However, EIS measurement is substantially more convenient and efficient as compared to all the other measurements of membrane property or performance. For example, constructing each surface potential curve in Figure 6.5A, B, and C require the fabrication of ten membrane samples and at least ten surface potential measurements (even without replicate). The same number of membrane samples and measurements are also required for constructing the permeability and rejection curves in Figure 6.5D, E, and F. All these series of measurements are time-consuming and laborious due to the requirements of fabricating multiple membranes and performing separate experiments on different membrane samples. In many cases when a membrane with the highest rejection is of primary interest, one can simply perform a single EIS measurement to identify the minimum deposition time for reaching surface saturation.

The EIS measurements do not only provide insights into the dynamics of polyelectrolyte adsorption in each step of LbL deposition, but the film resistance of the membrane also correlates with the membrane performance such as water permeance and solute rejection. Specifically, this film resistances, R_m, were extracted from the EIS spectra at the end of each deposition step (i.e., the final points of R_m in Figure 6.5A, B, and C). As discussed before, R_m quantifies the resistance of ion transport through the PEM layer and is dependent on both film thickness and surface charge. The small difference between R_m of the three PS-capped PEMs, which was nonetheless detectable by the four-electrode EIS setup, led to a substantial variation of water permeability and Na_2SO_4 rejection of the resulting NF membranes (Figure 6.6). Specifically, Na_2SO_4 rejection increases with increasing R_m, as more difficult ion transport results in higher salt rejection; whereas water permeability decreases substantially with increasing R_m, primarily due to the increase of PEM film thickness.

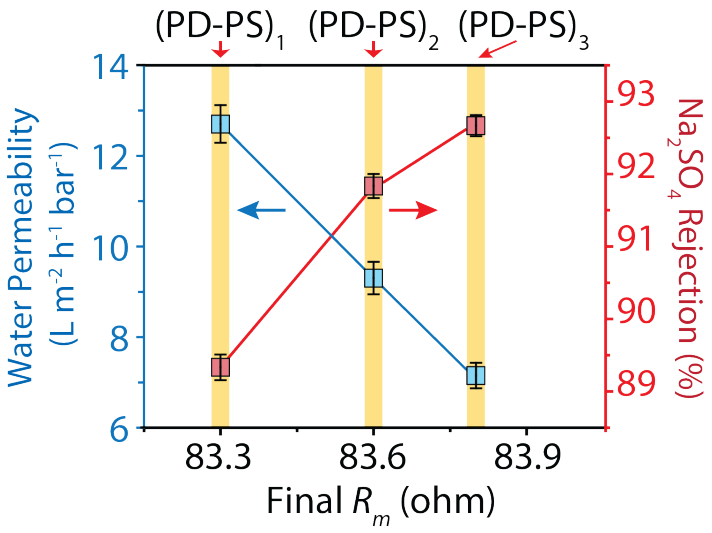

Figure 6.6 Dependence of water permeability and Na_2SO_4 rejection on film resistance, R_m, extracted from the EIS spectrum at the end of each deposition step for PS-capped PEM. Such an R_m was measured when polyelectrolyte adsorption reached equilibrium.

6.4.Conclusion

In summary, we have developed a novel approach for in-situ and non-destructive monitoring of the adsorption kinetics of polyelectrolytes in the process of fabricating PEM-NF membranes using LbL deposition. The four-electrode EIS system is capable of detecting subtle electro-chemical changes of the properties in the solution near the membrane surface (interfacial solution resistance) and in the PEM layer (film resistance). The measurements of these properties in the adsorption process can reflect the status of the adsorption process. Moreover, the film resistance extracted from EIS also correlates with the NF performance of the PEM membrane.

Although the EIS technique cannot provide spatial distribution of the PEM properties, the ability to in-situ monitor global kinetics of the dynamic growth of the polyelectrolyte thin film has substantial practical implications for fabricating NF membranes using LbL deposition of polyelectrolytes. One obvious application of this EIS-based monitoring technique, as shown in this study, is to identify the minimum adsorption time to achieve surface saturation, which is critical for achieving the most efficient fabrication without compromising membrane performance. This technique may also help us better understand how the kinetics of polyelectrolyte deposition and membrane performance is affected by fabrication conditions such as temperature, pH, ionic strength, and the addition of solvents. Specifically, the dynamic information extracted from EIS

can provide fundamental insights that cannot be derived from merely testing the performance of the fabricated membrane. Last but not least, this EIS-based monitoring approach applies not only to NF membrane fabrication but also to any process of modifying membrane surfaces and many other substrate surfaces with polyelectrolyte adsorption.

CHAPTER 7

CONCLUSION

To sum up, membrane-based processes represent a highly efficient approach to cope with the growing global freshwater scarcity. In general, membrane separations are fast and continuous as compared to chromatography-based separations, and more energy-efficient as compared to distillation-based separations. Nanofiltration is a low-pressure membrane-based process that is widely used in brackish water desalination and wastewater reclamation. With properties in between reverse osmosis (RO) and ultrafiltration (UF), NF membranes are potent in the separation of monovalent/divalent inorganic salts and small organic molecules (Molecular weight cutoff, MWCO > 200 Da) with several folds' water permeability higher than RO.

Increasing demands for more precise and more energy-efficient separations have stimulated the vigorous research interests in designing the next generation separation membranes to exceed the current trade-off between membrane permeance and selectivity in the current generation of separation membranes. Precise separations require membranes with highly uniform pore sizes to obtain precise molecular sieving and solute differentiation, which has been technically challenging to achieve. While the fabrication of highly precise membranes has been attempted recently using approaches such as stacking 2D nanomaterials or integrating aligned synthetic or biological channels, these approaches face substantial technical challenges for scalable fabrication of defect-free membranes.

On the contrary, TFC-PA based NF membranes have served the desalination industry for more than three decades because of high perm-selectivity, low separation cost, long membrane lifetime, and most importantly scalable fabrication. Therefore, TFC-PA-based NF membrane is an ideal candidate as the next-generation separation membrane for precise separation. However, the challenge for fabricating TFC-PA membranes suitable for solute/solute separations remains difficult to achieve uniform pore size distribution using IP, especially considering that IP is a very fast interfacial process involving multiple phenomena and is thus prone to generate heterogeneity. In chapter 2 and 3, we demonstrate that precise solute-solute separation can be achieved using polyamide membranes formed via surfactant-assembly regulated interfacial polymerization

(SARIP). The dynamic, self-assembled network of surfactants facilitates faster and more homogeneous diffusion of amine monomers across the water/hexane interface during interfacial polymerization, thereby forming a polyamide active layer with more uniform sub-nanometre pores compared to those formed via conventional interfacial polymerization. The polyamide membrane formed by SARIP exhibits highly size-dependent sieving of solutes, yielding a step-wise transition from low rejection to near-perfect rejection over a solute size range smaller than half Angstrom. SARIP represents an approach for the scalable fabrication of ultra-selective membranes with uniform nanopores for precise separation of ions and small solutes.

Another important direction of designing the next-generation separation membranes is to significantly enhance water permeability of membranes without sacrificing its selectivity, which potentially results in a drastic reduction of required membrane area, which leads to appreciable saving of capital cost and energy consumption. In chapter 4, we demonstrate for the first time that the intercalation of surfactant self-assemblies in the polyelectrolyte multilayer (PEM) can lead to significant performance enhancement (up to 300% increase of membrane permeability) of salt-rejecting dense NF membranes fabricated using Layer-by-Layer assembly of polyelectrolyte. More importantly, we seek molecular understandings of the unique function of surfactant micelles on both the adsorption kinetics and structure of the resulting surfactant-intercalated polyelectrolyte multilayer nanofiltration membranes. In chapter 5, we employ a similar concept to design a novel 'loose' nanofiltration using LbL deposition of surfactant micelles and polyelectrolyte for natural organic matter removal. The intercalation of surfactant micelles achieves up to 500% enhancement of LNF membrane permeability without compromising the rejection of humic acid.

In chapter 6, we develop a novel approach based on electrochemical impedance spectroscopy (EIS) for in-situ monitoring of the adsorption kinetics in preparing polyelectrolyte multilayer nanofiltration membranes using layer-by-layer (LbL) deposition. Unlike existing methods for monitoring adsorption kinetics, this new approach is non-destructive and applicable to various substrates (as it does not use the substrate as a sensor). The extent of polyelectrolyte deposition as probed by the EIS measurements is well corroborated by independent measurements of the membrane performance. Therefore, this EIS-based approach enables the optimization of membrane fabrication using LbL deposition by conveniently identifying the minimum deposition time required to attain surface saturation.

REFERENCES

(1) Elimelech, M.; Phillip, W. A. The Future of Seawater Desalination: Energy, Technology, and the Environment. *Science (80-.).* **2011**, *333* (6043), 712–717. https://doi.org/10.1126/science.1200488.

(2) Service, R. F. Desalination Freshens Up. *Science (80-.).* **2006**, *313* (5790), 1088–1090. https://doi.org/10.1126/science.313.5790.1088.

(3) Bohn, P. W.; Elimelech, M.; Georgiadis, J. G.; Mariñas, B. J.; Mayes, A. M.; Mayes, A. M. Science and Technology for Water Purification in the Coming Decades. In *Nanoscience and Technology: A Collection of Reviews from Nature Journals*; World Scientific, 2009; pp 337–346. https://doi.org/10.1142/9789814287005_0035.

(4) Lin, S. Energy Efficiency of Desalination: Fundamental Insights from Intuitive Interpretation. *Environ. Sci. Technol.* **2020**. https://doi.org/10.1021/acs.est.9b04788.

(5) Van der Bruggen, B.; Vandecasteele, C. Distillation vs. Membrane Filtration: Overview of Process Evolutions in Seawater Desalination. *Desalination* **2002**, *143* (3), 207–218. https://doi.org/10.1016/S0011-9164(02)00259-X.

(6) Fritzmann, C.; Löwenberg, J.; Wintgens, T.; Melin, T. State-of-the-Art of Reverse Osmosis Desalination. *Desalination* **2007**, *216* (1–3), 1–76. https://doi.org/10.1016/j.desal.2006.12.009.

(7) Petersen, R. J. Composite Reverse Osmosis and Nanofiltration Membranes. *Journal of Membrane Science*. Elsevier August 12, 1993, pp 81–150. https://doi.org/10.1016/0376-7388(93)80014-O.

(8) Strathmann, H. Electrodialysis, a Mature Technology with a Multitude of New Applications. *Desalination* **2010**, *264* (3), 268–288. https://doi.org/10.1016/j.desal.2010.04.069.

(9) Suss, M. E.; Porada, S.; Sun, X.; Biesheuvel, P. M.; Yoon, J.; Presser, V. Water Desalination via Capacitive Deionization: What Is It and What Can We Expect from It? *Energy Environ. Sci.* **2015**, *8* (8), 2296–2319. https://doi.org/10.1039/c5ee00519a.

(10) Marchetti, P.; Jimenez Solomon, M. F.; Szekely, G.; Livingston, A. G. Molecular Separation with Organic Solvent Nanofiltration: A Critical Review. *Chem. Rev.* **2014**, *114* (21), 10735–10806. https://doi.org/10.1021/cr500006j.

(11) Ulvestad, U.; Singer, A.; Clark, J. N.; Cho, H. M.; Kim, J. W.; Harder, R.; Maser, J.; Meng, Y. S.; Shpyrko, O. G. Topological Defect Dynamics in Operando Battery Nanoparticles. *Science (80-.).* **2015**, *348* (6241), 1344–1347. https://doi.org/10.1126/science.aaa1313.

(12) Park, H. B.; Kamcev, J.; Robeson, L. M.; Elimelech, M.; Freeman, B. D. Maximizing the Right Stuff: The Trade-off between Membrane Permeability and Selectivity. *Science (80-.).* **2017**, *356* (6343), 1138–1148. https://doi.org/10.1126/science.aab0530.

(13) Baker, R. W. *Membrane Technology and Applications*; John Wiley & Sons, 2012. https://doi.org/10.1002/9781118359686.

(14) Brehant, A.; Bonnelye, V.; Perez, M. Comparison of MF/UF Pretreatment with Conventional Filtration Prior to RO Membranes for Surface Seawater Desalination. *Desalination* **2002**, *144* (1–3), 353–360. https://doi.org/10.1016/S0011-9164(02)00343-0.

(15) Shaffer, D. L.; Yip, N. Y.; Gilron, J.; Elimelech, M. Seawater Desalination for Agriculture by Integrated Forward and Reverse Osmosis: Improved Product Water Quality for

Potentially Less Energy. *J. Memb. Sci.* **2012**, *415–416*, 1–8. https://doi.org/10.1016/j.memsci.2012.05.016.
(16) Nagasawa, H.; Iizuka, A.; Yamasaki, A.; Yanagisawa, Y. Boron Removal from Aqueous Solution by Bipolar Electrodialysis. *AIChE Annu. Meet. Conf. Proc.* **2008**, *223* (1–3), 1–9.
(17) Malaeb, L.; Ayoub, G. M. Reverse Osmosis Technology for Water Treatment: State of the Art Review. *Desalination* **2011**, *267* (1), 1–8. https://doi.org/10.1016/j.desal.2010.09.001.
(18) Uchymiak, M.; Lyster, E.; Glater, J.; Cohen, Y. Kinetics of Gypsum Crystal Growth on a Reverse Osmosis Membrane. *J. Memb. Sci.* **2008**, *314* (1–2), 163–172. https://doi.org/10.1016/j.memsci.2008.01.041.
(19) Mohammad, A. W.; Teow, Y. H.; Ang, W. L.; Chung, Y. T.; Oatley-Radcliffe, D. L.; Hilal, N. Nanofiltration Membranes Review: Recent Advances and Future Prospects. *Desalination* **2015**, *356*, 226–254. https://doi.org/10.1016/j.desal.2014.10.043.
(20) Hilal, N.; Al-Zoubi, H.; Darwish, N. A.; Mohammad, A. W.; Abu Arabi, M. A Comprehensive Review of Nanofiltration Membranes: Treatment, Pretreatment, Modelling, and Atomic Force Microscopy. *Desalination* **2004**, *170* (3), 281–308. https://doi.org/10.1016/j.desal.2004.01.007.
(21) Gleick, P. H. Global Freshwater Resources: Soft-Path Solutions for the 21st Century. *Science (80-.).* **2003**, *302* (5650), 1524–1528. https://doi.org/10.1126/science.1089967.
(22) Mekonnen, M. M.; Hoekstra, A. Y. Sustainability: Four Billion People Facing Severe Water Scarcity. *Sci. Adv.* **2016**, *2* (2), e1500323. https://doi.org/10.1126/sciadv.1500323.
(23) Walha, K.; Amar, R. Ben; Firdaous, L.; Quéméneur, F.; Jaouen, P. Brackish Groundwater Treatment by Nanofiltration, Reverse Osmosis and Electrodialysis in Tunisia: Performance and Cost Comparison. *Desalination* **2007**, *207* (1–3), 95–106. https://doi.org/10.1016/j.desal.2006.03.583.
(24) Setiawan, L.; Shi, L.; Wang, R. Dual Layer Composite Nanofiltration Hollow Fiber Membranes for Low-Pressure Water Softening. *Polymer (Guildf).* **2014**, *55* (6), 1367–1374. https://doi.org/10.1016/j.polymer.2013.12.032.
(25) Tang, C.; Chen, V. Nanofiltration of Textile Wastewater for Water Reuse. *Desalination* **2002**, *143* (1), 11–20. https://doi.org/10.1016/S0011-9164(02)00216-3.
(26) Van Der Bruggen, B.; Vandecasteele, C.; Van Gestel, T.; Doyen, W.; Leysen, R. A Review of Pressure-Driven Membrane Processes in Wastewater Treatment and Drinking Water Production. *Environ. Prog.* **2003**, *22* (1), 46–56. https://doi.org/10.1002/ep.670220116.
(27) Van Der Bruggen, B.; Vandecasteele, C. Removal of Pollutants from Surface Water and Groundwater by Nanofiltration: Overview of Possible Applications in the Drinking Water Industry. *Environ. Pollut.* **2003**, *122* (3), 435–445. https://doi.org/10.1016/S0269-7491(02)00308-1.
(28) Fernandes, P. A.; Natália, M.; Cordeiro, D. S.; Gomes, J. A. N. F. Influence of Ion Size and Charge in Ion Transfer Processes Across a Liquid|Liquid Interface. *J. Phys. Chem. B* **2000**, *104* (10), 2278–2286. https://doi.org/10.1021/jp993045z.
(29) Van Der Bruggen, B.; Koninckx, A.; Vandecasteele, C. Separation of Monovalent and Divalent Ions from Aqueous Solution by Electrodialysis and Nanofiltration. *Water Res.* **2004**, *38* (5), 1347–1353. https://doi.org/10.1016/j.watres.2003.11.008.
(30) Childress, A. E.; Elimelech, M. Relating Nanofiltration Membrane Performance to Membrane Charge (Electrokinetic) Characteristics. *Environ. Sci. Technol.* **2000**, *34* (17), 3710–3716. https://doi.org/10.1021/es0008620.

(31) Radjenović, J.; Petrović, M.; Ventura, F.; Barceló, D. Rejection of Pharmaceuticals in Nanofiltration and Reverse Osmosis Membrane Drinking Water Treatment. *Water Res.* **2008**, *42* (14), 3601–3610. https://doi.org/10.1016/j.watres.2008.05.020.
(32) Logan, B. E.; Elimelech, M. Membrane-Based Processes for Sustainable Power Generation Using Water. *Nature* **2012**, *488* (7411), 313–319. https://doi.org/10.1038/nature11477.
(33) Lee, K. P.; Arnot, T. C.; Mattia, D. A Review of Reverse Osmosis Membrane Materials for Desalination-Development to Date and Future Potential. *J. Memb. Sci.* **2011**, *370* (1–2), 1–22. https://doi.org/10.1016/j.memsci.2010.12.036.
(34) Lau, W. J.; Ismail, A. F.; Misdan, N.; Kassim, M. A. A Recent Progress in Thin Film Composite Membrane: A Review. *Desalination* **2012**, *287*, 190–199. https://doi.org/10.1016/j.desal.2011.04.004.
(35) Wittbecker, E. L.; Morgan, P. W. Interfacial Polycondensation. I. *J. Polym. Sci.* **1959**, *40* (137), 289–297.
(36) Morgan, P. W. Interfacial Polycondensation. 11. Fundamentals of Polymer Formation. *J. Polym. Sci.* **1959**, *327* (September 1958).
(37) Liang, Y.; Zhu, Y.; Liu, C.; Lee, K. R.; Hung, W. S.; Wang, Z.; Li, Y.; Elimelech, M.; Jin, J.; Lin, S. Polyamide Nanofiltration Membrane with Highly Uniform Sub-Nanometre Pores for Sub-1 Å Precision Separation. *Nat. Commun.* **2020**, *11* (1), 1–9. https://doi.org/10.1038/s41467-020-15771-2.
(38) Ouyang, L.; Malaisamy, R.; Bruening, M. L. Multilayer Polyelectrolyte Films as Nanofiltration Membranes for Separating Monovalent and Divalent Cations. *J. Memb. Sci.* **2008**, *310* (1–2), 76–84. https://doi.org/10.1016/j.memsci.2007.10.031.
(39) Stanton, B. W.; Harris, J. J.; Miller, M. D.; Bruening, M. L. Ultrathin, Multilayered Polyelectrolyte Films as Nanofiltration Membranes. *Langmuir* **2003**, *19* (17), 7038–7042. https://doi.org/10.1021/la034603a.
(40) Borges, J.; Mano, J. F. Molecular Interactions Driving the Layer-by-Layer Assembly of Multilayers. *Chem. Rev.* **2014**, *114* (18), 8883–8942. https://doi.org/10.1021/cr400531v.
(41) Ariga, K.; Hill, J. P.; Ji, Q. Layer-by-Layer Assembly as a Versatile Bottom-up Nanofabrication Technique for Exploratory Research and Realistic Application. *Phys. Chem. Chem. Phys.* **2007**, *9* (19), 2319–2340. https://doi.org/10.1039/b700410a.
(42) Bertrand, P.; Jonas, A.; Laschewsky, A.; Legras, R. Ultrathin Polymer Coatings by Complexation of Polyelectrolytes at Interfaces: Suitable Materials, Structure and Properties. *Macromol. Rapid Commun.* **2000**, *21* (7), 319–348. https://doi.org/10.1002/(SICI)1521-3927(20000401)21:7<319::AID-MARC319>3.0.CO;2-7.
(43) Penfold, N. J. W.; Parnell, A. J.; Molina, M.; Verstraete, P.; Smets, J.; Armes, S. P. Layer-By-Layer Self-Assembly of Polyelectrolytic Block Copolymer Worms on a Planar Substrate. *Langmuir* **2017**, *33* (50), 14425–14436. https://doi.org/10.1021/acs.langmuir.7b03571.
(44) Kujawa, P.; Moraille, P.; Sanchez, J.; Badia, A.; Winnik, F. M. Effect of Molecular Weight on the Exponential Growth and Morphology of Hyaluronan/Chitosan Multilayers: A Surface Plasmon Resonance Spectroscopy and Atomic Force Microscopy Investigation. *J. Am. Chem. Soc.* **2005**, *127* (25), 9224–9234. https://doi.org/10.1021/ja044385n.
(45) Deng, H. Y.; Xu, Y. Y.; Zhu, B. K.; Wei, X. Z.; Liu, F.; Cui, Z. Y. Polyelectrolyte Membranes Prepared by Dynamic Self-Assembly of Poly (4-Styrenesulfonic Acid-Co-

Maleic Acid) Sodium Salt (PSSMA) for Nanofiltration (I). *J. Memb. Sci.* **2008**, *323* (1), 125–133. https://doi.org/10.1016/j.memsci.2008.06.028.
(46) Dubas, S. T.; Schlenoff, J. B. Factors Controlling the Growth of Polyelectrolyte Multilayers. *Macromolecules* **1999**, *32* (24), 8153–8160. https://doi.org/10.1021/ma981927a.
(47) V. Klitzing, R. Internal Structure of Polyelectrolyte Multilayer Assemblies. *Phys. Chem. Chem. Phys.* **2006**, *8* (43), 5012–5033. https://doi.org/10.1039/b607760a.
(48) Lösche, M.; Schmitt, J.; Decher, G.; Bouwman, W. G.; Kjaer, K. Detailed Structure of Molecularly Thin Polyelectrolyte Multilayer Films on Solid Substrates as Revealed by Neutron Reflectometry. *Macromolecules* **1998**, *31* (25), 8893–8906. https://doi.org/10.1021/ma980910p.
(49) Choi, J.; Rubner, M. F. Influence of the Degree of Ionization on Weak Polyelectrolyte Multilayer Assembly. *Macromolecules* **2005**, *38* (1), 116–124. https://doi.org/10.1021/ma048596o.
(50) Schönhoff, M.; Bieker, P. Linear and Exponential Growth Regimes of Multilayers of Weak Polyelectrolytes in Dependence on PH. *Macromolecules* **2010**, *43* (11), 5052–5059. https://doi.org/10.1021/ma1007489.
(51) Shiratori, S. S.; Rubner, M. F. PH-Dependent Thickness Behavior of Sequentially Adsorbed Layers of Weak Polyelectrolytes. *Macromolecules* **2000**, *33* (11), 4213–4219. https://doi.org/10.1021/ma991645q.
(52) Salomäki, M.; Vinokurov, I. A.; Kankare, J. Effect of Temperature on the Buildup of Polyelectrolyte Multilayers. *Langmuir* **2005**, *21* (24), 11232–11240. https://doi.org/10.1021/la051600k.
(53) Tan, H. L.; McMurdo, M. J.; Pan, G.; Van Patten, P. G. Temperature Dependence of Polyelectrolyte Multilayer Assembly. *Langmuir* **2003**, *19* (22), 9311–9314. https://doi.org/10.1021/la035094f.
(54) Liu, Y.; Zheng, S.; Gu, P.; Ng, A. J.; Wang, M.; Wei, Y.; Urban, J. J.; Mi, B. Graphene-Polyelectrolyte Multilayer Membranes with Tunable Structure and Internal Charge. *Carbon N. Y.* **2020**, *160*, 219–227. https://doi.org/10.1016/j.carbon.2019.12.092.
(55) Wang, M.; Wang, Z.; Wang, X.; Wang, S.; Ding, W.; Gao, C. Layer-by-Layer Assembly of Aquaporin z-Incorporated Biomimetic Membranes for Water Purification. *Environ. Sci. Technol.* **2015**, *49* (6), 3761–3768. https://doi.org/10.1021/es5056337.
(56) Werber, J. R.; Deshmukh, A.; Elimelech, M. The Critical Need for Increased Selectivity, Not Increased Water Permeability, for Desalination Membranes. *Environ. Sci. Technol. Lett.* **2016**, *3* (4), 112–120. https://doi.org/10.1021/acs.estlett.6b00050.
(57) Park, H. B.; Sagle, A. C.; McGrath, J. E.; Freeman, B. D. Water Permeability and Water/Salt Selectivity Tradeoff in Polymers for Desalination. *AIChE Annu. Meet. Conf. Proc.* **2008**, *369* (1–2), 130–138.
(58) Gin, D. L.; Noble, R. D. Designing the next Generation of Chemical Separation Membranes. *Science (80-.).* **2011**, *332* (6030), 674–676. https://doi.org/10.1126/science.1203771.
(59) Werber, J. R.; Osuji, C. O.; Elimelech, M. Materials for Next-Generation Desalination and Water Purification Membranes. *Nature Reviews Materials*. 2016. https://doi.org/10.1038/natrevmats.2016.18.
(60) Schäfer, A. I.; Fane, A. G.; Waite, T. D. Cost Factors and Chemical Pretreatment Effects in the Membrane Filtration of Waters Containing Natural Organic Matter. *Water Res.*

2001, *35* (6), 1509–1517. https://doi.org/10.1016/S0043-1354(00)00418-8.
(61) Song, Z.; Fathizadeh, M.; Huang, Y.; Chu, K. H.; Yoon, Y.; Wang, L.; Xu, W. L.; Yu, M. TiO2 Nanofiltration Membranes Prepared by Molecular Layer Deposition for Water Purification. *J. Memb. Sci.* **2016**, *510*, 72–78. https://doi.org/10.1016/j.memsci.2016.03.011.
(62) Alsohaimi, I. H.; Kumar, M.; Algamdi, M. S.; Khan, M. A.; Nolan, K.; Lawler, J. Antifouling Hybrid Ultrafiltration Membranes with High Selectivity Fabricated from Polysulfone and Sulfonic Acid Functionalized TiO2 Nanotubes. *Chem. Eng. J.* **2017**, *316*, 573–583. https://doi.org/10.1016/j.cej.2017.02.001.
(63) Guo, H.; Zhao, S.; Wu, X.; Qi, H. Fabrication and Characterization of TiO2/ZrO2 Ceramic Membranes for Nanofiltration. *Microporous Mesoporous Mater.* **2018**, *260*, 125–131. https://doi.org/10.1016/j.micromeso.2016.03.011.
(64) Yu, L.; Zhang, Y.; Wang, Y.; Zhang, H.; Liu, J. High Flux, Positively Charged Loose Nanofiltration Membrane by Blending with Poly (Ionic Liquid) Brushes Grafted Silica Spheres. *J. Hazard. Mater.* **2015**, *287*, 373–383. https://doi.org/10.1016/j.jhazmat.2015.01.057.
(65) Puthai, W.; Kanezashi, M.; Nagasawa, H.; Wakamura, K.; Ohnishi, H.; Tsuru, T. Effect of Firing Temperature on the Water Permeability of SiO2-ZrO2 Membranes for Nanofiltration. *J. Memb. Sci.* **2016**, *497*, 348–356. https://doi.org/10.1016/j.memsci.2015.09.040.
(66) Ding, W.; Zhuo, H.; Bao, M.; Li, Y.; Lu, J. Fabrication of Organic-Inorganic Nanofiltration Membrane Using Ordered Stacking SiO2 Thin Film as Rejection Layer Assisted with Layer-by-Layer Method. *Chem. Eng. J.* **2017**, *330*, 337–344. https://doi.org/10.1016/j.cej.2017.07.159.
(67) Lee, S. Y.; Kim, H. J.; Patel, R.; Im, S. J.; Kim, J. H.; Min, B. R. Silver Nanoparticles Immobilized on Thin Film Composite Polyamide Membrane: Characterization, Nanofiltration, Antifouling Properties. *Polym. Adv. Technol.* **2007**, *18* (7), 562–568. https://doi.org/10.1002/pat.918.
(68) Andrade, P. F.; de Faria, A. F.; Oliveira, S. R.; Arruda, M. A. Z.; Gonçalves, M. do C. Improved Antibacterial Activity of Nanofiltration Polysulfone Membranes Modified with Silver Nanoparticles. *Water Res.* **2015**, *81*, 333–342. https://doi.org/10.1016/j.watres.2015.05.006.
(69) Nagata, S.; Kokado, K.; Sada, K. Metal-Organic Framework Tethering PNIPAM for ON-OFF Controlled Release in Solution. *Chem. Commun.* **2015**, *51* (41), 8614–8617. https://doi.org/10.1039/c5cc02339d.
(70) Yang, L.; Wang, Z.; Zhang, J. Zeolite Imidazolate Framework Hybrid Nanofiltration (NF) Membranes with Enhanced Permselectivity for Dye Removal. *J. Memb. Sci.* **2017**, *532*, 76–86. https://doi.org/10.1016/j.memsci.2017.03.014.
(71) Peng, Y.; Li, Y.; Ban, Y.; Jin, H.; Jiao, W.; Liu, X.; Yang, W. Metal- Organic Framework Nanosheets as Building Blocks for Molecular Sieving Membranes. *Science (80-.).* **2014**, *346* (6215), 1356–1359. https://doi.org/10.1126/science.1254227.
(72) Zhao, S.; Song, P.; Wang, Z.; Zhu, H. The PEGylation of Plant Polyphenols/Polypeptide-Mediated Loose Nanofiltration Membrane for Textile Wastewater Treatment and Antibacterial Application. *J. Taiwan Inst. Chem. Eng.* **2018**, *82*, 42–55. https://doi.org/10.1016/j.jtice.2017.11.005.
(73) You, X.; Ma, T.; Su, Y.; Wu, H.; Wu, M.; Cai, H.; Sun, G.; Jiang, Z. Enhancing the

Permeation Flux and Antifouling Performance of Polyamide Nanofiltration Membrane by Incorporation of PEG-POSS Nanoparticles. *J. Memb. Sci.* **2017**, *540*, 454–463. https://doi.org/10.1016/j.memsci.2017.06.084.

(74) Panda, S. R.; De, S. Preparation, Characterization and Performance of ZnCl2 Incorporated Polysulfone (PSF)/Polyethylene Glycol (PEG) Blend Low Pressure Nanofiltration Membranes. *Desalination* **2014**, *347*, 52–65. https://doi.org/10.1016/j.desal.2014.05.030.

(75) Zhu, J.; Wang, J.; Uliana, A. A.; Tian, M.; Zhang, Y.; Zhang, Y.; Volodin, A.; Simoens, K.; Yuan, S.; Li, J.; Lin, J.; Bernaerts, K.; Van Der Bruggen, B. Mussel-Inspired Architecture of High-Flux Loose Nanofiltration Membrane Functionalized with Antibacterial Reduced Graphene Oxide-Copper Nanocomposites. *ACS Appl. Mater. Interfaces* **2017**, *9* (34), 28990–29001. https://doi.org/10.1021/acsami.7b05930.

(76) Zhang, S.; Fu, F.; Chung, T. S. Substrate Modifications and Alcohol Treatment on Thin Film Composite Membranes for Osmotic Power. *Chem. Eng. Sci.* **2013**, *87*, 40–50. https://doi.org/10.1016/j.ces.2012.09.014.

(77) Yang, H. C.; Hou, J.; Wan, L. S.; Chen, V.; Xu, Z. K. Janus Membranes with Asymmetric Wettability for Fine Bubble Aeration. *Adv. Mater. Interfaces* **2016**, *3* (9), 1–5. https://doi.org/10.1002/admi.201500774.

(78) Chen, W.; Su, Y.; Peng, J.; Dong, Y.; Zhao, X.; Jiang, Z. Engineering a Robust, Versatile Amphiphilic Membrane Surface through Forced Surface Segregation for Ultralow Flux-Decline. *Adv. Funct. Mater.* **2011**, *21* (1), 191–198. https://doi.org/10.1002/adfm.201001384.

(79) Cho, K. L.; Hill, A. J.; Caruso, F.; Kentish, S. E. Chlorine Resistant Glutaraldehyde Crosslinked Polyelectrolyte Multilayer Membranes for Desalination. *Adv. Mater.* **2015**, *27* (17), 2791–2796. https://doi.org/10.1002/adma.201405783.

(80) Cheng, X. Q.; Liu, Y.; Guo, Z.; Shao, L. Nanofiltration Membrane Achieving Dual Resistance to Fouling and Chlorine for "Green" Separation of Antibiotics. *J. Memb. Sci.* **2015**, *493*, 156–166. https://doi.org/10.1016/j.memsci.2015.06.048.

(81) Wang, Z.; Wang, Z.; Lin, S.; Jin, H.; Gao, S.; Zhu, Y.; Jin, J. Nanoparticle-Templated Nanofiltration Membranes for Ultrahigh Performance Desalination. *Nat. Commun.* **2018**, *9* (1), 1–9. https://doi.org/10.1038/s41467-018-04467-3.

(82) Wang, L.; Fang, M.; Liu, J.; He, J.; Li, J.; Lei, J. Layer-by-Layer Fabrication of High-Performance Polyamide/ZIF-8 Nanocomposite Membrane for Nanofiltration Applications. *ACS Appl. Mater. Interfaces* **2015**, *7* (43), 24082–24093. https://doi.org/10.1021/acsami.5b07128.

(83) Bao, Y.; Chen, Y.; Lim, T. T.; Wang, R.; Hu, X. A Novel Metal–Organic Framework (MOF)–Mediated Interfacial Polymerization for Direct Deposition of Polyamide Layer on Ceramic Substrates for Nanofiltration. *Adv. Mater. Interfaces* **2019**, *6* (9), 1900132. https://doi.org/10.1002/admi.201900132.

(84) Fang, S.-Y.; Zhang, P.; Gong, J.-L.; Tang, L.; Zeng, G.-M.; Song, B.; Cao, W.-C.; Li, J.; Ye, J. Construction of Highly Water-Stable Metal-Organic Framework UiO-66 Thin-Film Composite Membrane for Dyes and Antibiotics Separation. *Chem. Eng. J.* **2020**, *385*, 123400.

(85) Karan, S.; Jiang, Z.; Livingston, A. G. Sub-10 Nm Polyamide Nanofilms with Ultrafast Solvent Transport for Molecular Separation. *Science (80-.).* **2015**, *348* (6241), 1347–1351. https://doi.org/10.1126/science.aaa5058.

(86) Zhao, S.; Zhu, H.; Wang, Z.; Song, P.; Ban, M.; Song, X. A Loose Hybrid Nanofiltration

Membrane Fabricated via Chelating-Assisted in-Situ Growth of Co/Ni LDHs for Dye Wastewater Treatment. *Chem. Eng. J.* **2018**, *353*, 460–471. https://doi.org/10.1016/j.cej.2018.07.081.
(87) Apel, P. Track Etching Technique in Membrane Technology. *Radiat. Meas.* **2001**, *34* (1–6), 559–566. https://doi.org/10.1016/S1350-4487(01)00228-1.
(88) Pendergast, M. M.; Hoek, E. M. V. A Review of Water Treatment Membrane Nanotechnologies. *Energy Environ. Sci.* **2011**, *4* (6), 1946–1971. https://doi.org/10.1039/c0ee00541j.
(89) Pronk, W.; Palmquist, H.; Biebow, M.; Boller, M. Nanofiltration for the Separation of Pharmaceuticals from Nutrients in Source-Separated Urine. *Water Res.* **2006**, *40* (7), 1405–1412. https://doi.org/10.1016/j.watres.2006.01.038.
(90) Liu, K.; Feng, J.; Kis, A.; Radenovic, A. Atomically Thin Molybdenum Disulfide Nanopores with High Sensitivity for Dna Translocation. *ACS Nano* **2014**, *8* (3), 2504–2511. https://doi.org/10.1021/nn406102h.
(91) Ren, Y.; Zhu, J.; Cong, S.; Wang, J.; Van der Bruggen, B.; Liu, J.; Zhang, Y. High Flux Thin Film Nanocomposite Membranes Based on Porous Organic Polymers for Nanofiltration. *J. Memb. Sci.* **2019**, *585* (40), 19–28. https://doi.org/10.1016/j.memsci.2019.05.022.
(92) Mi, B. Graphene Oxide Membranes for Ionic and Molecular Sieving. *Science (80-.).* **2014**, *343* (6172), 740–742. https://doi.org/10.1126/science.1250247.
(93) Yang, Q.; Su, Y.; Chi, C.; Cherian, C. T.; Huang, K.; Kravets, V. G.; Wang, F. C.; Zhang, J. C.; Pratt, A.; Grigorenko, A. N.; Guinea, F.; Geim, A. K.; Nair, R. R. Ultrathin Graphene-Based Membrane with Precise Molecular Sieving and Ultrafast Solvent Permeation. *Nat. Mater.* **2017**, *16* (12), 1198–1202. https://doi.org/10.1038/nmat5025.
(94) Joshi, R. K.; Carbone, P.; Wang, F. C.; Kravets, V. G.; Su, Y.; Grigorieva, I. V.; Wu, H. A.; Geim, A. K.; Nair, R. R. Precise and Ultrafast Molecular Sieving through Graphene Oxide Membranes. *Science (80-.).* **2014**, *343* (6172), 752–754. https://doi.org/10.1126/science.1245711.
(95) Lin, Y.; Zhou, B.; Fernando, K. A. S.; Liu, P.; Allard, L. F.; Sun, Y. P. Polymeric Carbon Nanocomposites from Carbon Nanotubes Functionalized with Matrix Polymer. *Macromolecules* **2003**, *36* (19), 7199–7204. https://doi.org/10.1021/ma0348876.
(96) Sung, J. H.; Kim, H. S.; Jin, H. J.; Choi, H. J.; Chin, I. J. Nanofibrous Membranes Prepared by Multiwalled Carbon Nanotube/Poly(Methyl Methacrylate) Composites. *Macromolecules* **2004**, *37* (26), 9899–9902. https://doi.org/10.1021/ma048355g.
(97) Hu, X. B.; Chen, Z.; Tang, G.; Hou, J. L.; Li, Z. T. Single-Molecular Artificial Transmembrane Water Channels. *J. Am. Chem. Soc.* **2012**, *134* (20), 8384–8387. https://doi.org/10.1021/ja302292c.
(98) Kumar, M.; Grzelakowski, M.; Zilles, J.; Clark, M.; Meier, W. Highly Permeable Polymeric Membranes Based on the Incorporation of the Functional Water Channel Protein Aquaporin Z. *Proc. Natl. Acad. Sci. U. S. A.* **2007**, *104* (52), 20719–20724. https://doi.org/10.1073/pnas.0708762104.
(99) Freger, V. Nanoscale Heterogeneity of Polyamide Membranes Formed by Interfacial Polymerization. *Langmuir* **2003**, *19* (11), 4791–4797. https://doi.org/10.1021/la020920q.
(100) Feng, X.; Imran, Q.; Zhang, Y.; Sixdenier, L.; Lu, X.; Kaufman, G.; Gabinet, U.; Kawabata, K.; Elimelech, M.; Osuji, C. O. Precise Nanofiltration in a Fouling-Resistant Self-Assembled Membrane with Water-Continuous Transport Pathways. *Sci. Adv.* **2019**, *5*

(8), eaav9308. https://doi.org/10.1126/sciadv.aav9308.
(101) Yang, Y.; Yang, X.; Liang, L.; Gao, Y.; Cheng, H.; Li, X.; Zou, M.; Cao, A.; Ma, R.; Yuan, Q.; Duan, X. Large-Area Graphene-Nanomesh/ Carbon-Nanotube Hybrid Membranes for Ionic and Molecular Nanofiltration. *Science (80-.).* **2019**, *364* (6445), 1057–1062. https://doi.org/10.1126/science.aau5321.
(102) Hinds, B. J.; Chopra, N.; Rantell, T.; Andrews, R.; Gavalas, V.; Bachas, L. G. Aligned Multiwalled Carbon Nanotube Membranes. *Science (80-.).* **2004**, *303* (5654), 62–65. https://doi.org/10.1126/science.1092048.
(103) Chen, L.; Shi, G.; Shen, J.; Peng, B.; Zhang, B.; Wang, Y.; Bian, F.; Wang, J.; Li, D.; Qian, Z.; Xu, G.; Liu, G.; Zeng, J.; Zhang, L.; Yang, Y.; Zhou, G.; Wu, M.; Jin, W.; Li, J.; Fang, H. Ion Sieving in Graphene Oxide Membranes via Cationic Control of Interlayer Spacing. *Nature* **2017**, *550* (7676), 1–4. https://doi.org/10.1038/nature24044.
(104) Werber, J. R.; Elimelech, M. Permselectivity Limits of Biomimetic Desalination Membranes. *Sci. Adv.* **2018**, *4* (6), eaar8266. https://doi.org/10.1126/sciadv.aar8266.
(105) Ritt, C. L.; Werber, J. R.; Deshmukh, A.; Elimelech, M. Monte Carlo Simulations of Framework Defects in Layered Two-Dimensional Nanomaterial Desalination Membranes: Implications for Permeability and Selectivity. *Environ. Sci. Technol.* **2019**, *53* (11), 6214–6224. https://doi.org/10.1021/acs.est.8b06880.
(106) Morgan, P. W.; Kwolek, S. L. Interfacial Polycondensation. II. Fundamentals of Polymer Formation at Liquid Interfaces. *J. Polym. Sci. Part A Polym. Chem.* **1996**, *34* (4), 531–559. https://doi.org/10.1002/pola.1996.816.
(107) Freger, V. Kinetics of Film Formation by Interfacial Polycondensation. *Langmuir* **2005**, *21* (5), 1884–1894. https://doi.org/10.1021/la048085v.
(108) Tan, Z.; Chen, S.; Peng, X.; Zhang, L.; Gao, C. Polyamide Membranes with Nanoscale Turing Structures for Water Purification. *Science (80-.).* **2018**, *360* (6388), 518–521. https://doi.org/10.1126/science.aar6308.
(109) Chowdhury, M. R.; Steffes, J.; Huey, B. D.; McCutcheon, J. R. 3D Printed Polyamide Membranes for Desalination. *Science (80-.).* **2018**, *361* (6403), 682–686. https://doi.org/10.1126/science.aar2122.
(110) Mansourpanah, Y.; Madaeni, S. S.; Rahimpour, A. Fabrication and Development of Interfacial Polymerized Thin-Film Composite Nanofiltration Membrane Using Different Surfactants in Organic Phase; Study of Morphology and Performance. *J. Memb. Sci.* **2009**, *343* (1–2), 219–228. https://doi.org/10.1016/j.memsci.2009.07.033.
(111) Hung, W. S.; Lo, C. H.; Cheng, M. L.; Chen, H.; Liu, G.; Chakka, L.; Nanda, D.; Tung, K. L.; Huang, S. H.; Lee, K. R.; Lai, J. Y.; Sun, Y. M.; Yu, C. C.; Zhang, R.; Jean, Y. C. Polymeric Membrane Studied Using Slow Positron Beam. *Appl. Surf. Sci.* **2008**, *255* (1), 201–204. https://doi.org/10.1016/j.apsusc.2008.05.240.
(112) Chen, G. E.; Liu, Y. J.; Xu, Z. L.; Tang, Y. J.; Huang, H. H.; Sun, L. Fabrication and Characterization of a Novel Nanofiltration Membrane by the Interfacial Polymerization of 1,4-Diaminocyclohexane (DCH) and Trimesoyl Chloride (TMC). *RSC Adv.* **2015**, *5* (51), 40742–40752. https://doi.org/10.1039/c5ra02560e.
(113) Duong, P. H. H.; Anjum, D. H.; Peinemann, K. V.; Nunes, S. P. Thin Porphyrin Composite Membranes with Enhanced Organic Solvent Transport. *J. Memb. Sci.* **2018**, *563*, 684–693. https://doi.org/10.1016/j.memsci.2018.04.038.
(114) Cui, Y.; Liu, X. Y.; Chung, T. S. Ultrathin Polyamide Membranes Fabricated from Free-Standing Interfacial Polymerization: Synthesis, Modifications, and Post-Treatment. *Ind.*

Eng. Chem. Res. **2017**, *56* (2), 513–523. https://doi.org/10.1021/acs.iecr.6b04283.
(115) Saha, N. K.; Joshi, S. V. Performance Evaluation of Thin Film Composite Polyamide Nanofiltration Membrane with Variation in Monomer Type. *J. Memb. Sci.* **2009**, *342* (1–2), 60–69. https://doi.org/10.1016/j.memsci.2009.06.025.
(116) Azarteimour, F.; Amirinejad, M.; Parvini, M.; Yarvali, M. Organic Phase Addition of Anionic/Non-Ionic Surfactants to Poly(Paraphenyleneterephthalamide) Thin Film Composite Nanofiltration Membranes. *Chem. Eng. Process. Process Intensif.* **2016**, *106*, 13–25. https://doi.org/10.1016/j.cep.2015.11.016.
(117) Chen, H.; Hung, W. S.; Lo, C. H.; Huang, S. H.; Cheng, M. L.; Liu, G.; Lee, K. R.; Lai, J. Y.; Sun, Y. M.; Hu, C. C.; Suzuki, R.; Ohdaira, T.; Oshima, N.; Jean, Y. C. Free-Volume Depth Profile of Polymeric Membranes Studied by Positron Annihilation Spectroscopy: Layer Structure from Interfacial Polymerization. *Macromolecules* **2007**, *40* (21), 7542–7557. https://doi.org/10.1021/ma071493w.
(118) Liu, T. Y.; Bian, L. X.; Yuan, H. G.; Pang, B.; Lin, Y. K.; Tong, Y.; Van der Bruggen, B.; Wang, X. L. Fabrication of a High-Flux Thin Film Composite Hollow Fiber Nanofiltration Membrane for Wastewater Treatment. *J. Memb. Sci.* **2015**, *478*, 25–36. https://doi.org/10.1016/j.memsci.2014.12.029.
(119) Tang, C. Y.; Kwon, Y. N.; Leckie, J. O. Effect of Membrane Chemistry and Coating Layer on Physiochemical Properties of Thin Film Composite Polyamide RO and NF Membranes. I. FTIR and XPS Characterization of Polyamide and Coating Layer Chemistry. *Desalination* **2009**, *242* (1–3), 149–167. https://doi.org/10.1016/j.desal.2008.04.003.
(120) Donnan, F. G. Theory of Membrane Equilibria and Membrane Potentials in the Presence of Non-Dialysing Electrolytes. A Contribution to Physical-Chemical Physiology. *J. Memb. Sci.* **1995**, *100* (1), 45–55. https://doi.org/10.1016/0376-7388(94)00297-C.
(121) Peeters, J. M. M.; Boom, J. P.; Mulder, M. H. V.; Strathmann, H. Retention Measurements of Nanofiltration Membranes with Electrolyte Solutions. *J. Memb. Sci.* **1998**, *145* (2), 199–209. https://doi.org/10.1016/S0376-7388(98)00079-9.
(122) Wu, D.; Huang, Y.; Yu, S.; Lawless, D.; Feng, X. Thin Film Composite Nanofiltration Membranes Assembled Layer-by-Layer via Interfacial Polymerization from Polyethylenimine and Trimesoyl Chloride. *J. Memb. Sci.* **2014**, *472*, 141–153. https://doi.org/10.1016/j.memsci.2014.08.055.
(123) Jiang, C.; Tian, L.; Zhai, Z.; Shen, Y.; Dong, W.; He, M.; Hou, Y.; Niu, Q. J. Thin-Film Composite Membranes with Aqueous Template-Induced Surface Nanostructures for Enhanced Nanofiltration. *J. Memb. Sci.* **2019**, *589* (July), 117244. https://doi.org/10.1016/j.memsci.2019.117244.
(124) Cadotte, J. E.; Petersen, R. J.; Larson, R. E.; Erickson, E. E. A New Thin-Film Composite Seawater Reverse Osmosis Membrane. *Desalination* **1980**, *32* (C), 25–31. https://doi.org/10.1016/S0011-9164(00)86003-8.
(125) Mansourpanah, Y.; Alizadeh, K.; Madaeni, S. S.; Rahimpour, A.; Soltani Afarani, H. Using Different Surfactants for Changing the Properties of Poly(Piperazineamide) TFC Nanofiltration Membranes. *Desalination* **2011**, *271* (1–3), 169–177. https://doi.org/10.1016/j.desal.2010.12.026.
(126) Dinarvand, R.; Moghadam, S. H.; Sheikhi, A.; Atyabi, F. Effect of Surfactant HLB and Different Formulation Variables on the Properties of Poly-D,L-Lactide Microspheres of Naltrexone Prepared by Double Emulsion Technique. *J. Microencapsul.* **2005**, *22* (2),

139–151. https://doi.org/10.1080/02652040400026392.
(127) Boyd, J.; Parkinson, C.; Sherman, P. Factors Affecting Emulsion Stability, and the HLB Concept. *J. Colloid Interface Sci.* **1972**, *41* (2), 359–370. https://doi.org/10.1016/0021-9797(72)90122-1.
(128) Schott, H. Hydrophilic–Lipophilic Balance, Solubility Parameter, and Oil–Water Partition Coefficient as Universal Parameters of Nonionic Surfactants. *J. Pharm. Sci.* **1995**, *84* (10), 1215–1222. https://doi.org/10.1002/jps.2600841014.
(129) Ng, L. Y.; Mohammad, A. W.; Ng, C. Y. A Review on Nanofiltration Membrane Fabrication and Modification Using Polyelectrolytes: Effective Ways to Develop Membrane Selective Barriers and Rejection Capability. *Adv. Colloid Interface Sci.* **2013**, *197–198*, 85–107. https://doi.org/10.1016/j.cis.2013.04.004.
(130) Boo, C.; Wang, Y.; Zucker, I.; Choo, Y.; Osuji, C. O.; Elimelech, M. High Performance Nanofiltration Membrane for Effective Removal of Perfluoroalkyl Substances at High Water Recovery. *Environ. Sci. Technol.* **2018**, *52* (13), 7279–7288. https://doi.org/10.1021/acs.est.8b01040.
(131) Washington, J. W.; Jenkins, T. M.; Rankin, K.; Naile, J. E. Decades-Scale Degradation of Commercial, Side-Chain, Fluorotelomer-Based Polymers in Soils and Water. *Environ. Sci. Technol.* **2015**, *49* (2), 915–923. https://doi.org/10.1021/es504347u.
(132) Choo, K. H.; Kwon, D. J.; Lee, K. W.; Choi, S. J. Selective Removal of Cobalt Species Using Nanofiltration Membranes. *Environ. Sci. Technol.* **2002**, *36* (6), 1330–1336. https://doi.org/10.1021/es010724q.
(133) Luo, J.; Ding, L.; Wan, Y.; Paullier, P.; Jaffrin, M. Y. Application of NF-RDM (Nanofiltration Rotating Disk Membrane) Module under Extreme Hydraulic Conditions for the Treatment of Dairy Wastewater. *Chem. Eng. J.* **2010**, *163* (3), 307–316. https://doi.org/10.1016/j.cej.2010.08.007.
(134) Epsztein, R.; Shaulsky, E.; Dizge, N.; Warsinger, D. M.; Elimelech, M. Role of Ionic Charge Density in Donnan Exclusion of Monovalent Anions by Nanofiltration. *Environ. Sci. Technol.* **2018**, *52* (7), 4108–4116. https://doi.org/10.1021/acs.est.7b06400.
(135) Semiat, R. Energy Issues in Desalination Processes. *Environ. Sci. Technol.* **2008**, *42* (22), 8193–8201. https://doi.org/10.1021/es801330u.
(136) Nghiem, L. D.; Schäfer, A. I.; Elimelech, M. Pharmaceutical Retention Mechanisms by Nanofiltration Membranes. *Environ. Sci. Technol.* **2005**, *39* (19), 7698–7705. https://doi.org/10.1021/es0507665.
(137) Zhu, W. P.; Sun, S. P.; Gao, J.; Fu, F. J.; Chung, T. S. Dual-Layer Polybenzimidazole/Polyethersulfone (PBI/PES) Nanofiltration (NF) Hollow Fiber Membranes for Heavy Metals Removal from Wastewater. *J. Memb. Sci.* **2014**, *456*, 117–127. https://doi.org/10.1016/j.memsci.2014.01.001.
(138) Hong, S. U.; Ouyang, L.; Bruening, M. L. Recovery of Phosphate Using Multilayer Polyelectrolyte Nanofiltration Membranes. *J. Memb. Sci.* **2009**, *327* (1–2), 2–5. https://doi.org/10.1016/j.memsci.2008.11.035.
(139) Ali, N.; Halim, N. S. A.; Jusoh, A.; Endut, A. The Formation and Characterisation of an Asymmetric Nanofiltration Membrane for Ammonia-Nitrogen Removal: Effect of Shear Rate. *Bioresour. Technol.* **2010**, *101* (5), 1459–1465. https://doi.org/10.1016/j.biortech.2009.08.070.
(140) Liang, Y.; Lin, S. Intercalation of Zwitterionic Surfactants Dramatically Enhances the Performance of Low-Pressure Nanofiltration Membrane. *J. Memb. Sci.* **2020**, *596*

(November 2019), 117726. https://doi.org/10.1016/j.memsci.2019.117726.
(141) Pica, N. E.; Funkhouser, J.; Yin, Y.; Zhang, Z.; Ceres, D. M.; Tong, T.; Blotevogel, J. Electrochemical Oxidation of Hexafluoropropylene Oxide Dimer Acid (GenX): Mechanistic Insights and Efficient Treatment Train with Nanofiltration. *Environ. Sci. Technol.* **2019**, *53* (21), 12602–12609. https://doi.org/10.1021/acs.est.9b03171.
(142) Teng, X.; Fang, W.; Liang, Y.; Lin, S.; Lin, H.; Liu, S.; Wang, Z.; Zhu, Y.; Jin, J. High-Performance Polyamide Nanofiltration Membrane with Arch-Bridge Structure on a Highly Hydrated Cellulose Nanofiber Support. *Sci. China Mater.* **2020**. https://doi.org/10.1007/s40843-020-1335-x.
(143) Richardson, J. J.; Björnmalm, M.; Caruso, F. Technology-Driven Layer-by-Layer Assembly of Nanofilms. *Science (80-.).* **2015**, *348* (6233). https://doi.org/10.1126/science.aaa2491.
(144) Richardson, J. J.; Cui, J.; Björnmalm, M.; Braunger, J. A.; Ejima, H.; Caruso, F. Innovation in Layer-by-Layer Assembly. *Chem. Rev.* **2016**, *116* (23), 14828–14867. https://doi.org/10.1021/acs.chemrev.6b00627.
(145) Shan, W.; Bacchin, P.; Aimar, P.; Bruening, M. L.; Tarabara, V. V. Polyelectrolyte Multilayer Films as Backflushable Nanofiltration Membranes with Tunable Hydrophilicity and Surface Charge. *J. Memb. Sci.* **2010**, *349* (1–2), 268–278. https://doi.org/10.1016/j.memsci.2009.11.059.
(146) Shan, L.; Liang, Y.; Prozorovska, L.; Jennings, G. K.; Ji, S.; Lin, S. Multifold Enhancement of Loose Nanofiltration Membrane Performance by Intercalation of Surfactant Assemblies. *Environ. Sci. Technol. Lett.* **2018**, *5* (11), 668–674. https://doi.org/10.1021/acs.estlett.8b00430.
(147) Gutierrez, L.; Aubry, C.; Cornejo, M.; Croue, J. P. Citrate-Coated Silver Nanoparticles Interactions with Effluent Organic Matter: Influence of Capping Agent and Solution Conditions. *Langmuir* **2015**, *31* (32), 8865–8872. https://doi.org/10.1021/acs.langmuir.5b02067.
(148) Chen, K. L.; Elimelech, M. Aggregation and Deposition Kinetics of Fullerene (C60) Nanoparticles. *Langmuir* **2006**, *22* (26), 10994–11001. https://doi.org/10.1021/la062072v.
(149) Guzmán, E.; Ritacco, H.; Ortega, F.; Svitova, T.; Radke, C. J.; Rubio, R. G. Adsorption Kinetics and Mechanical Properties of Ultrathin Polyelectrolyte Multilayers: Liquid-Supported versus Solid-Supported Films. *J. Phys. Chem. B* **2009**, *113* (20), 7128–7137. https://doi.org/10.1021/jp811178a.
(150) Notley, S. M.; Eriksson, M.; Wågberg, L. Visco-Elastic and Adhesive Properties of Adsorbed Polyelectrolyte Multilayers Determined in Situ with QCM-D and AFM Measurements. *J. Colloid Interface Sci.* **2005**, *292* (1), 29–37. https://doi.org/10.1016/j.jcis.2005.05.057.
(151) Iturri Ramos, J. J.; Stahl, S.; Richter, R. P.; Moya, S. E. Water Content and Buildup of Poly(Diallyldimethylammonium Chloride)/Poly(Sodium 4-Styrenesulfonate) and Poly(Allylamine Hydrochloride)/Poly(Sodium 4-Styrenesulfonate) Polyelectrolyte Multilayers Studied by an in Situ Combination of a Quartz Crystal Microb. *Macromolecules* **2010**, *43* (21), 9063–9070. https://doi.org/10.1021/ma1015984.
(152) Porcel, C.; Lavalle, P.; Ball, V.; Decher, G.; Senger, B.; Voegel, J. C.; Schaaf, P. From Exponential to Linear Growth in Polyelectrolyte Multilayers. *Langmuir* **2006**, *22* (9), 4376–4383. https://doi.org/10.1021/la053218d.
(153) McAloney, R. A.; Sinyor, M.; Dudnik, V.; Cynthia Goh, M. Atomic Force Microscopy

Studies of Salt Effects on Polyelectrolyte Multilayer Film Morphology. *Langmuir* **2001**, *17* (21), 6655–6663. https://doi.org/10.1021/la010136q.
(154) Bhalerao, U. M.; Acharya, J.; Halve, A. K.; Kaushik, M. P. Controlled Drug Delivery of Antileishmanial Chalcones from Layer-by-Layer (LbL) Self Assembled PSS/PDADMAC Thin Films. *RSC Adv.* **2014**, *4* (10), 4970–4977. https://doi.org/10.1039/c3ra44611e.
(155) Viana, R. B.; Da Silva, A. B. F.; Pimentel, A. S. Infrared Spectroscopy of Anionic, Cationic, and Zwitterionic Surfactants. *Adv. Phys. Chem.* **2012**, *2012*. https://doi.org/10.1155/2012/903272.
(156) Sperline, R. P. Infrared Spectroscopic Study of the Crystalline Phases of Sodium Dodecyl Sulfate. *Langmuir* **1997**, *13* (14), 3715–3726. https://doi.org/10.1021/la9702087.
(157) Prosser, A. J.; Franses, E. I. Infrared Reflection Absorption Spectroscopy (IRRAS) of Aqueous Nonsurfactant Salts, Ionic Surfactants, and Mixed Ionic Surfactants. *Langmuir* **2002**, *18* (24), 9234–9242. https://doi.org/10.1021/la020568g.
(158) SU, B.; Wang, T.; Wang, Z.; Gao, X.; Gao, C. Preparation and Performance of Dynamic Layer-by-Layer PDADMAC/PSS Nanofiltration Membrane. *J. Memb. Sci.* **2012**, *423–424*, 324–331. https://doi.org/10.1016/j.memsci.2012.08.041.
(159) Elzbieciak, M.; Kolasinska, M.; Warszynski, P. Characteristics of Polyelectrolyte Multilayers: The Effect of Polyion Charge on Thickness and Wetting Properties. *Colloids Surfaces A Physicochem. Eng. Asp.* **2008**, *321* (1–3), 258–261. https://doi.org/10.1016/j.colsurfa.2008.01.036.
(160) Yan, F.; Chen, H.; Lü, Y.; Lü, Z.; Yu, S.; Liu, M.; Gao, C. Improving the Water Permeability and Antifouling Property of Thin-Film Composite Polyamide Nanofiltration Membrane by Modifying the Active Layer with Triethanolamine. *J. Memb. Sci.* **2016**, *513*, 108–116. https://doi.org/10.1016/j.memsci.2016.04.049.
(161) Chen, Q.; Yu, P.; Huang, W.; Yu, S.; Liu, M.; Gao, C. High-Flux Composite Hollow Fiber Nanofiltration Membranes Fabricated through Layer-by-Layer Deposition of Oppositely Charged Crosslinked Polyelectrolytes for Dye Removal. *J. Memb. Sci.* **2015**, *492*, 312–321. https://doi.org/10.1016/j.memsci.2015.05.068.
(162) Park, S. Y.; Rubner, M. F.; Mayes, A. M. Free Energy Model for Layer-by-Layer Processing of Polyelectrolyte Multilayer Films. *Langmuir* **2002**, *18* (24), 9600–9604. https://doi.org/10.1021/la026111o.
(163) Lin, M. Y.; Lindsay, H. M.; Weitz, D. A.; Ball, R. C.; Klein, R.; Meakin, P. Universality in Colloid Aggregation. *Nature* **1989**, *339* (6223), 360–362. https://doi.org/10.1038/339360a0.
(164) Weitz, D. A.; Huang, J. S.; Lin, M. Y.; Sung, J. Limits of the Fractal Dimension for Irreversible Kinetic Aggregation of Gold Colloids. *Phys. Rev. Lett.* **1985**, *54* (13), 1416–1419. https://doi.org/10.1103/PhysRevLett.54.1416.
(165) DuChanois, R. M.; Epsztein, R.; Trivedi, J. A.; Elimelech, M. Controlling Pore Structure of Polyelectrolyte Multilayer Nanofiltration Membranes by Tuning Polyelectrolyte-Salt Interactions. *J. Memb. Sci.* **2019**, *581* (March), 413–420. https://doi.org/10.1016/j.memsci.2019.03.077.
(166) Schoeler, B.; Kumaraswamy, G.; Caruso, F. Investigation of the Influence of Polyelectrolyte Charge Density on the Growth of Multilayer Thin Films Prepared by the Layer-by-Layer Technique. *Macromolecules* **2002**, *35* (3), 889–897. https://doi.org/10.1021/ma011349p.
(167) Schönhoff, M. Layered Polyelectrolyte Complexes: Physics of Formation and Molecular

Properties. *J. Phys. Condens. Matter* **2003**, *15* (49), R1781. https://doi.org/10.1088/0953-8984/15/49/R01.
(168) Yang, Z.; Guo, H.; Yao, Z. K.; Mei, Y.; Tang, C. Y. Hydrophilic Silver Nanoparticles Induce Selective Nanochannels in Thin Film Nanocomposite Polyamide Membranes. *Environ. Sci. Technol.* **2019**, *53* (9), 5301–5308. https://doi.org/10.1021/acs.est.9b00473.
(169) Carswell, A. D. W.; Lowe, A. M.; Wei, X.; Grady, B. P. CMC Determination in the Presence of Surfactant-Adsorbing Inorganic Particulates. *Colloids Surfaces A Physicochem. Eng. Asp.* **2003**, *212* (2–3), 147–153. https://doi.org/10.1016/S0927-7757(02)00329-1.
(170) Banipal, T. S.; Kaur, H.; Banipal, P. K.; Sood, A. K. Effect of Head Groups, Temperature, and Polymer Concentration on Surfactant - Polymer Interactions. *J. Surfactants Deterg.* **2014**, *17* (6), 1181–1191. https://doi.org/10.1007/s11743-014-1633-y.
(171) Elshof, M. G.; de Vos, W. M.; de Grooth, J.; Benes, N. E. On the Long-Term PH Stability of Polyelectrolyte Multilayer Nanofiltration Membranes. *J. Memb. Sci.* **2020**, *615*, 118532. https://doi.org/10.1016/j.memsci.2020.118532.
(172) Galanakis, C. M.; Fountoulis, G.; Gekas, V. Nanofiltration of Brackish Groundwater by Using a Polypiperazine Membrane. *Desalination* **2012**, *286*, 277–284. https://doi.org/10.1016/j.desal.2011.11.035.
(173) Fang, W.; Shi, L.; Wang, R. Mixed Polyamide-Based Composite Nanofiltration Hollow Fiber Membranes with Improved Low-Pressure Water Softening Capability. *J. Memb. Sci.* **2014**, *468*, 52–61. https://doi.org/10.1016/j.memsci.2014.05.047.
(174) Lin, J.; Ye, W.; Zeng, H.; Yang, H.; Shen, J.; Darvishmanesh, S.; Luis, P.; Sotto, A.; Van der Bruggen, B. Fractionation of Direct Dyes and Salts in Aqueous Solution Using Loose Nanofiltration Membranes. *J. Memb. Sci.* **2015**, *477*, 183–193. https://doi.org/10.1016/j.memsci.2014.12.008.
(175) Nghiem, L. D.; Schäfer, A. I.; Elimelech, M. Removal of Natural Hormones by Nanofiltration Membranes: Measurement, Modeling and Mechanisms. *Environ. Sci. Technol.* **2004**, *38* (6), 1888–1896. https://doi.org/10.1021/es034952r.
(176) Košutić, K.; Furač, L.; Sipos, L.; Kunst, B. Removal of Arsenic and Pesticides from Drinking Water by Nanofiltration Membranes. *Sep. Purif. Technol.* **2005**, *42* (2), 137–144. https://doi.org/10.1016/j.seppur.2004.07.003.
(177) Verliefde, A.; Cornelissen, E.; Amy, G.; Van der Bruggen, B.; van Dijk, H. Priority Organic Micropollutants in Water Sources in Flanders and the Netherlands and Assessment of Removal Possibilities with Nanofiltration. *Environ. Pollut.* **2007**, *146* (1), 281–289. https://doi.org/10.1016/j.envpol.2006.01.051.
(178) Shan, L.; Guo, H.; Qin, Z.; Wang, N.; Ji, S.; Zhang, G.; Zhang, Z. Covalent Crosslinked Polyelectrolyte Complex Membrane with High Negative Charges towards Anti-Natural Organic Matter Fouling Nanofiltration. *RSC Adv.* **2015**, *5* (15), 11515–11523. https://doi.org/10.1039/c4ra11602j.
(179) Gur-Reznik, S.; Katz, I.; Dosoretz, C. G. Removal of Dissolved Organic Matter by Granular-Activated Carbon Adsorption as a Pretreatment to Reverse Osmosis of Membrane Bioreactor Effluents. *Water Res.* **2008**, *42* (6–7), 1595–1605. https://doi.org/10.1016/j.watres.2007.10.004.
(180) Lin, Y. L.; Chiang, P. C.; Chang, E. E. Reduction of Disinfection By-Products Precursors by Nanofiltration Process. *J. Hazard. Mater.* **2006**, *137* (1), 324–331. https://doi.org/10.1016/j.jhazmat.2006.02.016.

(181) Zhu, J.; Tian, M.; Zhang, Y.; Zhang, H.; Liu, J. Fabrication of a Novel "Loose" Nanofiltration Membrane by Facile Blending with Chitosan-Montmorillonite Nanosheets for Dyes Purification. *Chem. Eng. J.* **2015**, *265*, 184–193. https://doi.org/10.1016/j.cej.2014.12.054.
(182) Jin, W.; Toutianoush, A.; Tieke, B. Use of Polyelectrolyte Layer-by-Layer Assemblies as Nanofiltration and Reverse Osmosis Membranes. *Langmuir* **2003**, *19* (7), 2550–2553. https://doi.org/10.1021/la020926f.
(183) Liu, C.; Shi, L.; Wang, R. Crosslinked Layer-by-Layer Polyelectrolyte Nanofiltration Hollow Fiber Membrane for Low-Pressure Water Softening with the Presence of SO42- in Feed Water. *J. Memb. Sci.* **2015**, *486*, 169–176. https://doi.org/10.1016/j.memsci.2015.03.050.
(184) Malaisamy, R.; Bruening, M. L. High-Flux Nanofiltration Membranes Prepared by Adsorption of Multilayer Polyelectrolyte Membranes on Polymeric Supports. *Langmuir* **2005**, *21* (23), 10587–10592. https://doi.org/10.1021/la051669s.
(185) Ishigami, T.; Amano, K.; Fujii, A.; Ohmukai, Y.; Kamio, E.; Maruyama, T.; Matsuyama, H. Fouling Reduction of Reverse Osmosis Membrane by Surface Modification via Layer-by-Layer Assembly. *Sep. Purif. Technol.* **2012**, *99*, 1–7. https://doi.org/10.1016/j.seppur.2012.08.002.
(186) Liu, L.; Kang, H.; Wang, W.; Xu, Z.; Mai, W.; Li, J.; Lv, H.; Zhao, L.; Qian, X. Layer-by-Layer Self-Assembly of Polycation/GO/OCNTs Nanofiltration Membrane with Enhanced Stability and Flux. *J. Mater. Sci.* **2018**, *53* (15), 10879–10890. https://doi.org/10.1007/s10853-018-2317-1.
(187) Schlenoff, J. B.; Dubas, S. T. Mechanism of Polyelectrolyte Multilayer Growth: Charge Overcompensation and Distribution. *Macromolecules* **2001**, *34* (3), 592–598. https://doi.org/10.1021/ma0003093.
(188) Krasemann, L.; Tieke, B. Selective Ion Transport across Self-Assembled Alternating Multilayers of Cationic and Anionic Polyelectrolytes. *Langmuir* **2000**, *16* (2), 287–290. https://doi.org/10.1021/la991240z.
(189) Liu, Y.; Chen, G. Q.; Yang, X.; Deng, H. Preparation of Layer-by-Layer Nanofiltration Membranes by Dynamic Deposition and Crosslinking. *Membranes (Basel).* **2019**, *9* (2). https://doi.org/10.3390/membranes9020020.
(190) Hu, M.; Mi, B. Layer-by-Layer Assembly of Graphene Oxide Membranes via Electrostatic Interaction. *J. Memb. Sci.* **2014**, *469*, 80–87. https://doi.org/10.1016/j.memsci.2014.06.036.
(191) Zhao, F. Y.; An, Q. F.; Ji, Y. L.; Gao, C. J. A Novel Type of Polyelectrolyte Complex/MWCNT Hybrid Nanofiltration Membranes for Water Softening. *J. Memb. Sci.* **2015**, *492*, 412–421. https://doi.org/10.1016/j.memsci.2015.05.041.
(192) Katano, H.; Tatsumi, H.; Senda, M. Ion-Transfer Voltammetry at 1,6-Dichlorohexane|water and 1,4-Dichlorobutane|water Interfaces. *Talanta* **2004**, *63* (1), 185–193. https://doi.org/10.1016/j.talanta.2003.10.044.
(193) Tanford, C. Micelle Shape and Size. *J. Phys. Chem.* **1972**, *76* (21), 3020–3024. https://doi.org/10.1021/j100665a018.
(194) Santos, D. P.; Longo, R. L. Molecular Dynamics Simulations of Specific Anion Adsorption on Sulfobetaine (SB3-14) Micelles. *J. Phys. Chem. B* **2016**, *120* (10), 2771–2780. https://doi.org/10.1021/acs.jpcb.5b12475.
(195) Grant, L. M.; Ducker, W. A. Effect of Substrate Hydrophobicity on Surface-Aggregate

Geometry: Zwitterionic and Nonionic Surfactants. *J. Phys. Chem. B* **1997**, *101* (27), 5337–5345. https://doi.org/10.1021/jp964014w.
(196) Ducker, W. A.; Grant, L. M. Effect of Substrate Hydrophobicity on Surfactant Surface-Aggregate Geometry. *J. Phys. Chem.* **1996**, *100* (28), 11507–11511. https://doi.org/10.1021/jp9607024.
(197) Park, S. Y.; Barrett, C. J.; Rubner, M. F.; Mayes, A. M. Anomalous Adsorption of Polyelectrolyte Layers. *Macromolecules* **2001**, *34* (10), 3384–3388. https://doi.org/10.1021/ma001601d.
(198) Shepherd, E. J.; Kitchener, J. A. The Ionization of Ethyleneimine and Polyethyleneimine. *J. Chem. Soc.* **1956**, 2419–2427. https://doi.org/10.1039/jr9560002448.
(199) Xia, S.; Yao, L.; Zhao, Y.; Li, N.; Zheng, Y. Preparation of Graphene Oxide Modified Polyamide Thin Film Composite Membranes with Improved Hydrophilicity for Natural Organic Matter Removal. *Chem. Eng. J.* **2015**, *280*, 720–727. https://doi.org/10.1016/j.cej.2015.06.063.
(200) Shan, L.; Fan, H.; Guo, H.; Ji, S.; Zhang, G. Natural Organic Matter Fouling Behaviors on Superwetting Nanofiltration Membranes. *Environ. Div. 2016 - Core Program. Area 2016 AIChE Annu. Meet.* **2016**, *93*, 211–213.
(201) Adams, F. V.; Nxumalo, E. N.; Krause, R. W. M.; Hoek, E. M. V.; Mamba, B. B. Application of Polysulfone/Cyclodextrin Mixed-Matrix Membranes in the Removal of Natural Organic Matter from Water. *Phys. Chem. Earth* **2014**, *67–69*, 71–78. https://doi.org/10.1016/j.pce.2013.11.001.
(202) Ates, N.; Yilmaz, L.; Kitis, M.; Yetis, U. Removal of Disinfection By-Product Precursors by UF and NF Membranes in Low-SUVA Waters. *J. Memb. Sci.* **2009**, *328* (1–2), 104–112. https://doi.org/10.1016/j.memsci.2008.11.044.
(203) Zhao, Y.; Li, N.; Xia, S. Polyamide Nanofiltration Membranes Modified with Zn–Al Layered Double Hydroxides for Natural Organic Matter Removal. *Compos. Sci. Technol.* **2016**, *132*, 84–92. https://doi.org/10.1016/j.compscitech.2016.06.016.
(204) Peeva, P. D.; Palupi, A. E.; Ulbricht, M. Ultrafiltration of Humic Acid Solutions through Unmodified and Surface Functionalized Low-Fouling Polyethersulfone Membranes - Effects of Feed Properties, Molecular Weight Cut-off and Membrane Chemistry on Fouling Behavior and Cleanability. *Sep. Purif. Technol.* **2011**, *81* (2), 124–133. https://doi.org/10.1016/j.seppur.2011.07.005.
(205) Xia, S.; Ni, M. Preparation of Poly(Vinylidene Fluoride) Membranes with Graphene Oxide Addition for Natural Organic Matter Removal. *J. Memb. Sci.* **2015**, *473*, 54–62. https://doi.org/10.1016/j.memsci.2014.09.018.
(206) Kumar, M.; Gholamvand, Z.; Morrissey, A.; Nolan, K.; Ulbricht, M.; Lawler, J. Preparation and Characterization of Low Fouling Novel Hybrid Ultrafiltration Membranes Based on the Blends of GO-TiO2 Nanocomposite and Polysulfone for Humic Acid Removal. *J. Memb. Sci.* **2016**, *506*, 38–49. https://doi.org/10.1016/j.memsci.2016.02.005.
(207) Wang, N.; Ji, S.; Zhang, G.; Li, J.; Wang, L. Self-Assembly of Graphene Oxide and Polyelectrolyte Complex Nanohybrid Membranes for Nanofiltration and Pervaporation. *Chem. Eng. J.* **2012**, *213*, 318–329. https://doi.org/10.1016/j.cej.2012.09.080.
(208) Tang, H.; Ji, S.; Gong, L.; Guo, H.; Zhang, G. Tubular Ceramic-Based Multilayer Separation Membranes Using Spray Layer-by-Layer Assembly. *Polym. Chem.* **2013**, *4* (23), 5621–5628. https://doi.org/10.1039/c3py00617d.
(209) Yu, S.; Cheng, Q.; Huang, C.; Liu, J.; Peng, X.; Liu, M.; Gao, C. Cellulose Acetate

Hollow Fiber Nanofiltration Membrane with Improved Permselectivity Prepared through Hydrolysis Followed by Carboxymethylation. *J. Memb. Sci.* **2013**, *434*, 44–54. https://doi.org/10.1016/j.memsci.2013.01.044.

(210) Ye, C. C.; Zhao, F. Y.; Wu, J. K.; Weng, X. D.; Zheng, P. Y.; Mi, Y. F.; An, Q. F.; Gao, C. J. Sulfated Polyelectrolyte Complex Nanoparticles Structured Nanoflitration Membrane for Dye Desalination. *Chem. Eng. J.* **2017**, *307*, 526–536. https://doi.org/10.1016/j.cej.2016.08.122.

(211) Srivastava, H. P.; Arthanareeswaran, G.; Anantharaman, N.; Starov, V. M. Performance of Modified Poly(Vinylidene Fluoride) Membrane for Textile Wastewater Ultrafiltration. *Desalination* **2011**, *282*, 87–94. https://doi.org/10.1016/j.desal.2011.05.054.

(212) Yu, S.; Chen, Z.; Cheng, Q.; Lü, Z.; Liu, M.; Gao, C. Application of Thin-Film Composite Hollow Fiber Membrane to Submerged Nanofiltration of Anionic Dye Aqueous Solutions. *Sep. Purif. Technol.* **2012**, *88*, 121–129. https://doi.org/10.1016/j.seppur.2011.12.024.

(213) Liu, M.; Chen, Q.; Lu, K.; Huang, W.; Lü, Z.; Zhou, C.; Yu, S.; Gao, C. High Efficient Removal of Dyes from Aqueous Solution through Nanofiltration Using Diethanolamine-Modified Polyamide Thin-Film Composite Membrane. *Sep. Purif. Technol.* **2017**, *173*, 135–143. https://doi.org/10.1016/j.seppur.2016.09.023.

(214) Zhao, S.; Wang, Z. A Loose Nano-Filtration Membrane Prepared by Coating HPAN UF Membrane with Modified PEI for Dye Reuse and Desalination. *J. Memb. Sci.* **2017**, *524* (November 2016), 214–224. https://doi.org/10.1016/j.memsci.2016.11.035.

(215) Kang, H.; Shi, J.; Liu, L.; Shan, M.; Xu, Z.; Li, N.; Li, J.; Lv, H.; Qian, X.; Zhao, L. Sandwich Morphology and Superior Dye-Removal Performances for Nanofiltration Membranes Self-Assemblied via Graphene Oxide and Carbon Nanotubes. *Appl. Surf. Sci.* **2018**, *428*, 990–999. https://doi.org/10.1016/j.apsusc.2017.09.212.

(216) Daraei, P.; Madaeni, S. S.; Salehi, E.; Ghaemi, N.; Ghari, H. S.; Khadivi, M. A.; Rostami, E. Novel Thin Film Composite Membrane Fabricated by Mixed Matrix Nanoclay/Chitosan on PVDF Microfiltration Support: Preparation, Characterization and Performance in Dye Removal. *J. Memb. Sci.* **2013**, *436*, 97–108. https://doi.org/10.1016/j.memsci.2013.02.031.

(217) Acero, J. L.; Benitez, F. J.; Leal, A. I.; Real, F. J.; Teva, F. Membrane Filtration Technologies Applied to Municipal Secondary Effluents for Potential Reuse. *J. Hazard. Mater.* **2010**, *177* (1–3), 390–398. https://doi.org/10.1016/j.jhazmat.2009.12.045.

(218) Lau, W. J.; Ismail, A. F. Polymeric Nanofiltration Membranes for Textile Dye Wastewater Treatment: Preparation, Performance Evaluation, Transport Modelling, and Fouling Control - a Review. *Desalination* **2009**, *245* (1–3), 321–348. https://doi.org/10.1016/j.desal.2007.12.058.

(219) Yang, S.; Wang, J.; Fang, L.; Lin, H.; Liu, F.; Tang, C. Y. Electrosprayed Polyamide Nanofiltration Membrane with Intercalated Structure for Controllable Structure Manipulation and Enhanced Separation Performance. *J. Memb. Sci.* **2020**, *602*, 117971. https://doi.org/10.1016/j.memsci.2020.117971.

(220) Han, G.; Chung, T. S.; Weber, M.; Maletzko, C. Low-Pressure Nanofiltration Hollow Fiber Membranes for Effective Fractionation of Dyes and Inorganic Salts in Textile Wastewater. *Environ. Sci. Technol.* **2018**, *52* (6), 3676–3684. https://doi.org/10.1021/acs.est.7b06518.

(221) Zhu, X.; Cheng, X.; Luo, X.; Liu, Y.; Xu, D.; Tang, X.; Gan, Z.; Yang, L.; Li, G.; Liang, H. Ultrathin Thin-Film Composite Polyamide Membranes Constructed on Hydrophilic

Poly(Vinyl Alcohol) Decorated Support Toward Enhanced Nanofiltration Performance. *Environ. Sci. Technol.* **2020**, *54* (10), 6365–6374. https://doi.org/10.1021/acs.est.9b06779.
(222) Zhang, H.; Quan, X.; Fan, X.; Yi, G.; Chen, S.; Yu, H.; Chen, Y. Improving Ion Rejection of Conductive Nanofiltration Membrane through Electrically Enhanced Surface Charge Density. *Environ. Sci. Technol.* **2019**, *53* (2), 868–877. https://doi.org/10.1021/acs.est.8b04268.
(223) Wang, J.; Dlamini, D. S.; Mishra, A. K.; Pendergast, M. T. M.; Wong, M. C. Y.; Mamba, B. B.; Freger, V.; Verliefde, A. R. D.; Hoek, E. M. V. A Critical Review of Transport through Osmotic Membranes. *J. Memb. Sci.* **2014**, *454*, 516–537. https://doi.org/10.1016/j.memsci.2013.12.034.
(224) Li, Q.; Elimelech, M. Organic Fouling and Chemical Cleaning of Nanofiltration Membranes: Measurements and Mechanisms. *Environ. Sci. Technol.* **2004**, *38* (17), 4683–4693. https://doi.org/10.1021/es0354162.
(225) Paul, M.; Jons, S. D. Chemistry and Fabrication of Polymeric Nanofiltration Membranes: A Review. *Polymer (Guildf).* **2016**, *103*, 417–456. https://doi.org/10.1016/j.polymer.2016.07.085.
(226) Zhu, Y.; Ahmad, M.; Yang, L.; Misovich, M.; Yaroshchuk, A.; Bruening, M. L. Adsorption of Polyelectrolyte Multilayers Imparts High Monovalent/Divalent Cation Selectivity to Aliphatic Polyamide Cation-Exchange Membranes. *J. Memb. Sci.* **2017**, *537*, 177–185. https://doi.org/10.1016/j.memsci.2017.05.043.
(227) Ahmad, M.; Tang, C.; Yang, L.; Yaroshchuk, A.; Bruening, M. L. Layer-by-Layer Modification of Aliphatic Polyamide Anion-Exchange Membranes to Increase Cl−/SO42− Selectivity. *J. Memb. Sci.* **2019**, *578*, 209–219. https://doi.org/10.1016/j.memsci.2019.02.018.
(228) Virga, E.; de Grooth, J.; Žvab, K.; de Vos, W. M. Stable Polyelectrolyte Multilayer-Based Hollow Fiber Nanofiltration Membranes for Produced Water Treatment. *ACS Appl. Polym. Mater.* **2019**, *1* (8), 2230–2239. https://doi.org/10.1021/acsapm.9b00503.
(229) Hong, S. U.; Malaisamy, R.; Bruening, M. L. Separation of Fluoride from Other Monovalent Anions Using Multilayer Polyelectrolyte Nanofiltration Membranes. *Langmuir* **2007**, *23* (4), 1716–1722. https://doi.org/10.1021/la061701y.
(230) Picart, C.; Mutterer, J.; Richert, L.; Luo, Y.; Prestwich, G. D.; Schaaf, P.; Voegel, J. C.; Lavalle, P. Molecular Basis for the Explanation of the Exponential Growth of Polyelectrolyte Multilayers. *Proc. Natl. Acad. Sci. U. S. A.* **2002**, *99* (20), 12531–12535. https://doi.org/10.1073/pnas.202486099.
(231) Decher, G.; Hong, J. D.; Schmitt, J. Buildup of Ultrathin Multilayer Films by a Self-Assembly Process: III. Consecutively Alternating Adsorption of Anionic and Cationic Polyelectrolytes on Charged Surfaces. *Thin Solid Films* **1992**, *210–211* (PART 2), 831–835. https://doi.org/10.1016/0040-6090(92)90417-A.
(232) Hu, Y.; Neil, C.; Lee, B.; Jun, Y. S. Control of Heterogeneous Fe(III) (Hydr)Oxide Nucleation and Growth by Interfacial Energies and Local Saturations. *Environ. Sci. Technol.* **2013**, *47* (16), 9198–9206. https://doi.org/10.1021/es401160g.
(233) Norgren, M.; Gärdlund, L.; Notley, S. M.; Htun, M.; Wågberg, L. Smooth Model Surfaces from Lignin Derivatives. II. Adsorption of Polyelectrolytes and PECs Monitored by QCM-D. *Langmuir* **2007**, *23* (7), 3737–3743. https://doi.org/10.1021/la063439z.
(234) Contreras, A. E.; Steiner, Z.; Miao, J.; Kasher, R.; Li, Q. Studying the Role of Common Membrane Surface Functionalities on Adsorption and Cleaning of Organic Foulants Using

QCM-D. *Environ. Sci. Technol.* **2011**, *45* (15), 6309–6315. https://doi.org/10.1021/es200570t.
(235) Bonekamp, B. C.; Lyklema, J. Conductometric and Potentiometric Monitoring of Polyelectrolyte Adsorption on Charged Surfaces. *J. Colloid Interface Sci.* **1986**, *113* (1), 67–75. https://doi.org/10.1016/0021-9797(86)90206-7.
(236) Poghossian, A.; Abouzar, M. H.; Sakkari, M.; Kassab, T.; Han, Y.; Ingebrandt, S.; Offenhäusser, A.; Schöning, M. J. Field-Effect Sensors for Monitoring the Layer-by-Layer Adsorption of Charged Macromolecules. *Sensors Actuators, B Chem.* **2006**, *118* (1–2), 163–170. https://doi.org/10.1016/j.snb.2006.04.013.
(237) Jüttner, K. Electrochemical Impedance Spectroscopy (EIS) of Corrosion Processes on Inhomogeneous Surfaces. *Electrochim. Acta* **1990**, *35* (10), 1501–1508. https://doi.org/10.1016/0013-4686(90)80004-8.
(238) Mansfeld, F. Use of Electrochemical Impedance Spectroscopy for the Study of Corrosion Protection by Polymer Coatings. *J. Appl. Electrochem.* **1995**, *25* (3), 187–202. https://doi.org/10.1007/BF00262955.
(239) Chen, W. F.; Wang, C. H.; Sasaki, K.; Marinkovic, N.; Xu, W.; Muckerman, J. T.; Zhu, Y.; Adzic, R. R. Highly Active and Durable Nanostructured Molybdenum Carbide Electrocatalysts for Hydrogen Production. *Energy Environ. Sci.* **2013**, *6* (3), 943–951. https://doi.org/10.1039/c2ee23891h.
(240) Song, H. K.; Jung, Y. H.; Lee, K. H.; Dao, L. H. Electrochemical Impedance Spectroscopy of Porous Electrodes: The Effect of Pore Size Distribution. *Electrochim. Acta* **1999**, *44* (20), 3513–3519. https://doi.org/10.1016/S0013-4686(99)00121-8.
(241) Barreira, S. V. P.; García-Morales, V.; Pereira, C. M.; Manzanares, J. A.; Silva, F. Electrochemical Impedance Spectroscopy of Polyelectrolyte Multilayer Modified Electrodes. *J. Phys. Chem. B* **2004**, *108* (46), 17973–17982. https://doi.org/10.1021/jp0466845.
(242) Chirea, M.; García-Morales, V.; Manzanares, J. A.; Pereira, C.; Gulaboski, R.; Silva, F. Electrochemical Characterization of Polyelectrolyte/Gold Nanoparticle Multilayers Self-Assembled on Gold Electrodes. *J. Phys. Chem. B* **2005**, *109* (46), 21808–21817. https://doi.org/10.1021/jp0537815.
(243) Cheng, W.; Liu, C.; Tong, T.; Epsztein, R.; Sun, M.; Verduzco, R.; Ma, J.; Elimelech, M. Selective Removal of Divalent Cations by Polyelectrolyte Multilayer Nanofiltration Membrane: Role of Polyelectrolyte Charge, Ion Size, and Ionic Strength. *J. Memb. Sci.* **2018**, *559* (January), 98–106. https://doi.org/10.1016/j.memsci.2018.04.052.
(244) Grossi, M.; Riccò, B. Electrical Impedance Spectroscopy (EIS) for Biological Analysis and Food Characterization: A Review. *J. Sensors Sens. Syst.* **2017**, *6* (2), 303–325. https://doi.org/10.5194/jsss-6-303-2017.
(245) Bason, S.; Oren, Y.; Freger, V. Characterization of Ion Transport in Thin Films Using Electrochemical Impedance Spectroscopy. II: Examination of the Polyamide Layer of RO Membranes. *J. Memb. Sci.* **2007**, *302* (1–2), 10–19. https://doi.org/10.1016/j.memsci.2007.05.007.
(246) Yun, D. J.; Ra, H.; Rhee, S. W. Concentration Effect of Multiwalled Carbon Nanotube and Poly(3, 4-Ethylenedioxythiophene) Polymerized with Poly(4-Styrenesulfonate) Conjugated Film on the Catalytic Activity for Counter Electrode in Dye Sensitized Solar Cells. *Renew. Energy* **2013**, *50*, 692–700. https://doi.org/10.1016/j.renene.2012.06.056.
(247) Stolov, M.; Freger, V. Degradation of Polyamide Membranes Exposed to Chlorine: An

Impedance Spectroscopy Study. *Environ. Sci. Technol.* **2019**, *53* (5), 2618–2625. https://doi.org/10.1021/acs.est.8b04790.
(248) Freger, V.; Bason, S. Characterization of Ion Transport in Thin Films Using Electrochemical Impedance Spectroscopy. I. Principles and Theory. *J. Memb. Sci.* **2007**, *302* (1–2), 1–9. https://doi.org/10.1016/j.memsci.2007.06.046.
(249) Stolov, M.; Freger, V. Membrane Charge Weakly Affects Ion Transport in Reverse Osmosis. *Environ. Sci. Technol. Lett.* **2020**, *7* (6), 440–445. https://doi.org/10.1021/acs.estlett.0c00291.
(250) Fridman-Bishop, N.; Freger, V. What Makes Aromatic Polyamide Membranes Superior: New Insights into Ion Transport and Membrane Structure. *J. Memb. Sci.* **2017**, *540* (June), 120–128. https://doi.org/10.1016/j.memsci.2017.06.035.
(251) Shaffer, D. L.; Feldman, K. E.; Chan, E. P.; Stafford, G. R.; Stafford, C. M. Characterizing Salt Permeability in Polyamide Desalination Membranes Using Electrochemical Impedance Spectroscopy. *J. Memb. Sci.* **2019**, *583*, 248–257. https://doi.org/10.1016/j.memsci.2019.04.062.
(252) Squillace, O.; Esnault, C.; Pilard, J. F.; Brotons, G. Electrodes for Membrane Surface Science. Bilayer Lipid Membranes Tethered by Commercial Surfactants on Electrochemical Sensors. *ACS Sensors* **2019**, *4* (5), 1337–1345. https://doi.org/10.1021/acssensors.9b00267.
(253) Delgado, A. V.; González-Caballero, F.; Hunter, R. J.; Koopal, L. K.; Lyklema, J. Measurement and Interpretation of Electrokinetic Phenomena. *J. Colloid Interface Sci.* **2007**, *309* (2), 194–224. https://doi.org/10.1016/j.jcis.2006.12.075.
(254) Yaroshchuk, A.; Luxbacher, T. Interpretation of Electrokinetic Measurements with Porous Films: Role of Electric Conductance and Streaming Current within Porous Structure. *Langmuir* **2010**, *26* (13), 10882–10889. https://doi.org/10.1021/la100777z.
(255) Fievet, P.; Sbaï, M.; Szymczyk, A.; Vidonne, A. Determining the ζ-Potential of Plane Membranes from Tangential Streaming Potential Measurements: Effect of the Membrane Body Conductance. *J. Memb. Sci.* **2003**, *226* (1–2), 227–236. https://doi.org/10.1016/j.memsci.2003.09.007.
(256) Sbaï, M.; Szymczyk, A.; Fievet, P.; Sorin, A.; Vidonne, A.; Pellet-Rostaing, S.; Favre-Reguillon, A.; Lemaire, M. Influence of the Membrane Pore Conductance on Tangential Streaming Potential. *Langmuir* **2003**, *19* (21), 8867–8871. https://doi.org/10.1021/la034966a.
(257) Nestler, P.; Paßvogel, M.; Helm, C. A. Influence of Polymer Molecular Weight on the Parabolic and Linear Growth Regime of PDADMAC/PSS Multilayers. *Macromolecules* **2013**, *46* (14), 5622–5629. https://doi.org/10.1021/ma400333f.
(258) Guzmán, E.; Ritacco, H.; Rubio, J. E. F.; Rubio, R. G.; Ortega, F. Salt-Induced Changes in the Growth of Polyelectrolyte Layers of Poly(Diallyl-Dimethylammonium Chloride) and Poly(4-Styrene Sulfonate of Sodium). *Soft Matter* **2009**, *5* (10), 2130–2142. https://doi.org/10.1039/b901193e.
(259) Kleber, C.; Bruns, M.; Lienkamp, K.; Rühe, J.; Asplund, M. An Interpenetrating, Microstructurable and Covalently Attached Conducting Polymer Hydrogel for Neural Interfaces. *Acta Biomater.* **2017**, *58*, 365–375. https://doi.org/10.1016/j.actbio.2017.05.056.
(260) Tanaka, F.; Tanaka, F. *Polymer Solutions*; John Wiley & Sons, Inc, 2011. https://doi.org/10.1017/cbo9780511975691.003.

(261) Kok, C. M.; Rudin, A. Relationship between the Hydrodynamic Radius and the Radius of Gyration of a Polymer in Solution. *Die Makromol. Chemie, Rapid Commun.* **1981**, *2* (11), 655–659. https://doi.org/10.1002/marc.1981.030021102.
(262) Nightingale, E. R. Phenomenological Theory of Ion Solvation. Effective Radii of Hydrated Ions. *J. Phys. Chem.* **1959**, *63* (9), 1381–1387. https://doi.org/10.1021/j150579a011.
(263) Nathan, A. J.; Scobell, A. How China Sees America. *Foreign Aff.* **2012**, *91* (5), 713–718. https://doi.org/10.1017/CBO9781107415324.004.
(264) Beverly, S.; Seal, S.; Hong, S. Identification of Surface Chemical Functional Groups Correlated to Failure of Reverse Osmosis Polymeric Membranes. *J. Vac. Sci. Technol. A Vacuum, Surfaces, Film.* **2000**, *18* (4), 1107–1113. https://doi.org/10.1116/1.582308.
(265) Ariza, M. J.; Benavente, J.; Rodríguez-Castellón, E.; Palacio, L. Effect of Hydration of Polyamide Membranes on the Surface Electrokinetic Parameters: Surface Characterization by X-Ray Photoelectronic Spectroscopy and Atomic Force Microscopy. *J. Colloid Interface Sci.* **2002**, *247* (1), 149–158. https://doi.org/10.1006/jcis.2001.8071.
(266) Akin, O.; Temelli, F. Probing the Hydrophobicity of Commercial Reverse Osmosis Membranes Produced by Interfacial Polymerization Using Contact Angle, XPS, FTIR, FE-SEM and AFM. *Desalination* **2011**, *278* (1–3), 387–396. https://doi.org/10.1016/j.desal.2011.05.053.
(267) France, R. M.; Short, R. D. Plasma Treatment of Polymers Effects of Energy Transfer from an Argon Plasma on the Surface Chemistry of Poly(Styrene), Low Density Poly(Ethylene), Poly(Propylene) and Poly(Ethylene Terephthalate). *J. Chem. Soc. - Faraday Trans.* **1997**, *93* (17), 3173–3178. https://doi.org/10.1039/a702311a.
(268) Onaizi, S. A. Dynamic Surface Tension and Adsorption Mechanism of Surfactin Biosurfactant at the Air–Water Interface. *Eur. Biophys. J.* **2018**, *47* (6), 631–640. https://doi.org/10.1007/s00249-018-1289-z.
(269) Matijević, E.; Pethica, B. A. The Properties of Ionized Monolayers: Part 1. - Sodium Dodecyl Sulphate at the Air/Water Interface. *Trans. Faraday Soc.* **1958**, *54*, 1382–1389. https://doi.org/10.1039/TF9585401382.
(270) Elworthy, P. H.; Mysels, K. J. The Surface Tension of Sodium Dodecylsulfate Solutions and the Phase Separation Model of Micelle Formation. *J. Colloid Interface Sci.* **1966**, *21* (3), 331–347. https://doi.org/10.1016/0095-8522(66)90017-1.

APPENDIX

A SUPPLEMENTARY MATERIALS FOR CHAPTER 2

a. Separation mechanism in NF

Table A.1 Ionic radius, hydrated radius, hydration energy, and separation performance of ions investigated in this study. For consistency, data was collected from the same source[262,263]

	Ionic Radius (Å)	*Stokes Radius (Å)*	*Hydrated Radius (Å)*	*Hydration energy (kcal mol^{-1})*	*Salt used in the test*	*Rejection (%)*	
Cations						IP	SARIP
Zn^{2+}	0.74	3.49	4.30	467.3	$ZnCl_2$	61%	96%
Co^{2+}	0.72	3.35	4.23	457.7	$CoCl_2$	38%	96%
Mg^{2+}	0.65	3.47	4.23	437.4	$MgCl_2$	45%	95%
Cu^{2+}	0.72	3.25	4.19	480.4	$CuCl_2$	44%	94%
Ca^{2+}	0.99	3.10	4.12	359.7	$CaCl_2$	25%	93%
Ni^{2+}	0.70	2.92	4.04	473.2	$NiCl_2$	24%	93%
Ba^{2+}	1.35	2.90	4.04	298.8	$BaCl_2$	17%	93%
Li^{+}	0.60	2.38	3.82	113.5	LiCl	19%	30%
Na^{+}	0.95	1.84	3.58	87.2	NaCl	15%	27%
K^{+}	1.33	1.25	3.31	70.5	KCl	9.5%	20%
Rb^{+}	1.48	1.18	3.29	65.7	RbCl	13%	18%
Cs^{+}	1.69	1.19	3.29	59.8	CsCl	7.3%	16%
Anions							
$Fe(CN)_6^{3-}$	4.35	3.32	4.22	*596.3	$K_3Fe(CN)_6$	97%	100%
SO_4^{2-}	2.90	2.30	3.82	258.1	Na_2SO_4	96%	99%
NO_3^{-}	2.64	1.29	3.35	71.7	$NaNO_3$	8.4%	16%

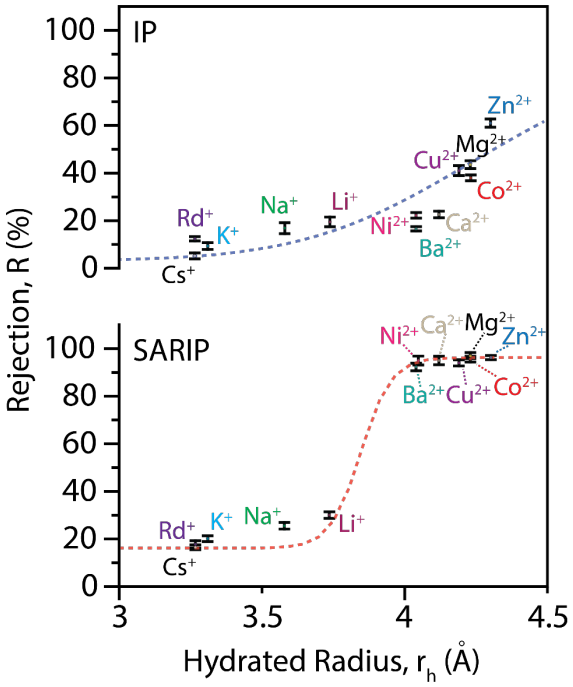

Figure A.1 Rejection of different ions as a function of hydrated radius for PA-TFC membranes fabricated using conventional IP (top) and SARIP (bottom). Hydrated radii of ions are presented in Table A.1. Rejection data of each solute represents the average of three runs and the error bars represent the standard deviation of the rejection from the three runs.

Separation mechanisms in NF include mainly steric (size sieving) and Donnan (charge) exclusion[120,121]. Solute molecules with a size that is larger than the membrane pore size are sterically blocked, while the transport of solutes with a size similar to that of the membrane pores may also be hindered. A membrane surface with a fixed charge repels ions with the same charge and attracts ions with the opposite charge. Because the poly(piperazine-amide) nanofiltration membrane has a net negative surface charge from the hydrolysis of unreacted TMC groups, it exhibits high rejection of SO_4^{2-} but relatively low rejection of Mg^{2+} and Ca^{2+}. The difference in selectivity for different cations with similar net charges and radii (Figure 1D and Figure A.1) could be further explained based on the dehydration mechanism, i.e., an ion that approaches the membrane pore can strip and readjust its water shells temporarily in order to fit into the membrane pores. In general, smaller ionic size results in higher hydration energy, and ions with higher

hydration energy are rejected more effectively by NF and RO membranes[134]. Ion dehydration, which is significant in NF because of the small pore sizes, offers an additional explanation for the differences in the rejection of ions with similar charge and hydrated radii, e.g., Ni^{2+} (24%) and Ba^{2+} (17%), in the PA-TFC prepared from conventional IP.

b. Mean free-volume radius and free-volume radius distribution of PA from conventional IP and SARIP (with SDS) as assessed by Positron Annihilation Lifetime Spectroscopy (PALS)

Table A.2 Positron Lifetime results of polyamide active layer from conventional IP and SARIP (with SDS).

Sample	*τ3 (ns)*	*Δτ3(ns)*	*I3 (%)*	*ΔI3 (%)*	*R (Å)*	*ΔR (Å)*	*ffv (%)*	*Δffv (%)*
IP	1.434	0.039	12.155	0.417	2.266	0.044	1.066	0.099
SARIP (SDS)	1.297	0.043	14.831	0.434	2.095	0.054	1.028	0.110

τ3: o-Ps lifetime; I3: o-Ps density; R: mean free-volume radius; ffv: fractional free volume.

c. Surface streaming potential of TFC-PA membrane from conventional IP and SARIP (with SDS)

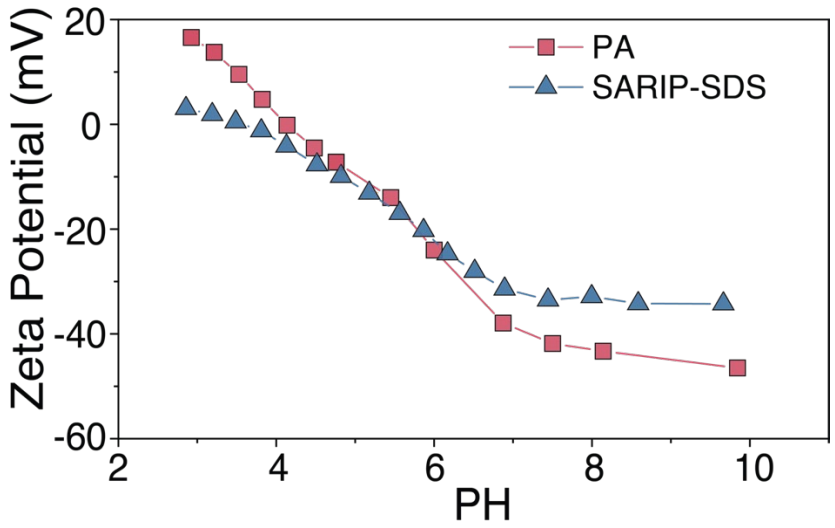

Figure A.2 Surface streaming potential of TFC-PA membranes from conventional IP and SARIP with SDS. (SDS Concentration: 1 CMC)

Both TFC-PA membranes from conventional IP and SARIP with SDS are negatively charged to a similar extent when pH is at 3 to 7. At a pH higher than 7, the surface of TFC-PA membrane prepared via conventional IP has a higher negative charge than that from SARIP because of the existence of more hydroxyl groups on the PA surface from the hydrolysis of unreacted TMC groups. It is in a good agreement with the XPS data in Table A.4.

d. XPS chemical characterization of the PA active layer from SARIP (with SDS)

(a) XPS survey spectra of the PA active layer from conventional from SARIP (with SDS)

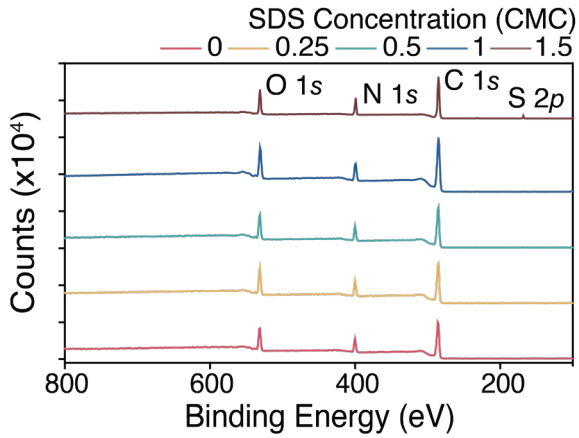

Figure A.3 XPS survey of polyamide active layer prepared via SARIP as a function of SDS concentration.

(b) Calculation of degree of cross-linking of polyamide network

Table A.3 The elemental composition results and calculation of crosslinking degree of polyamide network obtained using SARIP (with SDS).

	C(%)	*N(%)*	*O(%)*	*S(%)*	*Br(%)*	*Degree of crosslinking*
SDS 0	70.24	13.63	15.96	0.17	0	0.76
SDS 0.25	70.38	13.64	15.69	0.29	0	0.79
SDS 0.5	71.03	13.48	15.28	0.2	0	0.81
SDS 1	72.03	12.92	14.71	0.34	0	0.81
SDS 1.5	70.78	12.81	14.9	1.51	0	0.77

The chemical compositions (C, N, O, S, Br) of polyamide active layer obtained using conventional IP and SARIP with SDS are listed in Table A.5. The degree of crosslinking for each system is calculated based on the following equation[119]:

$$\frac{O}{N} = \frac{3X + 4Y}{3X + 2Y}$$

$$degree\ of\ crosslinking = \frac{X}{X + Y} \times 100\%$$

(c) High-resolution XPS spectra of poly(piperazine-amide) active layer from conventional IP and SARIP (with SDS)

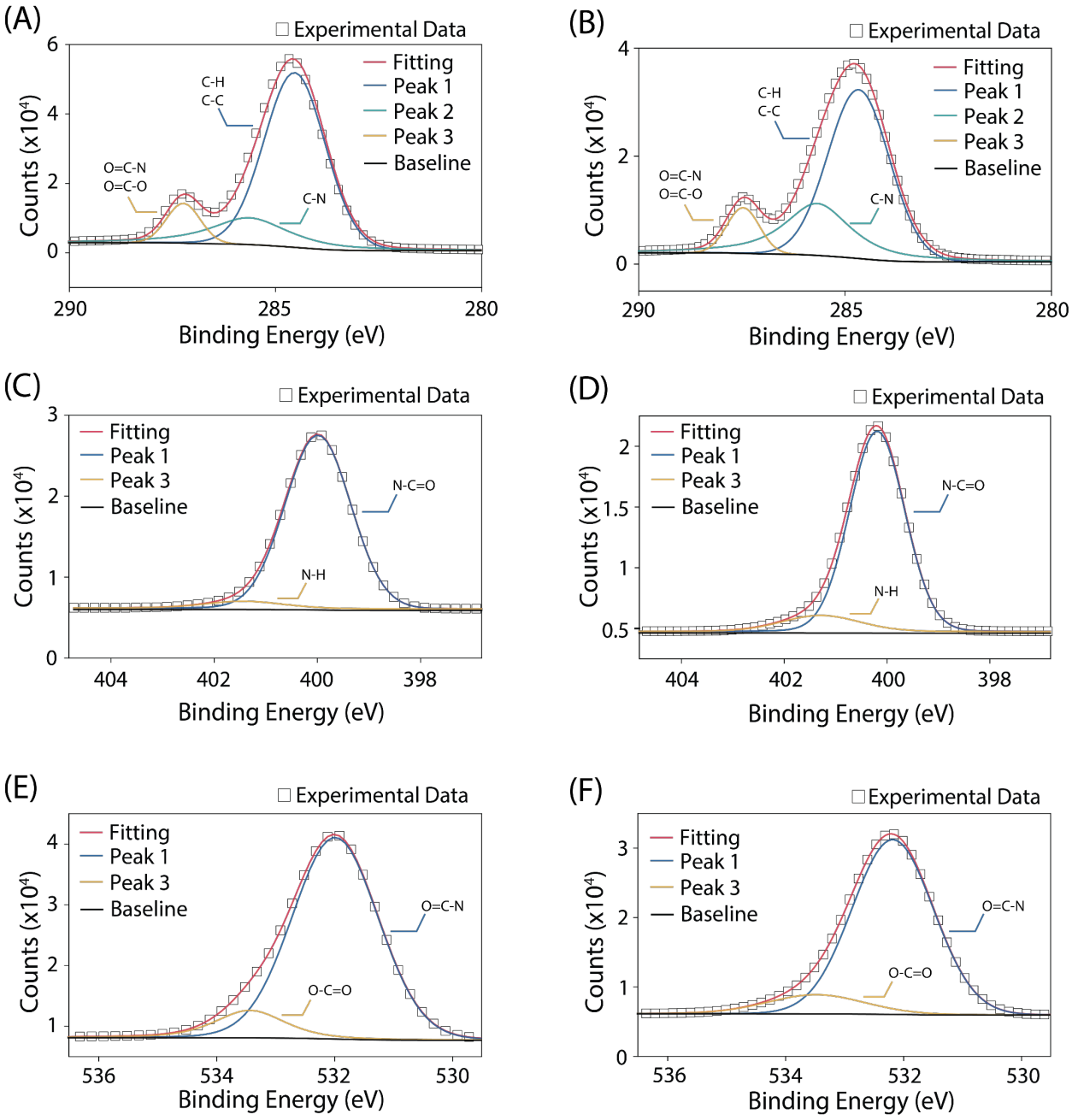

Figure A.4 High-resolution XPS spectra of polyamide active layer obtained using conventional IP and SARIP with SDS. (A and B) C 1s spectrum of conventional TFC-PA membrane and SARIP TFC-PA membrane. (C and D) N 1s spectrum of conventional TFC-PA membrane and SARIP TFC-PA membrane. (E and F) O 1s spectrum of conventional TFC-PA membrane and SARIP TFC-PA membrane. The chemical environment of carbon, nitrogen and oxygen was the same in both TFC-PA membranes. Three C 1s peaks were detected, one at 284.6 eV

(aliphatic/aromatic C-H or C-C bonds), the second one at 286 eV (C-N), and the other at 288 eV (amide O-C-N and carboxy O-C-O groups). Two N 1s signals were observed, peak one at 400 eV (N-C=O) and peak two at 401.7 eV (R-N-H). Both O 1s peaks at 532.0 eV (O=C-N) and 533.5 eV (O-C=O) were found in the TFC-PA from conventional IP and SARIP with SDS[264–267].

Table A.4 XPS results from the polyamide active layer from conventional IP and SARIP with SDS. Binding energies, plausible species and their content ratios were determined from the high-resolution C1s, N1s, and O1s XPS spectra.

Polyamide	C1*s*			N1*s*			O1*s*		
	Energy (eV)	Species	(%)	Energy (eV)	Species	(%)	Energy (eV)	Species	(%)
IP	284.6	C-H, C-C	66.8	400	N-C=O	92.2	532	O=C-N	88.1
	286	C-N	23.6						
	288	O-C=O, O-C=N	9.56	401.7	$-N^+H_2$	7.8	533.5	$O=C-O^-$ (H^+)	11.9
SARIP	284.8	C-H, C-C	59.7	400	N-C=O	95.1	532	O=C-N	90
	286	C-N	28.7						
	288	O-C=O, O-C=N	11.6	401.7	$-N^+H_2$	4.9	533.5	$O=C-O^-$ (H^+)	10

XPS C1*s*, N1*s* and O1*s* spectra of TFC-PA membrane prepared via conventional IP and from SARIP with SDS provided more detailed information of the chemical compositions of the PA active layer. The fractions of carboxylic acid groups and unreacted amine groups in the PA active layer from conventional IP were 11.9% and 7.8%, respectively; whereas the corresponding fractions of PA active layer from SARIP with SDS were 10% and 4.9%. This result indicated that the polyamide network prepared from SARIP with SDS contained more amide bonds and fewer unreacted PIP and TMC species compared to that from conventional IP.

e. Computational Simulations

(a) Molecular Dynamics (MD) modeling of PIP diffusion with and without SDS

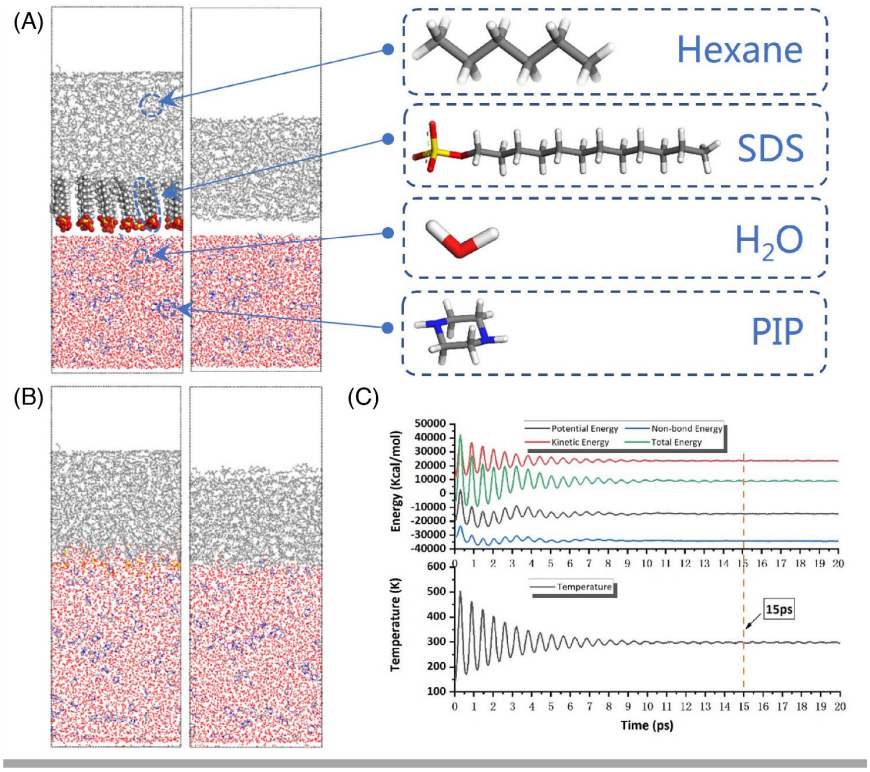

Figure A.5 (A) Initial MD models of PIP interfacial diffusion with and without self-assembled SDS network. (B) Two MD models at equilibrium. (C) Reference energy.

An Amorphous Cell module in Materials Studio was used to simulate the water-hexane interface. Two MD systems were constructed, one with a self-assembled SDS network at the water/hexane interface (Figure A. 5A, B left) and the other without SDS (Figure A. 5 A, B right). Both systems were comprised of the same numbers of H_2O (5000), pip (100) and C_6H_{14} (500) molecules in a lattice cell (50×50×140 $Å^3$). In the MD model with SDS network, a total number of 36 SDS molecules were placed between water and hexane phases (Figure A.5A left). After that, both MD systems were simulated for 20 picoseconds with NVE thermodynamic ensemble at 298.0 K temperature. As shown in Fig S6 (c), all the four reference energies (potential, non-bond, kinetic,

and total energy) have reached the steady values after 10ps. Meanwhile, the system temperature remained at the present value.

The configurations at 15ps in both MD systems were captured to analyze the population of pip molecules with and without the self-assembled SDS network (Figure A. 6). The relative concentrations of PIP, water and SDS molecules were shown in Fig S8. The water/hexane interfaces in both MD systems were determined at 70 Å in the Z direction from two methods: in the MD system with SDS network, the interface could be informed from the crest of S atoms population where SDS molecules formed a dynamic self-assembled network with an interfacial areal density of 1.1 nm^{-1}; in the other system without SDS, the interface was determined by the minimum concentration of O atoms from water molecules. Due to the presence of the SDS network, a locally concentrated population of PIP molecules was observed at the water/hexane interface. A total number of 18 PIP molecules were found near the interface due to the formation of a dynamic SDS network vs. 8 PIP molecules near the interface without SDS. This result indicated that the presence of SDS promoted the accumulation of PIP monomers near the water/hexane interface.

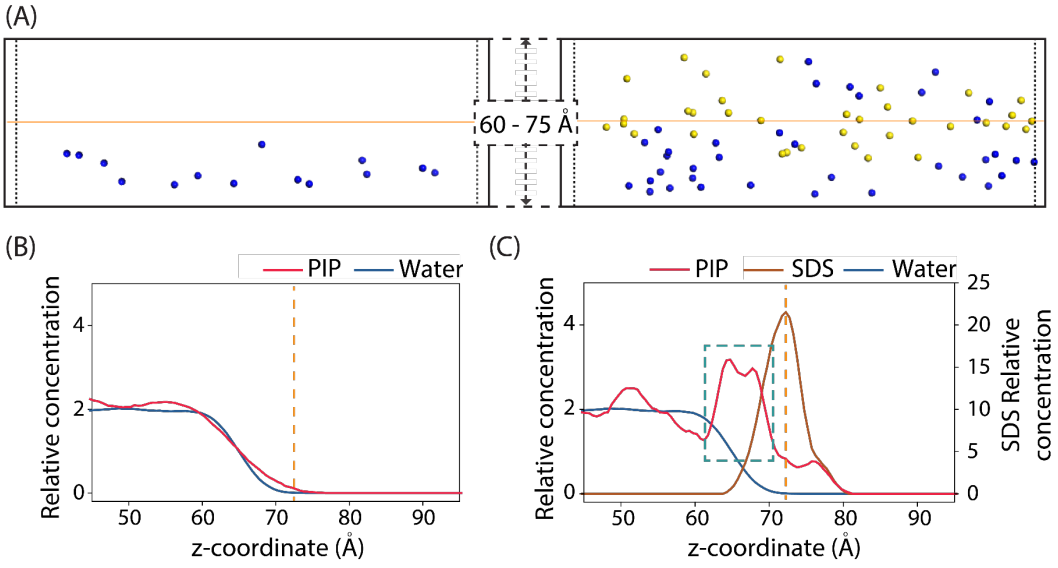

Figure A.6 (A) Distribution of PIP in the two MD models at equilibrium. Left: no SDS; Right: with SDS network. (B) Relative concentration of PIP (red) and water (blue) molecules close to the water/hexane interface in the absence of SDS. (C) Relative concentration of PIP (red), water (blue), and SDS (Orange) molecules close to the water/hexane interface.

To further explore the effect of the SDS dynamic network on the kinetics of PIP interfacial diffusion, we calculated the binding energy ($E_{binding}$) of a PIP molecule to its surroundings at three sites: PIP bulk solution (site 1), water/hexane interface with and without SDS (site 2), and hexane (site 3).

$$E_{binding} = E_{X+pip} - E_X - E_{pip} \quad (10)$$

where E_{pip} is the energy of one PIP molecule, E_{X+pip} is the total energy of the system including the PIP molecule and its surrounding, and E_X is the energy of the system without the PIP molecule, respectively.

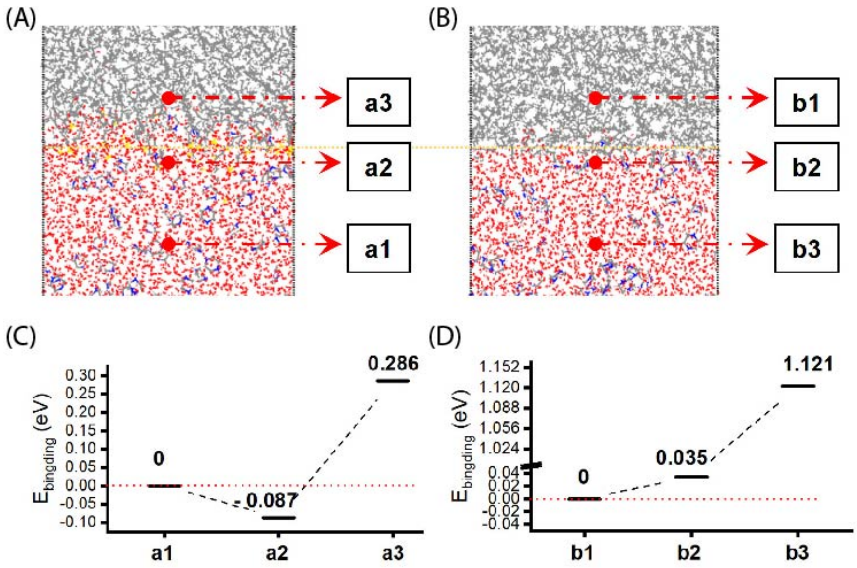

Figure A.7 Binding energy of one PIP molecule to its surrounding in the two MD systems, (A, C) with a self-assembled network of SDS at water-hexane interface, (B, D) without SDS network, at three sites: a1, b1, water; a2, b2, water/hexane interface; a3, b3, hexane.

In the presence of an SDS dynamic network, $E_{binding}$ at the water/hexane interface (site a2), is calculated to be negative, which indicates that the transport of PIP molecules from bulk solution towards the interface is an energetically favorable process. This result is in good

agreement with the locally concentrated population of PIP molecules near the interface. The further transport of a PIP molecule from the water/hexane interface into hexane needs to overcome an additional binding energy penalty of 0.29 eV with the presence of SDS network. Whereas, in the MD system without SDS network, the energy of PIP molecules at the interface is higher than that in the bulk solution, meaning that transport of PIP molecules to the interface is energetically unfavorable. The energy gain for a PIP to transport from the interface into hexane is 1.12 eV in the absence of SDS network, more than three times larger than that with SDS. Therefore, the formation of a self-assembled SDS network at the water/hexane interface reduces the energy required for PIP to diffuse across the water/hexane interface.

While the results presented in Figure A.7 (C, D) seem to suggest that the diffusion of PIP from the aqueous to the hexane phase is both energetically unfavorable, the MD simulation performed to generate these results only consider the interaction between a PIP molecule and its medium but does not consider the effect of concentration gradient and the polymerization reaction in the hexane phase that depletes the PIP in hexane. The overall diffusion-reaction process is still energetically favorable if both the enthalpic (i.e., binding energy) and entropic contributions are considered. While the MD simulation of the entire diffusion-reaction process is technically highly challenging, the simulation of the binding energy presented in Figure A.7 is meant to semi-quantitatively show that the presence of the SDS will dramatically reduce the enthalpic gain of the diffusion and thus reduce the barrier of Gibbs free energy for the diffusion-reaction process.

(b) Calculation of surface excess concentration (SEC)

The adsorption of surfactant molecules at the interface is driven by reducing the Gibbs free energy of the system[268–270]. Therefore, the concentration of surfactants at the interface is much higher than that of the bulk volume. Such difference of the concentration at the surface and any virtual interface in the bulk volume is called the surface excess concentration (SEC), Γ,

$$\Gamma = \Gamma_{\mathrm{I}} - \Gamma_{\mathrm{V}} \tag{8}$$

where the Γ_{I} is the interfacial concentration and Γ_{V} is the concentration at a virtual interface in the bulk solution.

The surface excess concentration is directly related to the interfacial surface tension (IFT) and can be calculated with the Gibbs adsorption isotherm equation[268]:

$$\Gamma = -\frac{1}{nRT}\frac{d\sigma}{dln(C)} \tag{9}$$

where the σ is the interfacial surface tension ($mN \cdot m$), C is the surfactant molar concentration in the bulk ($mol\,L^{-1}$), T is the absolute temperature (K), R is the universal gas constant and n depends on the type of surfactant. (For ionic surfactants without extra electrolytes, like SDS, CTAB, etc., n equals 2)

Table A.5 Surface excess concentration results calculated from IFT data (Figure A.13).

Type of surfactant (CMC)	*SDS (8.2 mM)*	*CTAB (0.92 mM)*	*SB3-14 (0.4 mM)*	*SDBS (1.2 mM)*
SEC ($x10^{-6}$ mol m^{-2})	1.82	1.64	1.47	1.50

(c) Density Functional Theory (DFT) modeling of the interaction between PIP and SDS

To get the insight of how the interaction between a PIP molecule and an SDS molecule changed during the transport of PIP from water to hexane, we also performed a DFT simulation with Dmol modules in Material Studio. The molecular Frontier Orbital of the PIP molecule and SDS molecule was calculated first in order to identify the population of the Highest Occupied Molecular Orbital (HOMO) and the Lowest Unoccupied Molecular Orbital (LUMO). As shown in Fig S9 (a), in a PIP molecule, HOMO was located on the top area close to N and H atoms, and LUMO was located on the lateral area of the circle (Figure A.8B). In an SDS molecule, HOMO was located on the O atoms and LUMO was located in the middle of the alkane backbone (Figure A.8C, D).

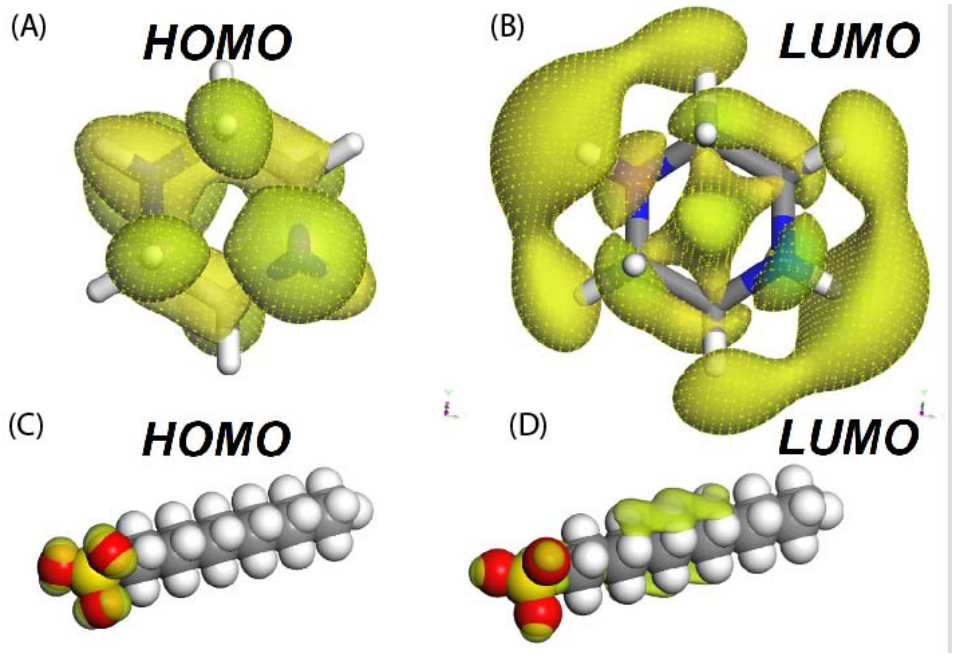

Figure A. 8 Schematic illustration of HOMO and LUMO orbitals in the PIP and SDS molecule.

To simplify the DFT calculation, the transport of one PIP molecule along one SDS molecule was divided into three parts according to the location of PIP relative to SDS (Figure A.10). Part 1 described the attraction between the SDS sulfate group and the PIP molecule in bulk solution (The

distance between pip and SDS is around 5Å); Part 2 was the engagement of the PIP molecule with the sulfate group; and in part 3, five different sites along the SDS alkane backbone were selected to discuss the change of interaction between PIP and SDS during transport. The adsorption energy (E_{ads}) of PIP at each site was calculated by the following equation,

$$\mathrm{E_{ads}} = E_{*+\text{pip}} - E_{*} - E_{\text{pip}} \tag{11}$$

where E_{pip} was the energy of a single PIP molecule, $E_{*+\text{pip}}$ was the energy of the SDS molecule with the adsorption of PIP, and E_{*} was the corresponding energy of the SDS molecule without adsorption of PIP.

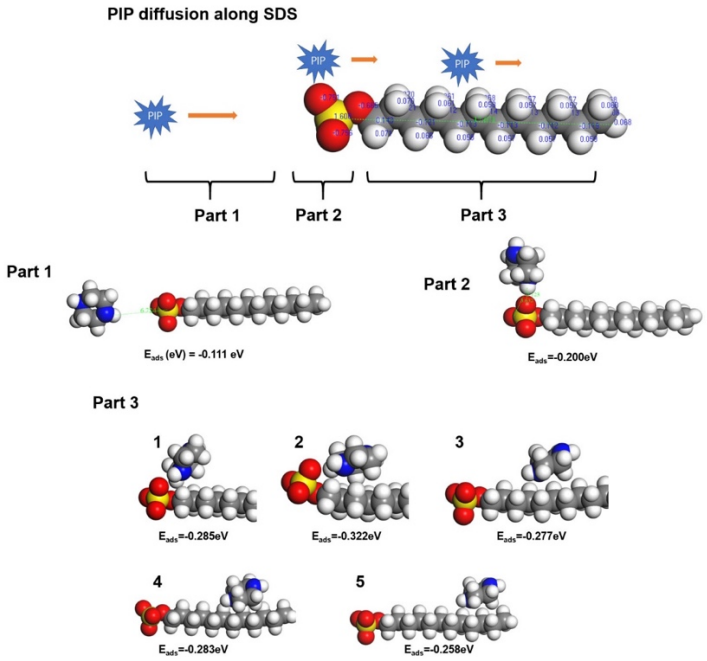

Figure A.9 Adsorption energy of a PIP molecule to a SDS molecule during the transport from water to hexane.

The negative adsorption energy in part 1 revealed the electrostatic attraction between the SDS sulfate group and PIP in bulk solution. The adsorption energy from part 1 to part 2 decreased because of the overlap of PIP's LUMO orbital and SDS's HOMO orbital. As the PIP molecule

kept going along the SDS backbone, the adsorption energy started to increase when SDS's LUMO orbital triggered the overlap with PIP's HOMO orbital. This was in good agreement with the adsorption configuration. Combing the analysis from Molecular Frontier Orbital and the calculation of adsorption energy by DFT, we can interpret the formation of an SDS self-assembled network promoted the diffusion of PIP from water to hexane.

(d) Monte Carlo simulation of molecular diffusion across interface with different levels of energy barriers

With the results from the MD and DFT simulations consistently showing that the presence of SDS may reduce the energy barrier for PIP diffusion across the water/hexane interface, we perform simplified Monte Carlo (MC) simulations to illustrate why a lower energy barrier for diffusion can lead to more homogenous diffusive flux. In such an MC simulation, a group of generic particles (mimicking PIP molecules) attempt to pass a grid of cells (10 × 10 in this study) with a certain energy barrier, ΔE_B. We assume that the intrinsic kinetic energy of these particles follows a Maxwell-Boltzmann distribution as expressed in the following equation

$$\frac{dN}{N} = \left(\frac{m}{2\pi k_B T}\right)^{1/2} exp\left(-\frac{mv^2}{2k_B T}\right) dv$$

where dN/N is the fraction of PIP molecules moving at velocity v to $v + dv$, m is the mass of the PIP molecule, k_B is the Boltzmann constant and T is the absolute temperature. Therefore, the probability of one PIP molecule moving with a speed of v in three dimensions can be expressed as

$$p(v) = 4\pi \left(\frac{m}{2\pi k_B T}\right)^{3/2} v^2 exp\left(-\frac{mv^2}{2k_B T}\right)$$

For each "diffusion attempt" across a cell in the grid, we randomly assign kinetic energy to a particle according to the Maxwell-Boltzmann distribution. If the energy of that particle is higher than the energy barrier (i.e., $\varepsilon_i > \Delta E_B$), the attempt is considered as successful and one additional particle is recorded as passing that specific cell. Otherwise, the attempt is considered as a failure and we move onto the next cell for the next "diffusion attempt". Each cell has one diffusion attempt in each round (which comprises 100 attempts). The simulation continues until 1,000 particles have successfully "diffused" across the 10 × 10 grids, resulting in an average of 10 particles per grid.

With the cumulative number of successful diffusions for each cell, we create a map of "diffusion flux" for the grid, with an example shown in Figure 3 (F) in the main text. The value of E_B has an impact on the distribution of diffusion flux, with a higher E_B leading to a more heterogeneous of diffusion flux and a lower E_B resulting in a more homogeneous diffusion flux. The heterogeneity can be quantified by calculating the standard deviation of the number of successful diffusions for different grids. We perform such simulations for a range of E_B to obtain the standard deviation and the total number of diffusion attempts (to generate 1,000 successful

diffusions) for each E_{B}. The results presented in Figure 3 (E) in the main text show that a lower E_B leads to both faster diffusion (as quantified by fewer diffusion attempts) and a more homogeneous distribution of diffusion flux (as quantified by a lower standard deviation).

Notes: The MC simulations described above are highly simplified and are meant to illustrate qualitatively how reducing energy barrier leads to more uniformly distributed diffusion of molecules across an interface. The impact of the level of energy barrier on diffusion homogeneity may likely be even more significant due to the "positive feedback" mechanism. Specifically, when a PIP molecule successfully diffuses across an interface and reacts with TMC, a considerable amount of heat will be generated locally as the reaction of PIP and TMC is strongly exothermic. A large fraction of such released heat may propagate back to the water phase near the water/hexane interface (water is significantly more thermally conductive than hexane) and thereby increase the local temperature. The increased local temperature will result in higher thermal energy for the particles attempting to diffuse across and thus enhance the chance of successful subsequent diffusion. In short, a successful diffusion event will facilitate further successful diffusion near the same location, which is a positive feedback mechanism that tends to make the diffusion more heterogeneous. Accurately modeling this positive feedback mechanism is difficult and adds little to the already-highly-simplified MC simulation that is only qualitatively meaningful. We, therefore, do not attempt to perform such a simulation but only discuss the mechanism qualitatively.

f. Control experiment: Poly(piperazine-amide) nanofiltration membrane from conventional IP

(a) XPS chemical characterization of the PA active layer from conventional IP

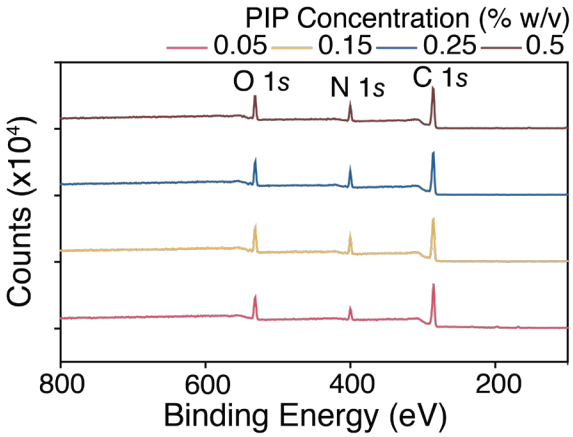

Figure A.10 XPS survey of polyamide active layer prepared via conventional IP as a function of PIP concentration.

(b) Calculation of degree of cross-linking of polyamide network

Table A.6 The elemental composition results and calculation of crosslinking degree of polyamide network obtained using conventional IP.

	C(%)	*N(%)*	*O(%)*	*S(%)*	*Br(%)*	*Degree of crosslinking*
PIP 0.05%	73.05	10.58	15.4	0.97	0	0.44
PIP 0.15%	71.08	12.59	15.87	0.45	0	0.65
PIP 0.25%	70.24	13.63	15.96	0.17	0	0.76
PIP 0.5%	71.16	13.82	14.87	0.15	0	0.89

(c) MWCO and pore size of TFC-PA membrane from conventional IP and SARIP (with SDS)

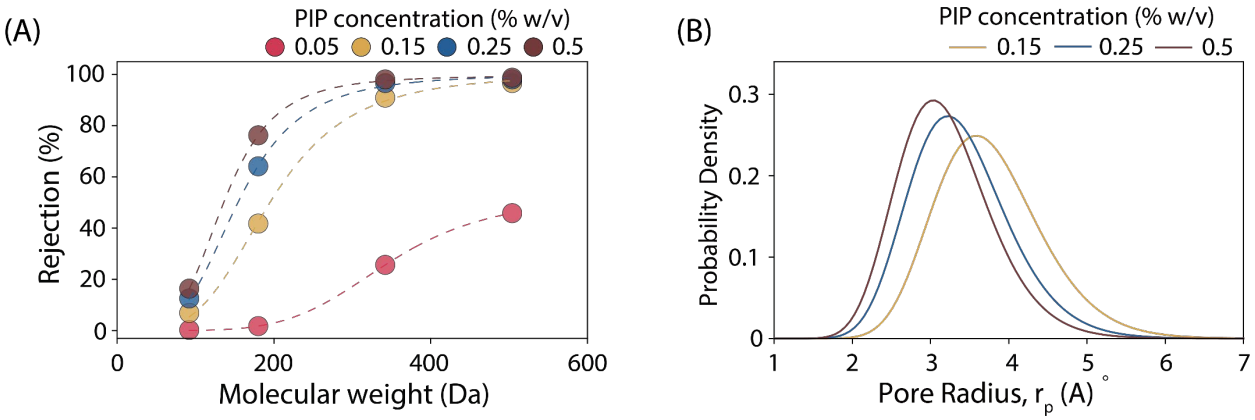

Figure A.11 (A) Rejection of neutral organic solutes of different MW by TFC-PA membranes fabricated using conventional IP with different PIP concentrations. (B) Pore size distribution estimated with data presented in (A).

Table A.7 Mean pore size, standard deviation and MWCO of TFC-PA membrane from conventional IP with different PIP concentrations.

PIP Concentration (% w v^{-1})	μ_p (nm)	σ_p	*MWCO*
0.05	N/A	N/A	N/A
0.15	0.371	1.200	346
0.25	0.334	1.219	274
0.5	0.314	1.207	232

(d) Ion selectivity of TFC-PA membrane from conventional IP

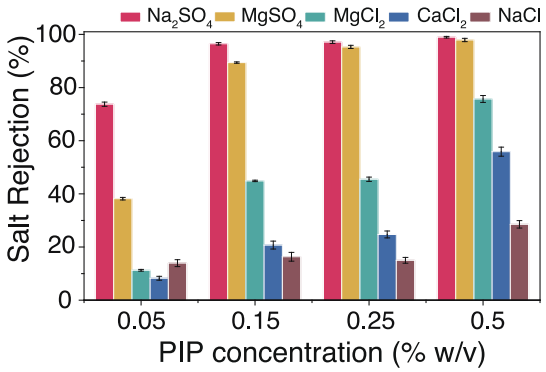

Figure A.12 Rejection of different solutes by TFC-PA membranes fabricated using conventional IP with different PIP concentrations.

Increasing the PIP concentration in IP increases the rejection of all ions systematically (Figure A.12), which is attributable to a higher degree of crosslinking of the PA layer (Table A.7) and smaller mean pore size (Figure A.11 A,C). However, even with the highest PIP concentration (0.5 % w v^{-1}, twice as the concentration used in SARIP), the rejection of Mg^{2+} and Ca^{2+} is still moderate as compared to that with TFC-PA membrane obtained using SARIP (with SDS). Therefore, even though one of the effects of SDS interfacial network is to enhance the interfacial concentration of PIP, the increase of PIP concentration at the interface is not the only mechanism for achieving a step-wise selectivity (e.g., Figure A.1B with 0.25 CMC of SDS) that is required for precise ion or molecular separation.

g. Interfacial Surface Tension (IFT) of piperazine aqueous solution and hexane with the addition of varieties of surfactants

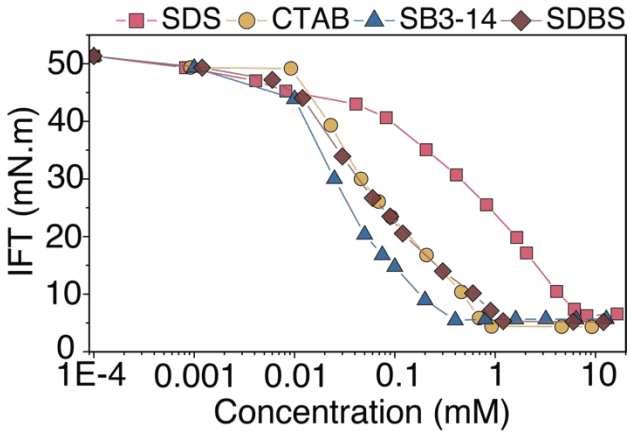

Figure A.13 IFT of hexane and piperazine aqueous solution with the addition of various concentrations of surfactants.

h. Wettability of piperazine aqueous solution on polyethersulfone ultrafiltration substrates with addition of various surfactants

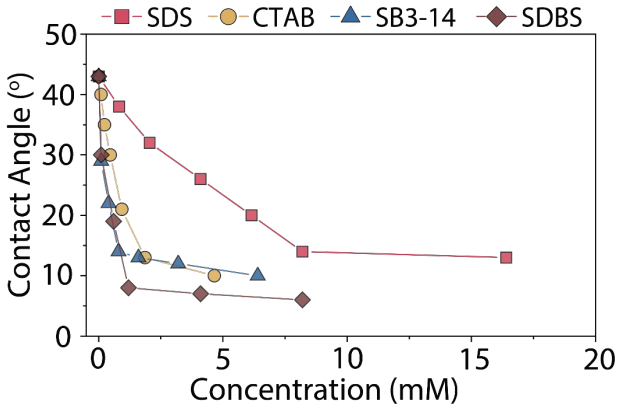

Figure A.14 Wettability of piperazine aqueous solution on polyethersulfone ultrafiltration substrate with addition of various surfactants. The addition of surfactants into the PIP aqueous solution lowers the water contact angle on the PES substrate. It indicates that the PIP solution could spread out better on the PES substrate, which leads to a complete water film and a more uniform distribution of PIP molecules on the substrate.

Table A.8 Water contact angle (WCA) of PIP solution on the PES substrate as a function of PIP concentration. Increasing PIP concentration did not affect the wettability of PIP solution on the PES substrate.

PIP Concentration (% w v^{-1})	*0%*	*0.05%*	*0.15%*	*0.25%*	*0.5%*
WCA	43 ± 2	37 ± 2	36 ± 2	36 ± 2	35 ± 2

i. Poly(piperazine-amide) nanofiltration membrane from SARIP (with SDBS)

(a) Ion selectivity and permeate flux of TFC-PA membrane from SARIP (with SDBS)

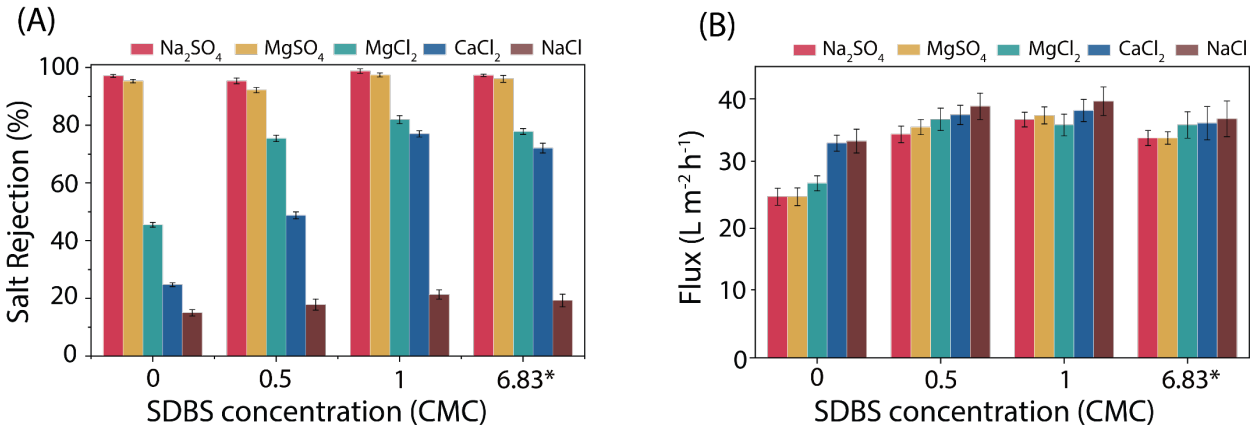

Figure A.15 (A) Rejection of different solutes by TFC-PA membrane fabricated using SARIP with different SDBS concentrations (B) permeate flux of TFC-PA membrane fabricated using SARIP with different SDBS concentrations. The flux was measured using different feed solution with a hydraulic pressure of 4 bar. *Note: The concentration of 6.83 CMC for SDBS corresponds to the same molar concentration (8.2 mM) as 1 CMC for SDS.

(b) MWCO and pore size of TFC-PA membrane from SARIP (with SDBS)

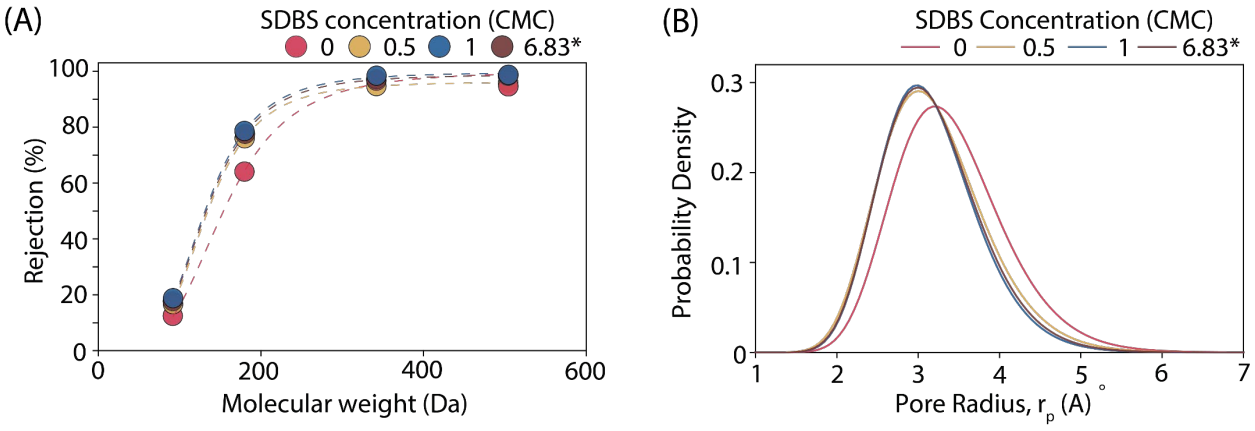

Figure A.16 (A) Rejection of neutral organic solutes of different MW by TFC-PA membrane fabricated using SARIP (with SDBS) with different SDBS concentrations. (B) Pore size distribution estimated with data presented in (A). *Note: The concentration of 6.83 CMC for SDBS corresponds to the same molar concentration (8.2 mM) as 1 CMC for SDS.

Table A.9 Mean pore size, standard deviation and MWCO of TFC-PA from SARIP with different SDBS concentrations (corresponding to Figure A.16A, B).

SDBS Concentration (CMC)	μ_p (nm)	σ_p	MWCO (Da)
0	0.334	1.219	274
0.5	0.313	1.224	246
1	0.309	1.208	224
6.83 (~ 8.2 mM, 1 CMC for SDS)	0.311	1.213	231

Similar to the effect of SDS on the formation of polyamide membranes, the pore size of TFC-PA from SARIP with SDBS became smaller than that of conventional TFC-PA. However, the relative low packing density of SDBS molecules (low surface excess concentration) leading to a less increase of PIP diffusion gradient, and the steric hindrance of the benzene ring on each SDBS molecule increased the diffusion difficulty. Therefore, the effect of SDBS on regulating the

diffusion rate and uniformity of PIP was less effective than that of SDS. It could also be treated as a less reduction of diffusion activation energy in the Monte Carlo simulation.

(c) XPS chemical characterization of the PA active layer from SARIP (with SDBS)

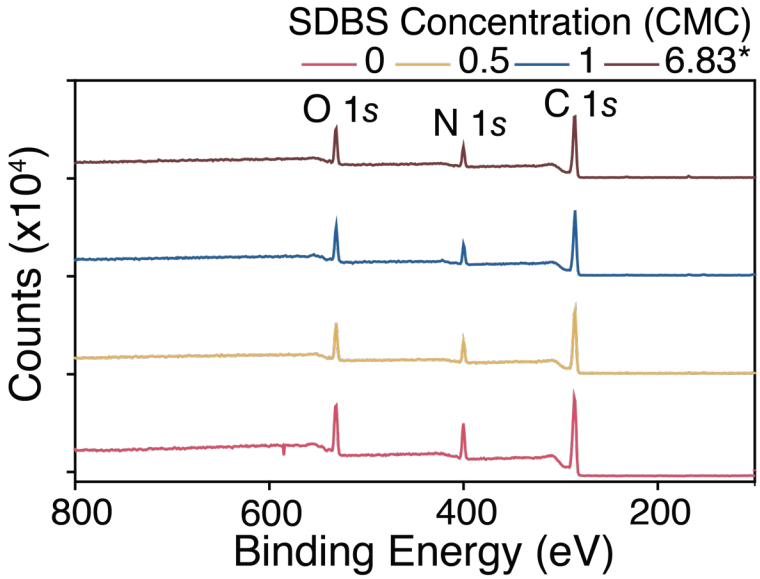

Figure A.17 XPS survey of polyamide active layer from SARIP as a function of SDBS concentration. *Note: The concentration of 6.83 CMC for SDBS corresponds to the same molar concentration (8.2 mM) as 1 CMC for SDS.

(d) Calculation of degree of cross-linking of polyamide network

Table A.10 The elemental compositions and crosslinking degree of polyamide network from SARIP with SDBS.

SDBS concentration (CMC)	*C(%)*	*N(%)*	*O(%)*	*S(%)*	*Br(%)*	*Degree of crosslinking*
0	70.24	13.63	15.96	0.17	0	0.76
0.5	72.62	12.36	14.66	0.36	0	0.74
1	71.9	12.8	14.8	0.49	0	0.78
6.83 (~ 8.2 mM, 1 CMC for SDS)	71.41	12.87	14.98	0.73	0	0.77

j. Poly(piperazine-amide) nanofiltration membrane from SARIP (with CTAB)

(a) Ion selectivity and permeate flux of TFC-PA membrane from SARIP (with CTAB)

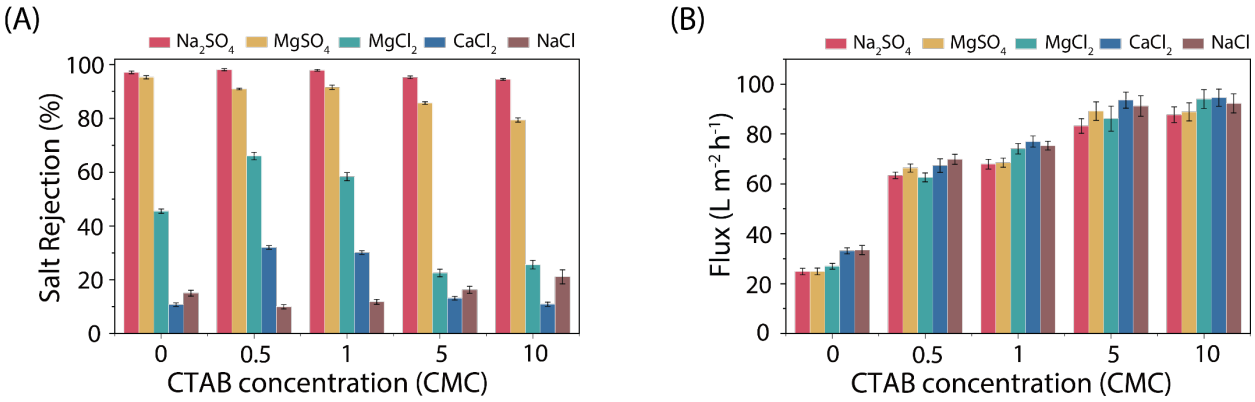

Figure A.18 (A) Rejection of different solutes by TFC-PA membrane fabricated using SARIP with different CTAB concentrations (B) permeate flux of TFC-PA membrane fabricated using SARIP with different CTAB concentrations. The flux was measured using different feed solution with a hydraulic pressure of 4 bar.

On the contrary to the function of SDS, the cationic surfactant, CTAB, exhibited the opposite effect on the ion selectivity performance of TFC-PA membranes from SARIP. In Figure A.18, an increase of CTAB concentration used in SARIP reduced the rejection of Na_2SO_4 and $MgSO_4$, and the rejection of $MgCl_2$, $CaCl_2$ and NaCl only increased a little at low concentrations and then dropped drastically. The initial increase of rejection of divalent ions and decreasing rejection of Na_2SO_4 and $MgSO_4$ could be caused by the change of surface charge density. In Figure A.26, the surface of TFC-PA from SARIP with CTAB was less negatively charged at the pH of 7. Such an increase in surface charge could be caused by the implementation of CTAB molecules into the polyamide network. Since the hydrophilic-lipophilic balance value of CTAB was 10 (HLB<10: water-insoluble and HLB>10: lipid insoluble), thus CTAB was a good O/W emulsifier. During the contact of aqueous PIP and organic phase TMC during interfacial polymerization, CTAB molecules were very likely to dissolve in hexane and competed with PIP to react with TMC. TFC-PA membrane prepared via SARIP with CTAB had a lower crosslinking degree and an increase of O/N ratio than that of the TFC-PA membrane prepared via conventional IP because

each CTAB molecule had one-half of nitrogen atoms than a PIP molecule when they reacted with TMC. The presence of CTAB molecules in polyamide network added more free volumes and reduced the surface negative charge. Overall this caused the reduction of rejection of $MgSO_4$ and Na_2SO_4 and higher selectivity of $MgCl_2$ and $CaCl_2$ at a low concentration of CTAB. As the concentration of CTAB increased, the more CTAB molecules reacted with TMC in hexane, causing more defects in the polyamide network, leading to the increasing reduction of ion selectivity of the polyamide nanofiltration membrane.

(b) MWCO and pore size of TFC-PA membrane from SARIP (with CTAB)

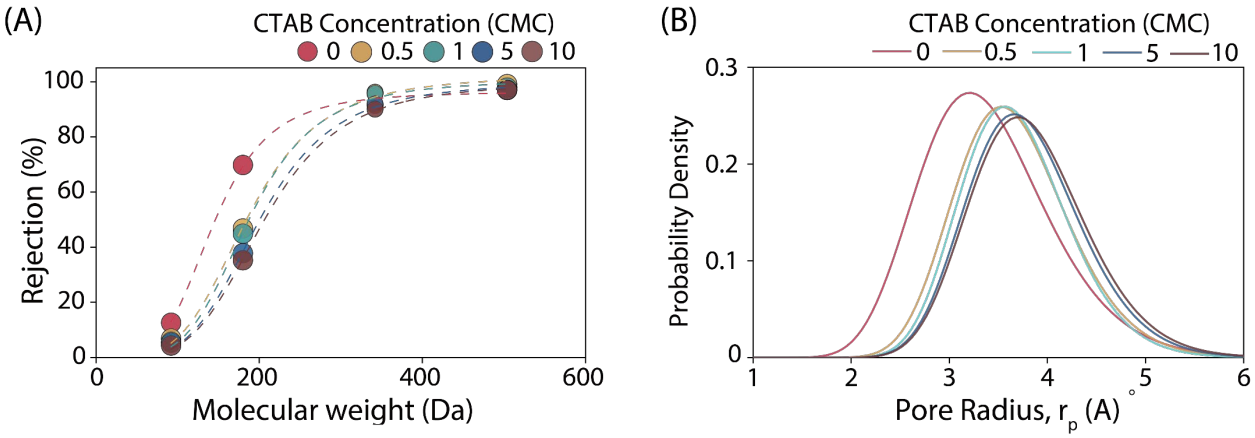

Figure A.19 (A) Rejection of neutral organic solutes of different MW by TFC-PA membrane fabricated using SARIP (with CTAB) with different CTAB concentrations. (B) Pore size distribution estimated with data presented in (A).

Table A.11 Mean pore size, standard deviation and MWCO of TFC-PA membrane from SARIP with different CTAB concentrations (corresponding to Figure A.19A, B).

CTAB concentration (CMC)	μ_p (nm)	σ_p	MWCO (Da)
0	0.334	1.219	274
0.5	0.362	1.194	303
1	0.365	1.201	301
5	0.375	1.206	335
10	0.379	1.208	347

(c) XPS chemical characterization of PA active layer from SARIP (with CTAB)

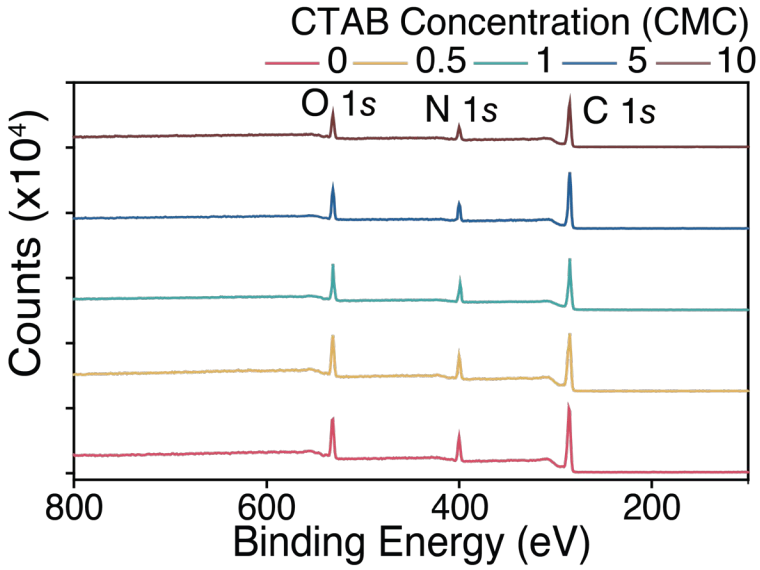

Figure A.20 XPS survey of polyamide active layer from SARIP as a function of CTAB concentration.

(d) Calculation of degree of cross-linking of polyamide network

Table A.12 The elemental composition and crosslinking degree of polyamide network from SARIP with CTAB. The Bromine composition increased with the increase of CTAB concentration used in the SARIP.

CTAB Concentration (CMC)	*C(%)*	*N(%)*	*O(%)*	*S(%)*	*Br(%)*	*Degree of crosslinking*
0.5	71.46	12.51	15.88	0.12	0.03	0.64
1	72.5	12.08	15.12	0.23	0.07	0.66
5	75.15	10.44	14.1	0.26	0.05	0.55
10	74.7	10.62	14.28	0.31	0.1	0.56

(e) Cross-sectional TEM images of TFC-PA membranes from SARIP (with CTAB)

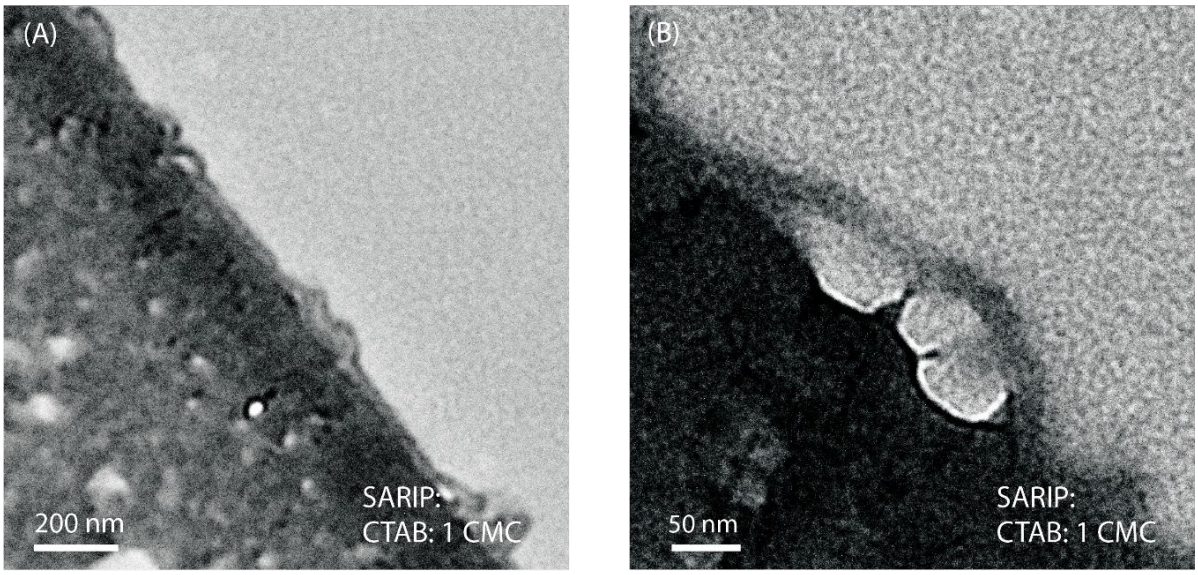

Figure A.21 Cross-sectional TEM images of TFC-PA membrane obtained using SARIP with CTAB (concentration: 1 CMC). Large voids were observed in the PA active layer, which contributed to the increase of membrane flux.

k. Poly(piperazine-amide) nanofiltration membrane from SARIP (with SB3-14)

(a) Ion selectivity and permeate flux of TFC-PA membrane from SARIP (with SB3-14)

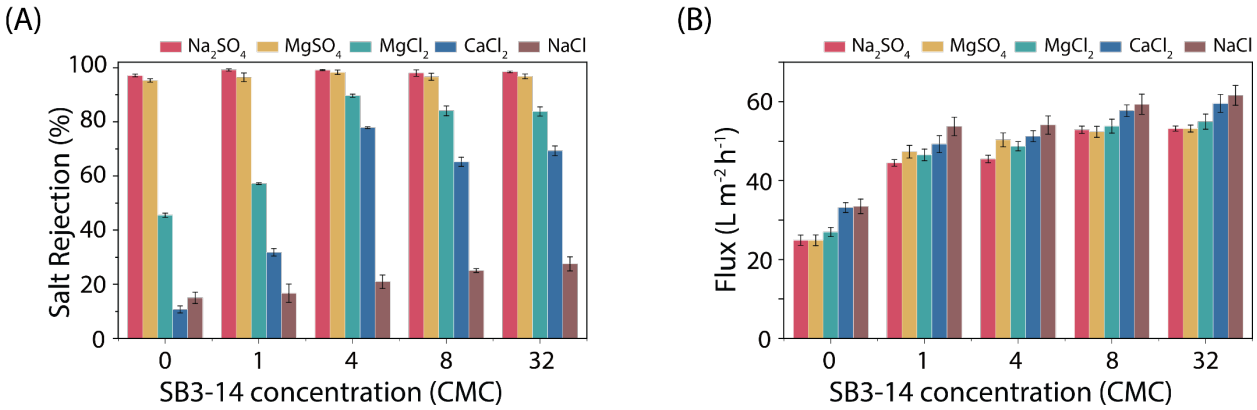

Figure A.22 (A) Rejection of different solutes by TFC-PA membrane fabricated using SARIP with different SB3-14 concentrations (B) permeate flux of TFC-PA membrane fabricated using SARIP with different SB3-14 concentrations. The flux was measured using different feed solution with a hydraulic pressure of 4 bar.

A zwitterionic surfactant was also explored to strengthen the gap between the cationic and anionic surfactant. Sulfobetaine 3-14 was chosen because it had a cationic tertiary amine group like CTAB and an anionic sulfate group like SDS, and its unique molecular structure did not form an intramolecular bond between its cationic group and anionic group. The HLB value of SB3-14 was 48.45 calculated with Davie's method, which was larger than the HLB value of SDS (40). Therefore, it was unlikely for SB3-14 to dissolve in hexane and interrupt the reaction between PIP and TMC (No sulfate element was detected in the XPS data). The general trend of the ion rejection of TFC-PA from SARIP with SB3-14 resembled the result of TFC-PA from SARIP with SDS. The pore size of TFC-PA prepared from SARIP with SB3-14 was slightly reduced than that of TFC-PA prepared from conventional IP as well as the pore size distribution, which contributed to the increase of ion selectivity.

(b) MWCO and pore size of TFC-PA membrane from SARIP (with SB3-14)

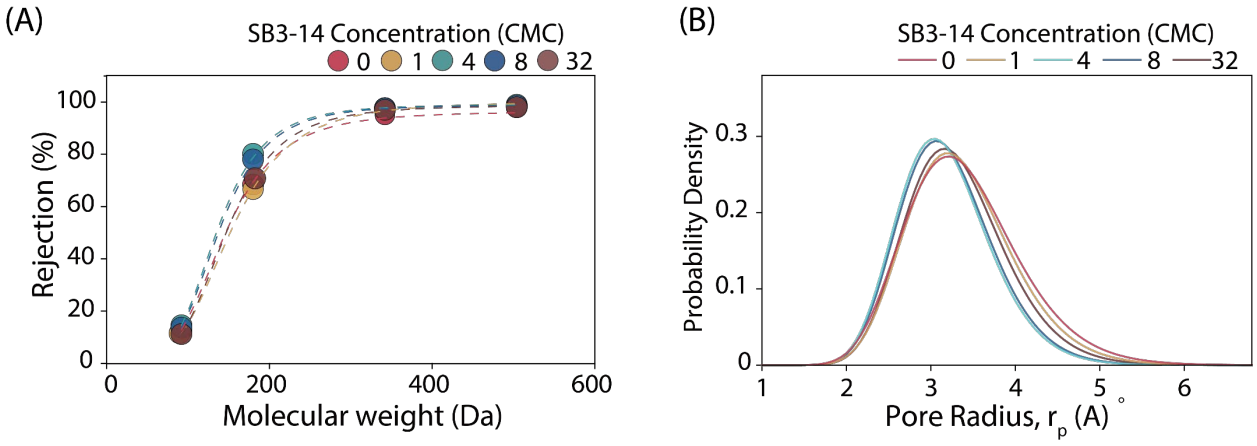

Figure A.23 (A) Rejection of neutral organic solutes of different MW by TFC-PA membranes fabricated using SARIP (with SB3-14) with different SB3-14 concentrations. (B) Pore size distribution estimated with data presented in (A).

Table A.13 Mean pore size, standard deviation and MWCO of TFC-PA membrane from SARIP as a function of SB3-14 concentration. (corresponding to Figure A.23 A, B)

SB3-14 concentration (CMC)	μ_p *(nm)*	σ_p	*MWCO (Da)*
0	0.334	1.219	274
1	0.331	1.204	259
4	0.313	1.189	220
8	0.316	1.190	226
32	0.326	1.196	246

The pore size of TFC-PA membrane from SARIP with SB3-14 decreased compared to TFC-PA membrane from conventional IP, so was the pore size distribution. The effect of SB3-14 on the formation of polyamide during interfacial polymerization resembled the function of SDS molecules, but less effectively. A monolayer of self-assembled SB3-14 network at the water/hexane interface attracted the PIP molecules to their hydrophilic ends, leading to an increase

of PIP diffusion gradient. However, transport of PIP molecules along the SB3-14 chain was arduous because of the electrostatic repulsion from the cationic tertiary amine group. Such a trade-off effect could be treated as a less pronounced reduction of the diffusion energy barrier compared with the effect of SDS self-assembly network. Based on the result from the Monte Carlo simulation, presence of SB3-14 self-assembly network at the water/hexane interface resulted in the formation of polyamide network with higher crosslinking density, smaller pore sizes, and narrower pore size distribution compared with the conventional IP, but not as good as the SDS self-assembly network.

(c) XPS chemical characterization of PA active layer from SARIP (with SB3-14)

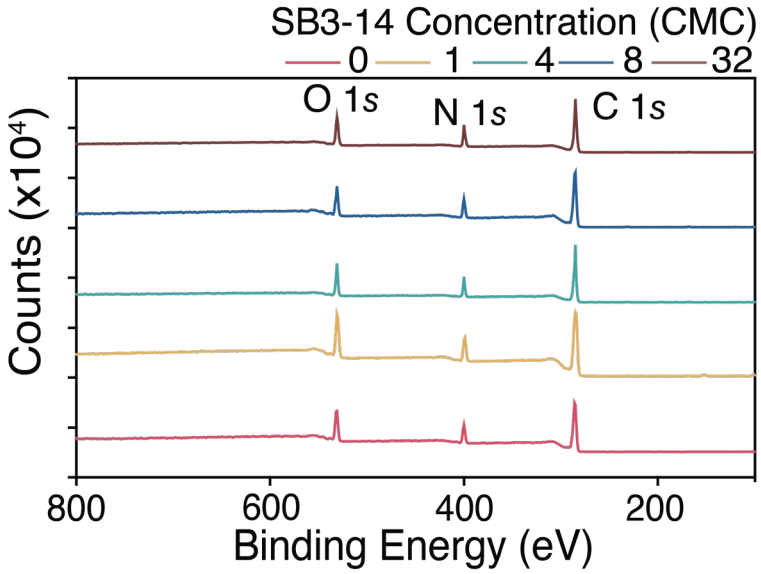

Figure A.24 XPS survey of polyamide active layer prepared from SARIP as a function of SB3-14 concentration.

l. Calculation of degree of cross-linking of PA active layer

Table A.14 The elemental composition and crosslinking degree of polyamide network from SARIP with SB3-14.

SB3-14 Concentration (CMC)	*C(%)*	*N(%)*	*O(%)*	*S(%)*	*Br(%)*	*Degree of crosslinking*
0	70.24	13.63	15.96	0.17	0	0.76
1	71.56	12.94	15.3	0.19	0	0.75
4	73.24	12.06	14.29	0.41	0	0.75
8	72.63	12.58	14.43	0.36	0	0.79
32	71.58	12.9	15.04	0.48	0	0.77

(a) Cross-sectional TEM images of TFC-PA membrane from SARIP (with SB3-14)

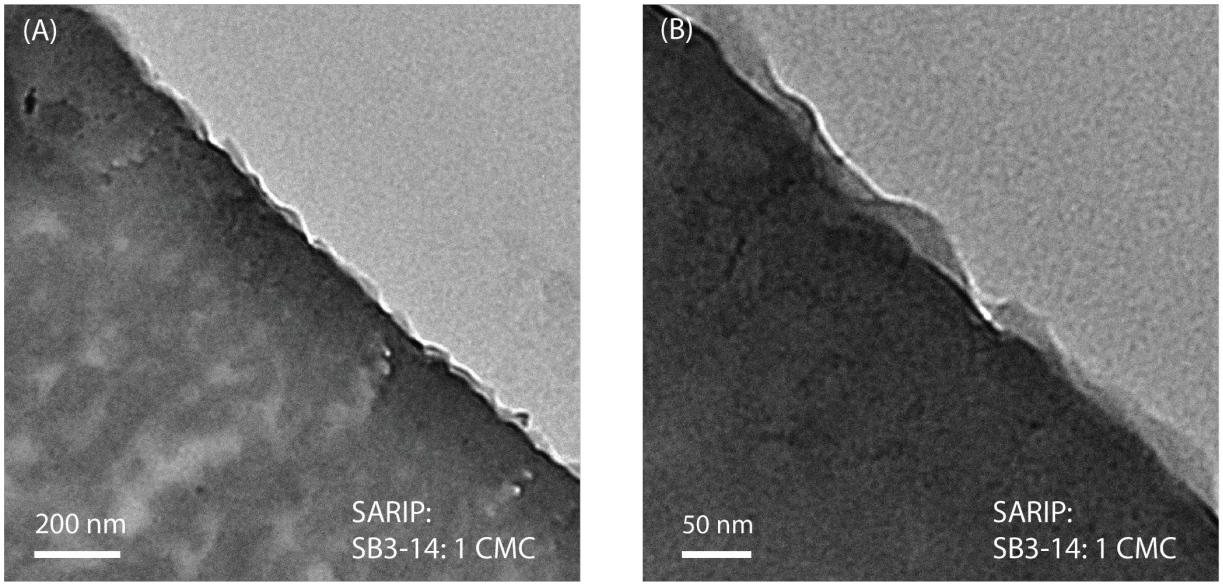

Figure A.25 Cross-sectional TEM images of TFC-PA membrane prepared from SARIP with SB3-14 (concentration: 1 CMC)

(b) Surface streaming potential of TFC-PA membrane from conventional IP and SARIP

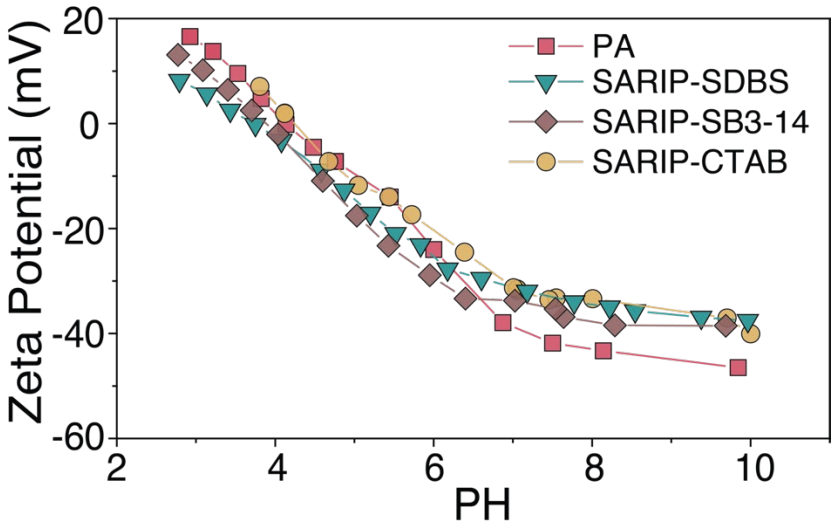

Figure A.26 Surface streaming potential of TFC-PA membranes from conventional IP and SARIP with different surfactants. (CMC concentration for each surfactant)

(c) Pure water permeability of TFC-PA membrane from conventional IP and SARIP

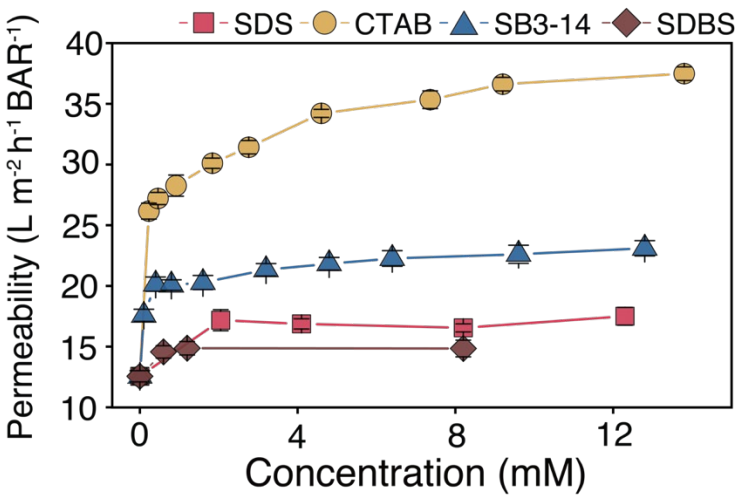

Figure A.27 Pure water permeability of TFC-PA membranes prepared via conventional IP and SARIP (with surfactants) as a function of surfactant concentrations. Note that the critical micelle concentration for each surfactant is 8.2 mM (SDS), 0.92 mM (CTAB), 0.4 mM (SB3-14) and 1.2 mM (SDBS).

m. Poly(piperazine-amide) nanofiltration membrane from conventional IP (with sodium p-toluenesulfonate)

(a) Interfacial property of Sodium p-tolienesulfonate

Table A.15 Contact angle (CA) of PIP solution on the PES substrate as a function of sodium p-toluene sulfonate concentration. The addition of sodium p-toluene sulfonate did not have any significant effect on the wettability of PIP solution on the PES substrate.

TS-Na Concentration (mM) (× CMC for SDS)	*0*	*4.1 (0.5)*	*8.2 (1)*	*12.3 (1.5)*
WCA	43 ± 2	35 ± 2	36± 2	34 ± 2

The addition of sodium p-toluenesulfonate did not change the value of surface tension at different concentrations, indicating that the presence of sulfate groups in the PIP solution did not influence the properties of the interface.

Table A.16 IFT of hexane and piperazine aqueous solution with the addition of sodium p-toluenesulfonate.

TS-Na Concentration (mM) (× CMC for SDS)	*0*	*4.1 (0.5)*	*8.2 (1)*	*12.3 (1.5)*
IFT (mN m)	50.92	50.56	50.29	50.17

(b) Ion selectivity and permeate flux of TFC-PA membrane from conventional IP (with sodium p-toluenesulfonate)

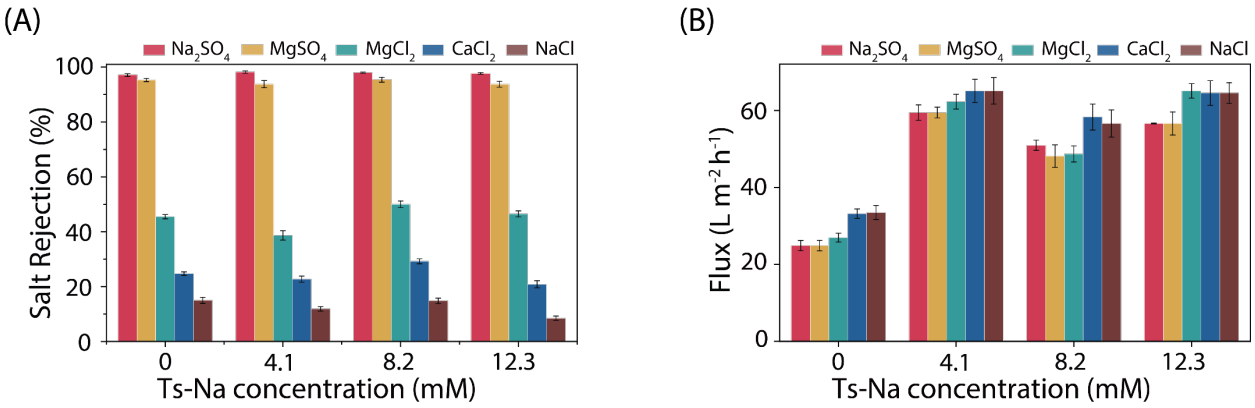

Figure A.28 (a) Rejection of different solutes by TFC-PA membrane fabricated using conventional IP with different sodium p-toluenesulfonate (Ts-Na) concentrations (b) permeate flux of TFC-PA membrane fabricated using conventional IP with different Ts-Na concentrations. The flux was measured using different feed solution with a hydraulic pressure of 4 bar. The concentrations chosen correspond to 0, 0.5, 1.0, and 1.5 of CMC for SDS.

(c) MWCO and pore size of the TFC-PA membrane from conventional IP (with sodium p-toluenesulfonate)

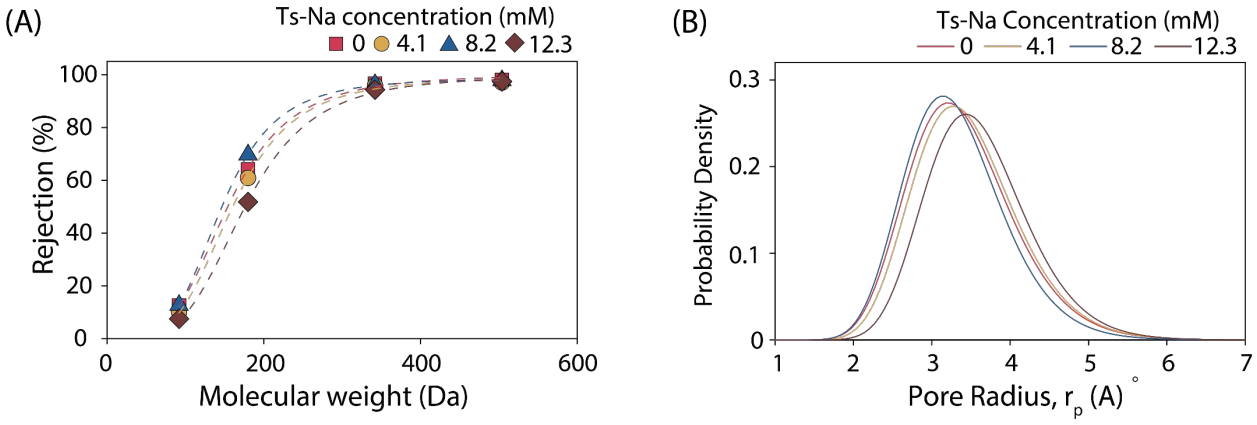

Figure A.29 (A) Rejection of neutral organic solutes of different MW by TFC-PA membranes fabricated using conventional IP (with Ts-Na) with different Ts-Na concentrations. (B) Pore size distribution estimated with data presented in (A). The concentrations chosen correspond to 0, 0.5, 1.0, and 1.5 of CMC for SDS.

Table A.17 Mean pore size, standard deviation and MWCO of TFC-PA membrane from conventional IP with different Ts-Na concentrations. (reference concentration: SDS CMC)

Ts-Na Concentration mM (CMC for SDS)	μ_p *(nm)*	σ_p	*MWCO*
0	0.334	1.219	274
4.1 (0.5)	0.340	1.212	283
8.2 (1)	0.329	1.211	256
12.3 (1.5)	0.355	1.198	306

In Figure A.29, the effect of sodium p-toluenesulfonate on the pore size of TFC-PA was negligible, which agrees with the membrane selectivity data in Figure A.28.

(d) XPS chemical characterization of polyamide active layer from conventional IP (with sodium p-toluenesulfonate)

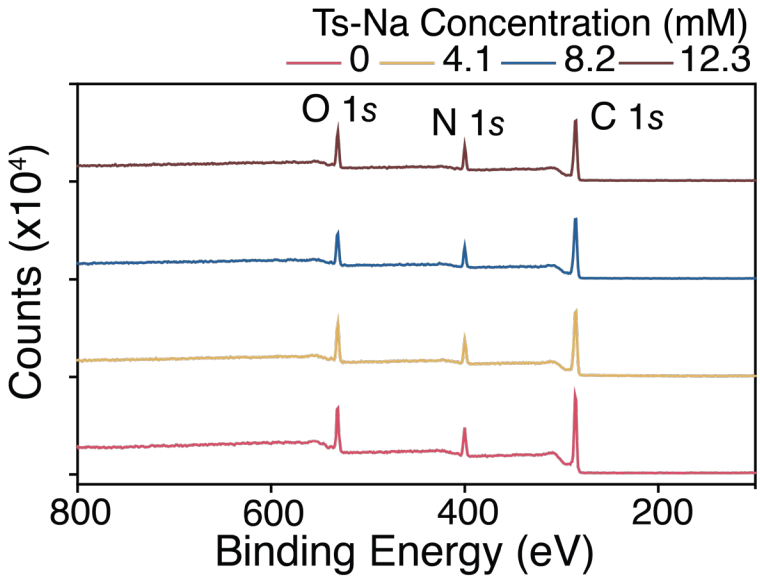

Figure A.30 XPS survey of polyamide active layer from conventional IP as a function of Ts-Na concentration. (reference concentration: SDS CMC)

Table A.18 The elemental composition and crosslinking degree of polyamide active layer from conventional IP with Ts-Na. (reference concentration: SDS CMC)

Ts-Na Concentration mM (CMC for SDS)	*C(%)*	*N(%)*	*O(%)*	*S(%)*	*Br(%)*	*Degree of crosslinking*
0	70.24	13.63	15.96	0.17	0	0.76
4.1 (0.5)	71.75	13.49	14.46	0.3	0	0.90
8.2 (1)	73.4	12.76	13.57	0.27	0	0.90
12.3 (1.5)	71.14	13.86	14.76	0.24	0	0.91

n. Poly(ethylenimine-amide) nanofiltration membrane from conventional IP and SARIP (with SDS)

(a) Ion selectivity and permeate flux of the TFC-PA membrane from conventional IP and SARIP (with SDS)

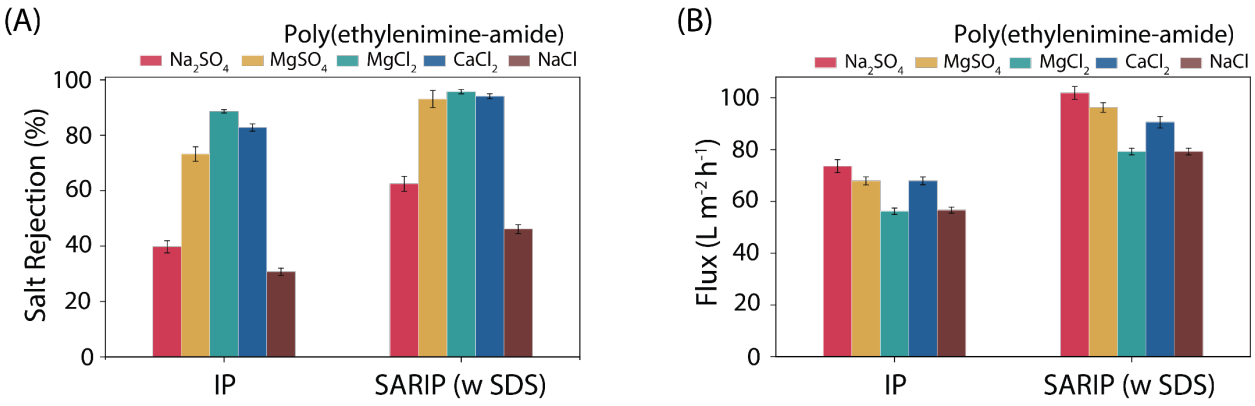

Figure A.31 Comparison of TFC-PA membranes from conventional IP and SARIP with SDS (1 CMC). (A) solute rejection (B) permeate flux.

The effectiveness of SARIP with SDS on increasing the membrane selectivity was proved in the poly(ethyleneimine-amide) nanofiltration system. An increase of salt rejection of TFC-PA membrane from SARIP with SDS was observed.

(b) MWCO and pore size of the TFC-PA membrane from conventional IP and SARIP (with SDS)

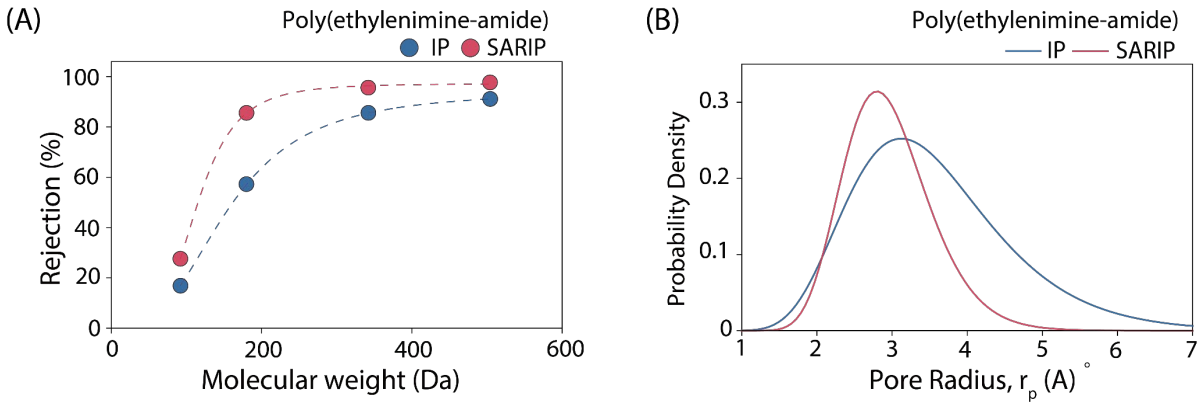

Figure A.32 Comparison of TFC-PA membranes prepared from conventional IP and SARIP with SDS (1 CMC). (A) MWCO and (B) pore size distribution.

Table A.19 Mean pore size, standard deviation and MWCO of the TFC-PA from conventional IP and SARIP with SDS (1 CMC) (corresponding to Figure A.32 A, B).

Poly(ethylenimine-amide)	μ_p *(nm)*	σ_p	*MWCO*
IP	0.341	1.345	449
SARIP	0.291	1.217	203

The TFC-PA membrane prepared via SARIP with SDS had much smaller pores than the TFC-PA membrane prepared via conventional IP: the MWCO was reduced to more than one half of the value of the conventional TFC-PA membrane, i.e., the mean pore size decreased from 0.34 nm to 0.29 nm and the distribution of pore size also decreased from 1.345 to 1.217. This provided another evidence of the role of self-assembled SDS dynamic network on the formation of polyamide with smaller and more uniform pore sizes.

(c) XPS chemical characterization of poly(ethyleneimine-amide) active layer from conventional IP and SARIP (with SDS)

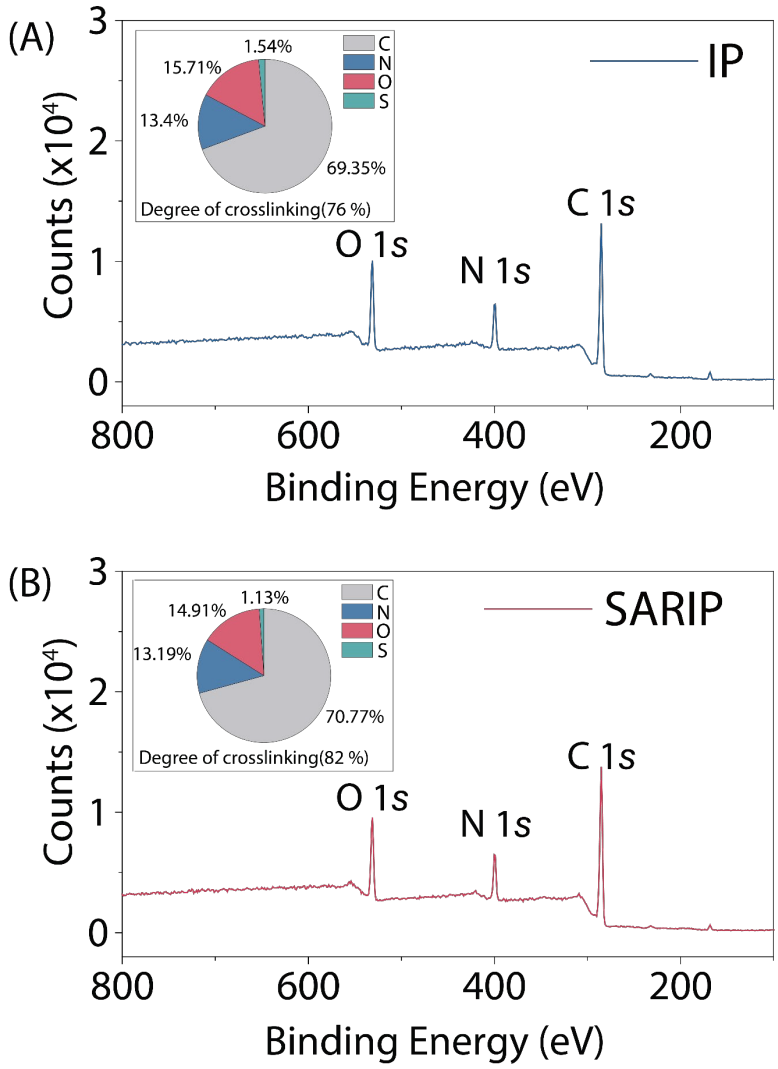

Figure A.33 XPS survey of poly(ethyleneimine-amide) active layers (A) from conventional IP. (B) from SARIP with SDS (1 CMC). The presence of the SDS self-assembled network promoted the formation of the PA network with a higher crosslinking degree.

o. TFC-PA NF membrane prepared via SARIP with 2 CMC SDS

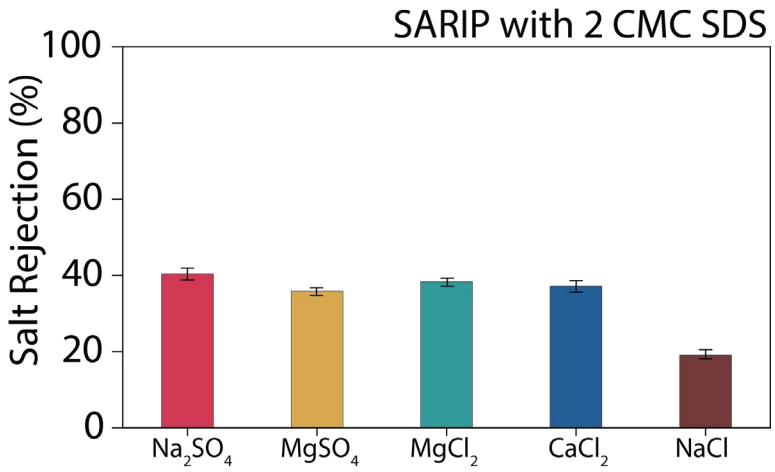

Figure A.34 Rejection of different solutes by TFC-PA membranes fabricated using SARIP with 2 CMC SDS.

p. MWCO and pore size of TFC-PA membrane from SARIP (with SDS)

Table A.20 Mean pore size, standard deviation and MWCO of TFC-PA membrane from SARIP with different SDS concentrations (corresponding to Figure 2.4B and inset)

SDS concentration (CMC)	μ_p (nm)	σ_p	MWCO
0	0.334	1.219	274
0.25	0.310	1.177	208
0.5	0.295	1.156	178
1	0.290	1.144	167
1.5	0.300	1.180	195

Increasing PIP concentration in conventional IP results in polyamide with smaller mean pore size and MWCO. However, the standard deviation remains nearly unchanged (Table A.3), i.e., the pore size is still widely distributed. In contrast, TFC-PA from SARIP does not only have a smaller mean pore size and MWCO but also a smaller standard deviation (Table A.7).

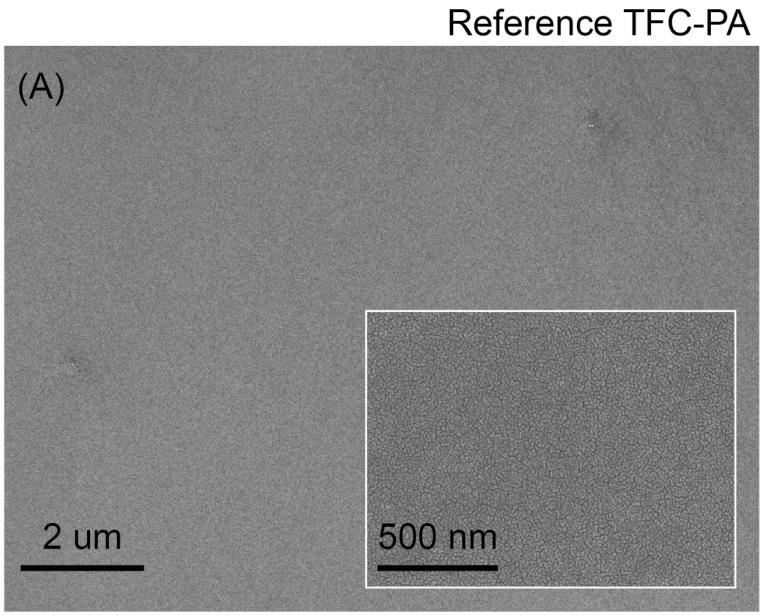

Figure B.1 SEM image of the surface morphology of TFC-PA NF membranes formed via conventional IP.

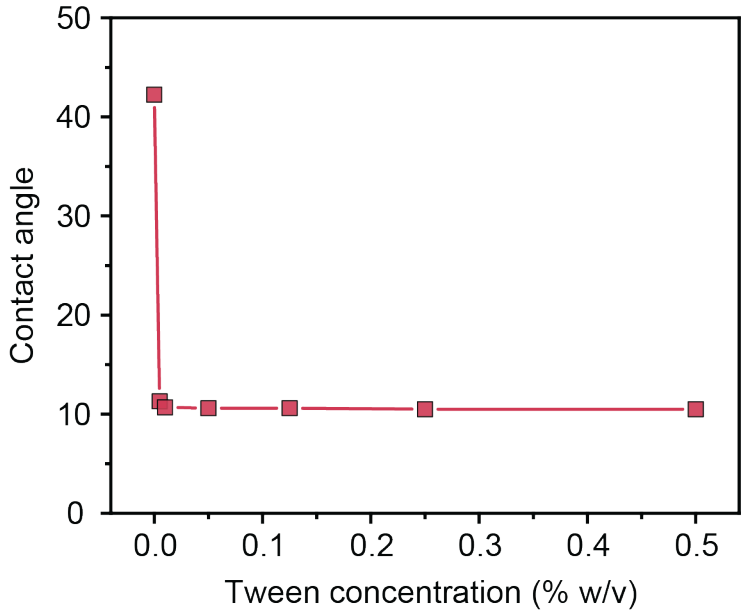

Figure B.2 Contact angle of PIP-Tween 80 aqueous solution on the PES UF substrate as a function of Tween 80 concentration.

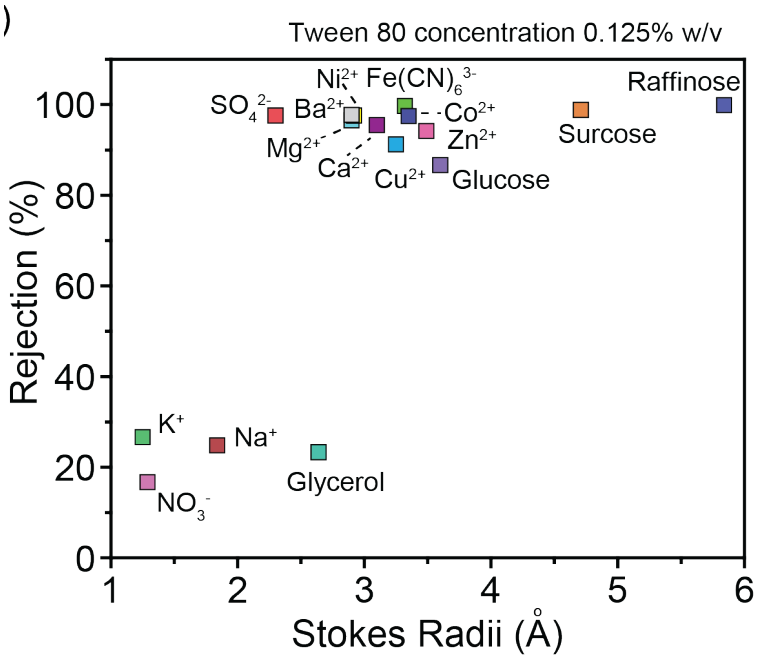

Figure B.3 Selectivity of different solutes as a function of Stokes radii for the PA-TFC NF membrane prepared via IP with 0.125% w/v Tween 80 in PIP solution.

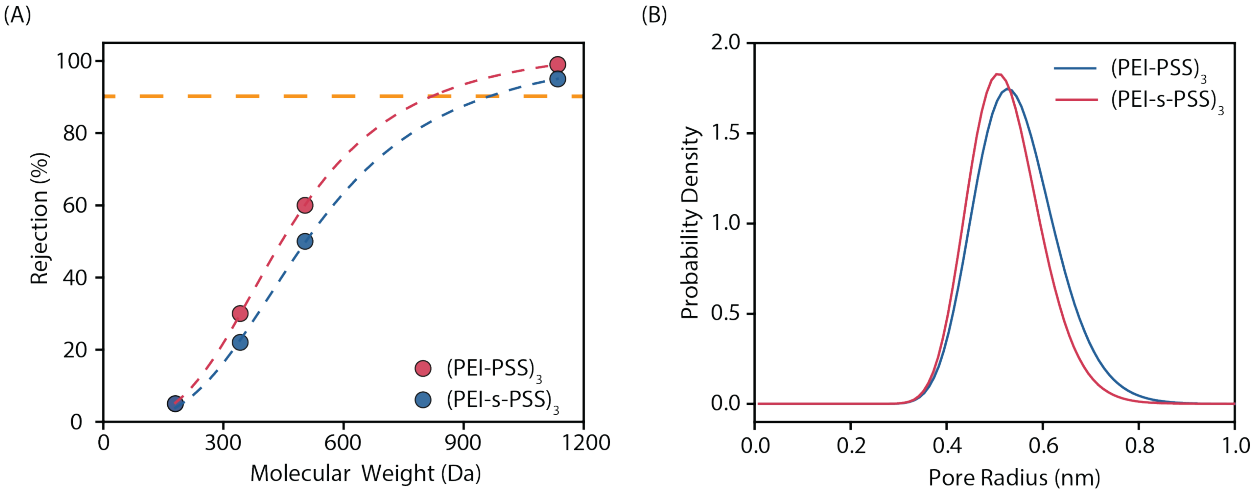

Figure C.1 (A) Rejection of neutral organic solutes of different MW by $(PEI\text{-}PSS)_3$ and $(PEI\text{-}s\text{-}PSS)_3$ LNF membrane (B) Pore size distribution estimated with data presented in (A).

D SUPPLEMENTARY MATERIALS FOR CHAPTER 6

a. Custom-made EIS cell

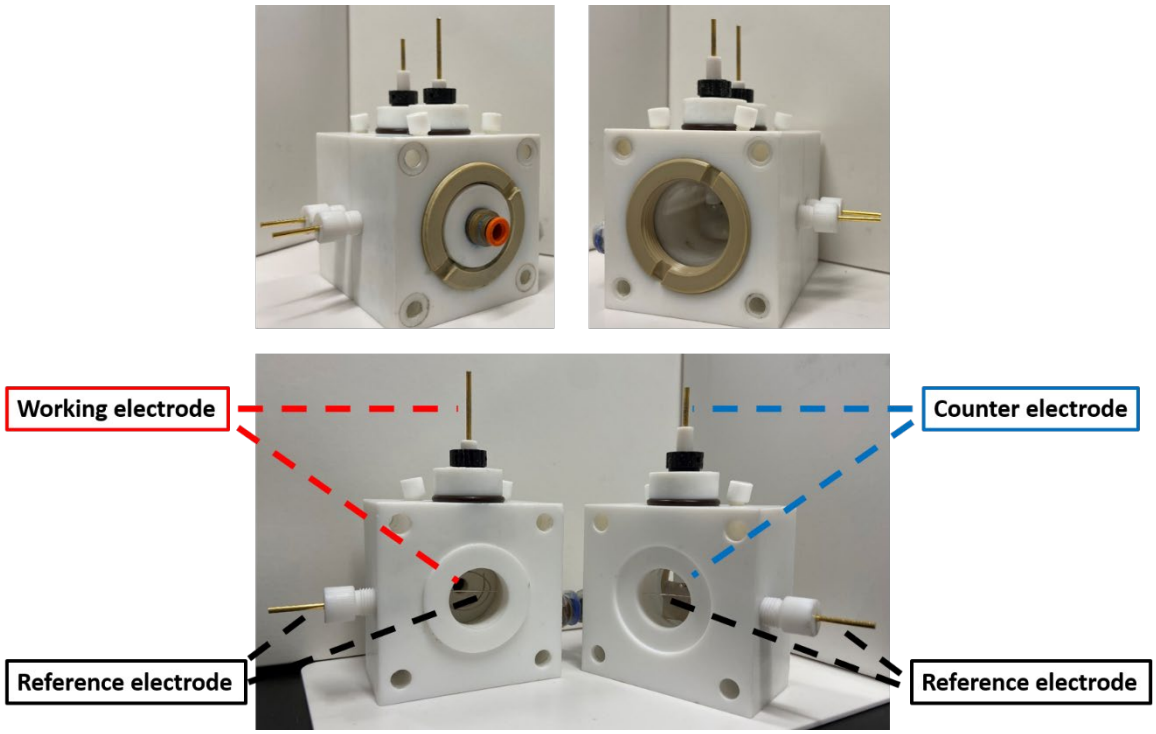

Figure D.1 Custom-made EIS cell.

b. Temporal evolution of solution resistance R_i and $R_{i,f}/R_i$ in the LbL assembly of polyelectrolyte multilayer films

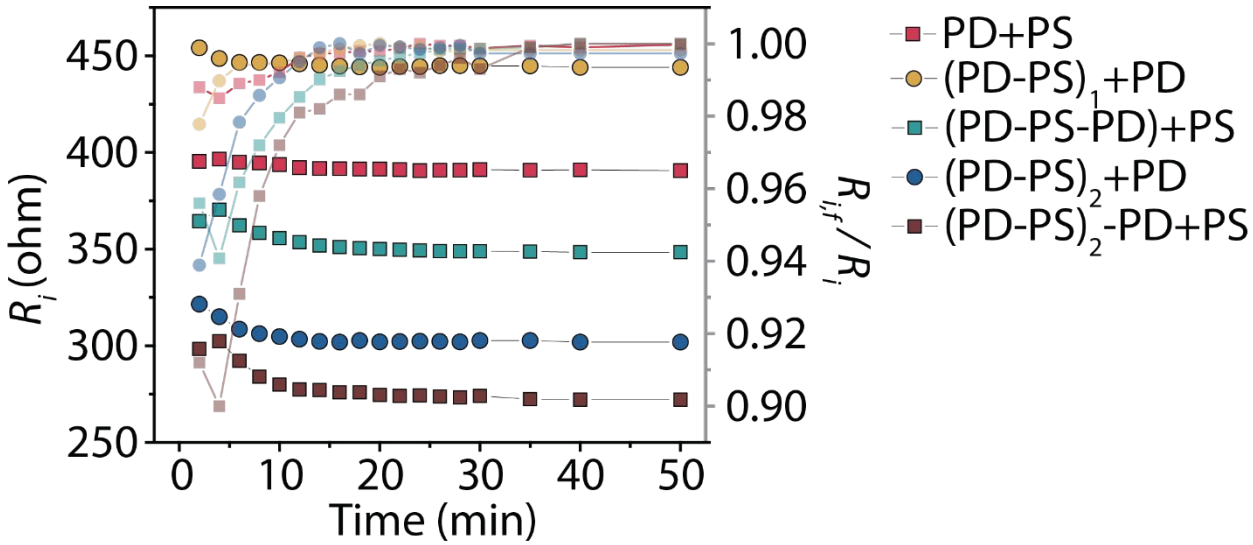

Figure D.2 Solution resistance (R_i) obtained from EIS measurements (opaque) and interfacial resistance, $R_{i,f}/R_i$ (transparent) as a function of time at different deposition stages during the fabrication of a 3-bilayer (PD-PS)$_3$ PEM-NF membrane.

c. Determination of Ri at the early stages of PDADMAC deposition via narrow frequency scan (10kHz to 300Hz)

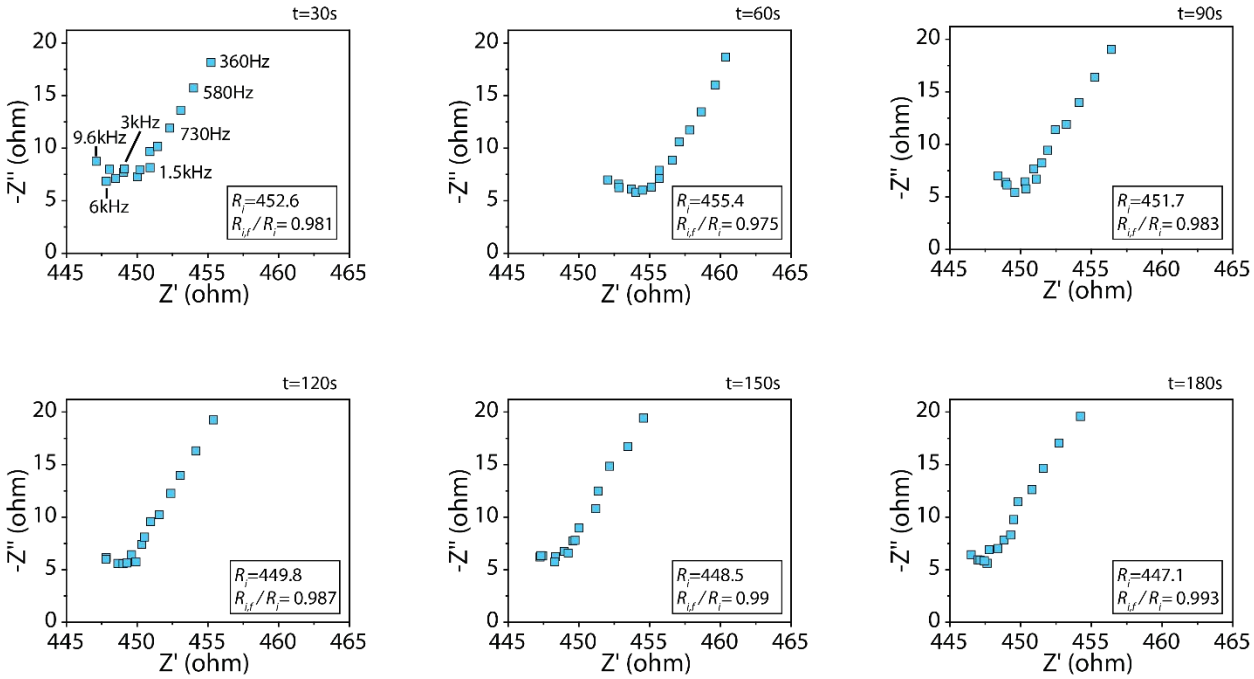

Figure D.3 Partial Nyquist plot of the impedance of the solution near the solution-membrane interface, in the frequency range of 10kHz to 300Hz, as a function of time in the deposition of the second PDADMAC layer, i.e., adsorption of PDADMAC onto the PAN-(PD-PS) surface.